



**26A6642AL
Revision 0
August 2005**



ESBWR Design Control Document

Tier 2

Chapter 3

Design of Structures, Components, Equipment, and Systems

Appendices 3A-3F

(Conditional Release - pending
closure of design verifications)



Contents

3A. SEISMIC SOIL-STRUCTURE INTERACTION ANALYSIS.....	3A-1
3A.1 Introduction.....	3A-1
3A.2 ESBWR Standard Plant Site Plan.....	3A-2
3A.3 Site Conditions.....	3A-4
3A.3.1 Generic Site Conditions.....	3A-4
3A.3.2 North Anna ESP Site Conditions.....	3A-4
3A.4 Input Motion and Damping Values.....	3A-6
3A.4.1 Input Motion.....	3A-6
3A.4.2 Damping Values.....	3A-6
3A.5 Soil-Structure Interaction Analysis Method.....	3A-7
3A.6 Soil-Structure Interaction Analysis Cases.....	3A-9
3A.7 Analysis Models.....	3A-11
3A.7.1 Method of Dynamic Structural Model Development.....	3A-11
3A.7.2 Lumped mass-Beam Stick Model for SSI Analysis.....	3A-12
3A.8 Analysis Results.....	3A-29
3A.9 Site Envelope Seismic Responses.....	3A-45
3A.9.1 Enveloping Maximum Structural Loads.....	3A-45
3A.9.2 Enveloping Floor Response Spectra.....	3A-45
3B. CONTAINMENT HYDRODYNAMIC LOADS.....	1
3B.1 Scope.....	1
3B.2 Description of Phenomena.....	2
3B.2.1 Loss-of-Coolant Accident.....	2
3B.2.1.1 Large Break Accident (Design Basis Accident).....	2
3B.2.1.2 Intermediate Break Accident.....	3
3B.2.1.3 Small Break Accident.....	4
3B.2.2 Safety Relief Valve Discharge.....	4
3B.2.3 Depressurization Valve Actuation.....	6
3B.3 Pool Swell Load.....	7
3B.3.1 Pool Swell (PS) Analytical Model.....	7
3B.3.1.1 Drywell Pressurization.....	7
3B.3.1.2 Hydrodynamic Loads.....	9
3B.3.2 Pool Boundary Loads.....	10
3B.3.3 Structural Impact and Drag Loads Above the Pool Surface.....	10
3B.3.4 Vacuum Breaker Load Due to Wetwell Nitrogen Compression.....	11
3B.3.5 Loads on Diaphragm Floor.....	11
3B.4 Condensation Oscillation Loads.....	12
3B.4.1 ABWR Horizontal Vent Test Program.....	12
3B.4.1.1 Description of CO Database.....	13
3B.4.1.2 Evaluation of CO Database.....	14

3B.4.2 Source Load Approach.....	14
3B.4.3 Basis for ESBWR Load Definition.....	15
3B.4.3.1 Review of ABWR and ESBWR Containment Geometry.....	15
3B.4.3.2 Review of Thermal-Hydraulic Conditions.....	16
3B.4.3.3 Frequency Content Evaluation.....	16
3B.4.4 Application of the ABWR CO Load to the ESBWR.....	18
3B.4.5 Local Condensation Oscillation Loads.....	18
3B.5 Chugging Loads.....	19
3B.5.1 Description of Chugging Data.....	19
3B.5.2 Evaluation of Chugging Data.....	19
3B.5.3 Chugging Load Definition.....	20
3B.5.4 Basis for ESBWR Chugging Load Definition.....	20
3B.5.4.1 Review of ABWR and ESBWR Containment Geometry.....	20
3B.5.4.2 Review of Thermal-hydraulic Conditions.....	20
3B.5.4.3 Frequency Content Evaluation.....	21
3B.5.5 Application of the ABWR Chugging Load To The ESBWR.....	21
3B.5.6 Horizontal Vent Loads.....	22
3B.6 Safety Relief Valve Loads.....	23
3B.6.1 SRV Design.....	23
3B.6.2 SRV Discharge Load.....	23
3B.6.3 Pool Boundary Loads.....	24
3B.6.3.1 Single Valve Discharge.....	25
3B.6.3.2 Multiple Valve Discharge.....	25
3B.6.3.3 SRV Bubble Pressure (Pb).....	26
3B.6.3.4 Quencher Steam Condensation Loads.....	27
3B.7 ESBWR Unique Design Features.....	28
3B.7.1 Passive Containment Cooling System.....	28
3B.7.1.1 PCCS Pool Swell Loads.....	28
3B.7.1.2 PCCS Condensation Loads.....	28
3B.7.2 Gravity-Driven Cooling System.....	28
3B.7.3 Lower Drywell Spillover Pipes.....	29
3B.8 Submerged Structure Loads.....	30
3B.8.1 Pool Swell Submerged Structure Loads.....	30
3B.8.2 CO Submerged Structure Loads.....	31
3B.8.3 CH Submerged Structure Loads.....	31
3B.8.4 SRV Submerged Structure Load.....	31
3B.8.5 PCCS Vent Discharge Load.....	31
3B.9 Load Combinations.....	32
3B.10 References.....	33
3C. COMPUTER PROGRAMS USED IN THE DESIGN AND ANALYSIS OF SEISMIC	
CATEGORY I STRUCTURES.....	3C-1
3C.1 Introduction.....	3C-1

3C.2 Static and Dynamic Structural Analysis Program (NASTRAN)	3C-1
3C.2.1 Description	3C-1
3C.2.2 Validation	3C-1
3C.2.3 Extent of Application	3C-1
3C.3 ABAQUS and ANACAP-U	3C-1
3C.3.1 Description	3C-1
3C.3.2 Validation	3C-2
3C.3.3 Extent of Application	3C-2
3C.4 Concrete Element Cracking Analysis Program (SSDP-2D)	3C-2
3C.4.1 Description	3C-2
3C.4.2 Validation	3C-2
3C.4.3 Extent of Application	3C-2
3C.1 Heat Transfer Analysis Program (TEMCOM2).....	3C-2
3C.4.4 Description	3C-2
3C.4.5 Validation	3C-3
3C.4.6 Extent of Application	3C-3
3C.5 Static and Dynamic Structural Analysis Systems: ANSYS	3C-3
3C.5.1 Description	3C-3
3C.5.2 Validation	3C-3
3C.5.3 Extent of Application	3C-3
3C.6 Soil-Structure Interaction	3C-3
3C.6.1 Dynamic Soil-Structure Interaction Analysis Program—DAC3N	3C-3
3C.6.1.1 Description	3C-3
3C.6.1.2 Validation	3C-4
3C.6.1.3 Extent of Application	3C-4
3D. COMPUTER PROGRAMS USED IN THE DESIGN OF COMPONENTS, EQUIPMENT	
AND Structures	3D-1
3D.1 Introduction	3D-1
3D.2 Fine Motion Control Rod Drive	3D-1
3D.2.1 Fine Motion Control Rod Drive - FMCRD01	3D-1
3D.2.2 Structural Analysis Programs	3D-1
3D.3 Reactor Pressure Vessel and Internals	3D-1
3D.4 Piping	3D-1
3D.4.1 Piping Analysis Program - PISYS	3D-1
3D.4.2 Component Analysis - ANSI7	3D-2
3D.4.3 Area Reinforcement - NOZAR	3D-2
3D.4.4 Dynamic Forcing Functions	3D-2
3D.4.4.1 Relief Valve Discharge Pipe Forces Computer Program - RVFOR	3D-2
3D.4.4.2 Turbine Stop Valve Closure - TSFOR	3D-2
3D.4.4.3 Hydraulic Transients-RELAP5/Mod 3.3	3D-2
3D.4.4.4 Subcompartment Pressurization - Contain 2.0	3D-3

3D.4.5 Integral Attachment - LUGST	3D-3
3D.4.6 Response Spectra Generation.....	3D-3
3D.4.6.1 ERSIN Computer Program	3D-3
3D.4.6.2 RINEX Computer Program.....	3D-3
3D.4.7 Piping Dynamic Analysis Program - PDA	3D-4
3D.4.8 Thermal Transient Program - LION	3D-4
3D.4.9 Engineering Analysis System - ANSYS05	3D-4
3D.4.10 Piping Analysis Program - EZPYP	3D-4
3D.4.11 Differential Displacement Program - DISPL.....	3D-4
3D.5 Pumps and Motors	3D-5
3D.5.1 Structural Analysis Program - SAP4G07.....	3D-5
3D.5.2 Effects of Flange Joint Connections - FTFLG01	3D-5
3D.6 Heat Exchangers	3D-5
3D.6.1 Structural Analysis Program - SAP4G07.....	3D-5
3D.6.2 Calculation of Shell Attachment Parameters and Coefficients - BILDR01	3D-5
3D.7 References.....	3D-5
3E. GUIDELINES FOR LEAK BEFORE BREAK APPLICATION.....	3E-1
3E.1 Introduction	3E-1
3E.1.1 Material Selection Guidelines	3E-1
3E.1.2 Deterministic Evaluation Procedure.....	3E-1
3E.2 Material Fracture Toughness Characterization	3E-4
3E.2.1 Fracture Toughness Characterization	3E-4
3E.2.2 Carbon Steels and Associated Welds	3E-5
3E.2.2.1 Fracture Toughness Test Program.....	3E-6
3E.2.2.2 Material (J/T) Curve Selection	3E-8
3E.2.3 Stainless Steels and Associated Welds.....	3E-9
3E.3 Fracture Mechanics Methods	3E-10
3E.3.1 Elastic-Plastic Fracture Mechanics or (J/T) Methodology	3E-10
3E.3.1.1 Basic (J/T) Methodology	3E-10
3E.3.1.2 J Estimation Scheme Procedure	3E-11
3E.3.1.3 Tearing Instability Evaluation Considering Both the Membrane and Bending Stresses	3E-12
3E.3.2 Application of (J/T) Methodology to Carbon Steel Piping	3E-13
3E.3.2.1 Determination of Ramberg-Osgood Parameters for 550°F Evaluation.....	3E-13
3E.3.2.2 Determination of Ramberg-Osgood Parameters for 420°F Evaluation.....	3E-13
3E.3.3 Modified Limit Load Methodology for Austenitic Stainless Steel Piping.....	3E-14
3E.3.4 Bimetallic Welds	3E-14
3E.4 Leak Rate Calculation Methods	3E-15
3E.4.1 Leak Rate Estimation for Pipes Carrying Water	3E-15
3E.4.1.1 Description of Basis for Flow Rate Calculation.....	3E-15
3E.4.1.2 Basic for Crack Opening Area Calculation	3E-16
3E.4.1.3 Comparison Verification with Experimental Data	3E-16

3E.4.2 Flow Rate Estimation for Saturated Steam	3E-16
3E.4.2.1 Evaluation Method	3E-16
3E.4.2.2 Selection of Appropriate Friction Factor.....	3E-16
3E.4.2.3 Crack Opening Area Formulation	3E-17
3E.5 Leak Detection Capabilities	3E-19
3E.6 References	3E-20
3F. RESPONSE OF STRUCTURES TO CONTAINMENT LOADS.....	3F-1
3F.1 Scope.....	3F-1
3F.2 Dynamic Response	3F-1
3F.2.1 Classification of Analytical Procedure	3F-1
3F.2.2 Analysis Models	3F-1
3F.2.3 Load Application	3F-1
3F.2.4 Analysis Method.....	3F-3
3F.3 Hydrodynamic Load Analysis Results	3F-3

List of Tables

Table 3A.2-1	Standard ESBWR Building Dimensions
Table 3A.3-1	Generic Site Properties for SSI Analysis ^{(1),(2)}
Table 3A.3-2	North Anna Site-specific Properties for SSI Analysis
Table 3A.5-1	Soil Spring and Damping Coefficient for RBFB complex
Table 3A.5-2	Soil Spring and Damping Coefficient for CB
Table 3A.6-1	Seismic SSI Analysis Cases
Table 3A.7-1	Eigenvalue Analysis Results for RBFB model at Soft Site
Table 3A.7-2	Eigenvalue Analysis Results for RBFB model at Medium Site
Table 3A.7-3	Eigenvalue Analysis Results for RBFB model at Hard Site
Table 3A.7-4	Eigenvalue Analysis Results for RBFB model in Fixed-base Case
Table 3A.7-5	Eigenvalue Analysis Results for RBFB model at Best-estimate North Anna Site
Table 3A.7-6	Eigenvalue Analysis Results for RBFB model at Upper-bound North Anna Site
Table 3A.7-7	Eigenvalue Analysis Results for RBFB model at Lower-bound North Anna Site
Table 3A.7-8	Eigenvalue Analysis Results for CB model at Soft Site
Table 3A.7-9	Eigenvalue Analysis Results for CB model at Medium Site
Table 3A.7-10	Eigenvalue Analysis Results for CB model at Hard Site
Table 3A.7-11	Eigenvalue Analysis Results for CB model in Fixed-base Case
Table 3A.7-12	Eigenvalue Analysis Results for CB model at Best-estimate North Anna Site
Table 3A.7-13	Eigenvalue Analysis Results for CB model at Upper-bound North Anna Site
Table 3A.7-14	Eigenvalue Analysis Results for CB model at Lower-bound North Anna Site
Table 3A.8-1	Maximum Forces - X Direction
Table 3A.8-2	Maximum Forces - Y Direction
Table 3A.9-1	Enveloping Seismic Loads: RBFB Stick
Table 3A.9-2	Enveloping Seismic Loads: RCCV Stick
Table 3A.9-3	Enveloping Seismic Loads: VW/PED Stick
Table 3A.9-4	Enveloping Seismic Loads: RSW Stick
Table 3A.9-5	Enveloping Seismic Loads: RPV Stick
Table 3A.9-6	Enveloping Seismic Loads: CB Stick
Table 3A.9-7	Enveloping Maximum Vertical Acceleration: RBFB
Table 3A.9-8	Enveloping Maximum Vertical Acceleration: RCCV
Table 3A.9-9	Enveloping Maximum Vertical Acceleration: VW/Pedestal
Table 3A.9-10	Enveloping Maximum Vertical Acceleration: RSW
Table 3A.9-11	Enveloping Maximum Vertical Acceleration: RBFB Flexible Slab Oscillators
Table 3A.9-12	Enveloping Maximum Acceleration: CB
Table 3B-1	Pool Swell Results
Table 3B-2	Standard Drag Coefficients for Various Objects
Table 3B-3	Hydrodynamic Mass and Acceleration Drag Volumes for Two-Dimensional Structural Component
Table 3B-4	SRV Bubble Pressure
Table 3E-1	Electrodes and Filler Metal Requirements for Carbon Steel Welds
Table 3E-2	Supplier Provided Chemical Composition and Mechanical Properties Information
Table 3E-3	Standard Tension Test Data at Temperature
Table 3E-4	Summary of Carbon Steel J-R Curve Tests
Table 3E-5	Mass Flow Rate Versus fl/D_h Values

Table 3F-1 Maximum Accelerations for AP Loadings (g)

Table 3F-2 Maximum Accelerations for Hydrodynamic Loads (g)

Table 3F-3 Maximum Displacements for AP Loadings (mm)

Table 3F-4 Maximum Displacements for Hydrodynamic Loads (mm)

List of Illustrations

Figure 3A.7-1. RBFB Stick Model
 Figure 3A.7-2. RCCV Stick Model
 Figure 3A.7-3. Pedestal Stick Model
 Figure 3A.7-4. ESBWR RBFB Complex Seismic Model
 Figure 3A.7-5. ESBWR Control Building Seismic Model
 Figure 3A.8-1a. Floor Response Spectra – RBFB Refueling Floor X
 Figure 3A.8-1b. Floor Response Spectra – RCCV Top Slab X
 Figure 3A.8-1c. Floor Response Spectra – Vent Wall Top X
 Figure 3A.8-1d. Floor Response Spectra – RSW Top X
 Figure 3A.8-1e. Floor Response Spectra – RPV Top X
 Figure 3A.8-1f. Floor Response Spectra – RBFB Basemat X
 Figure 3A.8-1g. Floor Response Spectra – CB Top X
 Figure 3A.8-2a. Floor Response Spectra – RBFB Refueling Floor Y
 Figure 3A.8-2b. Floor Response Spectra – RCCV Top Slab Y
 Figure 3A.8-2c. Floor Response Spectra – Vent Wall Top Y
 Figure 3A.8-2d. Floor Response Spectra – RSW Top Y
 Figure 3A.8-2e. Floor Response Spectra – RPV Top Y
 Figure 3A.8-2f. Floor Response Spectra – RBFB Basemat Y
 Figure 3A.8-2g. Floor Response Spectra – CB Top Y
 Figure 3A.8-3a. Floor Response Spectra – RBFB Refueling Floor Z
 Figure 3A.8-3b. Floor Response Spectra – RCCV Top Slab Z
 Figure 3A.8-3c. Floor Response Spectra – Vent Wall Top Z
 Figure 3A.8-3d. Floor Response Spectra – RSW Top Z
 Figure 3A.8-3e. Floor Response Spectra – RPV Top Z
 Figure 3A.8-3f. Floor Response Spectra – RBFB Basemat Z
 Figure 3A.8-3g. Floor Response Spectra – CB Top Z
 Figure 3A.9-1a. Enveloping Floor Response Spectra – RBFB Refueling Floor X
 Figure 3A.9-1b. Enveloping Floor Response Spectra – RCCV Top Slab X
 Figure 3A.9-1c. Enveloping Floor Response Spectra – Vent Wall Top X
 Figure 3A.9-1d. Enveloping Floor Response Spectra – RSW Top X
 Figure 3A.9-1e. Enveloping Floor Response Spectra – RPV Top X
 Figure 3A.9-1f. Enveloping Floor Response Spectra – RBFB Basemat X
 Figure 3A.9-1g. Enveloping Floor Response Spectra – CB Top X
 Figure 3A.9-2a. Enveloping Floor Response Spectra – RBFB Refueling Floor Y
 Figure 3A.9-2b. Enveloping Floor Response Spectra – RCCV Top Slab Y
 Figure 3A.9-2c. Enveloping Floor Response Spectra – Vent Wall Top Y
 Figure 3A.9-2d. Enveloping Floor Response Spectra – RSW Top Y
 Figure 3A.9-2e. Enveloping Floor Response Spectra – RPV Top Y
 Figure 3A.9-2f. Enveloping Floor Response Spectra – RBFB Basemat Y
 Figure 3A.9-2g. Enveloping Floor Response Spectra – CB Top Y
 Figure 3A.9-3a. Enveloping Floor Response Spectra – RBFB Refueling Floor Z
 Figure 3A.9-3b. Enveloping Floor Response Spectra – RCCV Top Slab Z
 Figure 3A.9-3c. Enveloping Floor Response Spectra – Vent Wall Top Z
 Figure 3A.9-3d. Enveloping Floor Response Spectra – RSW Top Z

- Figure 3A.9-3e. Enveloping Floor Response Spectra – RPV Top Z
- Figure 3A.9-3f. Enveloping Floor Response Spectra – RBFB Basemat Z
- Figure 3A.9-3g. Enveloping Floor Response Spectra – CB Top Z
- Figure 3B-1. Suppression Pool Swell Boundary Bubble Pressure Spatial Distribution, Normalized to Maximum Bubble Pressure
- Figure 3B-2. Containment CO Source Load Methodology
- Figure 3B-3. Spatial Load Distribution for CO
- Figure 3B-4. Containment CH Source Load Methodology
- Figure 3B-5. Spatial Load Distribution for CH
- Figure 3B-6. Load Distribution Region of Influence
- Figure 3B-7. Normalized Quencher Bubble Pressure Time History (Ideal)
- Figure 3B-8. SRV Boundary Pressure Spatial Distribution, Normalized to Maximum Pressure Amplitude
- Figure 3B-9. Typical Event – Time Relationship for a DBA
- Figure 3E-1. Schematic Representation of Material J-Integral R and J-T Curves
- Figure 3E-2. Carbon Steel Test Specimen Orientation Code
- Figure 3E-3. Toughness Anisotropy of ASTM 106 Pipe (152 mm Sch. 80)
- Figure 3E-4. Charpy Energies for Pipe Test Material as a Function of Orientation and Temperature
- Figure 3E-5. Charpy Energies for Plate Test Material as a Function of Orientation and Temperature
- Figure 3E-6. Comparison of Base Metal, Weld and HAZ Charpy Energies for SA 333 Grade 6
- Figure 3E-7. Plot of 550°F True Stress-True Strain Curves for SA 333 Grade 6 Carbon Steel
- Figure 3E-8. Plot of 550°F True Stress-True Strain Curves for SA 516 Grade 70 Carbon Steel
- Figure 3E-9. Plot of 350°F True Stress-True Strain Curves for SA 333 Grade 6 Carbon Steel
- Figure 3E-10. Plot of 350°F True Stress-True Strain Curves for SA 516 Grade 70 Carbon Steel
- Figure 3E-11. Plot of 550°F Test J-R Curve for Pipe Weld
- Figure 3E-12. Plot of 550°F Jmod, Tmod Data from Test J-R Curve
- Figure 3E-13. Carbon Steel J-T Curve for 420°F
- Figure 3E-14. Schematic Illustration of Tearing Stability Evaluation
- Figure 3E-15. Schematic Representation of Instability Tension and Bending Stresses as a Function of Flaw Strength
- Figure 3E-16. SA 333 Grade 6 Stress-Strain Data at 550°F in the Ramberg-Osgood Format
- Figure 3E-17. Carbon Steel Stress-Strain Data at 350°F in the Ramberg-Osgood Format
- Figure 3E-18. Comparison of PICEP Predictions with Measured Leak Rates
- Figure 3E-19. Pipe Flow Model
- Figure 3E-20. Mass Flow Rates for Steam/Water Mixtures
- Figure 3E-21. Friction Factors for Pipes
- Figure 3F-1. Beam Model for AP Load
- Figure 3F-2. Building Shell Model
- Figure 3F-3. RPV Shell Model
- Figure 3F-4. Floor Response Spectrum—AP Envelope, Node: 701, Horizontal
- Figure 3F-5. Floor Response Spectrum—AP Envelope, Node: 706, Horizontal
- Figure 3F-6. Floor Response Spectrum—AP Envelope, Node: 208, Horizontal
- Figure 3F-7. Floor Response Spectrum—SRV Envelope, Node: 1104, Vertical
- Figure 3F-8. Floor Response Spectrum—SRV Envelope, Node: 1254, Vertical

- Figure 3F-9. Floor Response Spectrum—SRV Envelope , Node: 1119, Vertical
Figure 3F-10. Floor Response Spectrum—SRV Envelope , Node: 1159, Vertical
Figure 3F-11. Floor Response Spectrum—SRV Envelope , Node: 1104, Horizontal
Figure 3F-12. Floor Response Spectrum—SRV Envelope , Node: 1254, Horizontal
Figure 3F-13. Floor Response Spectrum—SRV Envelope, Node: 1119, Vertical
Figure 3F-14. Floor Response Spectrum—SRV Envelope, Node: 1159, Horizontal
Figure 3F-15. Floor Response Spectrum—CH & CO Envelope, Node: 1104, Vertical
Figure 3F-16. Floor Response Spectrum—CH & CO Envelope, Node: 1254, Vertical
Figure 3F-17. Floor Response Spectrum—CH & CO Envelope, Node: 1119, Vertical
Figure 3F-18. Floor Response Spectrum—CH & CO Envelope, Node: 1159, Vertical
Figure 3F-19. Floor Response Spectrum—CH Envelope, Node: 1104, Horizontal
Figure 3F-20. Floor Response Spectrum—CH Envelope, Node: 1254, Horizontal
Figure 3F-21. Floor Response Spectrum—CH Envelope, Node: 1119, Horizontal
Figure 3F-22. Floor Response Spectrum—CH Envelope, Node: 1159, Horizontal

Global Abbreviations And Acronyms List

<u>Term</u>	<u>Definition</u>
10 CFR	Title 10, Code of Federal Regulations
A/D	Analog-to-Digital
AASHTO	American Association of Highway and Transportation Officials
AB	Auxiliary Boiler
ABS	Auxiliary Boiler System
ABWR	Advanced Boiling Water Reactor
ac / AC	Alternating Current
AC	Air Conditioning
ACF	Automatic Control Function
ACI	American Concrete Institute
ACS	Atmospheric Control System
AD	Administration Building
ADS	Automatic Depressurization System
AEC	Atomic Energy Commission
AFIP	Automated Fixed In-Core Probe
AGMA	American Gear Manufacturer's Association
AHS	Auxiliary Heat Sink
AISC	American Institute of Steel Construction
AISI	American Iron and Steel Institute
AL	Analytical Limit
ALARA	As Low As Reasonably Achievable
ALWR	Advanced Light Water Reactor
ANS	American Nuclear Society
ANSI	American National Standards Institute
AOO	Anticipated Operational Occurrence
AOV	Air Operated Valve
AP	Annulus Pressurization
API	American Petroleum Institute
APLHGR	Average Planar Linear Heat Generation Rate
APRM	Average Power Range Monitor
APR	Automatic Power Regulator
APRS	Automatic Power Regulator System
ARI	Alternate Rod Insertion
ARMS	Area Radiation Monitoring System
ARS	Amplified Response Spectrum
ASA	American Standards Association
ASD	Adjustable Speed Drive
ASHRAE	American Society of Heating, Refrigerating, and Air Conditioning Engineers
ASME	American Society of Mechanical Engineers

<u>Term</u>	<u>Definition</u>
AST	Alternate Source Term
ASTM	American Society of Testing Methods
AT	Unit Auxiliary Transformer
ATLM	Automated Thermal Limit Monitor
ATWS	Anticipated Transients Without Scram
AV	Allowable Value
AWS	American Welding Society
AWWA	American Water Works Association
B&PV	Boiler and Pressure Vessel
BAF	Bottom of Active Fuel
BHP	Brake Horse Power
BOP	Balance of Plant
BPU	Bypass Unit
BPWS	Banked Position Withdrawal Sequence
BRE	Battery Room Exhaust
BRL	Background Radiation Level
BTP	NRC Branch Technical Position
BTU	British Thermal Unit
BWR	Boiling Water Reactor
BWROG	Boiling Water Reactor Owners Group
CAV	Cumulative absolute velocity
C&FS	Condensate and Feedwater System
C&I	Control and Instrumentation
C/C	Cooling and Cleanup
CB	Control Building
CBHVAC	Control Building HVAC
CCI	Core-Concrete Interaction
CDF	Core Damage Frequency
CFR	Code of Federal Regulations
CIRC	Circulating Water System
CIS	Containment Inerting System
CIV	Combined Intermediate Valve
CLAVS	Clean Area Ventilation Subsystem of Reactor Building HVAC
CM	Cold Machine Shop
CMS	Containment Monitoring System
CMU	Control Room Multiplexing Unit
COL	Combined Operating License
COLR	Core Operating Limits Report
CONAVS	Controlled Area Ventilation Subsystem of Reactor Building HVAC
CPR	Critical Power Ratio

<u>Term</u>	<u>Definition</u>
CPS	Condensate Purification System
CPU	Central Processing Unit
CR	Control Rod
CRD	Control Rod Drive
CRDA	Control Rod Drop Accident
CRDH	Control Rod Drive Housing
CRDHS	Control Rod Drive Hydraulic System
CRGT	Control Rod Guide Tube
CRHA	Control Room Habitability Area
CRT	Cathode Ray Tube
CS&TS	Condensate Storage and Transfer System
CSDM	Cold Shutdown Margin
CS / CST	Condensate Storage Tank
CT	Main Cooling Tower
CTVCF	Constant Voltage Constant Frequency
CUF	Cumulative usage factor
CWS	Chilled Water System
D-RAP	Design Reliability Assurance Program
DAC	Design Acceptance Criteria
DAW	Dry Active Waste
DBA	Design Basis Accident
dc / DC	Direct Current
DCS	Drywell Cooling System
DCIS	Distributed Control and Information System
DEPSS	Drywell Equipment and Pipe Support Structure
DF	Decontamination Factor
D/F	Diaphragm Floor
DG	Diesel-Generator
DHR	Decay Heat Removal
DM&C	Digital Measurement and Control
DOF	Degree of freedom
DOI	Dedicated Operators Interface
DOT	Department of Transportation
dPT	Differential Pressure Transmitter
DPS	Diverse Protection System
DPV	Depressurization Valve
DR&T	Design Review and Testing
DTM	Digital Trip Module
DW	Drywell
EB	Electrical Building

<u>Term</u>	<u>Definition</u>
EBAS	Emergency Breathing Air System
EBHV	Electrical Building HVAC
ECCS	Emergency Core Cooling System
E-DCIS	Essential DCIS (Distributed Control and Information System)
EDO	Environmental Qualification Document
EFDS	Equipment and Floor Drainage System
EFPY	Effective full power years
EHC	Electrohydraulic Control (Pressure Regulator)
ENS	Emergency Notification System
EOC	Emergency Operations Center
EOC	End of Cycle
EOF	Emergency Operations Facility
EOP	Emergency Operating Procedures
EPDS	Electric Power Distribution System
EPG	Emergency Procedure Guidelines
EPRI	Electric Power Research Institute
EQ	Environmental Qualification
ERICP	Emergency Rod Insertion Control Panel
ERIP	Emergency Rod Insertion Panel
ESBWR	Economic Simplified Boiling Water Reactor
ESF	Engineered Safety Feature
ETS	Emergency Trip System
FAC	Flow-Accelerated Corrosion
FAPCS	Fuel and Auxiliary Pools Cooling System
FATT	Fracture Appearance Transition Temperature
FB	Fuel Building
FBHV	Fuel Building HVAC
FCI	Fuel-Coolant Interaction
FCM	File Control Module
FCS	Flammability Control System
FCU	Fan Cooling Unit
FDDI	Fiber Distributed Data Interface
FFT	Fast Fourier Transform
FFWTR	Final Feedwater Temperature Reduction
FHA	Fire Hazards Analysis
FIV	Flow-Induced Vibration
FMCRD	Fine Motion Control Rod Drive
FMEA	Failure Modes and Effects Analysis
FPS	Fire Protection System
FO	Diesel Fuel Oil Storage Tank

<u>Term</u>	<u>Definition</u>
FOAKE	First-of-a-Kind Engineering
FPE	Fire Pump Enclosure
FTDC	Fault-Tolerant Digital Controller
FTS	Fuel Transfer System
FW	Feedwater
FWCS	Feedwater Control System
FWS	Fire Water Storage Tank
GCS	Generator Cooling System
GDC	General Design Criteria
GDSCS	Gravity-Driven Cooling System
GE	General Electric Company
GE-NE	GE Nuclear Energy
GEN	Main Generator System
GETAB	General Electric Thermal Analysis Basis
GL	Generic Letter
GM	Geiger-Mueller Counter
GM-B	Beta-Sensitive GM Detector
GSIC	Gamma-Sensitive Ion Chamber
GSOS	Generator Sealing Oil System
GWSR	Ganged Withdrawal Sequence Restriction
HAZ	Heat-Affected Zone
HCU	Hydraulic Control Unit
HCW	High Conductivity Waste
HDVS	Heater Drain and Vent System
HEI	Heat Exchange Institute
HELB	High Energy Line Break
HEP	Human error probability
HEPA	High Efficiency Particulate Air/Absolute
HFE	Human Factors Engineering
HFF	Hollow Fiber Filter
HGCS	Hydrogen Gas Cooling System
HIC	High Integrity Container
HID	High Intensity Discharge
HIS	Hydraulic Institute Standards
HM	Hot Machine Shop & Storage
HP	High Pressure
HPNSS	High Pressure Nitrogen Supply System
HPT	High-pressure turbine
HRA	Human Reliability Assessment
HSI	Human-System Interface

<u>Term</u>	<u>Definition</u>
HSSS	Hardware/Software System Specification
HVAC	Heating, Ventilation and Air Conditioning
HVS	High Velocity Separator
HWCS	Hydrogen Water Chemistry System
HWS	Hot Water System
HX	Heat Exchanger
I&C	Instrumentation and Control
I/O	Input/Output
IAS	Instrument Air System
IASCC	Irradiation Assisted Stress Corrosion Cracking
IBC	International Building Code
IC	Ion Chamber
IC	Isolation Condenser
ICD	Interface Control Diagram
ICS	Isolation Condenser System
IE	Inspection and Enforcement
IEB	Inspection and Enforcement Bulletin
IED	Instrument and Electrical Diagram
IEEE	Institute of Electrical and Electronic Engineers
IGSCC	Intergranular Stress Corrosion Cracking
IIS	Iron Injection System
ILRT	Integrated Leak Rate Test
IOP	Integrated Operating Procedure
IMC	Induction Motor Controller
IMCC	Induction Motor Controller Cabinet
IRM	Intermediate Range Monitor
ISA	Instrument Society of America
ISI	In-Service Inspection
ISLT	In-Service Leak Test
ISM	Independent Support Motion
ISMA	Independent Support Motion Response Spectrum Analysis
ISO	International Standards Organization
ITA	Inspections, Tests or Analyses
ITAAC	Inspections, Tests, Analyses and Acceptance Criteria
ITA	Initial Test Program
LAPP	Loss of Alternate Preferred Power
LCO	Limiting Conditions for Operation
LCW	Low Conductivity Waste
LD	Logic Diagram
LDA	Lay down Area

<u>Term</u>	<u>Definition</u>
LD&IS	Leak Detection and Isolation System
LERF	Large early release frequency
LFCV	Low Flow Control Valve
LHGR	Linear Heat Generation Rate
LLRT	Local Leak Rate Test
LMU	Local Multiplexer Unit
LO	Dirty/Clean Lube Oil Storage Tank
LOCA	Loss-of-Coolant-Accident
LOFW	Loss-of-feedwater
LOOP	Loss of Offsite Power
LOPP	Loss of Preferred Power
LP	Low Pressure
LPCI	Low Pressure Coolant Injection
LPCRD	Locking Piston Control Rod Drive
LPMS	Loose Parts Monitoring System
LPRM	Local Power Range Monitor
LPSP	Low Power Setpoint
LWMS	Liquid Waste Management System
MAAP	Modular Accident Analysis Program
MAPLHGR	Maximum Average Planar Linear Head Generation Rate
MAPRAT	Maximum Average Planar Ratio
MBB	Motor Built-In Brake
MCC	Motor Control Center
MCES	Main Condenser Evacuation System
MCPR	Minimum Critical Power Ratio
MCR	Main Control Room
MCRP	Main Control Room Panel
MELB	Moderate Energy Line Break
MLHGR	Maximum Linear Heat Generation Rate
MMI	Man-Machine Interface
MMIS	Man-Machine Interface Systems
MOV	Motor-Operated Valve
MPC	Maximum Permissible Concentration
MPL	Master Parts List
MS	Main Steam
MSIV	Main Steam Isolation Valve
MSL	Main Steamline
MSLB	Main Steamline Break
MSLBA	Main Steamline Break Accident
MSR	Moisture Separator Reheater

<u>Term</u>	<u>Definition</u>
MSV	Mean Square Voltage
MT	Main Transformer
MTTR	Mean Time To Repair
MWS	Makeup Water System
NBR	Nuclear Boiler Rated
NBS	Nuclear Boiler System
NCIG	Nuclear Construction Issues Group
NDE	Nondestructive Examination
NE-DCIS	Non-Essential Distributed Control and Information System
NDRC	National Defense Research Committee
NDT	Nil Ductility Temperature
NFPA	National Fire Protection Association
NIST	National Institute of Standard Technology
NMS	Neutron Monitoring System
NOV	Nitrogen Operated Valve
NPHS	Normal Power Heat Sink
NPSH	Net Positive Suction Head
NRC	Nuclear Regulatory Commission
NRHX	Non-Regenerative Heat Exchanger
NS	Non-seismic (non-seismic Category I)
NSSS	Nuclear Steam Supply System
NT	Nitrogen Storage Tank
NTSP	Nominal Trip Setpoint
O&M	Operation and Maintenance
O-RAP	Operational Reliability Assurance Program
OBCV	Overboard Control Valve
OBE	Operating Basis Earthquake
OGS	Offgas System
OHLHS	Overhead Heavy Load Handling System
OIS	Oxygen Injection System
OLMCPR	Operating Limit Minimum Critical Power Ratio
OLU	Output Logic Unit
OOS	Out-of-service
ORNL	Oak Ridge National Laboratory
OSC	Operational Support Center
OSHA	Occupational Safety and Health Administration
OSI	Open Systems Interconnect
P&ID	Piping and Instrumentation Diagram
PA/PL	Page/Party-Line
PABX	Private Automatic Branch (Telephone) Exchange

<u>Term</u>	<u>Definition</u>
PAM	Post Accident Monitoring
PAR	Passive Autocatalytic Recombiner
PAS	Plant Automation System
PASS	Post Accident Sampling Subsystem of Containment Monitoring System
PCC	Passive Containment Cooling
PCCS	Passive Containment Cooling System
PCT	Peak cladding temperature
PCV	Primary Containment Vessel
PDF	Process Flow Diagram
PGA	Peak Ground Acceleration
PGCS	Power Generation and Control Subsystem of Plant Automation System
PH	Pump House
PL	Parking Lot
PM	Preventive Maintenance
PMCS	Performance Monitoring and Control Subsystem of NE-DCIS
PMF	Probable Maximum Flood
PMP	Probable Maximum Precipitation
PQCL	Product Quality Check List
PRA	Probabilistic Risk Assessment
PRMS	Process Radiation Monitoring System
PRNM	Power Range Neutron Monitoring
PS	Plant Stack
PSD	Power Spectra Density
PSS	Process Sampling System
PSWS	Plant Service Water System
PT	Pressure Transmitter
PWR	Pressurized Water Reactor
QA	Quality Assurance
RACS	Rod Action Control Subsystem
RAM	Reliability, Availability and Maintainability
RAPI	Rod Action and Position Information
RAT	Reserve Auxiliary Transformer
RB	Reactor Building
RBC	Rod Brake Controller
RBCC	Rod Brake Controller Cabinet
RBCWS	Reactor Building Chilled Water Subsystem
RBHV	Reactor Building HVAC
RBS	Rod Block Setpoint
RBV	Reactor Building Vibration
RC&IS	Rod Control and Information System

<u>Term</u>	<u>Definition</u>
RCC	Remote Communication Cabinet
RCCV	Reinforced Concrete Containment Vessel
RCCWS	Reactor Component Cooling Water System
RCPB	Reactor Coolant Pressure Boundary
RCS	Reactor Coolant System
RDA	Rod Drop Accident
RDC	Resolver-to-Digital Converter
REPAVS	Refueling and Pool Area Ventilation Subsystem of Fuel Building HVAC
RFP	Reactor Feed Pump
RG	Regulatory Guide
RHR	residual heat removal (function)
RHX	Regenerative Heat Exchanger
RMS	Root Mean Square
RMS	Radiation Monitoring Subsystem
RMU	Remote Multiplexer Unit
RO	Reverse Osmosis
ROM	Read-only Memory
RPS	Reactor Protection System
RPV	Reactor Pressure Vessel
RRPS	Reference Rod Pull Sequence
RSM	Rod Server Module
RSPC	Rod Server Processing Channel
RSS	Remote Shutdown System
RSSM	Reed Switch Sensor Module
RSW	Reactor Shield Wall
RTIF	Reactor Trip and Isolation Function(s)
RT _{NDT}	Reference Temperature of Nil-Ductility Transition
RTP	Reactor Thermal Power
RW	Radwaste Building
RWCU/SDC	Reactor Water Cleanup/Shutdown Cooling
RWE	Rod Withdrawal Error
RWM	Rod Worth Minimizer
SA	Severe Accident
SAR	Safety Analysis Report
SB	Service Building
S/C	Digital Gamma-Sensitive GM Detector
SC	Suppression Chamber
S/D	Scintillation Detector
S/DRSRO	Single/Dual Rod Sequence Restriction Override
S/N	Signal-to-Noise

<u>Term</u>	<u>Definition</u>
S/P	Suppression Pool
SAS	Service Air System
SB&PC	Steam Bypass and Pressure Control System
SBO	Station Blackout
SBWR	Simplified Boiling Water Reactor
SCEW	System Component Evaluation Work
SCRRI	Selected Control Rod Run-in
SDC	Shutdown Cooling
SDM	Shutdown Margin
SDS	System Design Specification
SEOA	Sealed Emergency Operating Area
SER	Safety Evaluation Report
SF	Service Water Building
SFP	Spent fuel pool
SIL	Service Information Letter
SIT	Structural Integrity Test
SIU	Signal Interface Unit
SJAE	Steam Jet Air Ejector
SLC	Standby Liquid Control
SLCS	Standby Liquid Control System
SLMCPR	Safety Limit Minimum Critical Power Ratio
SMU	SSLC Multiplexing Unit
SOV	Solenoid Operated Valve
SP	Setpoint
SPC	Suppression Pool Cooling
SPDS	Safety Parameter Display System
SPTMS	Suppression Pool Temperature Monitoring Subsystem of Containment Monitoring System
SR	Surveillance Requirement
SRM	Source Range Monitor
SRNM	Startup Range Neutron Monitor
SRO	Senior Reactor Operator
SRP	Standard Review Plan
SRS	Software Requirements Specification
SRSRO	Single Rod Sequence Restriction Override
SRSS	Sum of the squares
SRV	Safety Relief Valve
SRVDL	Safety relief valve discharge line
SSAR	Standard Safety Analysis Report
SSC(s)	Structure, System and Component(s)
SSE	Safe Shutdown Earthquake

<u>Term</u>	<u>Definition</u>
SSLC	Safety System Logic and Control
SSPC	Steel Structures Painting Council
ST	Spare Transformer
STP	Sewage Treatment Plant
STRAP	Scram Time Recording and Analysis Panel
STRP	Scram Time Recording Panel
SV	Safety Valve
SWH	Static water head
SWMS	Solid Waste Management System
SY	Switch Yard
TAF	Top of Active Fuel
TASS	Turbine Auxiliary Steam System
TB	Turbine Building
TBCE	Turbine Building Compartment Exhaust
TBE	Turbine Building Exhaust
TBLOE	Turbine Building Lube Oil Area Exhaust
TBS	Turbine Bypass System
TBHV	Turbine Building HVAC
TBV	Turbine Bypass Valve
TC	Training Center
TCCWS	Turbine Component Cooling Water System
TCS	Turbine Control System
TCV	Turbine Control Valve
TDH	Total Developed Head
TEMA	Tubular Exchanger Manufacturers' Association
TFSP	Turbine first stage pressure
TG	Turbine Generator
TGSS	Turbine Gland Seal System
THA	Time-history accelerograph
TLOS	Turbine Lubricating Oil System
TLU	Trip Logic Unit
TMI	Three Mile Island
TMSS	Turbine Main Steam System
TRM	Technical Requirements Manual
TS	Technical Specification(s)
TSC	Technical Support Center
TSI	Turbine Supervisory Instrument
TSV	Turbine Stop Valve
UBC	Uniform Building Code
UHS	ultimate heat sink

<u>Term</u>	<u>Definition</u>
UL	Underwriter's Laboratories Inc.
UPS	Uninterruptible Power Supply
USE	Upper Shelf Energy
USM	Uniform Support Motion
USMA	Uniform support motion response spectrum analysis
USNRC	United States Nuclear Regulatory Commission
USS	United States Standard
UV	Ultraviolet
V&V	Verification and Validation
Vac / VAC	Volts Alternating Current
Vdc / VDC	Volts Direct Current
VDU	Video Display Unit
VW	Vent Wall
VWO	Valves Wide Open
WD	Wash Down Bays
WH	Warehouse
WS	Water Storage
WT	Water Treatment
WW	Wetwell
XMFR	Transformer
ZPA	Zero period acceleration

3A. SEISMIC SOIL-STRUCTURE INTERACTION ANALYSIS

3A.1 INTRODUCTION

This appendix presents soil-structure interaction (SSI) analysis performed for two site conditions, generic site and North Anna ESP site-specific, adopted to establish seismic design loads for the Reactor Building (RB), Fuel Building (FB) and Control Building (CB) of the ESBWR standard plant under safe shutdown earthquake (SSE) excitation. The RB and FB are integrated and founded on a common basemat. They are termed RBFB hereafter. The SSE design ground motion at the foundation level for both site conditions are described in Subsection 3.7.1. The SSI analysis results are presented here in the form of site-enveloped seismic responses at key locations in the RBFB and CB. The structural adequacy calculations for the RB, FB and CB are shown in Appendix 3G.

For a standard plant design, the analysis must be performed over a range of site parameters. The site parameters considered and their ranges together form the generic site conditions. The generic site conditions are selected to provide an adequate seismic design margin for the standard plant located at any site with site parameters within the range of parameters considered in this study. In addition, the North Anna ESP site-specific condition is also considered in this study. When actual sites for these facilities are selected, site-specific geotechnical data will be developed and submitted to the NRC demonstrating compatibility with the site enveloping parameters considered in the standard design.

This appendix details the basis for selecting the site conditions and analysis cases, and the method of the seismic soil-structure interaction analysis. Descriptions of the input motion and damping values, the structural model, and the soil model are included. The parametric study SSI results as well as the enveloping seismic responses are also presented.

To demonstrate the seismic adequacy of the standard ESBWR design, a total of 7 SSI cases are analyzed using the sway-rocking stick model for the SSE condition. The enveloped results reported in this appendix form the design SSE loads.

3A.2 ESBWR STANDARD PLANT SITE PLAN

The typical site plan of the ESBWR standard plant is shown in Figure 1.1-1. The plan orientations are identified by 0°–180° (NS) and 90°–270° (EW) directions. The RBFB complex and the CB are rectangular in plan with dimensions and embedment depths shown in Table 3A.2-1.

In modeling the building, the 0°–180° (NS) and 90°–270° (EW) directions are designated as X- and Y-axes, respectively. The Z-axis is in the vertical direction.

Table 3A.2-1
Standard ESBWR Building Dimensions

	RBFB Complex Dimensions (m)	CB Dimension (m)
0°–180° (NS) width	70.0	30.3
90°–270° (EW) width	49.0	23.8
Embedment depth	20.15	15.05

3A.3 SITE CONDITIONS

This section describes the generic site conditions and the North Anna ESP site-specific conditions used in the SSI analysis.

3A.3.1 Generic Site Conditions

Design philosophy of the standard plant stipulates that the design should be applicable to as many practical sites as possible suitable for nuclear plant construction. To implement this philosophy, the effects of a wide range of subsurface conditions are considered in the seismic design. To evaluate these effects, a series of seismic soil-structure interaction (SSI) analyses in various subsurface conditions are performed. However, performing SSI analysis for combinations of all possible site properties and conditions where a nuclear power plant may be sited would be a formidable task. The purpose of this section is to define a limited number of bracketing subsurface conditions selected according to experience gained from previous generic SSI studies. Three subsurface conditions are finally selected to encompass a wide range of applicable site properties and conditions. They are classified as soft, medium and hard sites. The soft site is intended to cover a spectrum of soft soil conditions. The medium site is for medium stiff soil and soft rock conditions, and the hard site for competent rock conditions. For hard sites a fixed-base case is also considered to account for very stiff sites. These sites are considered to be uniform half-space with final enveloping properties provided in Table 3A.3-1 for SSI analysis.

3A.3.2 North Anna ESP Site Conditions

As described in Subsection 3.7.1, the North Anna ESP site-specific conditions are considered for the ESBWR design. North Anna is a rock site. The foundation properties considered in the SSI analysis are presented in Table 3A.3-2.

Table 3A.3-1
Generic Site Properties for SSI Analysis ^{(1),(2)}

	Soft	Medium	Hard	Fixed Base
Shear wave velocity (m/s)	300	800	1700	>1700
Mass density (kg/m ³)	2000	2200	2500	NA
Poisson's ratio	0.478	0.40	0.35	NA
Material damping (%)	5	4	3	NA

Notes:

The shear wave velocity and material damping specified above are used as strain compatible values.

The maximum ground water table is 0.61m (2 ft) below grade. The effect of ground water on SSI analysis is considered in the selected values for the Poisson's ratio, resulting in the P-wave velocity no less than the minimum P-wave velocity of water (1460 m/sec).

Table 3A.3-2
North Anna Site-specific Properties for SSI Analysis

	RBFB Complex			Control Building		
	(BE)	(UB)	(LB)	(BE)	(UB)	(LB)
Low strain shear modulus (kg/m ²)	G 6.70E+08	1.5G 1.00E+09	G/1.5 4.47E+08	G 4.97E+08	1.5G 7.46E+08	G/1.5 3.31E+08
Shear wave velocity (m/s)	1589	1946	1297	1369	1677	1118
Mass density (kg/m ³)	2606	2606	2606	2606	2606	2606
Poisson's ratio	0.33	0.33	0.33	0.33	0.33	0.33
Material damping (%)	2	2	2	2	2	2

Note: The rock properties are provided for three conditions, G, 1.5G, & G/1.5, which are considered as best-estimate (BE), upper bound (UB) and lower bound (LB) cases.

3A.4 INPUT MOTION AND DAMPING VALUES

3A.4.1 Input Motion

The time-history method is used in performing the seismic soil-structure interaction analysis. Earthquake input motion in the form of synthetic acceleration time histories are generated as described in Subsection 3.7.1.1 for three orthogonal components designated as H_1 , H_2 , and V . The H_1 and H_2 are the two horizontal components mutually perpendicular to each other. In the SSI analyses, H_1 and H_2 components are used in the horizontal X-(0°) and Y-(90°) directions, respectively. The V component is used in the vertical Z-direction.

Depending on the soil characteristics at the site and subject to availability of appropriate recorded ground-motion data, the control motion is defined on the soil surface at the top of finished grade or on an outcrop or a hypothetical outcrop at a location on the top of the competent material in accordance with the NRC Standard Review Plan (SRP) 3.7.1. For the generic sites defined in Section 3A.3.1, the design response spectra are conservatively applied at the level of foundation in the free field. The input motion for North Anna ESP site is also defined at the foundation level.

Vertically propagating plane seismic shear waves for the horizontal components and compression waves for the vertical component are assumed to generate the input motion.

3A.4.2 Damping Values

The structural components damping values used in the seismic analysis are in accordance with those specified in Regulatory Guide 1.61. These values for the SSE are summarized in Table 3.7-1.

3A.5 SOIL-STRUCTURE INTERACTION ANALYSIS METHOD

The seismic analysis is performed using the sway-rocking soil-structure interaction model.

The analysis model is a lumped mass-beam model with soil springs. The structural models are described in Subsection 3.7.2, and in Subsection 3A.7 in more detail.

To account for soil-structure interaction effect, sway-rocking base soil springs are attached to the structural model. The base spring is evaluated from vibration admittance theory, based on three-dimensional wave propagation theory for uniform half space soil. Though the spring values consist of frequency dependent real and imaginary parts, they are simplified and replaced with frequency independent soil spring K_c , and damping coefficient C_c , respectively, for the time history analysis solved in time domain. The calculated K_c and C_c values are tabulated in Tables 3A.5-1 and 3A.5-2 for the RBFB complex and the CB, respectively.

The effect of lateral soil/backfill on embedded foundations is conservatively accounted for by applying the control motion directly at the foundation level. Dynamic lateral soil pressures are calculated separately and considered in the design of external walls, using the elastic solution procedures in Section 3.5.3.2 of ASCE 4-98.

Because the three component ground motion time histories are statistically independent as described in Subsections 3.7.1.1.2 and 3.7.1.1.3, they are input simultaneously in the response analysis using the time history method of analysis. Structural responses in terms of accelerations, forces, and moments are computed directly. Floor response spectra are obtained from the calculated response acceleration time histories (Subsection 3.7.2.5).

Table 3A.5-1

Soil Spring and Damping Coefficient for RBFB complex

			Generic Site			North Anna Site		
			Soft 300 m/s	Medium 800 m/s	Hard 1700 m/s	BE 1589 m/s	UB 1946 m/s	LB 1297 m/s
Soil Spring Kc	X-dir	MN/m	2.910E+04	2.178E+05	1.087E+06	9.676E+05	1.451E+06	6.447E+05
	Y-dir	MN/m	3.085E+04	2.281E+05	1.131E+06	1.001E+06	1.501E+06	6.670E+05
	Z-dir	MN/m	4.366E+04	2.972E+05	1.408E+06	1.245E+06	1.868E+06	8.297E+05
	X-X Rot.	MN•m/rad	2.466E+07	1.678E+08	7.950E+08	6.871E+08	1.030E+09	4.578E+08
	Y-Y Rot.	MN•m/rad	4.280E+07	2.913E+08	1.379E+09	1.145E+09	1.717E+09	7.627E+08
	Z-Z Rot.	MN•m/rad	9.804E+15	9.804E+15	9.804E+15	9.804E+15	9.804E+15	9.804E+15
Damping coefficient Cc	X-dir	MN•sec/m	1.708E+03	4.837E+03	1.143E+04	1.083E+04	1.324E+04	8.870E+03
	Y-dir	MN•sec/m	1.910E+03	5.294E+03	1.236E+04	1.159E+04	1.416E+04	9.484E+03
	Z-dir	MN•sec/m	3.852E+03	9.740E+03	2.114E+04	2.011E+04	2.437E+04	1.663E+04
	X-X Rot.	MN•m•sec/rad	2.512E+05	4.378E+05	4.626E+05	4.631E+05	4.235E+05	4.877E+05
	Y-Y Rot.	MN•m•sec/rad	8.432E+05	1.590E+06	1.694E+06	1.567E+06	1.444E+06	1.643E+06
	Z-Z Rot.	MN•m•sec/rad	0.0	0.0	0.0	0.0	0.0	0.0

Table 3A.5-2

Soil Spring and Damping Coefficient for CB

			Generic Site			North Anna Site		
			Soft 300 m/s	Medium 800 m/s	Hard 1700 m/s	BE 1369 m/s	UB 1677 m/s	LB 1118 m/s
Soil Spring Kc	X-dir	MN/m	1.322E+04	9.876E+04	4.925E+05	3.297E+05	4.948E+05	2.199E+05
	Y-dir	MN/m	1.372E+04	1.017E+05	5.049E+05	3.375E+05	5.064E+05	2.250E+05
	Z-dir	MN/m	1.963E+04	1.336E+05	6.329E+05	4.157E+05	6.237E+05	2.773E+05
	X-X Rot.	MN•m/rad	2.508E+06	1.707E+07	8.085E+07	5.311E+07	7.969E+07	3.542E+07
	Y-Y Rot.	MN•m/rad	3.543E+06	2.411E+07	1.142E+08	7.501E+07	1.125E+08	5.003E+07
	Z-Z Rot.	MN•m/rad	9.804E+15	9.804E+15	9.804E+15	9.804E+15	9.804E+15	9.804E+15
Damping coefficient Cc	X-dir	MN•sec/m	3.515E+02	9.961E+02	2.349E+03	1.975E+03	2.412E+03	1.620E+03
	Y-dir	MN•sec/m	3.796E+02	1.058E+03	2.470E+03	2.071E+03	2.527E+03	1.698E+03
	Z-dir	MN•sec/m	7.794E+02	1.986E+03	4.307E+03	3.561E+03	4.314E+03	2.940E+03
	X-X Rot.	MN•m•sec/rad	1.421E+04	2.775E+04	3.073E+04	3.330E+04	3.163E+04	3.364E+04
	Y-Y Rot.	MN•m•sec/rad	2.720E+04	5.542E+04	6.489E+04	6.916E+04	6.670E+04	6.872E+04
	Z-Z Rot.	MN•m•sec/rad	0.0	0.0	0.0	0.0	0.0	0.0

3A.6 SOIL-STRUCTURE INTERACTION ANALYSIS CASES

To establish design envelopes of seismic responses of the RBFB complex, SSI analyses are performed for a total of 7 cases, as summarized in Table 3A.6-1. Similarly, SSI analyses are performed for the CB.

The enveloping results are obtained from the responses of all SSI cases to cover a wide range of site conditions.

Table 3A.6-1
Seismic SSI Analysis Cases

Case No.	Soil Properties							Input Wave (SSE)					
	Generic Site				North Anna ESP Site			RG 1.60			North Anna		
	Soft	Medium	Hard	Fixed Base	Best estimate	Upper bound	Lower bound	H1	H2	V	H1	H2	V
1	√							√	√	√			
2		√						√	√	√			
3			√					√	√	√			
4				√				√	√	√			
5					√						√	√	√
6						√					√	√	√
7							√				√	√	√

3A.7 ANALYSIS MODELS

The analysis model is a three-dimensional lumped mass-beam model that considers shear, bending, torsion and axial deformations. The structural elements of the reactor building outside containment and the fuel building are reduced to one set of stick models. The containment and the containment internal structures including the reactor pressure vessel are modeled as separate interconnected sticks. The control building is modeled with a single stick.

3A.7.1 Method of Dynamic Structural Model Development

Evaluation of stiffness for the seismic model is done according to the following assumptions.

- Exterior walls and those inner walls that are continuous up from the basemat and have 500 mm or more in thickness are treated as seismic walls.
- Those openings that have 2.0 m^2 or larger area are explicitly considered in the stiffness evaluation.

Effective Shear Area (S_x , S_y):

As effective shear area, seismic walls parallel to each of two earthquake directions are considered. When openings exist in a wall, equivalent shear area is calculated so that shear displacements of two walls, with and without openings, are equal

Moment of Inertia (I_{yy} , I_{xx}):

Moment of inertia of seismic walls is calculated according to the following procedures.

- Moment of inertia in each direction is calculated around a horizontal axis that goes through the centroid.
- When openings exist in a wall, equivalent moment of inertia is calculated so that angles of rotation of two walls, with and without openings, are equal
- The effective flange length is taken to be eight times the flange wall thickness, and it is limited to one-half of the flange wall length.

Torsional Constant (I_{zz}):

Torsional constant of seismic walls is calculated around the vertical axis that goes through the center of rigidity.

Vertical Axial Area (S_a):

Vertical axial area of each element is equal to summation of effective shear areas that are evaluated in two directions for the horizontal analysis. However, the overlap area at the corner of box wall is subtracted from the summation.

The locations (X_c and Y_c) of centroid of axial area for various sections determined in Step (4) above define the locations of center of rigidity of the equivalent beam stick model in the vertical direction.

Because the stick model has different center-of-rigidity locations in the horizontal and the vertical directions, the lumped mass-beam model comprises two stick models. One stick consists of elements with axial areas located at the centers of rigidity for axial area, and another stick consists of elements with all other remaining sectional properties (i.e., excluding axial area)

located at the centers of rigidity for shear and torsional deformations. Both sticks are connected at common centers of mass at various floor elevations.

As described above, the RBFB complex is represented by several stick models. These stick models are interconnected by horizontal links representing the floor diaphragm at respective elevations. These links are modeled as rigid springs for floor in-plane translational displacement and having no stiffness for all other deformations.

The vertical floor frequencies are obtained at major floor locations by independent modal analysis of the respective floor finite element model. These frequencies are included in the stick model by a series of vertical single degree-of-freedom oscillators at the corresponding floor elevations.

To obtain the mass properties for the stick model, the dead load, 25% of the respective live load and an additional 50 psf load for piping and cable trays, etc. were used to compute the lumped mass properties following the steps described below.

- (1) Depending on whether the floor has a regular or an irregular layout, hand calculations or floor finite element models are used to obtain the total mass (M_x , M_y , M_z), the mass moments of inertia (M_{xx} , M_{yy} , M_{zz}) and the center of mass of each floor. Similar calculations are performed for the tributary areas of the walls above and below the floors.
- (2) These properties are subsequently reduced to one center of mass with its associated properties at each floor elevation. The water masses in the pools are also included in this calculation.
- (3) The bending mass moment of inertia at various floor elevations are also added to each floor mass.

Based on the methodology described above, the lumped mass-beam stick model for SSI is developed as described in Section 3A.7.2.

3A.7.2 Lumped mass-Beam Stick Model for SSI Analysis

The lumped mass-beam stick models for the RBFB complex in the XZ- and YZ-planes are shown in Figures 3A.7-1. Similarly, the stick models corresponding to the RCCV and pedestal wall are shown in Figures 3A.7-2 and 3A.7-3. The overall integrated building model is shown in Figure 3A.7-4. As shown in the figure, the building model is also coupled to the vent wall (VW), the reactor shield wall (RSW) and the reactor pressure vessel (RPV). They are symmetric in both horizontal directions.

The stick models are interconnected at floor elevations by horizontal links. These links are rigid for floor in-plane displacements and have no stiffness for out-of-plane displacement and rotations.

The lumped mass-beam stick models for the CB in the XZ- and YZ-planes are shown in Figures 3A.7-5.

To account for soil-structure interaction effect, sway-rocking base soil springs are attached to this structural model, as described in Section 3A.5. Natural frequencies of the seismic model at all site conditions are shown in Tables 3A.7-1 through 3A.7-7 for the RBFB model and Tables 3A.7-8 through 3A.7-14 for the CB model.

Table 3A.7-1

Eigenvalue Analysis Results for RBFB model at Soft Site

Mode No.	Frequency (HZ)	Period (sec)	Participation Factor					
			X dir.	Y dir.	Z dir.	X rot.	Y rot.	Z rot.
1	1.19	0.84	0.02	1.56	-0.01	-1038	17	-38
2	1.40	0.71	1.44	-0.02	0.10	7	811	5
3	2.09	0.48	-0.23	0.01	2.34	2	220	0
4	2.78	0.36	-0.31	-0.20	-1.42	-373	942	1
5	2.89	0.35	0.02	0.63	-0.01	1314	-79	15
6	3.11	0.32	-0.46	0.03	-0.10	71	1809	8
7	3.81	0.26	-0.09	0.09	0.01	-120	-277	124
8	3.81	0.26	-0.07	-0.11	0.01	148	-201	-160
9	5.23	0.19	0.11	0.01	-0.09	24	-1005	-51
10	5.25	0.19	-0.06	0.01	-0.22	29	597	114
11	5.94	0.17	0.00	-0.05	0.00	1335	190	-12815
12	5.99	0.17	-0.11	0.00	-0.01	40	693	-153
13	5.99	0.17	-0.01	-0.08	0.00	-1874	-166	12660
14	6.76	0.15	-0.04	0.01	-0.12	60	347	-191
15	8.71	0.11	-0.01	-0.10	0.01	-548	79	302
16	9.53	0.10	-0.03	0.01	-0.04	13	4849	74
17	9.97	0.10	0.14	0.00	-0.05	-429	6204	95
18	10.27	0.10	-0.03	0.02	0.01	-5570	-1198	-2635
19	10.41	0.10	-0.06	-0.01	0.03	385	-3528	110
20	10.83	0.09	-0.11	0.00	-0.03	-103	-1451	-185

Note: The participation factors are calculated for mode vectors normalized by the maximum mode displacement.

Table 3A.7-2

Eigenvalue Analysis Results for RBFB model at Medium Site

Mode No.	Frequency (HZ)	Period (sec)	Participation Factor					
			X dir.	Y dir.	Z dir.	X rot.	Y rot.	Z rot.
1	2.58	0.39	0.01	1.68	0.02	-1173	14	-250
2	2.72	0.37	1.22	-0.22	1.48	120	1087	56
3	2.93	0.34	1.88	0.00	0.06	-3	1321	33
4	3.81	0.26	0.00	-0.29	-0.03	1024	-24	-49
5	3.81	0.26	-0.80	0.01	-0.19	-12	-1348	-36
6	4.93	0.20	-0.58	-0.17	5.96	-204	726	100
7	5.22	0.19	-0.97	-0.03	-0.08	-24	1490	-61
8	5.47	0.18	0.99	0.15	-5.04	206	-1696	-56
9	5.96	0.17	0.18	4.14	0.70	10031	129	-27285
10	5.98	0.17	1.87	-0.23	1.20	27	-4231	-2709
11	6.00	0.17	-0.12	0.87	-0.06	-2869	-335	30291
12	6.21	0.16	-0.05	-4.67	-0.43	-6804	174	-3195
13	6.50	0.15	2.78	-0.08	0.93	-141	-6411	69
14	6.77	0.15	-2.38	0.14	-2.14	267	5607	-207
15	9.77	0.10	-0.06	-0.70	0.03	-652	23	662
16	10.26	0.10	-1.23	0.27	0.01	1099	1143	43
17	10.30	0.10	-0.23	-0.27	-0.19	-2979	3197	-843
18	10.33	0.10	0.45	-0.01	-0.21	991	3266	591
19	10.91	0.09	-1.25	0.00	0.32	227	-7710	-233
20	11.19	0.09	0.10	-0.01	0.37	164	-5553	-53

Note: The participation factors are calculated for mode vectors normalized by the maximum mode displacement.

Table 3A.7-3

Eigenvalue Analysis Results for RBFB model at Hard Site

Mode No.	Frequency (HZ)	Period (sec)	Participation Factor					
			X dir.	Y dir.	Z dir.	X rot.	Y rot.	Z rot.
1	2.73	0.37	0.15	0.05	1.16	-56	252	-4
2	3.51	0.28	-0.03	3.70	0.07	-2570	-6	-1432
3	3.81	0.26	9.86	0.09	0.43	-112	6169	379
4	3.81	0.26	0.01	-2.61	-0.08	2538	-10	1157
5	3.93	0.25	-8.77	-0.06	-0.44	98	-6101	-394
6	5.20	0.19	-0.04	-0.14	1.95	-92	28	289
7	5.22	0.19	-0.71	0.00	-0.26	16	312	-133
8	5.98	0.17	0.15	0.63	-0.15	2714	69	-12791
9	5.99	0.17	0.60	-0.04	-0.13	-26	-1069	-178
10	6.05	0.17	-0.10	0.29	0.08	-1739	-152	13192
11	6.75	0.15	0.09	-0.30	2.32	-247	-104	-732
12	7.62	0.13	0.20	1.23	-0.45	1639	-438	904
13	8.05	0.12	-1.11	0.30	1.34	423	2411	200
14	8.82	0.11	0.63	0.07	2.21	91	-1101	-33
15	10.30	0.10	0.13	0.55	-0.34	-2312	352	-1390
16	10.36	0.10	0.02	0.02	-0.95	418	3408	291
17	10.62	0.09	1.57	0.12	-0.20	113	-3763	-138
18	11.22	0.09	-0.03	-0.69	0.00	320	-11	842
19	11.25	0.09	0.11	0.00	0.08	17	-1518	-41
20	11.64	0.09	-0.15	-2.92	-0.10	-2148	-28	2104

Note: The participation factors are calculated for mode vectors normalized by the maximum mode displacement.

Table 3A.7-4

Eigenvalue Analysis Results for RBFB model in Fixed-base Case

Mode No.	Frequency (HZ)	Period (sec)	Participation Factor					
			X dir.	Y dir.	Z dir.	X rot.	Y rot.	Z rot.
1	2.74	0.37	0.10	0.03	1.09	-45	191	-3
2	3.81	0.26	-0.16	7.02	0.15	-4075	-53	-3906
3	3.81	0.26	2.41	0.07	0.05	-42	943	63
4	3.94	0.25	0.11	-5.96	-0.16	4051	36	3613
5	4.36	0.23	1.66	0.03	0.07	-33	1090	107
6	5.21	0.19	-0.07	-0.16	1.63	-65	9	381
7	5.22	0.19	-0.82	0.00	-0.30	26	95	-186
8	5.98	0.17	0.12	0.50	-0.09	1955	55	-8551
9	5.99	0.17	0.49	-0.04	-0.07	-15	-829	-143
10	6.09	0.16	-0.08	0.26	0.06	-1236	-109	8979
11	6.75	0.15	0.15	-0.19	1.37	-86	-188	-697
12	8.02	0.12	0.15	1.33	-0.21	1889	-348	1273
13	8.58	0.12	1.47	-0.21	-0.71	-302	-3477	-237
14	10.24	0.10	0.65	0.19	4.42	-457	1077	-298
15	10.32	0.10	-0.10	0.38	-1.37	-1965	-845	-1088
16	10.52	0.10	-0.47	0.00	-4.23	35	1763	100
17	10.67	0.09	1.09	0.06	-1.52	55	-3554	-121
18	11.23	0.09	-0.01	-0.27	-0.01	408	-17	504
19	11.25	0.09	0.08	0.00	0.04	20	-1324	-39
20	11.89	0.08	0.87	0.23	2.13	-824	539	-576

Note: The participation factors are calculated for mode vectors normalized by the maximum mode displacement.

Table 3A.7-5

Eigenvalue Analysis Results for RBFB model at Best-estimate North Anna Site

Mode No.	Frequency (HZ)	Period (sec)	Participation Factor					
			X dir.	Y dir.	Z dir.	X rot.	Y rot.	Z rot.
1	2.73	0.37	0.17	0.05	1.17	-59	266	-5
2	3.46	0.29	-0.03	3.23	0.05	-2255	-4	-1182
3	3.81	0.26	20.00	0.13	0.96	-207	13513	793
4	3.81	0.26	0.00	-2.13	-0.07	2222	-13	909
5	3.86	0.26	-18.91	-0.11	-0.98	193	-13444	-806
6	5.19	0.19	-0.04	-0.14	2.00	-95	30	280
7	5.22	0.19	-0.71	0.00	-0.25	14	337	-128
8	5.98	0.17	0.15	0.65	-0.16	2852	68	-13591
9	5.99	0.17	0.63	-0.05	-0.15	-43	-1112	-100
10	6.05	0.17	-0.10	0.29	0.09	-1838	-162	13995
11	6.75	0.15	0.06	-0.33	2.56	-285	-61	-751
12	7.57	0.13	0.22	1.19	-0.52	1578	-474	848
13	7.95	0.13	-1.04	0.35	1.49	489	2248	218
14	8.65	0.12	0.68	0.06	1.94	89	-1247	-30
15	10.30	0.10	0.15	0.57	-0.31	-2328	389	-1421
16	10.36	0.10	0.02	0.02	-0.86	445	3490	304
17	10.62	0.09	1.62	0.14	-0.17	131	-3774	-139
18	11.21	0.09	-0.03	-0.85	-0.01	221	-9	954
19	11.25	0.09	0.12	0.00	0.08	18	-1571	-42
20	11.55	0.09	-0.12	-3.08	-0.06	-2317	-5	2117

Note: The participation factors are calculated for mode vectors normalized by the maximum mode displacement.

Table 3A.7-6**Eigenvalue Analysis Results for RBFB model at Upper-bound North Anna Site**

Mode No.	Frequency (HZ)	Period (sec)	Participation Factor					
			X dir.	Y dir.	Z dir.	X rot.	Y rot.	Z rot.
1	2.73	0.37	0.14	0.04	1.14	-53	238	-4
2	3.60	0.28	-0.05	4.98	0.10	-3452	-13	-2113
3	3.81	0.26	5.88	0.07	0.23	-76	3407	215
4	3.81	0.26	0.02	-3.89	-0.11	3419	-4	1835
5	4.01	0.25	-4.79	-0.04	-0.24	61	-3338	-232
6	5.20	0.19	-0.04	-0.14	1.86	-86	23	306
7	5.22	0.19	-0.73	0.00	-0.27	18	261	-143
8	5.98	0.17	0.14	0.59	-0.13	2516	68	-11713
9	5.99	0.17	0.58	-0.04	-0.11	-23	-1004	-163
10	6.06	0.17	-0.09	0.28	0.07	-1612	-143	12114
11	6.75	0.15	0.12	-0.26	1.98	-191	-154	-705
12	7.72	0.13	0.18	1.28	-0.36	1720	-397	997
13	8.21	0.12	1.21	-0.25	-1.09	-346	-2659	-188
14	9.18	0.11	0.46	0.06	2.25	63	-683	-36
15	10.30	0.10	0.11	0.52	-0.42	-2292	256	-1339
16	10.36	0.10	-0.01	0.02	-1.23	359	3329	263
17	10.64	0.09	1.48	0.10	-0.24	88	-3868	-140
18	11.22	0.09	-0.02	-0.50	0.00	412	-12	706
19	11.25	0.09	0.10	0.00	0.07	17	-1480	-41
20	11.79	0.08	0.49	2.25	0.52	1383	252	-1850

Note: The participation factors are calculated for mode vectors normalized by the maximum mode displacement.

Table 3A.7-7

Eigenvalue Analysis Results for RBFB model at Lower-bound North Anna Site

Mode No.	Frequency (HZ)	Period (sec)	Participation Factor					
			X dir.	Y dir.	Z dir.	X rot.	Y rot.	Z rot.
1	2.73	0.37	0.22	0.06	1.21	-71	316	-7
2	3.27	0.31	-0.01	2.34	0.03	-1645	1	-705
3	3.65	0.27	7.62	0.02	0.41	-56	5494	271
4	3.81	0.26	0.00	-1.23	-0.05	1615	-18	436
5	3.81	0.26	-6.52	0.00	-0.43	41	-5428	-281
6	5.19	0.19	-0.06	-0.14	2.30	-111	47	250
7	5.22	0.19	-0.71	-0.01	-0.23	10	452	-112
8	5.98	0.17	0.18	0.75	-0.23	3437	69	-16769
9	5.99	0.17	0.72	-0.05	-0.23	-45	-1315	-156
10	6.03	0.17	-0.11	0.32	0.12	-2216	-191	17187
11	6.74	0.15	-0.24	-0.59	4.53	-607	491	-970
12	7.28	0.14	0.56	1.18	-1.73	1553	-1162	794
13	7.49	0.13	-0.39	0.60	1.06	818	824	336
14	8.11	0.12	1.03	0.03	1.29	55	-2053	-34
15	10.29	0.10	0.19	0.70	-0.24	-2309	525	-1566
16	10.35	0.10	0.04	0.02	-0.61	540	3789	352
17	10.58	0.09	1.82	0.23	-0.13	254	-3484	-150
18	11.10	0.09	-0.04	-1.80	-0.01	-1061	5	1283
19	11.25	0.09	0.17	0.00	0.10	25	-1719	-41
20	11.27	0.09	-0.02	-1.84	-0.01	-2242	13	801

Note: The participation factors are calculated for mode vectors normalized by the maximum mode displacement.

Table 3A.7-8**Eigenvalue Analysis Results for CB model at Soft Site**

Mode No.	Frequency (HZ)	Period (sec)	Participation Factor					
			X dir.	Y dir.	Z dir.	X rot.	Y rot.	Z rot.
1	3.22	0.31	0.01	1.22	0.00	-306	4	-1
2	3.41	0.29	1.18	-0.01	0.00	3	368	1
3	5.19	0.19	0.00	0.00	1.37	-1	0	0
4	7.24	0.14	0.46	0.02	0.00	19	-755	0
5	7.42	0.13	-0.02	0.56	0.00	592	31	0
6	10.32	0.10	0.00	0.00	-0.37	-8	3	0
7	14.92	0.07	0.00	0.00	-0.19	-3	2	-1
8	16.66	0.06	0.00	0.00	0.00	0	0	25
9	20.80	0.05	0.00	0.00	-0.11	17	-3	2
10	22.65	0.04	-0.02	-0.01	0.00	277	-417	1

Note: The participation factors are calculated for mode vectors normalized by the maximum mode displacement.

Table 3A.7-9**Eigenvalue Analysis Results for CB model at Medium Site**

Mode No.	Frequency (HZ)	Period (sec)	Participation Factor					
			X dir.	Y dir.	Z dir.	X rot.	Y rot.	Z rot.
1	6.94	0.14	0.07	1.27	0.01	-299	22	-7
2	7.37	0.14	1.25	-0.07	0.00	15	378	7
3	9.64	0.10	-0.01	-0.01	2.22	-2	3	0
4	13.11	0.08	-0.02	-0.03	3.41	-16	18	0
5	15.43	0.06	0.04	0.05	-2.74	39	-41	0
6	16.66	0.06	0.00	0.00	0.00	0	-3	52
7	17.08	0.06	0.48	0.09	0.01	68	-610	-64
8	17.60	0.06	-0.09	0.58	0.01	444	118	10
9	20.83	0.05	0.00	-0.01	-1.02	-2	1	1
10	25.88	0.04	0.09	0.05	0.00	-254	323	-2

Note: The participation factors are calculated for mode vectors normalized by the maximum mode displacement.

Table 3A.7-10**Eigenvalue Analysis Results for CB model at Hard Site**

Mode No.	Frequency (HZ)	Period (sec)	Participation Factor					
			X dir.	Y dir.	Z dir.	X rot.	Y rot.	Z rot.
1	9.29	0.11	0.14	1.24	0.01	-231	39	-15
2	9.85	0.10	1.21	-0.14	0.04	23	300	18
3	9.90	0.10	-0.32	0.00	1.34	-2	-75	-4
4	14.62	0.07	-0.02	-0.02	1.87	-10	13	0
5	16.67	0.06	0.00	0.00	0.00	0	0	-30
6	20.55	0.05	-0.14	-0.14	6.63	-169	232	0
7	22.56	0.04	0.28	0.25	-5.70	320	-532	-3
8	24.13	0.04	0.27	0.09	0.08	116	-517	-7
9	25.30	0.04	-0.10	0.36	0.04	419	203	9
10	27.56	0.04	-0.05	-0.15	-2.92	-111	83	1

Note: The participation factors are calculated for mode vectors normalized by the maximum mode displacement.

Table 3A.7-11**Eigenvalue Analysis Results for CB model in Fixed-base Case**

Mode No.	Frequency (HZ)	Period (sec)	Participation Factor					
			X dir.	Y dir.	Z dir.	X rot.	Y rot.	Z rot.
1	9.94	0.10	0.03	0.07	1.20	-14	11	-1
2	10.30	0.10	0.18	1.18	0.00	-175	42	-21
3	10.90	0.09	1.17	-0.18	0.00	22	235	26
4	14.70	0.07	-0.02	-0.02	1.42	-9	11	0
5	16.70	0.06	0.00	0.00	0.00	0	0	-38
6	20.70	0.05	-0.04	-0.04	2.41	-63	84	0
7	25.70	0.04	-0.98	-0.56	1.25	-1000	2540	23
8	26.20	0.04	1.30	0.32	4.27	568	-3380	-44
9	27.00	0.04	-0.21	0.48	0.02	811	551	21
10	29.10	0.03	-0.11	-0.25	-4.42	-335	268	1

Note: The participation factors are calculated for mode vectors normalized by the maximum mode displacement.

Table 3A.7-12**Eigenvalue Analysis Results for CB model at Best-estimate North Anna Site**

Mode No.	Frequency (HZ)	Period (sec)	Participation Factor					
			X dir.	Y dir.	Z dir.	X rot.	Y rot.	Z rot.
1	8.85	0.11	0.12	1.25	0.01	-251	36	-13
2	9.40	0.11	1.23	-0.12	0.01	22	326	15
3	9.88	0.10	-0.04	-0.02	1.44	0	-6	0
4	14.56	0.07	-0.02	-0.02	2.22	-11	15	0
5	16.67	0.06	0.00	0.00	0.00	0	0	-27
6	19.92	0.05	-0.19	-0.20	9.40	-212	287	0
7	21.25	0.05	0.30	0.29	-8.64	323	-492	-2
8	23.09	0.04	0.33	0.10	0.05	107	-554	-8
9	24.18	0.04	-0.11	0.44	0.03	441	191	9
10	27.41	0.04	-0.03	-0.08	-1.98	-9	22	1

Note: The participation factors are calculated for mode vectors normalized by the maximum mode displacement.

Table 3A.7-13**Eigenvalue Analysis Results for CB model at Upper-bound North Anna Site**

Mode No.	Frequency (HZ)	Period (sec)	Participation Factor					
			X dir.	Y dir.	Z dir.	X rot.	Y rot.	Z rot.
1	9.28	0.11	0.14	1.24	0.01	-232	39	-15
2	9.84	0.10	1.21	-0.14	0.04	23	302	18
3	9.90	0.10	-0.29	0.00	1.34	-2	-69	-4
4	14.62	0.07	-0.02	-0.02	1.88	-10	13	0
5	16.67	0.06	0.00	0.00	0.00	0	0	-30
6	20.54	0.05	-0.14	-0.14	6.77	-172	236	0
7	22.51	0.04	0.28	0.25	-5.85	318	-525	-3
8	24.12	0.04	0.27	0.09	0.08	116	-516	-7
9	25.30	0.04	-0.10	0.36	0.04	420	203	9
10	27.55	0.04	-0.05	-0.15	-2.88	-109	82	1

Note: The participation factors are calculated for mode vectors normalized by the maximum mode displacement.

Table 3A.7-14

Eigenvalue Analysis Results for CB model at Lower-bound North Anna Site

Mode No.	Frequency (HZ)	Period (sec)	Participation Factor					
			X dir.	Y dir.	Z dir.	X rot.	Y rot.	Z rot.
1	8.30	0.12	0.10	1.26	0.01	-272	32	-11
2	8.82	0.11	1.24	-0.11	0.01	20	351	12
3	9.84	0.10	-0.02	-0.01	1.59	-1	-1	0
4	14.43	0.07	-0.02	-0.02	2.91	-14	19	0
5	16.67	0.06	0.00	0.00	0.00	0	0	-24
6	18.10	0.06	-0.06	-0.07	4.08	-60	76	-1
7	20.92	0.05	0.30	0.22	-3.50	207	-432	-5
8	21.51	0.05	0.39	0.10	0.03	90	-564	-10
9	22.42	0.04	-0.11	0.52	0.02	432	164	8
10	27.32	0.04	-0.01	-0.04	-1.33	53	-11	2

Note: The participation factors are calculated for mode vectors normalized by the maximum mode displacement.

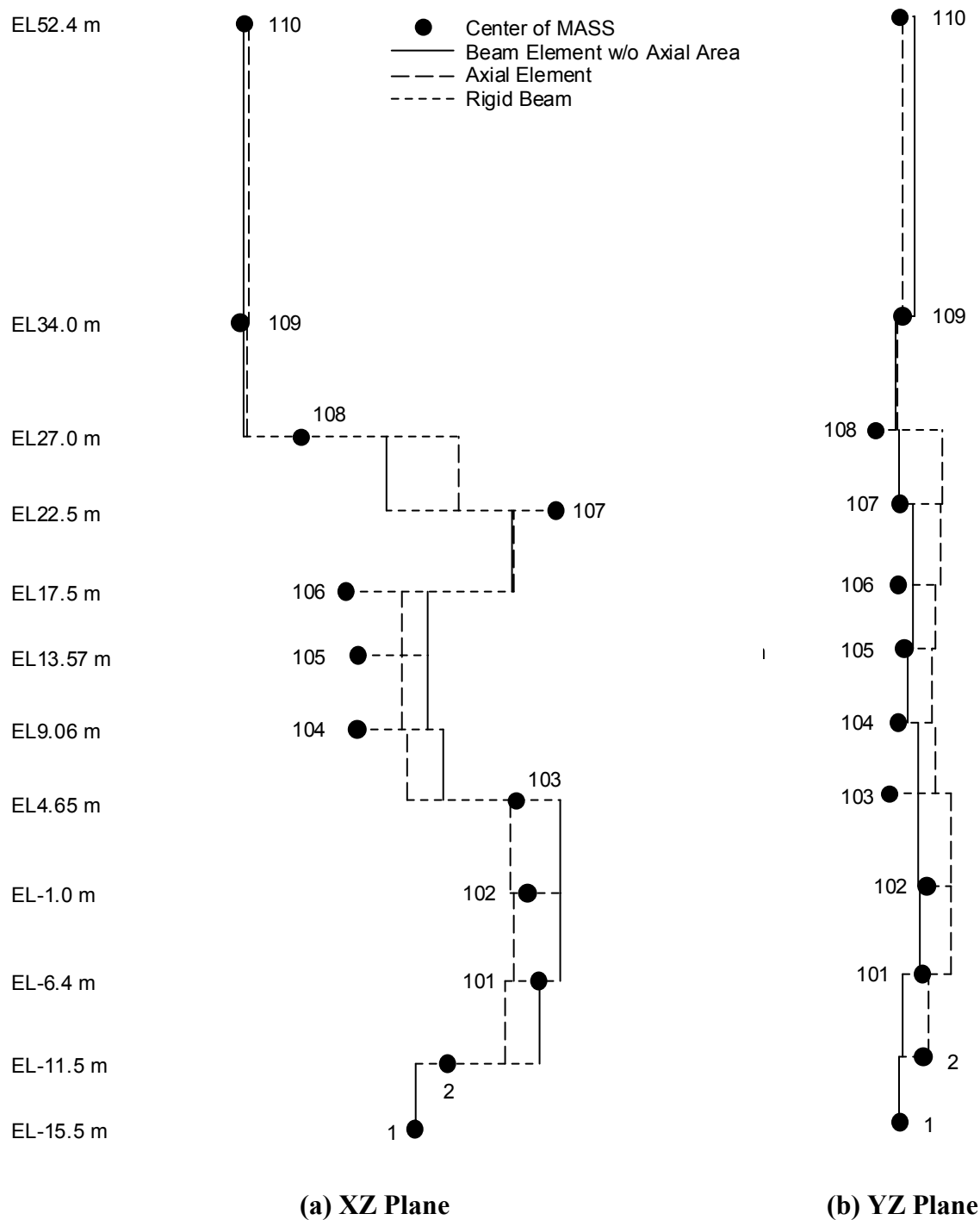


Figure 3A.7-1. RBFB Stick Model

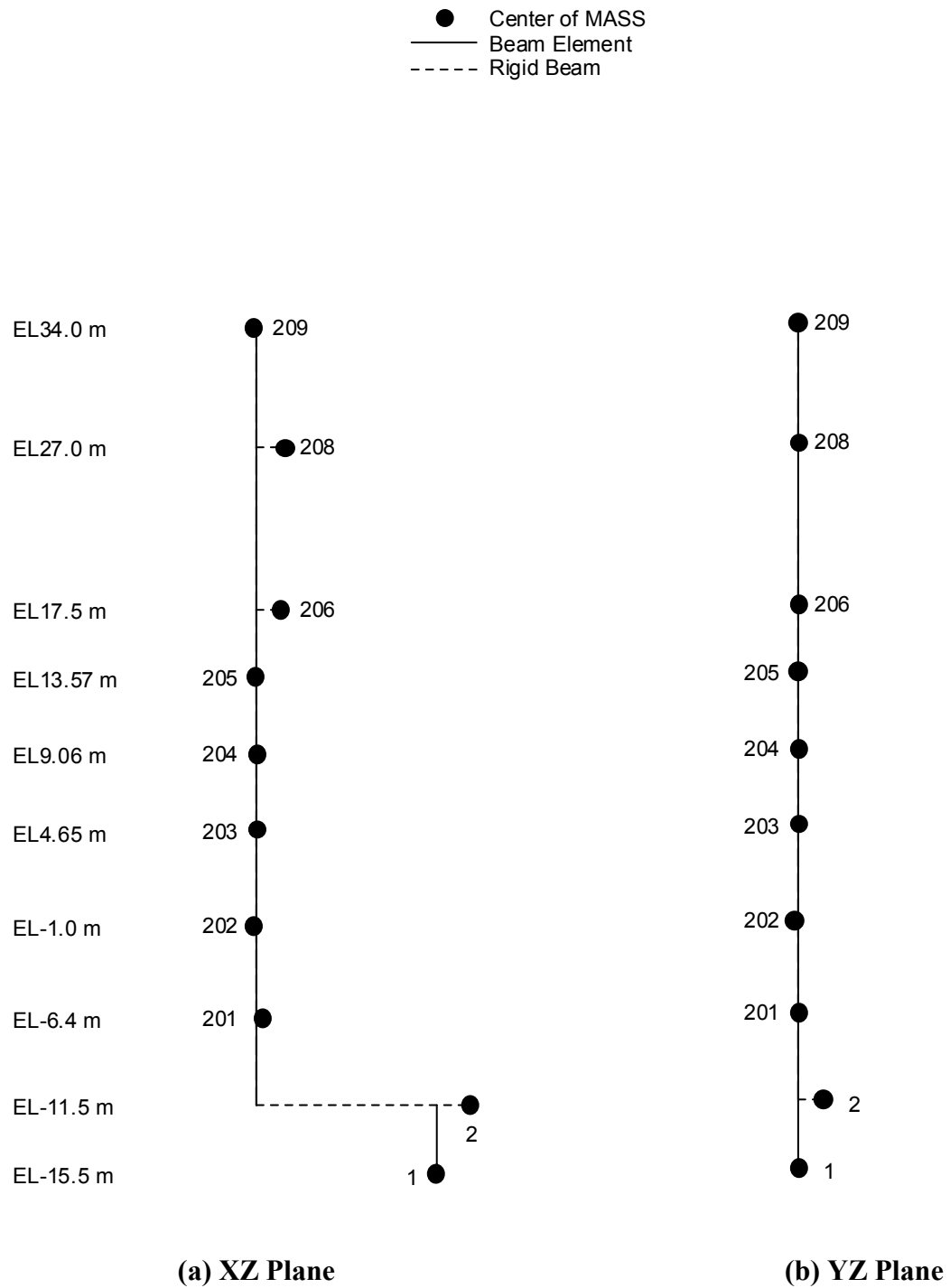


Figure 3A.7-2. RCCV Stick Model

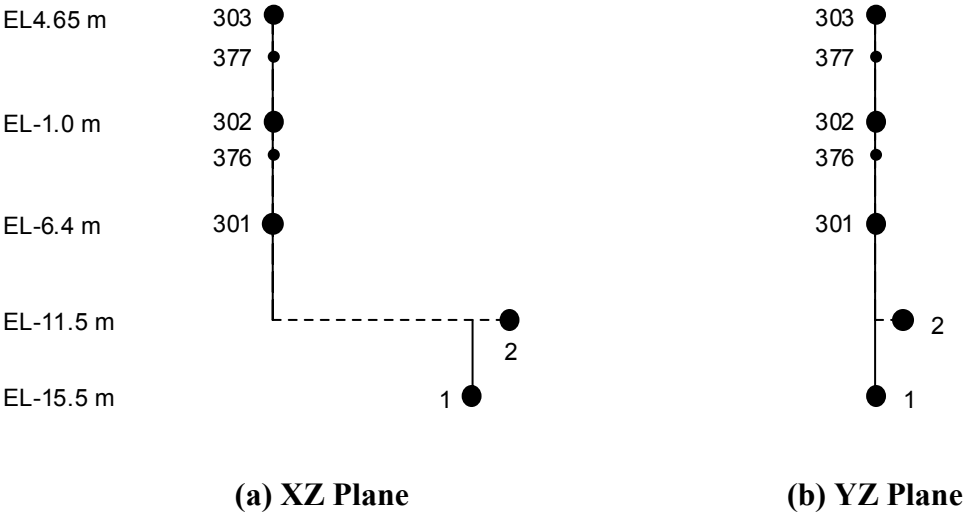
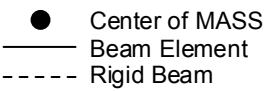
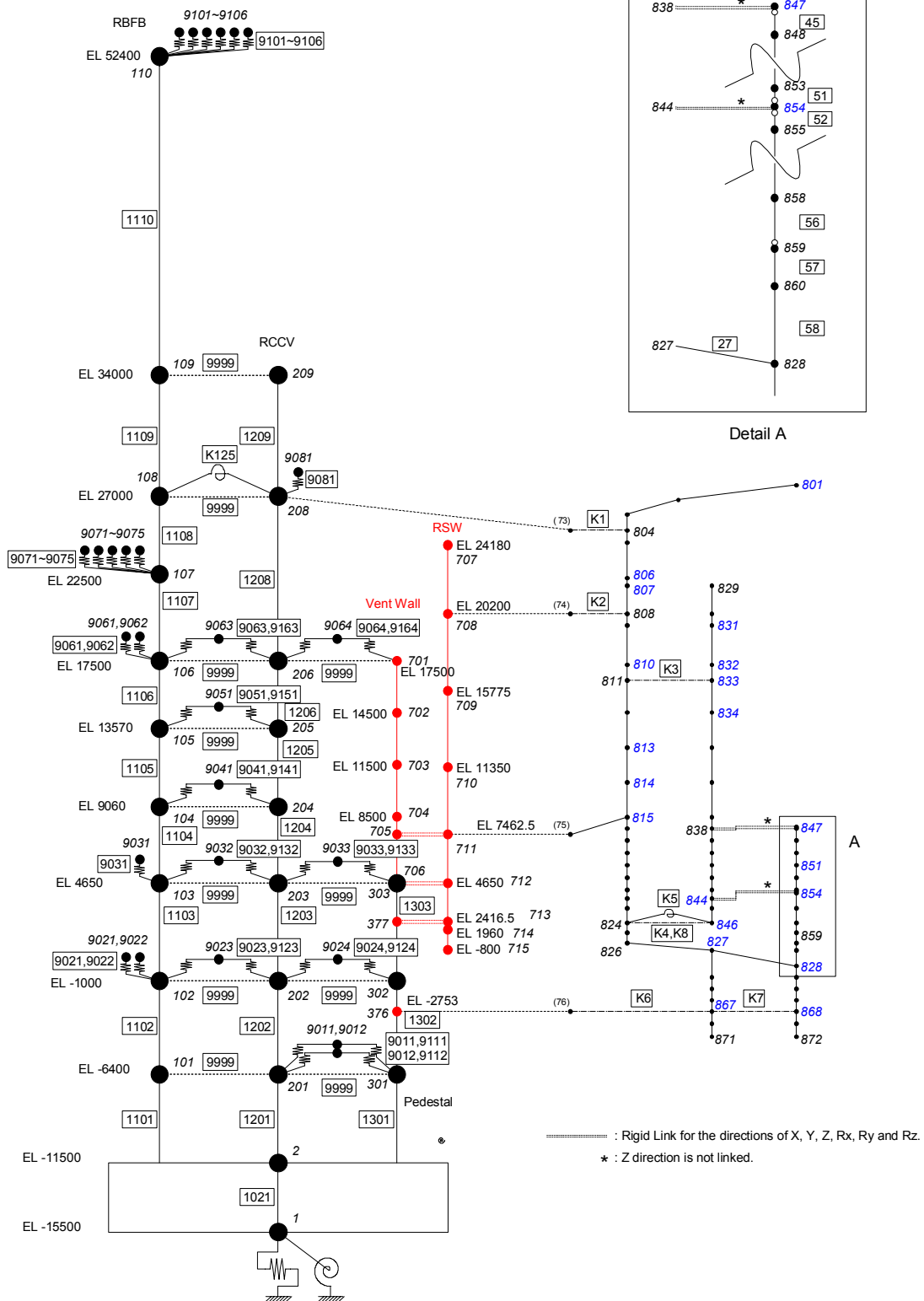


Figure 3A.7-3. Pedestal Stick Model



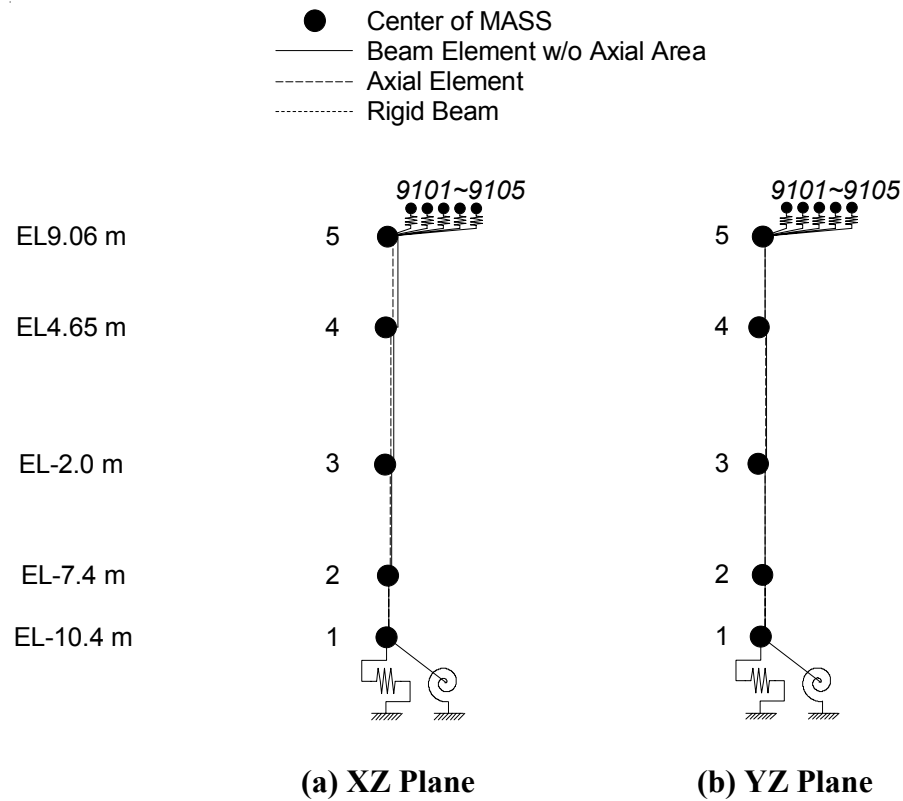


Figure 3A.7-5. ESBWR Control Building Seismic Model

3A.8 ANALYSIS RESULTS

In this section, typical SSI results are presented to show the effect of different soil properties on seismic responses at selected locations in terms of acceleration response spectra and seismic forces. The site-envelope seismic responses are presented in Section 3A.9.

For comparison study, the acceleration response spectra at 5% damping are shown for the following locations:

Location	Node Number
RBFB Refueling Floor	109
RCCV Top Slab	208
Vent Wall Top	701
RSW Top	707
RPV Top	801
RBFB Basemat	2
CB Top	5

The seismic forces are presented at the following locations:

Location	Connecting Nodes
RPV Support	815 – 711
RSW Base	710 – 711
Vent Wall Base	704 – 705
Pedestal Base	301 – 2
RCCV Base	201 – 2
RBFB Base	101 – 2
CB Base	3 – 2

The horizontal responses in X-direction are shown in Figures 3A.8-1a through 3A.8-1g. The responses in Y-direction are shown in Figures 3A.8-2a through 3A.8-2g. The vertical responses (Z-direction) are shown in Figure 3A.8-3a through 3A.8-3g. The results of the North Anna cases are the envelopes of the three soil conditions, Best-estimate (BE), Upper-bound (UB), and Lower-bound (LB). Generic site responses are higher at frequencies below 10 Hz, whereas North Anna responses are generally more dominant in the higher frequency range above 10 Hz.

The results in terms of seismic forces are compared in Tables 3A.8-1 and 3A.8-2, respectively for X direction and Y direction. As shown in these tables, the results of medium rock sites generally govern the seismic responses of the RBFB complex structure and the results of hard

rock sites generally govern the seismic responses of the CB structure. The results of all soil cases shown are used to obtain the enveloping results (Section 3A.9).

Table 3A.8-1
Maximum Forces - X Direction

Locations	Response Types	Soil Stiffness				
		SOFT	MEDIUM	HARD	FIX	North Anna
RPV Support	Shear Moment	5 24	13 59	15 89	13 85	9 115
RSW Base	Shear Moment	5 50	12 133	14 164	15 176	10 137
Vent Wall Base	Shear Moment	8 57	16 123	17 134	17 143	11 84
Pedestal Base	Shear Moment	47 711	101 1570	94 1472	91 1467	38 578
RCCV Base	Shear Moment	115 5277	252 10846	235 10611	226 9973	94 3888
RBFB Base	Shear Moment	413 18084	910 32284	848 33902	818 28822	339 10385
CB Base	Shear Moment	62 892	71 1078	70 979	60 842	80 1434

Units: Shear Forces in MN; Moment in MN-m

Table 3A.8-2
Maximum Forces - Y Direction

Locations	Response Types	Soil Stiffness				
		SOFT	MEDIUM	HARD	FIX	North Anna
RPV Support	Shear Moment	6 30	12 54	11 68	11 63	11 106
RSW Base	Shear Moment	6 66	11 122	11 127	10 117	10 123
Vent Wall Base	Shear Moment	10 78	21 166	17 145	16 128	12 77
Pedestal Base	Shear Moment	55 898	122 1970	97 1617	88 1452	40 560
RCCV Base	Shear Moment	137 6909	304 14269	244 11886	221 10895	97 4183
RBFB Base	Shear Moment	475 17620	1032 35490	804 28694	707 25752	342 8776
CB Base	Shear Moment	65 922	70 1003	73 1036	62 832	71 989

Units: Shear Forces in MN; Moment in MN-m

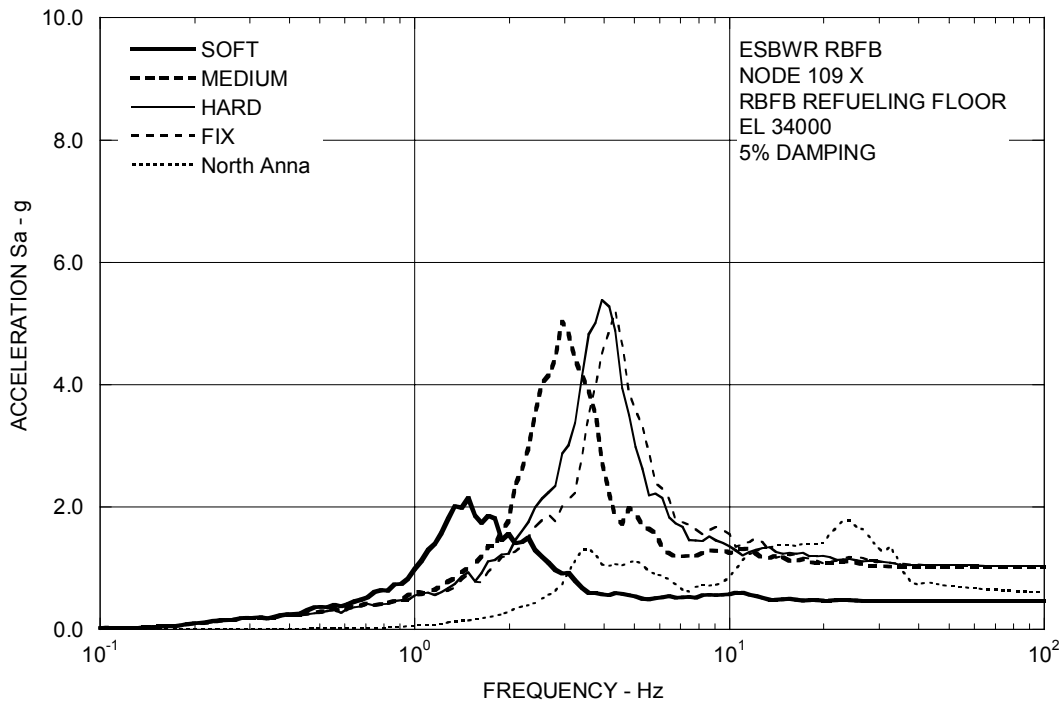


Figure 3A.8-1a. Floor Response Spectra – RBFB Refueling Floor X

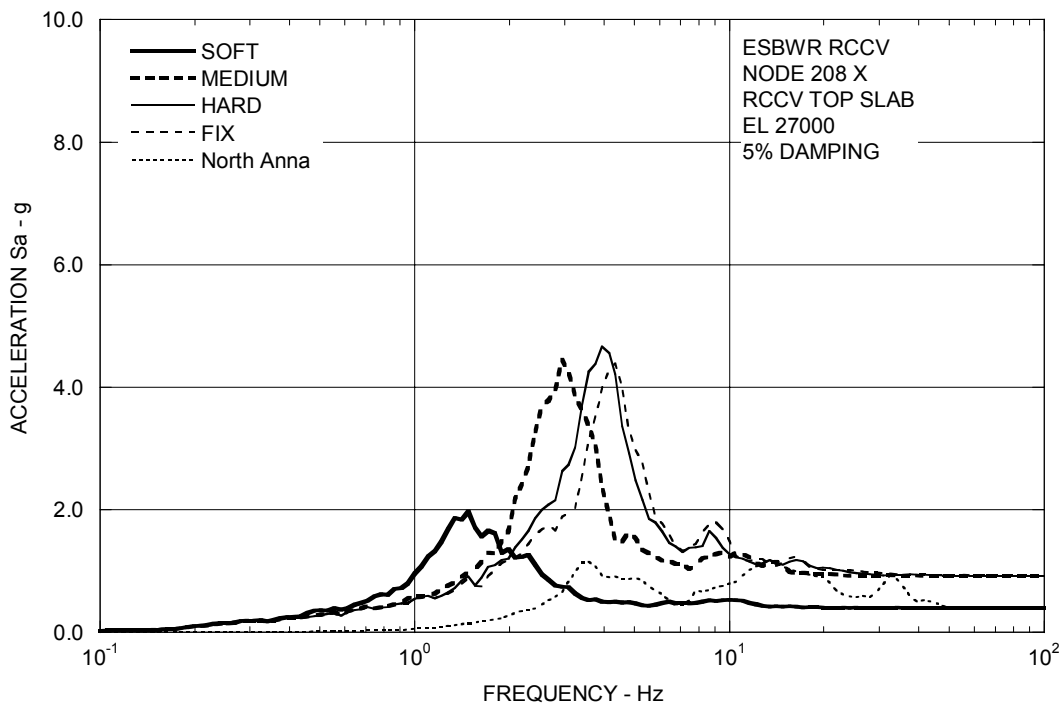
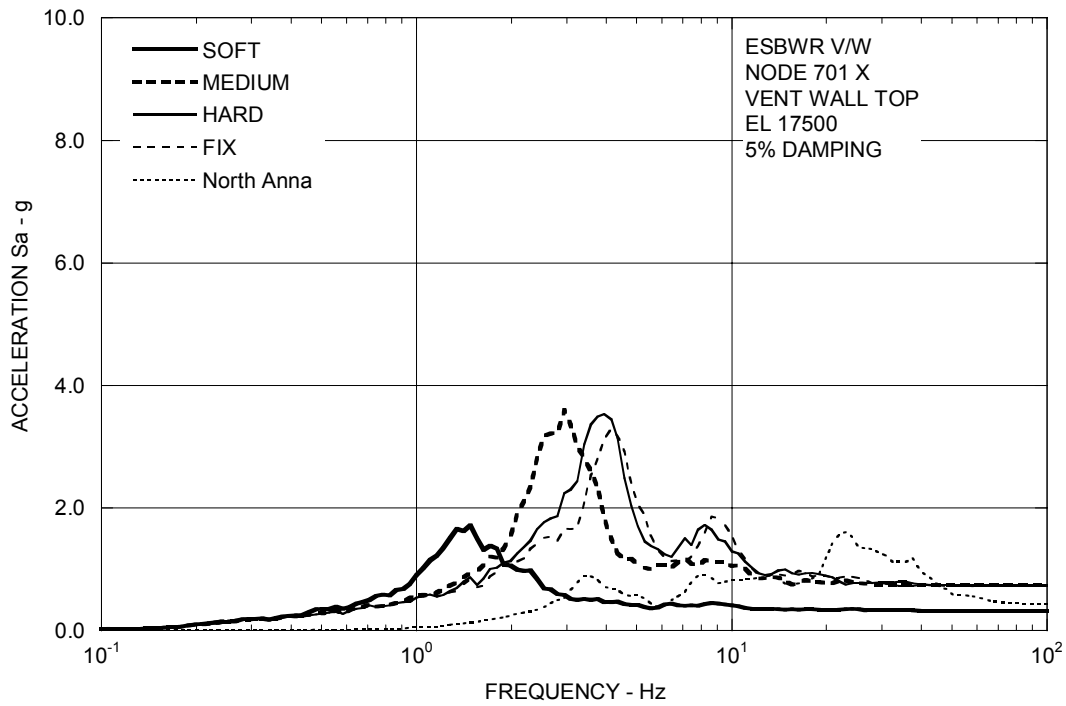
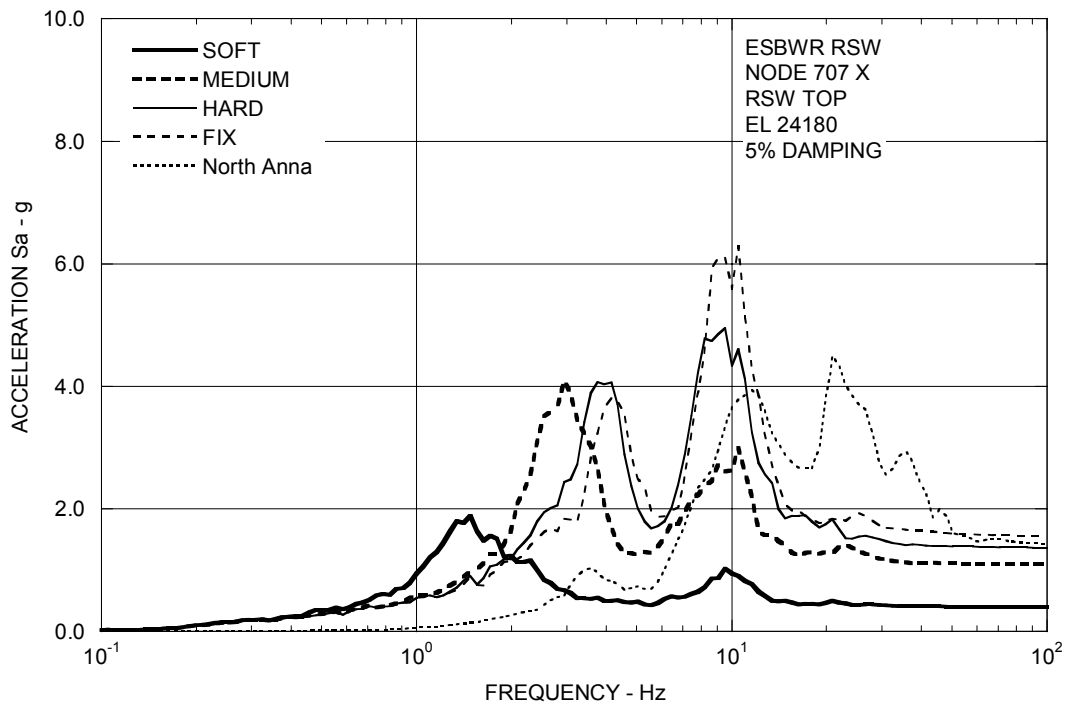


Figure 3A.8-1b. Floor Response Spectra – RCCV Top Slab X

**Figure 3A.8-1c. Floor Response Spectra – Vent Wall Top X****Figure 3A.8-1d. Floor Response Spectra – RSW Top X**

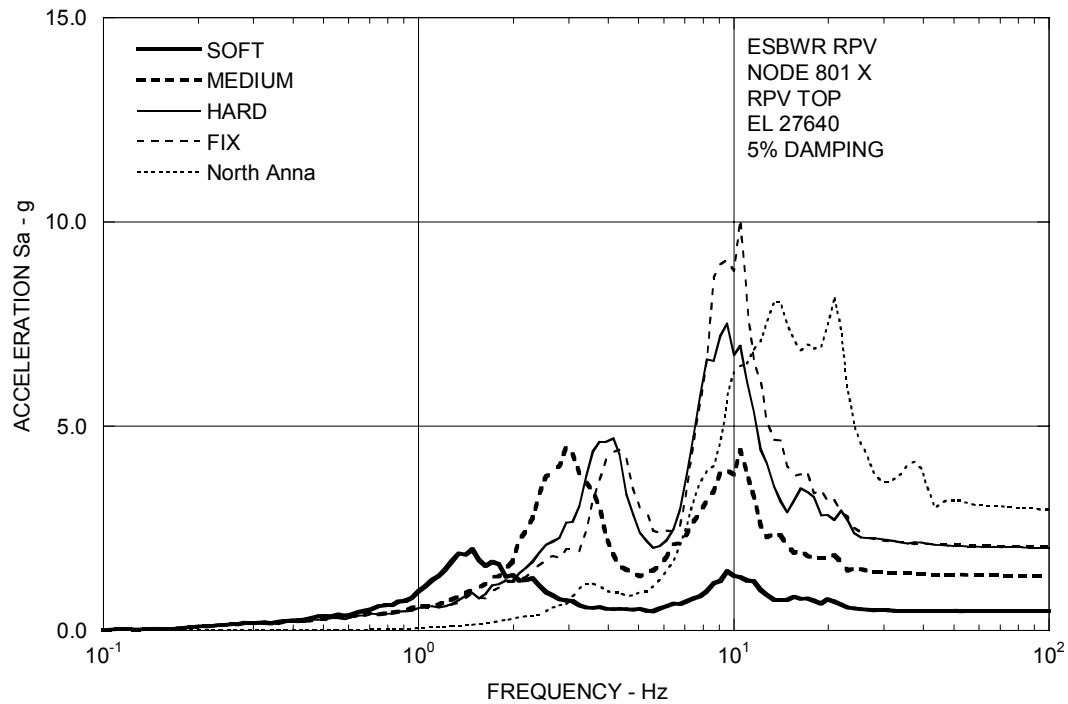


Figure 3A.8-1e. Floor Response Spectra – RPV Top X

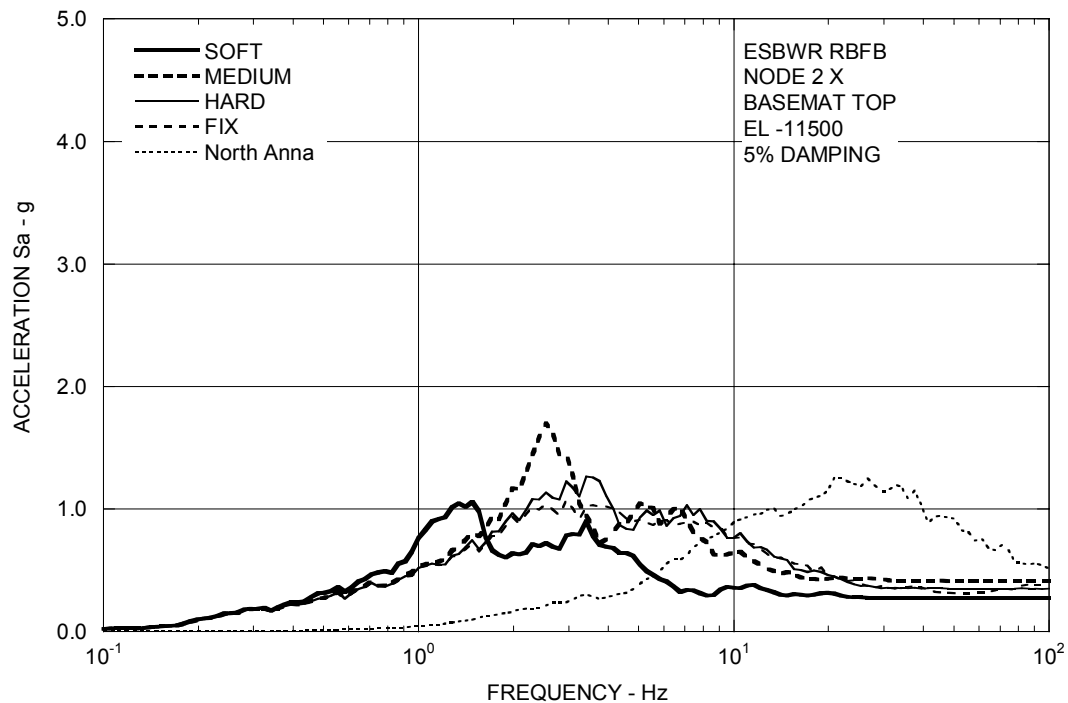


Figure 3A.8-1f. Floor Response Spectra – RBFB Basemat X

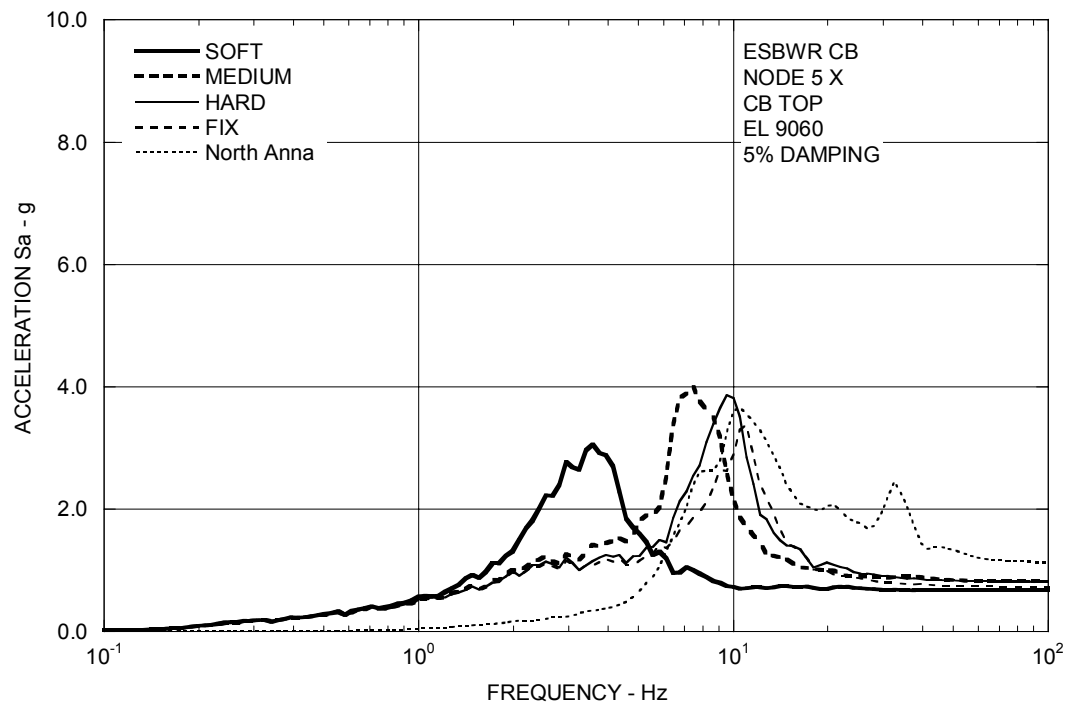


Figure 3A.8-1g. Floor Response Spectra – CB Top X

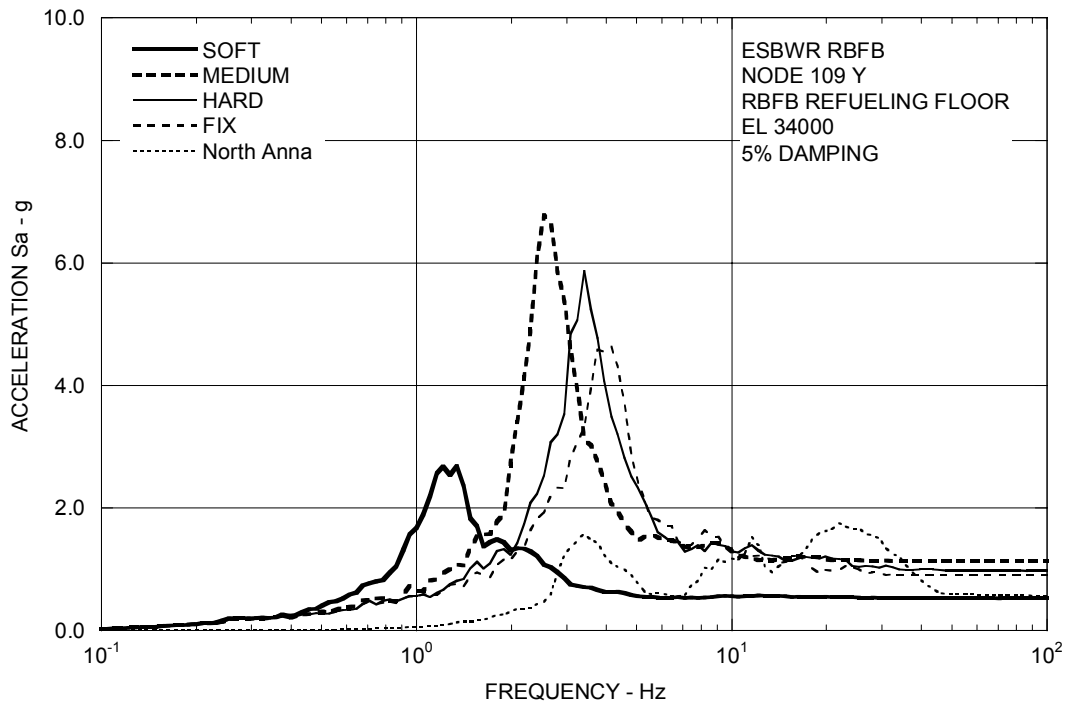


Figure 3A.8-2a. Floor Response Spectra – RBF Refueling Floor Y

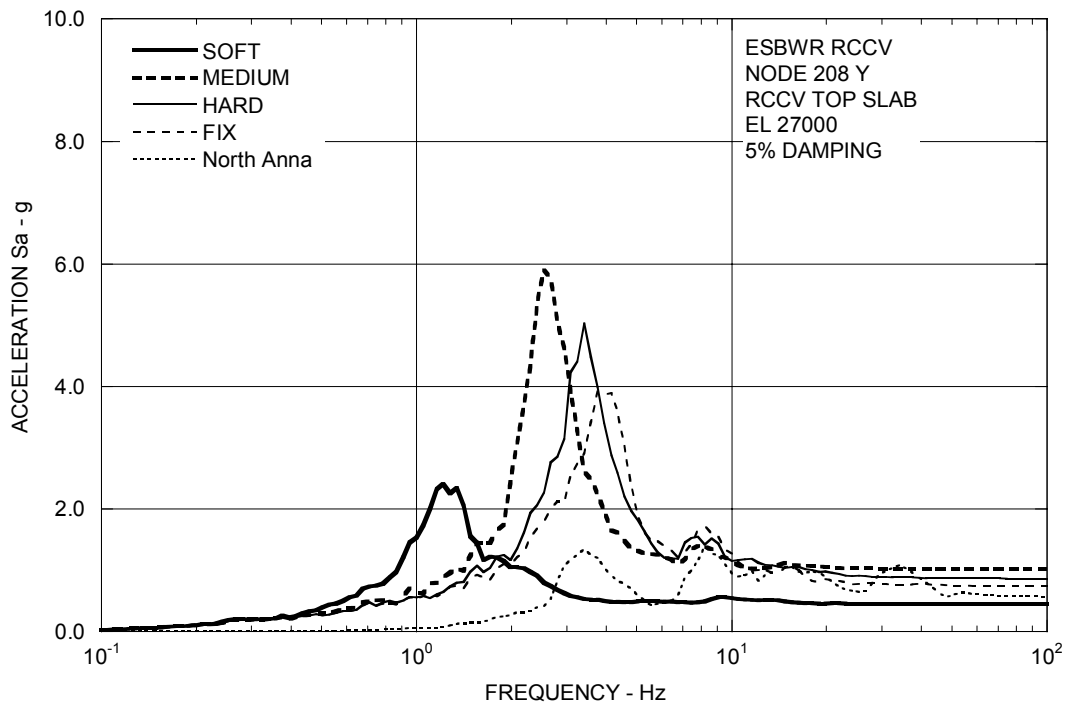
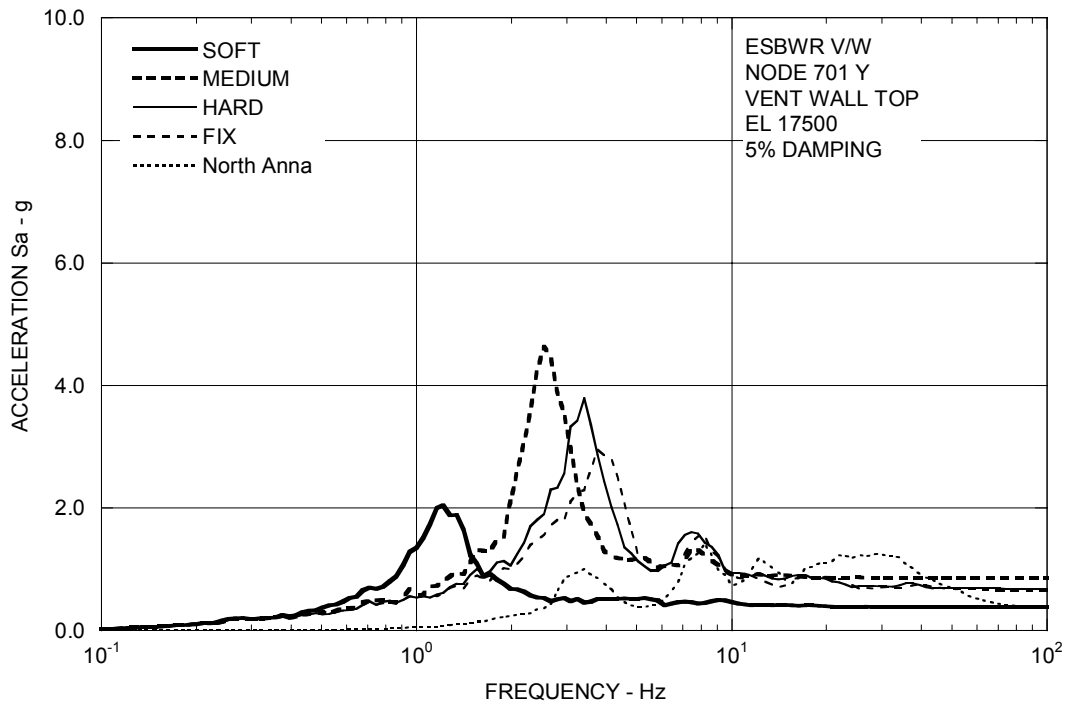
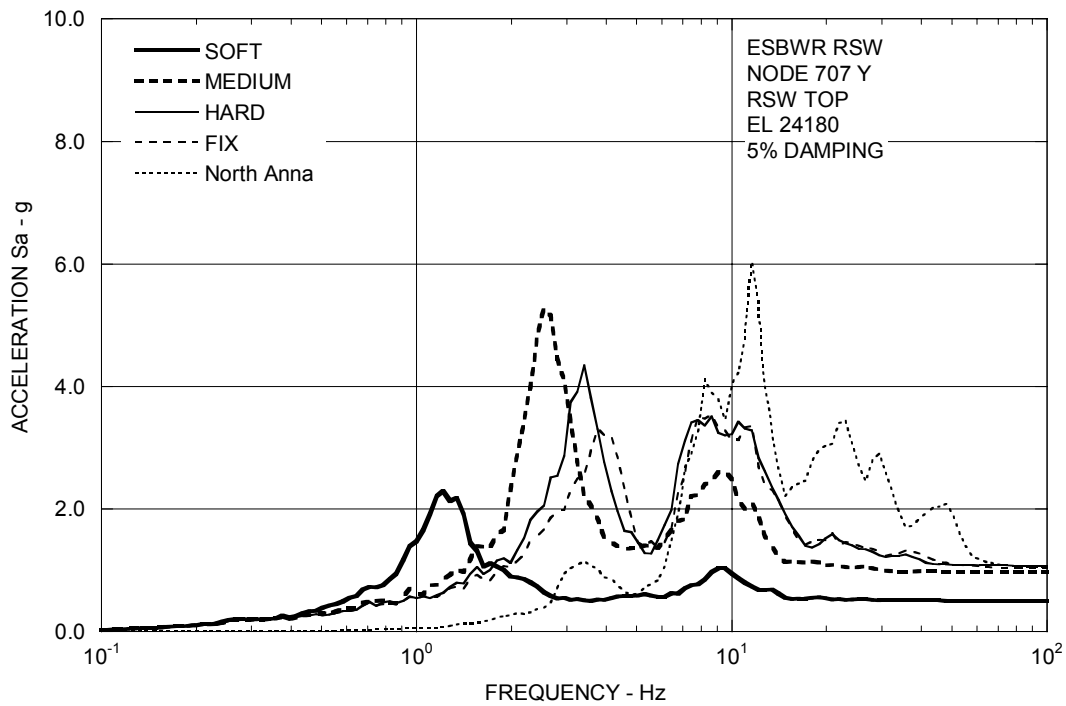


Figure 3A.8-2b. Floor Response Spectra – RCCV Top Slab Y

**Figure 3A.8-2c. Floor Response Spectra – Vent Wall Top Y****Figure 3A.8-2d. Floor Response Spectra – RSW Top Y**

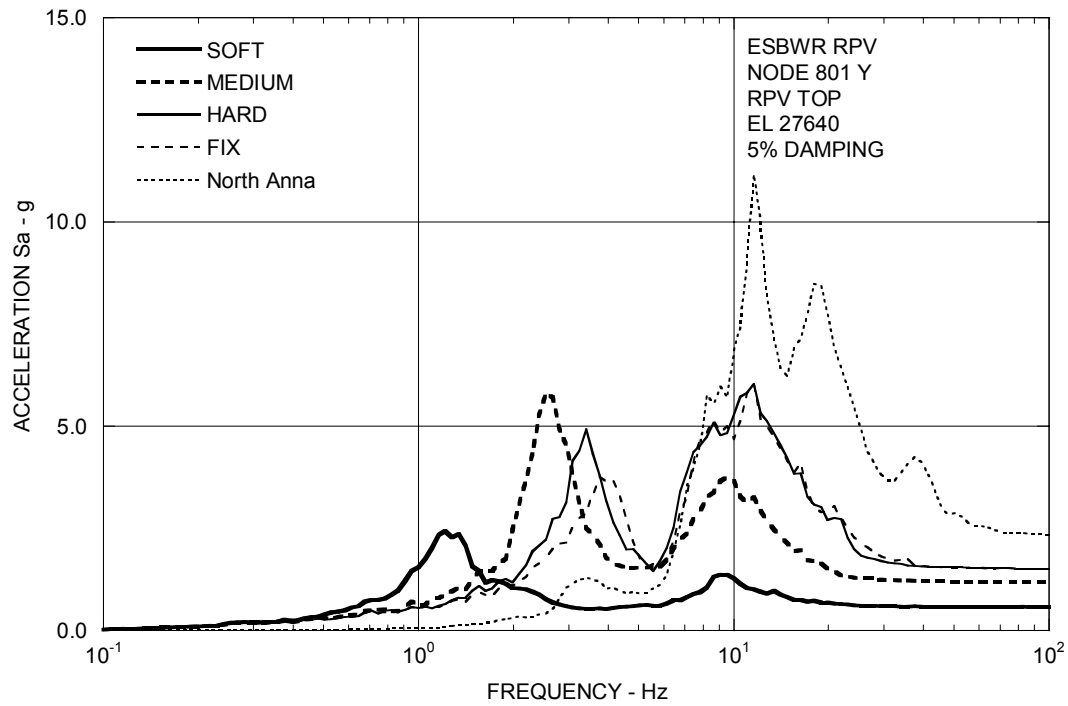


Figure 3A.8-2e. Floor Response Spectra – RPV Top Y

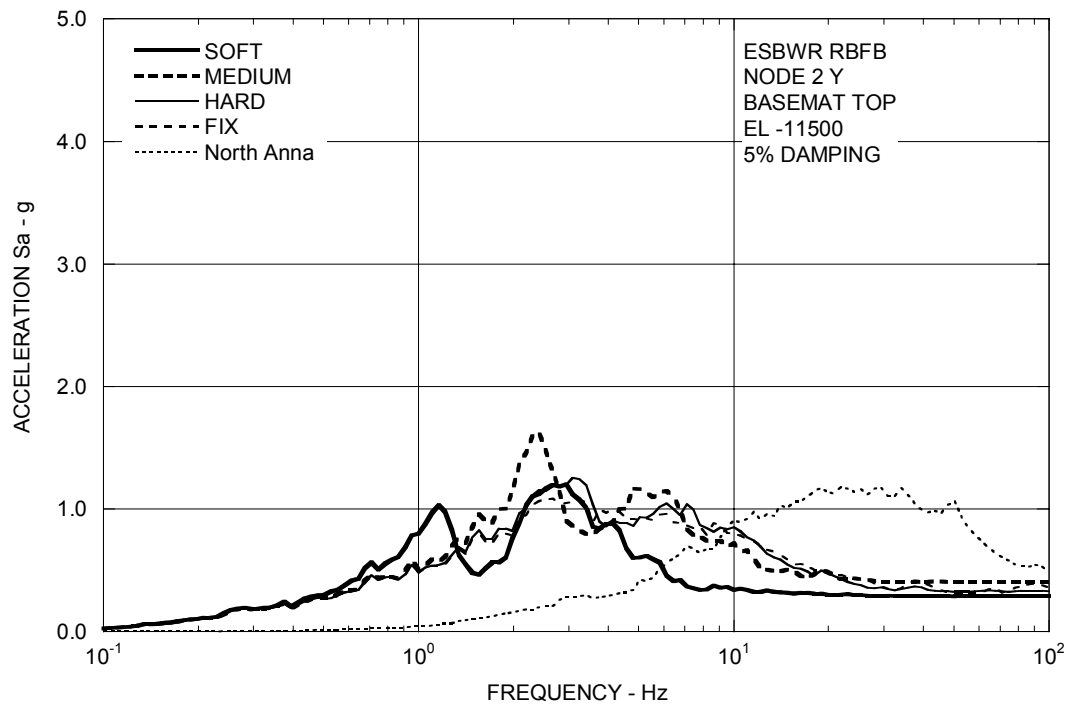


Figure 3A.8-2f. Floor Response Spectra – RBFB Basemat Y

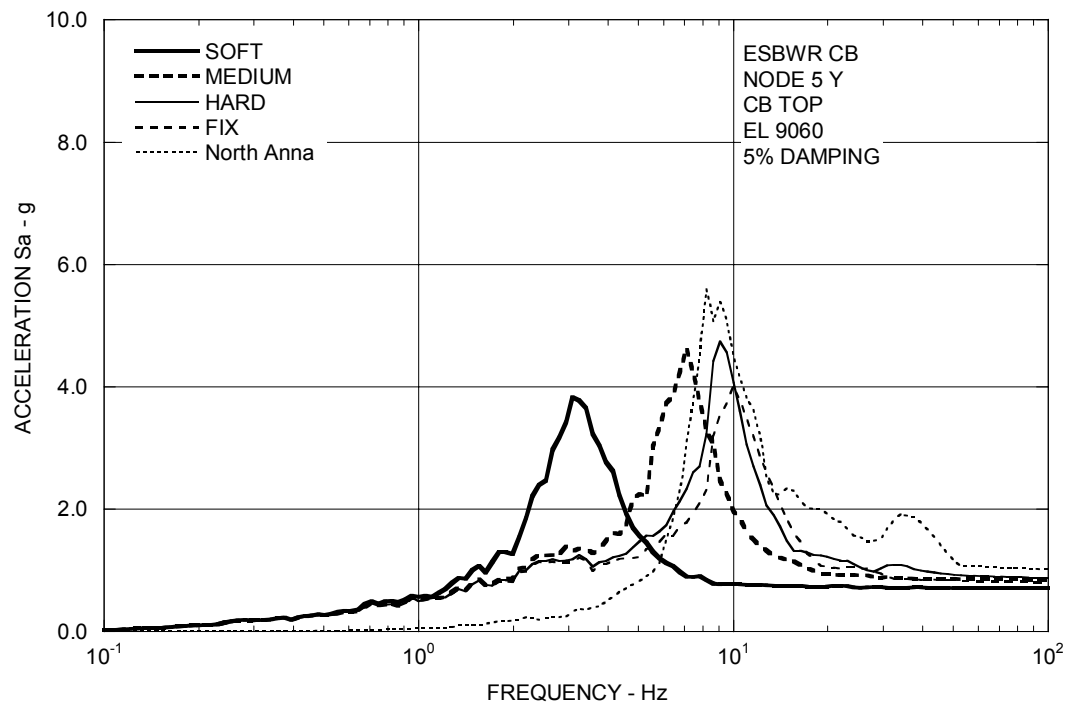


Figure 3A.8-2g. Floor Response Spectra – CB Top Y

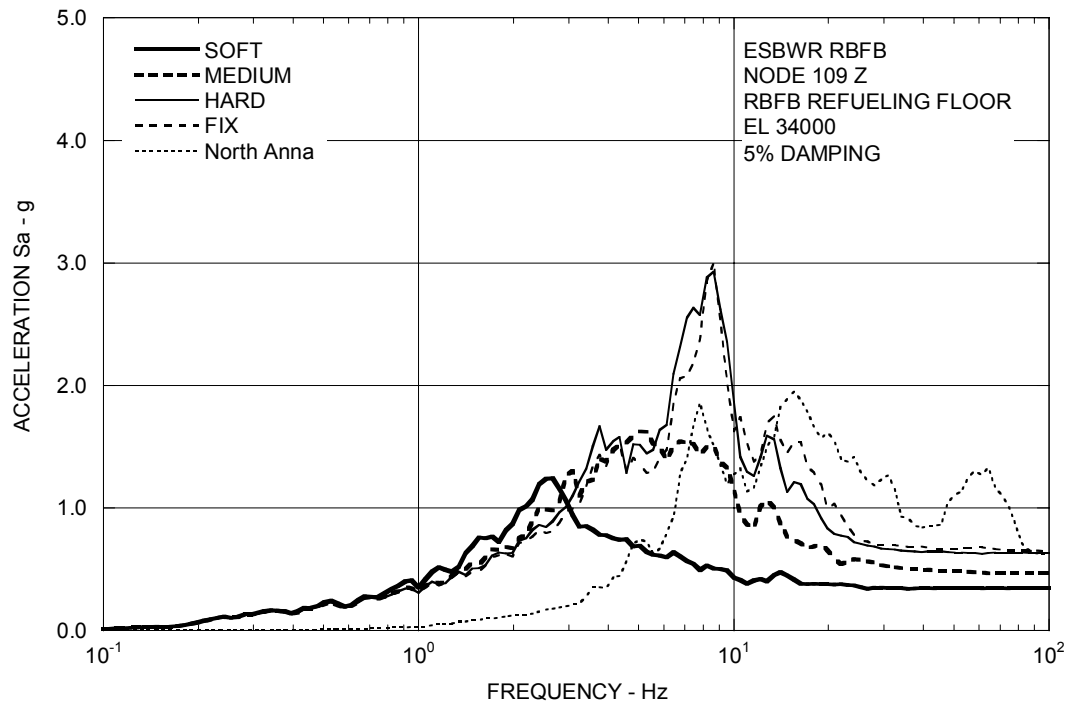


Figure 3A.8-3a. Floor Response Spectra – RBF Refueling Floor Z

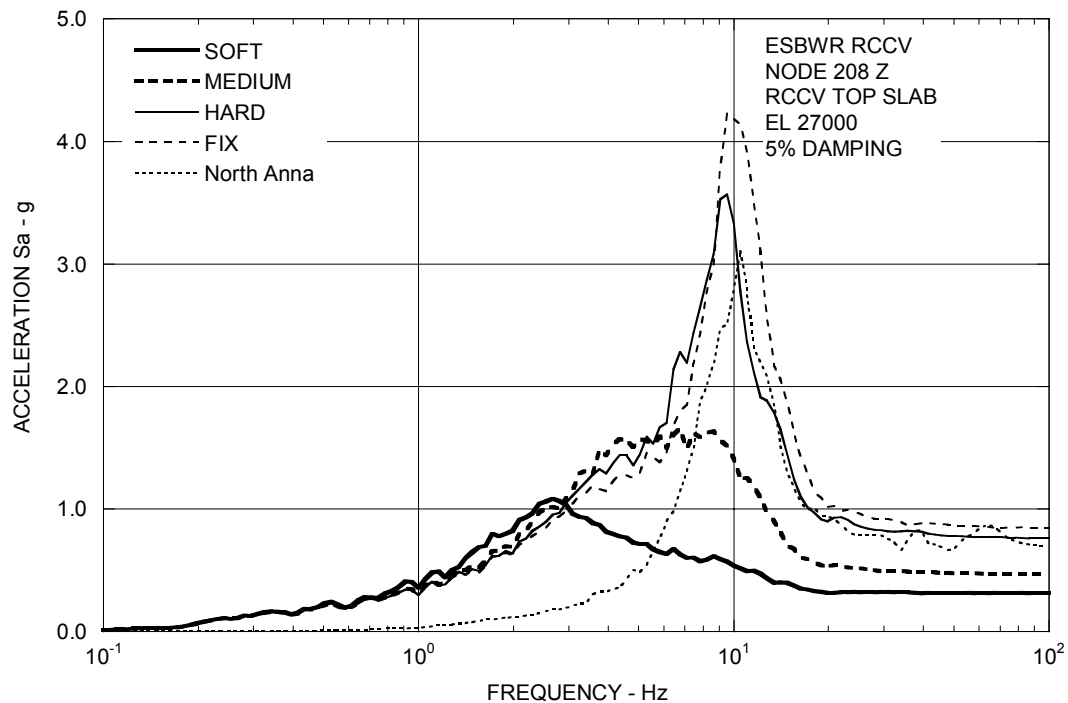
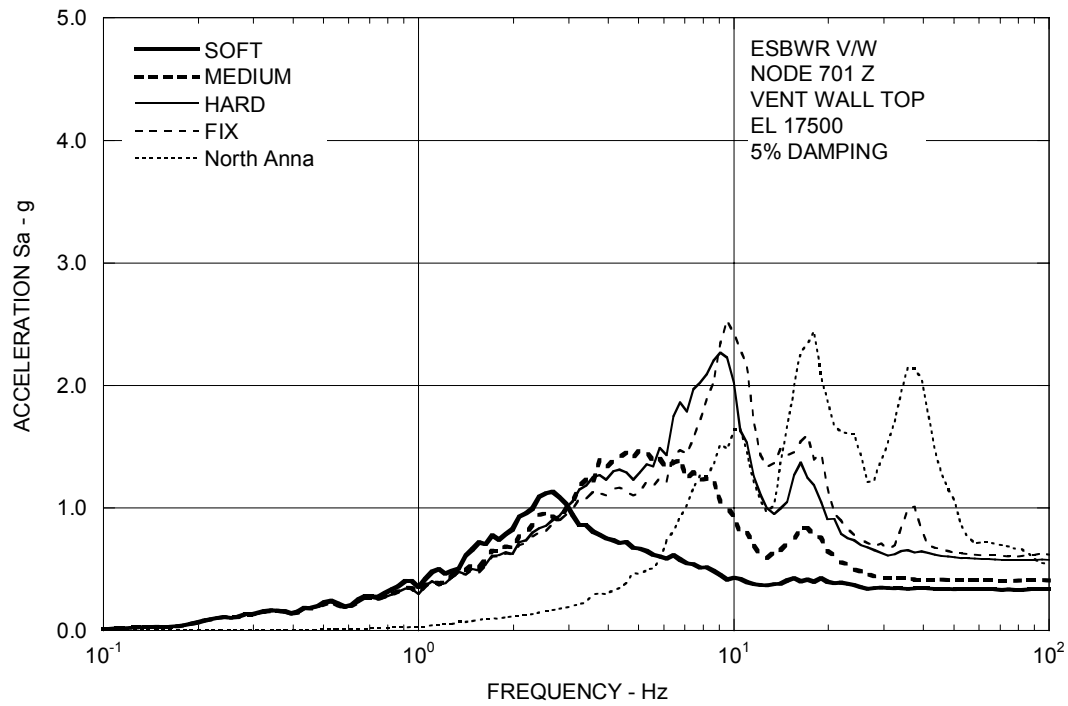
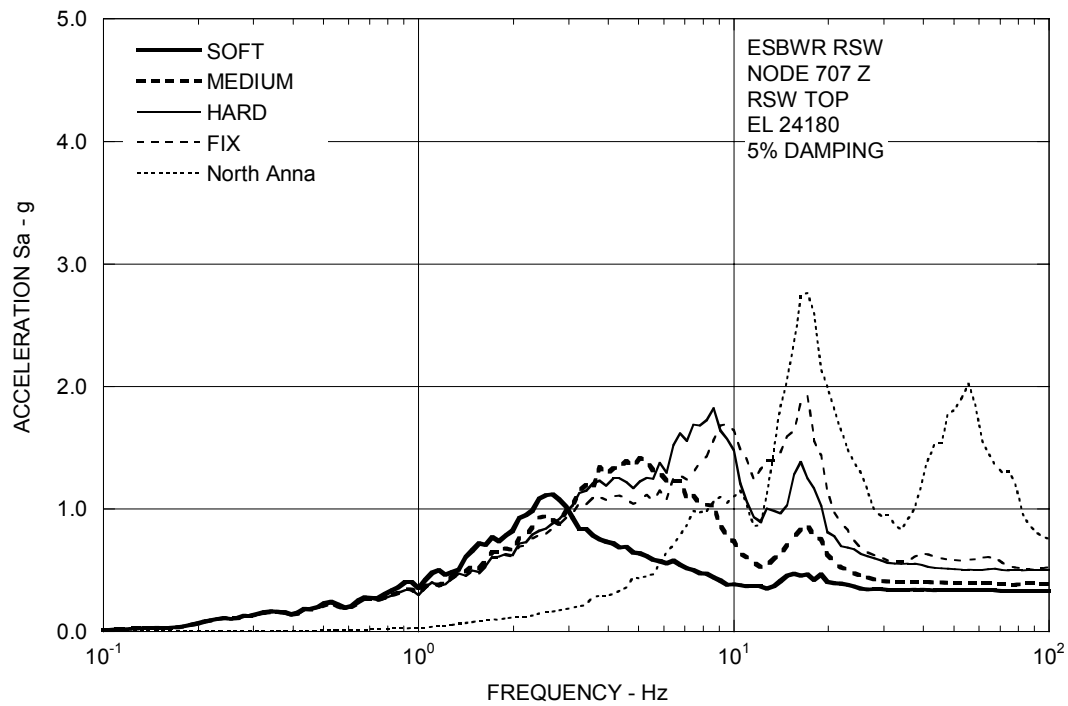


Figure 3A.8-3b. Floor Response Spectra – RCCV Top Slab Z

**Figure 3A.8-3c. Floor Response Spectra – Vent Wall Top Z****Figure 3A.8-3d. Floor Response Spectra – RSW Top Z**

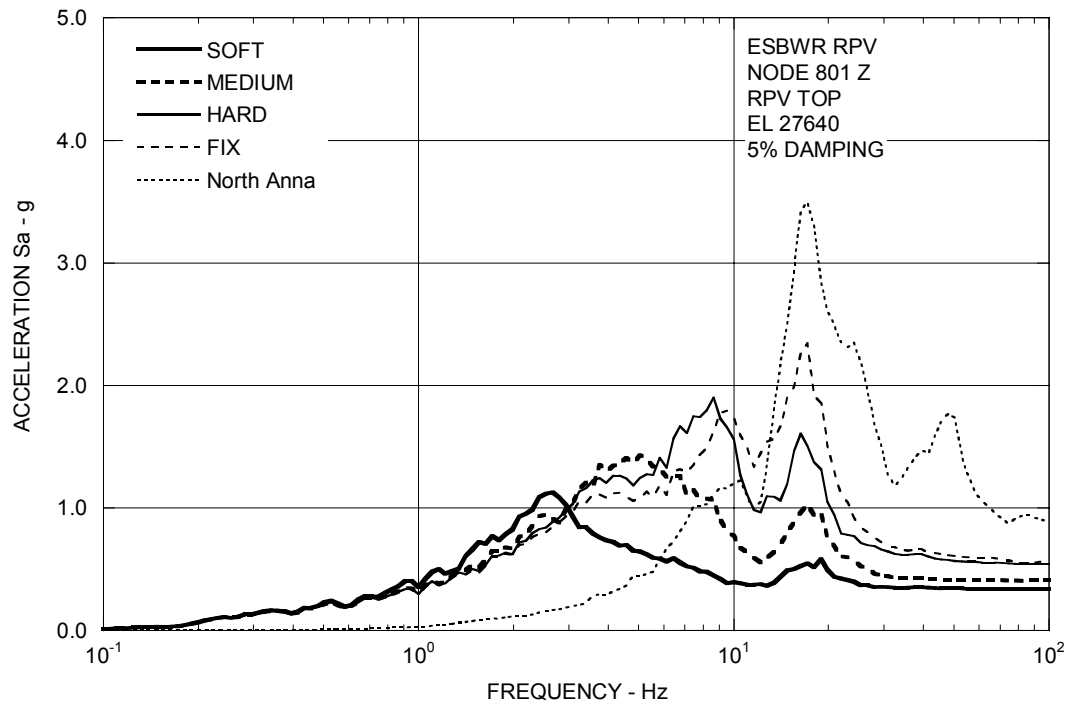


Figure 3A.8-3e. Floor Response Spectra – RPV Top Z

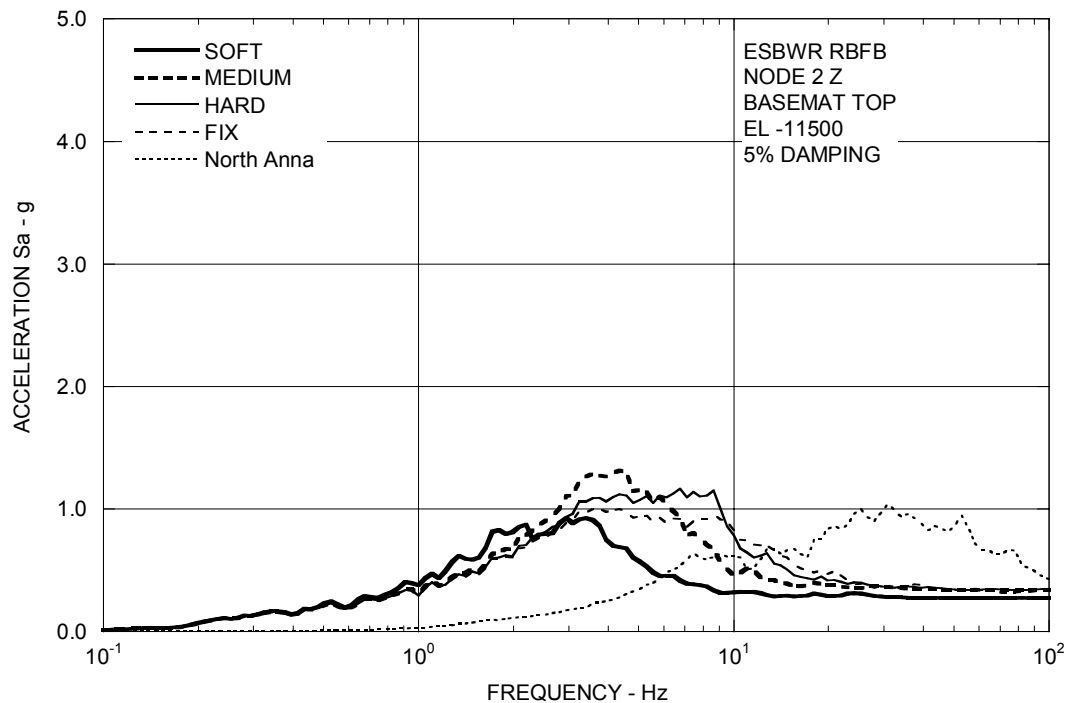


Figure 3A.8-3f. Floor Response Spectra – RBFB Basemat Z

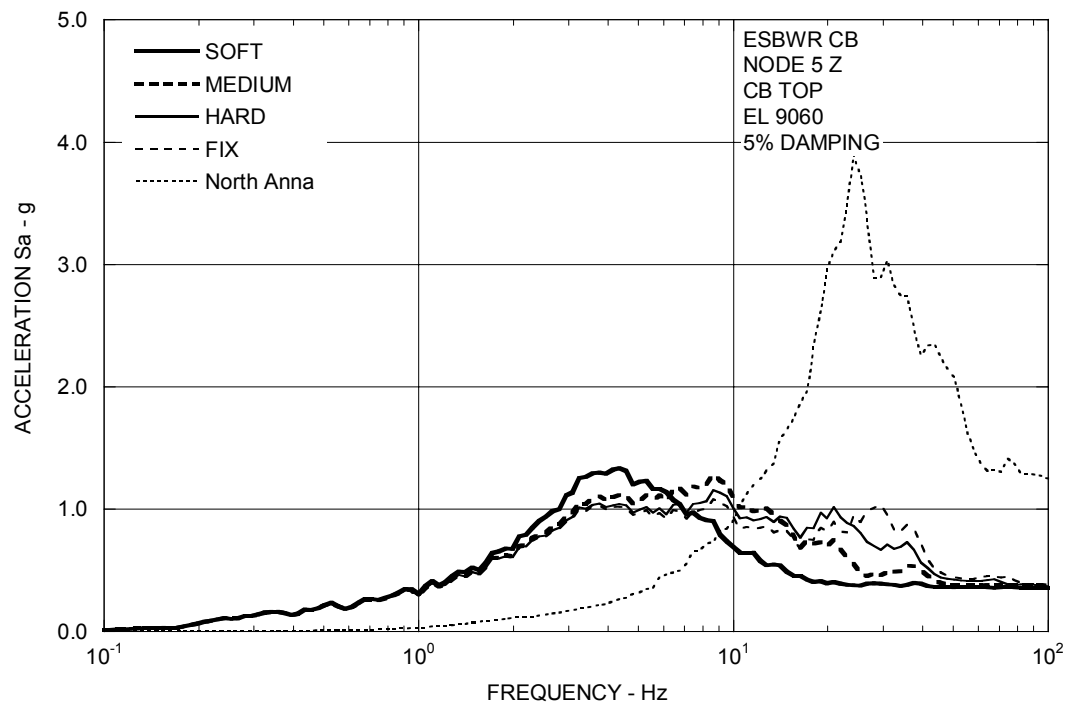


Figure 3A.8-3g. Floor Response Spectra – CB Top Z

3A.9 SITE ENVELOPE SEISMIC RESPONSES

The site-envelope seismic loads are established from the envelopes of all analysis results from SSI cases summarized in Table 3A.6-1. The site-envelope seismic loads obtained are applicable for the design of Seismic Category I (C-I) and II (C-II) structures, systems and components housed in the ESBWR standard plant.

3A.9.1 Enveloping Maximum Structural Loads

The enveloping maximum shear and moment distributions along the RBFB walls, RCCV, vent wall/pedestal, RSW, key RPV/internals, and the CB walls are shown in Tables 3A.9-1 through 3A.9-6. These shears and moments are the envelope of all SSI cases. The torsional moments for building structures are due to geometric eccentricities only. Additional torsion due to an accidental eccentricity of 5% of maximum floor dimension under consideration is added for the design of building structures.

The vertical loads are expressed in terms of enveloping absolute acceleration. The enveloping maximum acceleration values are shown in Tables 3A.9-7 through 3A.9-12. These acceleration values do not include the coupling effect and are only applicable for structural analysis in combination with the seismic loads due to horizontal shakings.

3A.9.2 Enveloping Floor Response Spectra

The site-envelope SSE floor response spectra are obtained according to the following steps:

- For each soil case analyzed, the calculated co-directional floor response spectra in X, Y, and Z directions are combined by the SRSS method to obtain floor response spectra at the building edges considering the coupling effects between vertical and rocking and between lateral and torsion motions.
- Individual site responses obtained in Step 1 are enveloped to form the site-envelope response spectra in each of the 3 directions.
- The reduction factors due to wave incoherence according to ASCE 4-98 are applied to the result of Step 2.
- The envelope spectra are subsequently peak broadened by $\pm 15\%$.

The site-envelope peak-broadened SSE floor response spectra at critical damping ratios 2, 3, 4, 5, 7, 10, and 20% for the RBFB and CB are shown in Figures 3A.9-1a through 3A.9-1g for the X direction, in Figures 3A.9-2a through 3A.9-2g for the Y direction, and in Figures 3A.9-3a through 3A.9-3g for the vertical direction. For seismic design of equipment and piping, the alternative seismic input can be individual floor response spectra of each site condition considered in generating the site-envelope spectra.

Table 3A.9-1
Enveloping Seismic Loads: RBFB Stick

EL (m)	Node No.	Elem No.	Shear		Moment		Torsion (MN-m)
			X-Dir. (MN)	Y-Dir. (MN)	X-Dir. (MN-m)	Y-Dir. (MN-m)	
52.40	110	1110	147.3	156.8	1559 4151	1324 4080	1091
34.00	109	1109	174.9	149.1	5686 6570	5404 6395	1703
27.00	108	1108	421.4	401.6	8686 10003	7449 9117	3091
22.50	107	1107	477.5	464.7	11219 12847	9713 11807	6081
17.50	106	1106	526.5	556.3	12866 14720	12396 14328	5056
13.57	105	1105	562.8	601.1	15181 17485	14808 17172	5233
9.06	104	1104	603.5	655.7	17878 20280	17623 20104	5959
4.65	103	1103	828.9	873.9	20908 24958	20722 24782	11484
-1.00	102	1102	860.6	940.2	25419 29381	25448 29508	11582
-6.40	101	1101	910.3	1031.7	29734 33902	30234 35490	11660
-11.50	2				45523	52731	
-15.50	1	1021	1355.3	1571.0	50426	59007	11366

Note: Total torsional moments are obtained by the absolute sum of the accidental torsional moments and the values of the geometric torsional moments shown. The accidental torsional moment is the product of the horizontal force component and an eccentricity of 5% of the larger horizontal dimension at various elevations.

Table 3A.9-2
Enveloping Seismic Loads: RCCV Stick

EL (m)	Node No.	Elem No.	Shear		Moment		Torsion (MN-m)
			X-Dir. (MN)	Y-Dir. (MN)	X-Dir. (MN-m)	Y-Dir. (MN-m)	
34.00	209	1209	137.7	188.1	129 1048	380 1533	25
27.00	208	1208	168.4	247.1	1638 3166	2143 4443	1815
17.50	206	1206	230.5	291.6	3506 4354	4793 5845	1976
13.57	205	1205	261.8	327.3	4532 5618	6033 7353	2181
9.06	204	1204	299.7	366.9	5841 7012	7610 9005	2605
4.65	203	1203	210.6	290.1	7215 8195	9268 10640	2885
-1.00	202	1202	257.3	331.4	8315 9453	10797 12582	2940
-6.40	201	1201	252.2	304.2	9560	12719	1958
-11.50	2				10846	14269	

Note: Total torsional moments are obtained by the absolute sum of the accidental torsional moments and the values of the geometric torsional moments shown. The accidental torsional moment is the product of the horizontal force component and an eccentricity of 5% of the larger horizontal dimension at various elevations.

Table 3A.9-3
Enveloping Seismic Loads: VW/PED Stick

EL (m)	Node No.	Elem No.	Shear		Moment		Torsion (MN-m)
			X-Dir. (MN)	Y-Dir. (MN)	X-Dir. (MN-m)	Y-Dir. (MN-m)	
17.50	701				63	50	
		701	12.1	12.3	64	49	31
14.50	702				82	61	
		702	14.0	14.3	85	87	32
11.50	703				88	90	
		703	15.5	17.8	127	143	34
8.50	704				126	145	
		704	16.6	20.6	143	166	34
7.4625	705				179	166	
		705	12.5	13.8	212	205	17
4.65	706,303				454	422	
		1303	28.7	45.0	493	522	142
2.4165	377				605	645	
		1377	42.8	66.5	697	872	173
-1.00	302				725	894	
		1302	61.2	81.6	820	1037	147
-2.75	376				820	1037	
		1376	61.4	81.9	1043	1335	147
-6.40 -11.50	301 2				1056	1350	
		1301	100.8	121.5	1570	1970	117

Note: Total torsional moments are obtained by the absolute sum of the accidental torsional moments and the values of the geometric torsional moments shown. The accidental torsional moment is the product of the horizontal force component and an eccentricity of 5% of the larger horizontal dimension at various elevations.

Table 3A.9-4
Enveloping Seismic Loads: RSW Stick

EL (m)	Node No.	Elem No.	Shear		Moment		Torsion (MN-m)
			X-Dir. (MN)	Y-Dir. (MN)	X-Dir. (MN-m)	Y-Dir. (MN-m)	
24.18	707	707	1.8	1.2	1.2 7.8	1.2 5.5	0.2
20.20	708	708	10.7	8.4	11.3 57.8	9.3 44.5	0.8
15.775	709	709	12.9	9.3	59.8 116.7	46.5 86.0	1.1
11.35	710	710	15.1	11.1	117.2 175.8	86.4 126.6	1.2
7.4625	711	711	32.2	35.7	164.4 251.0	149.1 247.8	18.2
4.65	712	712	12.5	19.5	95.2 112.1	81.7 124.9	30.4
2.4165	713	713	0.9	1.0	2.5 2.1	2.0 1.7	0.1
1.96 -0.80	714 715	714 714	0.5	0.6	1.8 0.4	1.5 0.3	0.1

Note: Total torsional moments are obtained by the absolute sum of the accidental torsional moments and the values of the geometric torsional moments shown. The accidental torsional moment is the product of the horizontal force component and an eccentricity of 5% of the larger horizontal dimension at various elevations.

Table 3A.9-5**Enveloping Seismic Loads: RPV Stick**

Components (m)	Node No.	Elem No.	Axial (MN)	Shear		Moment	
				X-Dir. (MN)	Y-Dir. (MN)	X-Dir. (MN-m)	Y-Dir. (MN-m)
Shroud	845					11.5	10.7
Bottom	846	844	4.4	5.0	3.4	14.9	12.4
RPV	815					114.9	105.3
Support	711	871	16.5	14.5	12.2	113.6	105.5

Table 3A.9-6**Enveloping Seismic Loads: CB Stick**

EL (m)	Node No.	Elem No.	Shear		Moment		Torsion (MN-m)
			X-Dir. (MN)	Y-Dir. (MN)	X-Dir. (MN-m)	Y-Dir. (MN-m)	
9.06	5	5	42.8	35.4	174 300	145 232	27.0
4.65	4	4	69.6	57.8	446 900	355 616	40.5
-2.00	3	3	80.1	73.2	1001 1434	642 1036	38.2
-7.40	2				1476	1048	
-10.40	1	2	82.8	85.6	1697	1305	34.1

Note: Total torsional moments are obtained by the absolute sum of the accidental torsional moments and the values of the geometric torsional moments shown. The accidental torsional moment is the product of the horizontal force component and an eccentricity of 5% of the larger horizontal dimension at various elevations.

Table 3A.9-7**Enveloping Maximum Vertical Acceleration: RBFB**

EL (m)	Node No.	Stick Model	Max. Vertical Acceleration (g)
52.40	110	RBFB	0.76
34.00	109	RBFB	0.65
27.00	108	RBFB	0.61
22.50	107	RBFB	0.50
17.50	106	RBFB	0.51
13.57	105	RBFB	0.50
9.06	104	RBFB	0.47
4.65	103	RBFB	0.44
-1.00	102	RBFB	0.43
-6.40	101	RBFB	0.41
-11.50	2	RBFB	0.38
-15.50	1	RBFB	0.34

Note: For structural design use only.

Table 3A.9-8**Enveloping Maximum Vertical Acceleration: RCCV**

EL (m)	Node No.	Stick Model	Max. Vertical Acceleration (g)
34.00	209	RCCV	0.84
27.00	208	RCCV	0.84
17.50	206	RCCV	0.71
13.57	205	RCCV	0.66
9.06	204	RCCV	0.57
4.65	203	RCCV	0.52
-1.00	202	RCCV	0.44
-6.40	201	RCCV	0.38

Note: For structural design use only.

Table 3A.9-9**Enveloping Maximum Vertical Acceleration: VW/Pedestal**

EL (m)	Node No.	Stick Model	Max. Vertical Acceleration (g)
17.50	701	VW	0.59
14.50	702	VW	0.57
11.50	703	VW	0.53
8.50	704	VW	0.49
7.4625	705	VW	0.50
4.65	706, 303	Pedestal	0.47
2.42	377	Pedestal	0.44
-1.00	302	Pedestal	0.46
-2.75	376	Pedestal	0.43
-6.40	301	Pedestal	0.43

Note: For structural design use only.

Table 3A.9-10**Enveloping Maximum Vertical Acceleration: RSW**

EL (m)	Node No.	Stick Model	Max. Vertical Acceleration (g)
24.18	707	RSW	0.67
20.20	708	RSW	0.65
15.775	709	RSW	0.61
11.35	710	RSW	0.56
7.4625	711	RSW	0.50
4.65	712	RSW	0.47
2.4615	713	RSW	0.44
1.96	714	RSW	0.44
-0.80	715	RSW	0.45

Note: For structural design use only.

Table 3A.9-11**Enveloping Maximum Vertical Acceleration: RBFB Flexible Slab Oscillators**

EL (m)	Node No.	Stick Model	Max. Vertical Acceleration (g)
52.40	9101	Oscillator	1.20
	9102	Oscillator	1.83
	9103	Oscillator	1.63
	9104	Oscillator	1.72
	9105	Oscillator	1.69
	9106	Oscillator	1.88
27.00	9081	Oscillator	0.94
22.50	9071	Oscillator	1.57
	9072	Oscillator	1.26
	9073	Oscillator	1.39
	9074	Oscillator	0.97
	9075	Oscillator	0.76
17.50	9061	Oscillator	1.08
	9062	Oscillator	0.92
	9063	Oscillator	0.59
	9064	Oscillator	1.17
13.57	9051	Oscillator	0.55
9.06	9041	Oscillator	0.52
4.65	9031	Oscillator	0.87
	9032	Oscillator	0.54
	9033	Oscillator	0.52
-1.00	9021	Oscillator	0.73
	9022	Oscillator	1.05
	9023	Oscillator	0.67
	9024	Oscillator	0.53
-6.40	9011	Oscillator	0.57
	9012	Oscillator	0.66

Note: For structural design use only.

Table 3A.9-12**Enveloping Maximum Acceleration: CB**

EL (m)	Node No.	Stick Model	Max. Vertical Acceleration (g)
9.06	5	CB	1.11
4.65	4	CB	0.92
-2.00	3	CB	0.62
-7.40	2	CB	0.47
-10.40	1	CB	0.47
9.06	9101	Oscillator	1.01
	9102	Oscillator	1.51
	9103	Oscillator	2.89
	9104	Oscillator	2.93
	9105	Oscillator	2.62

Note: For structural design use only.

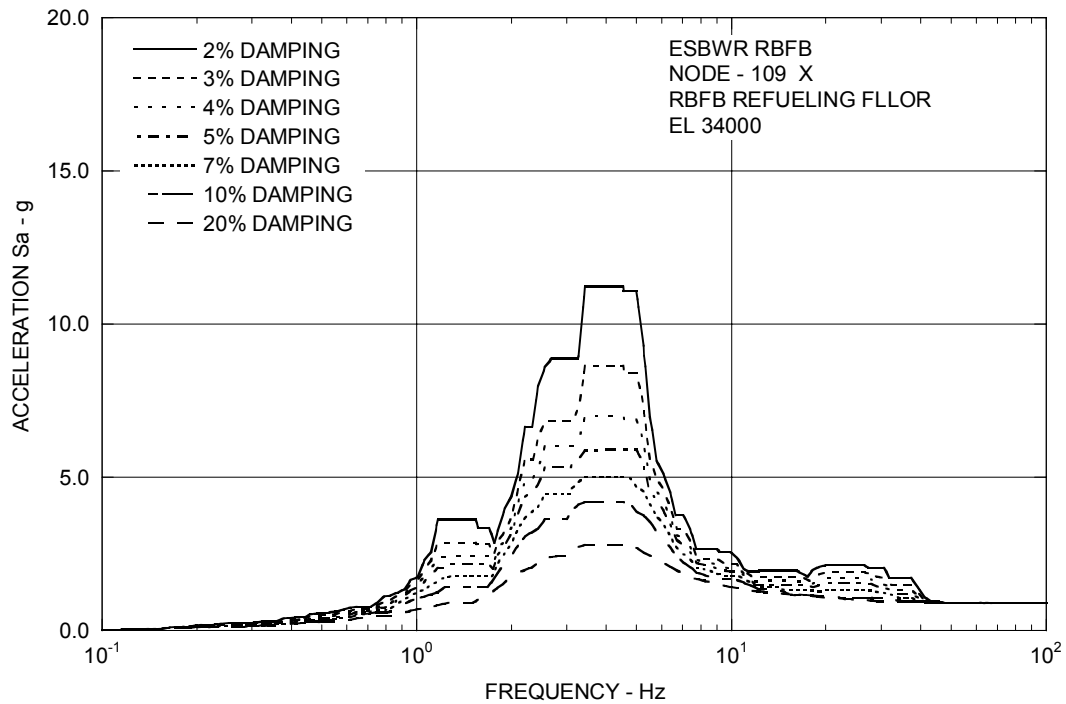


Figure 3A.9-1a. Enveloping Floor Response Spectra – RFBF Refueling Floor X

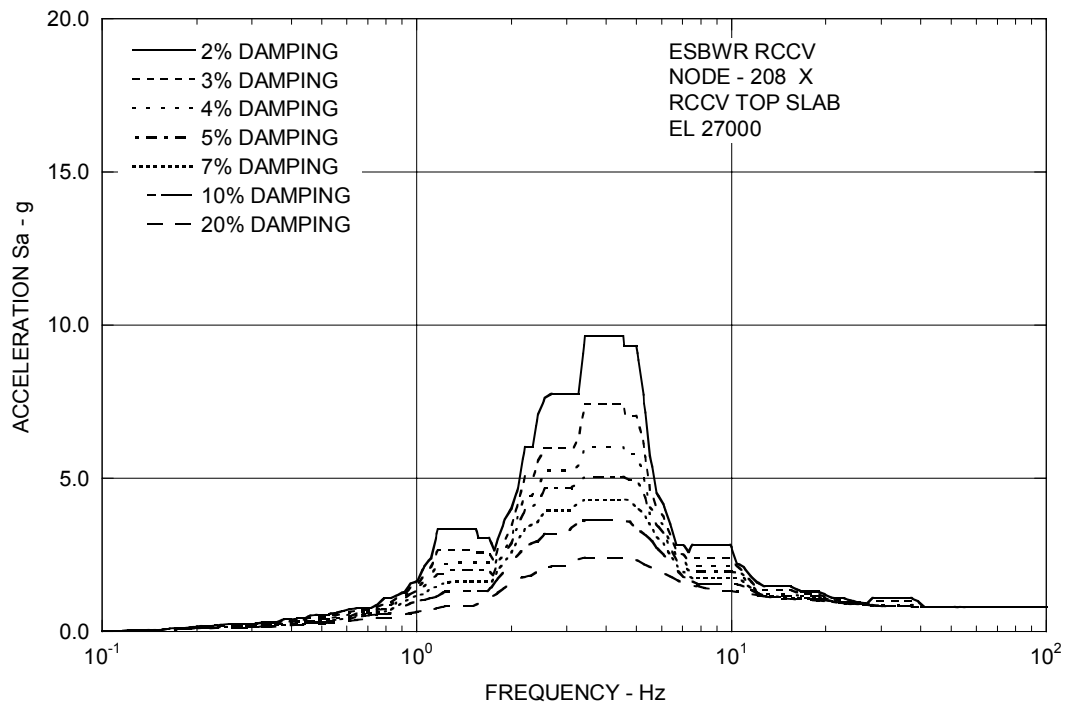


Figure 3A.9-1b. Enveloping Floor Response Spectra – RCCV Top Slab X

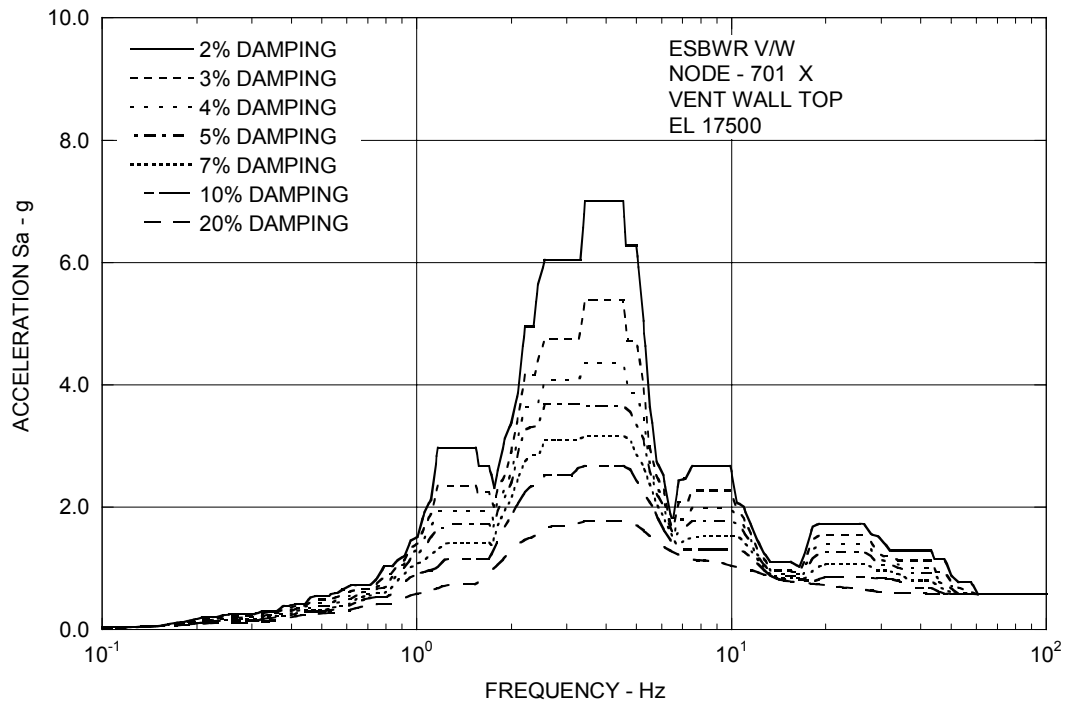


Figure 3A.9-1c. Enveloping Floor Response Spectra – Vent Wall Top X

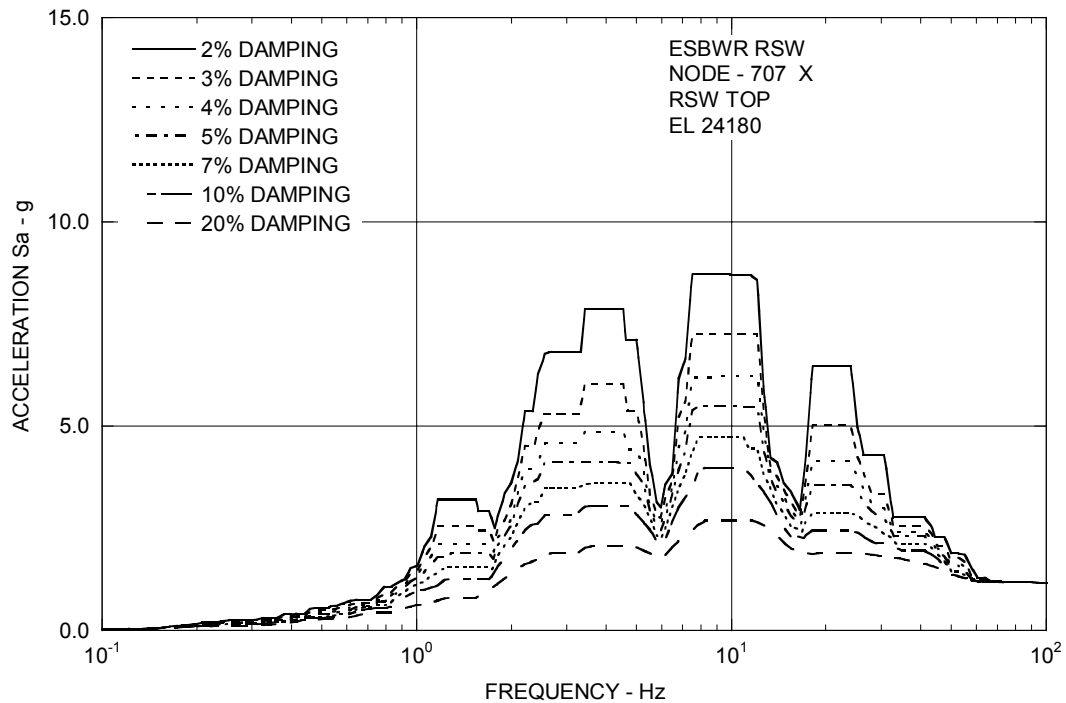


Figure 3A.9-1d. Enveloping Floor Response Spectra – RSW Top X

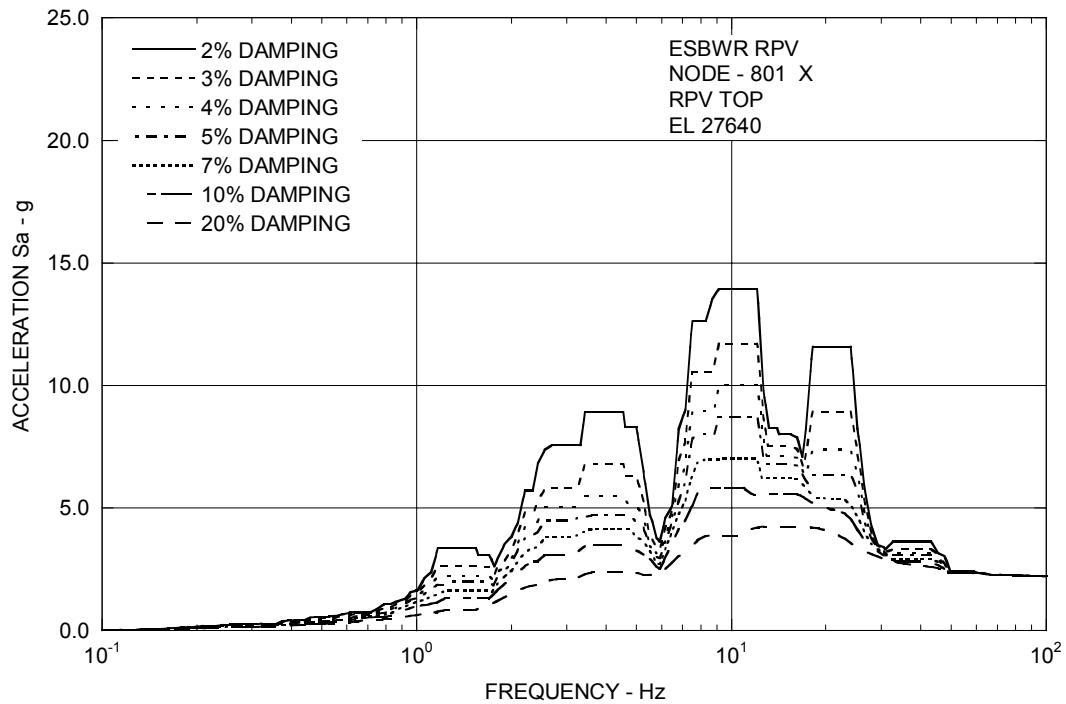


Figure 3A.9-1e. Enveloping Floor Response Spectra – RPV Top X

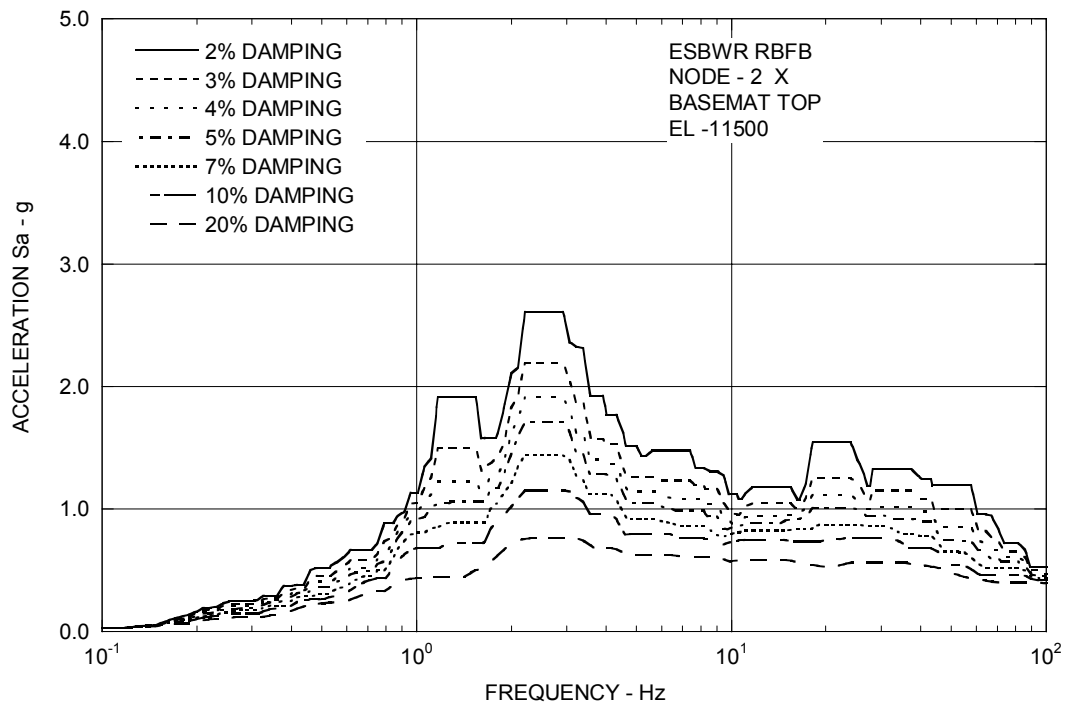


Figure 3A.9-1f. Enveloping Floor Response Spectra – RBFB Basemat X

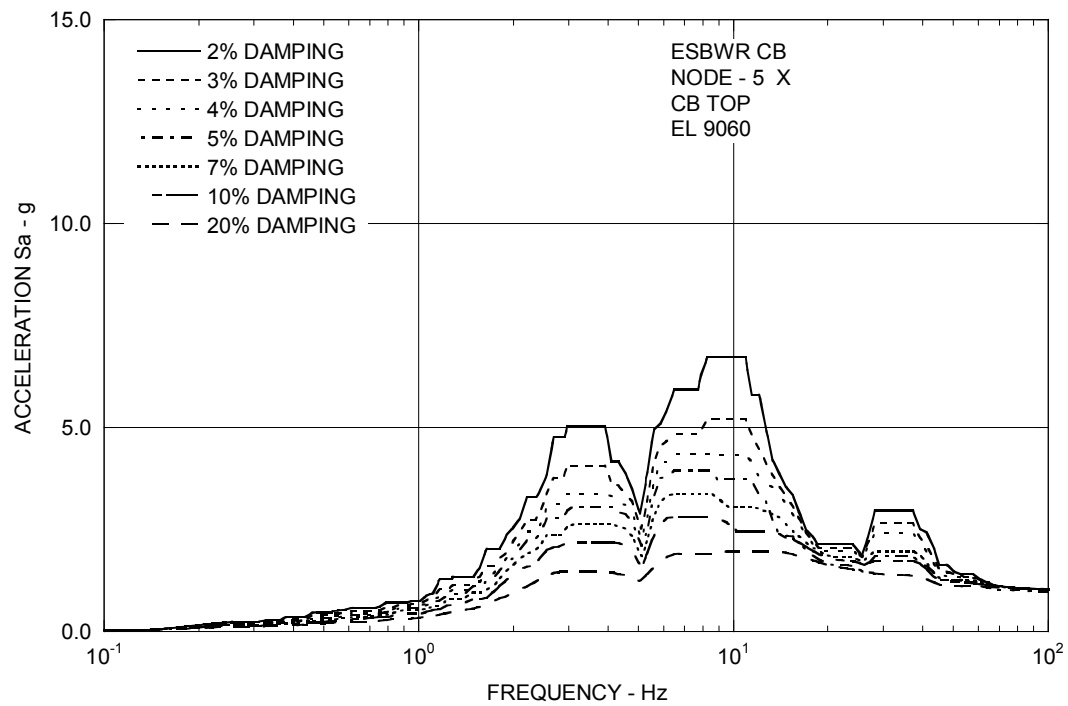


Figure 3A.9-1g. Enveloping Floor Response Spectra – CB Top X

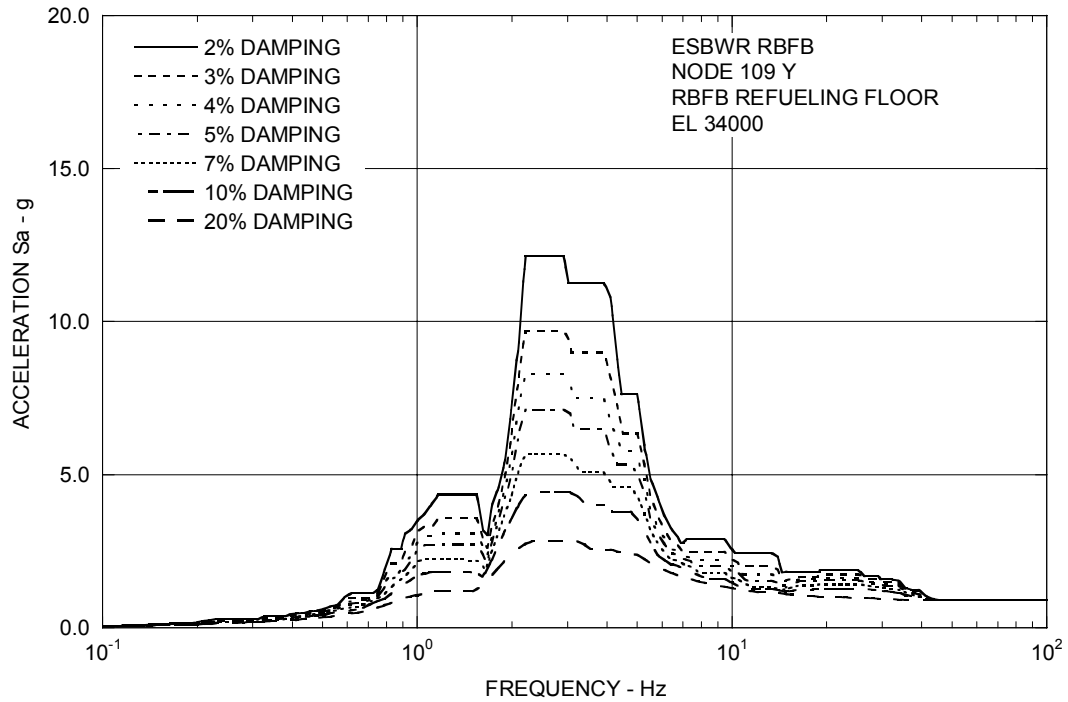


Figure 3A.9-2a. Enveloping Floor Response Spectra – RBF Refueling Floor Y

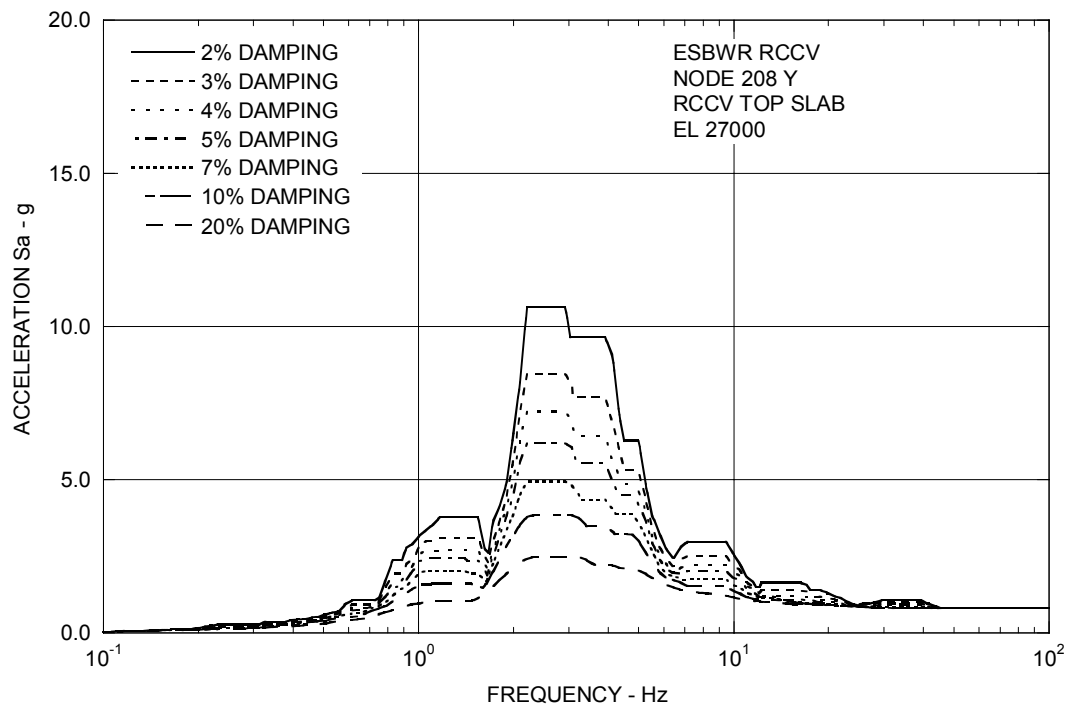


Figure 3A.9-2b. Enveloping Floor Response Spectra – RCCV Top Slab Y

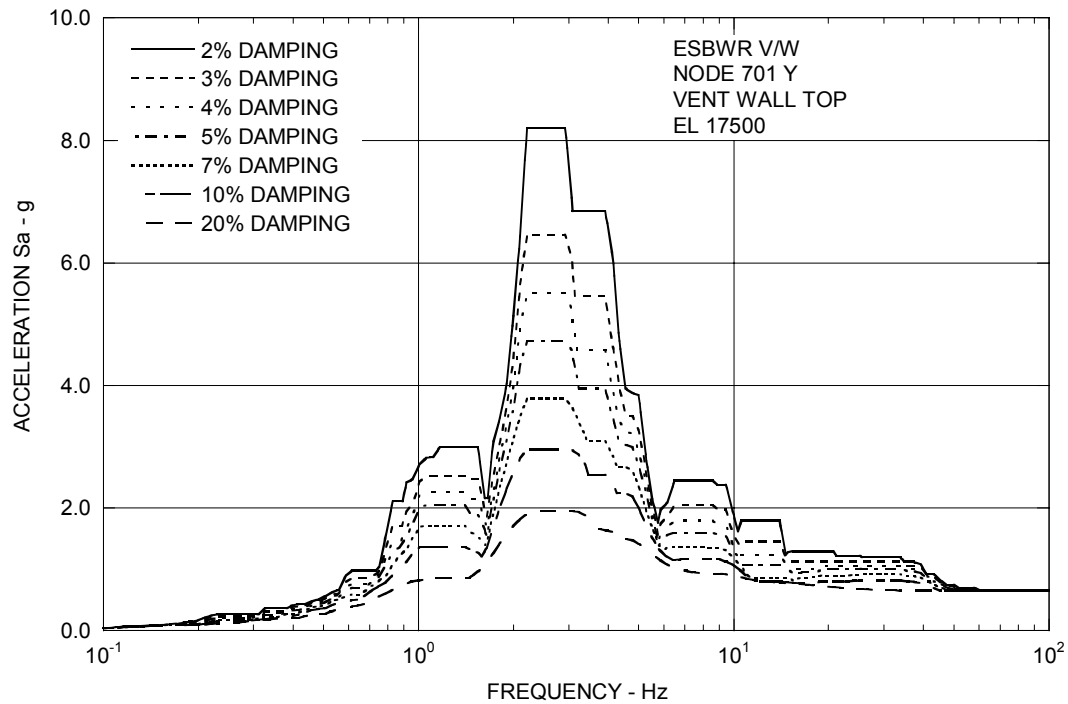


Figure 3A.9-2c. Enveloping Floor Response Spectra – Vent Wall Top Y

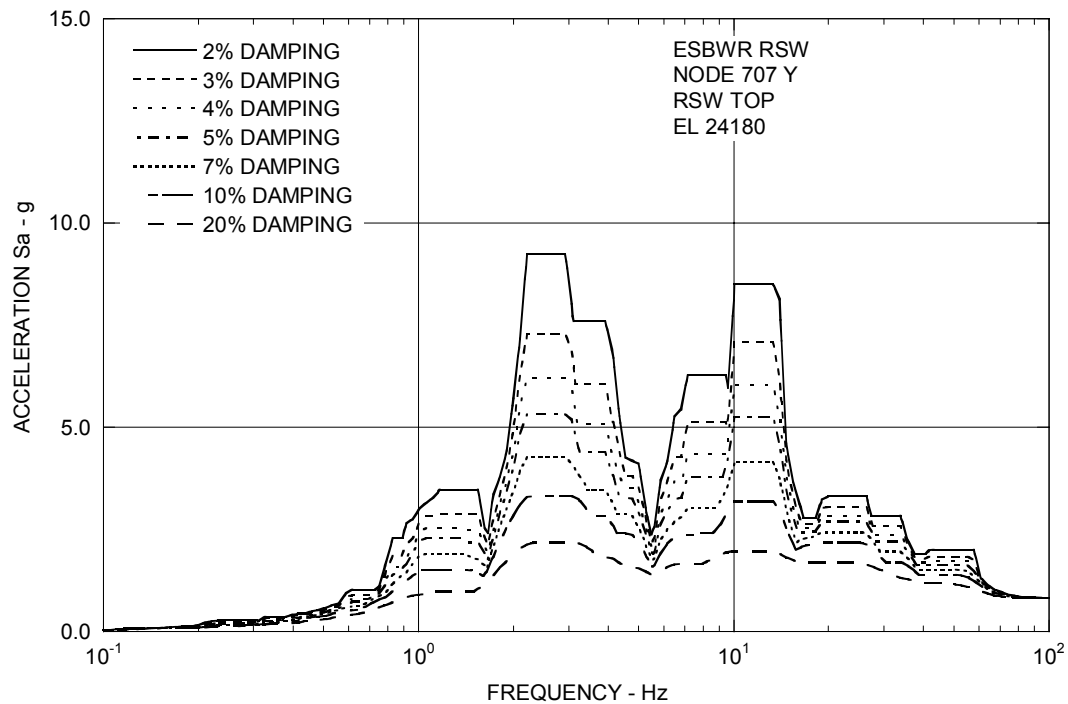


Figure 3A.9-2d. Enveloping Floor Response Spectra – RSW Top Y

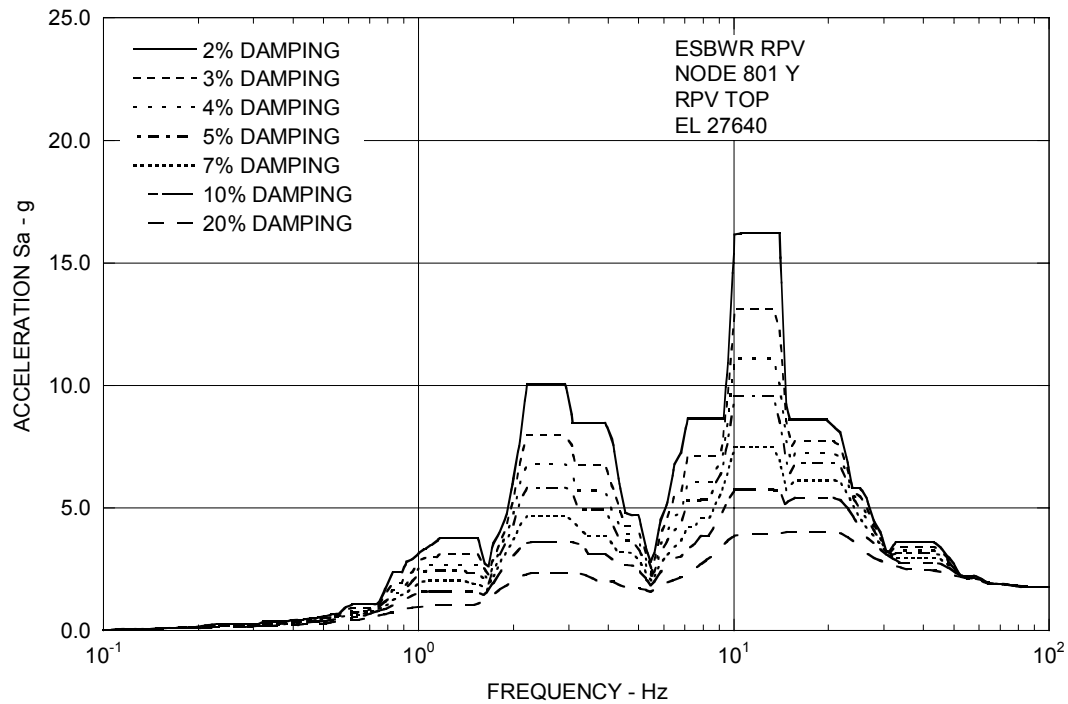


Figure 3A.9-2e. Enveloping Floor Response Spectra – RPV Top Y

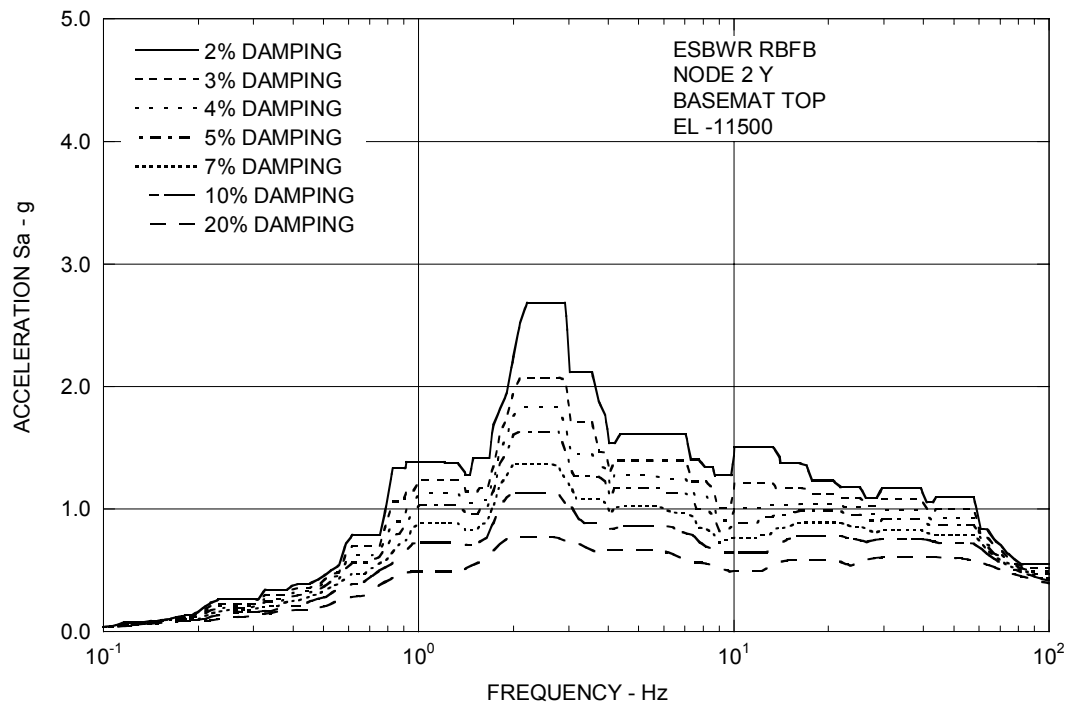


Figure 3A.9-2f. Enveloping Floor Response Spectra – RBFB Basemat Y

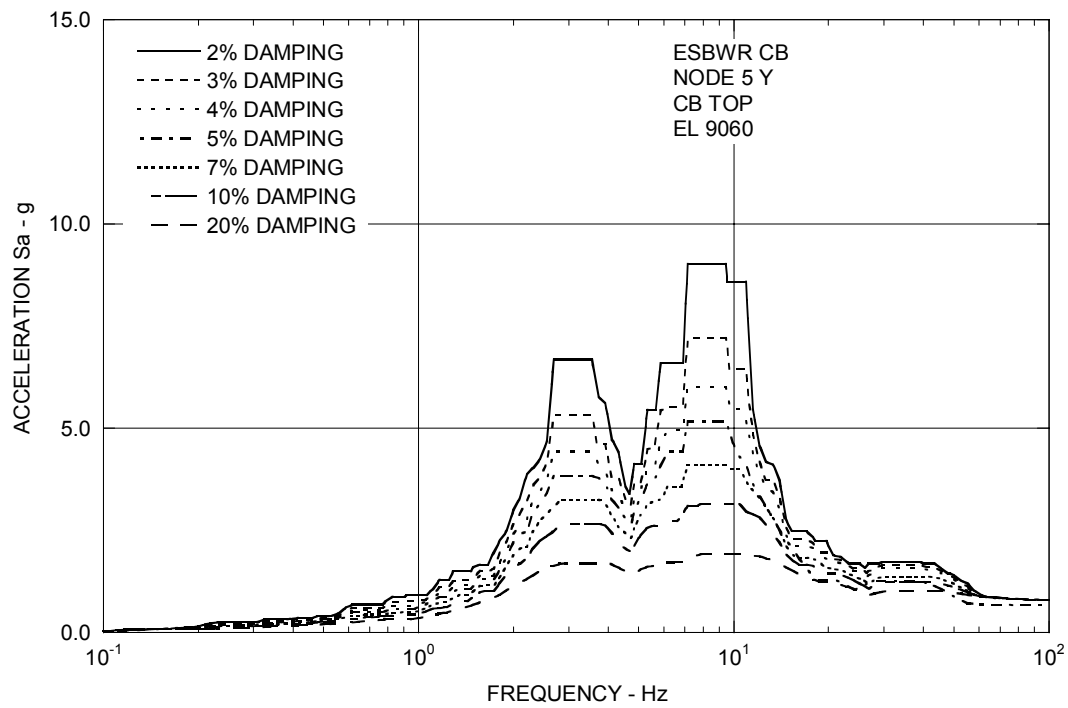


Figure 3A.9-2g. Enveloping Floor Response Spectra – CB Top Y

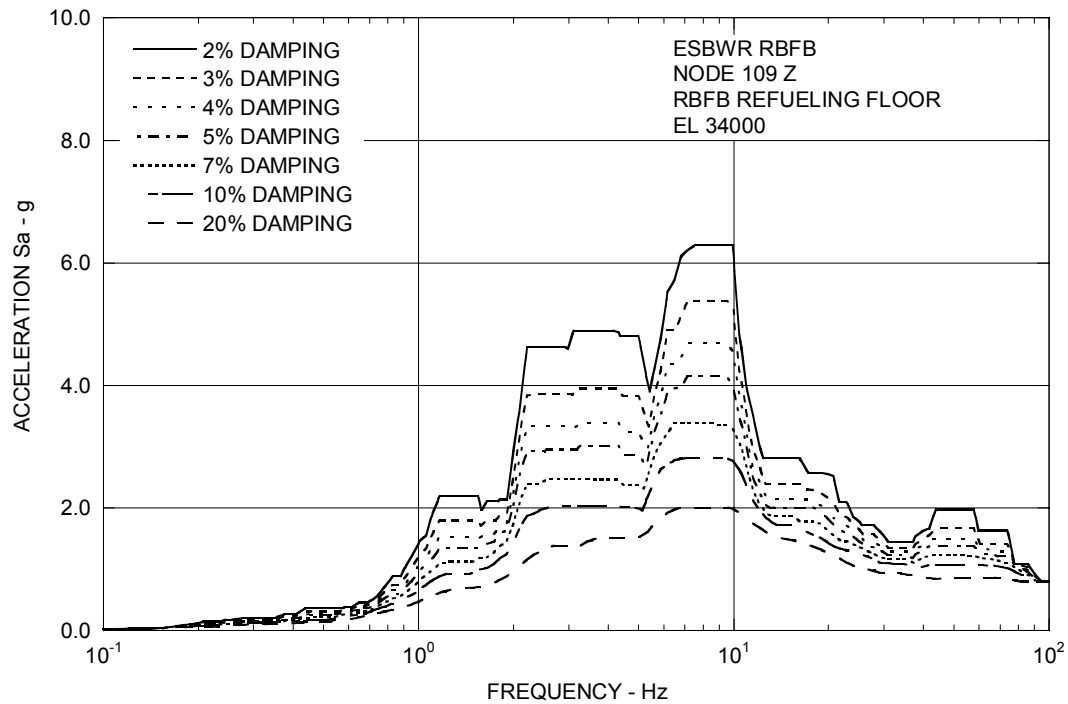


Figure 3A.9-3a. Enveloping Floor Response Spectra – RBF Refueling Floor Z

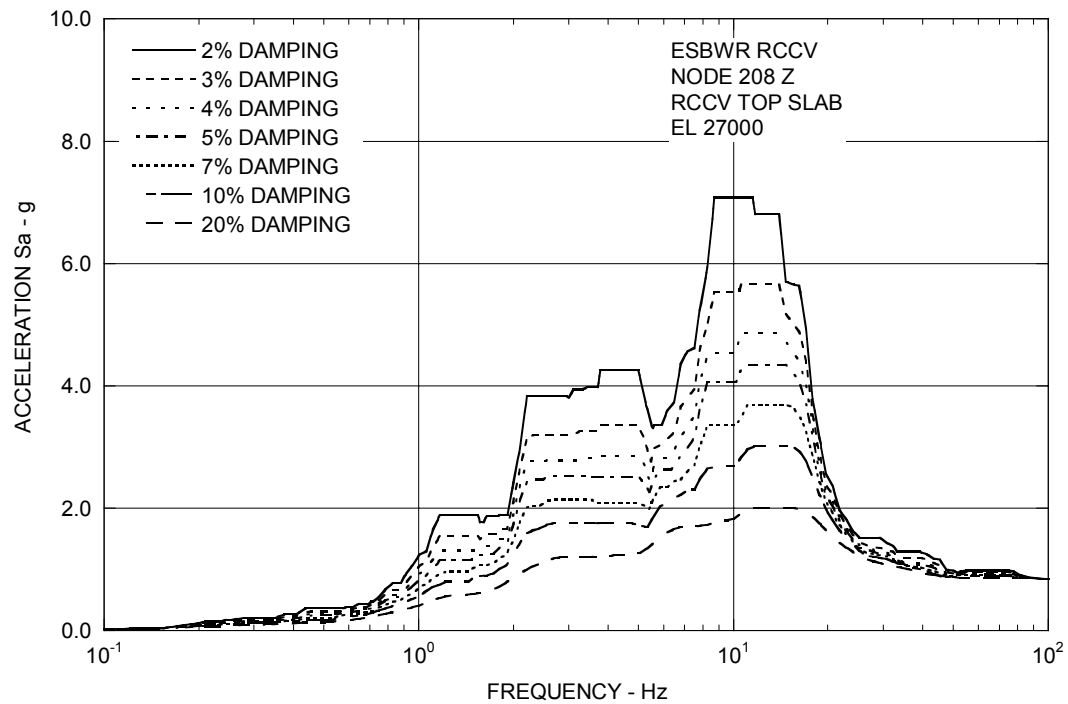


Figure 3A.9-3b. Enveloping Floor Response Spectra – RCCV Top Slab Z

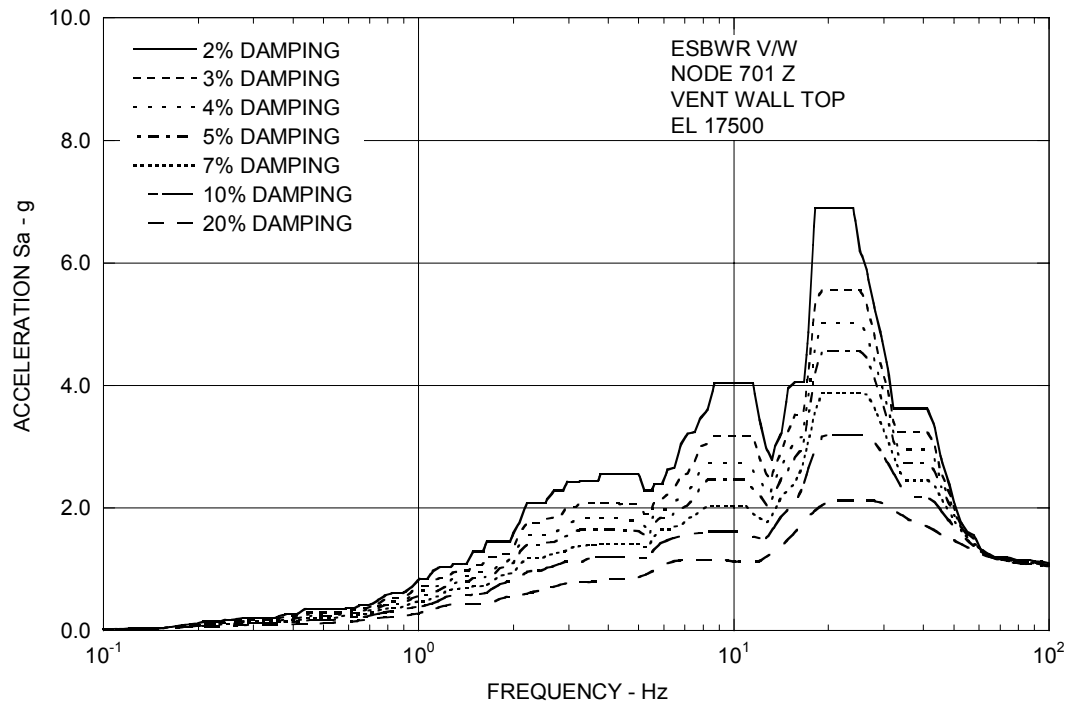


Figure 3A.9-3c. Enveloping Floor Response Spectra – Vent Wall Top Z

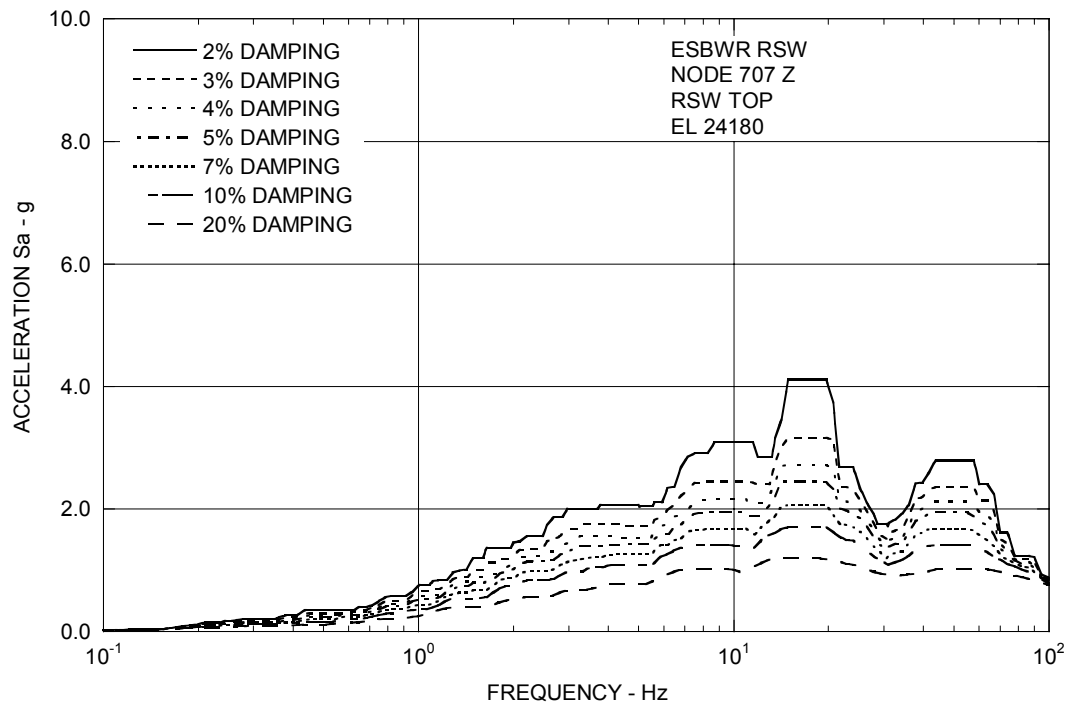


Figure 3A.9-3d. Enveloping Floor Response Spectra – RSW Top Z

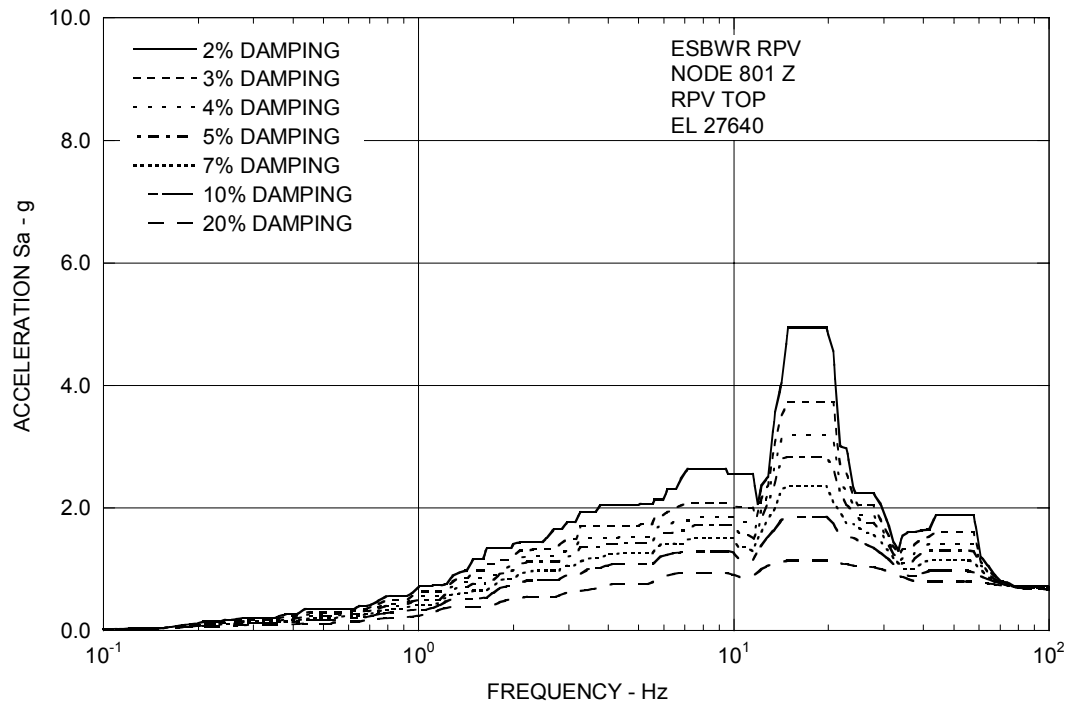


Figure 3A.9-3e. Enveloping Floor Response Spectra – RPV Top Z

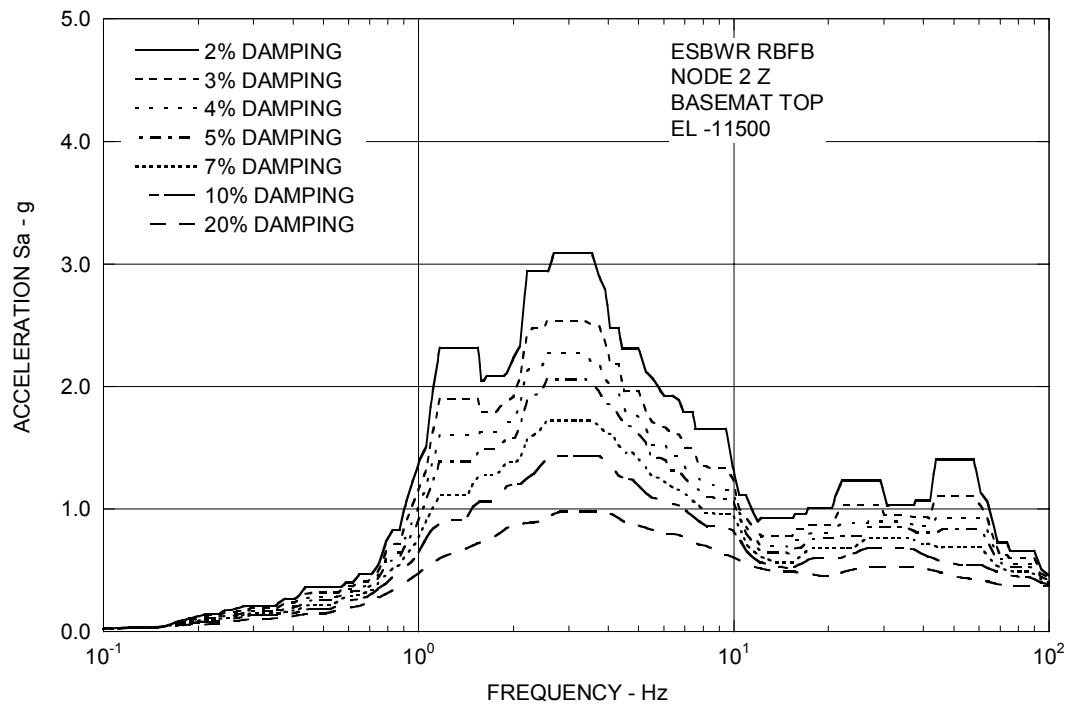


Figure 3A.9-3f. Enveloping Floor Response Spectra – RBFB Basemat Z

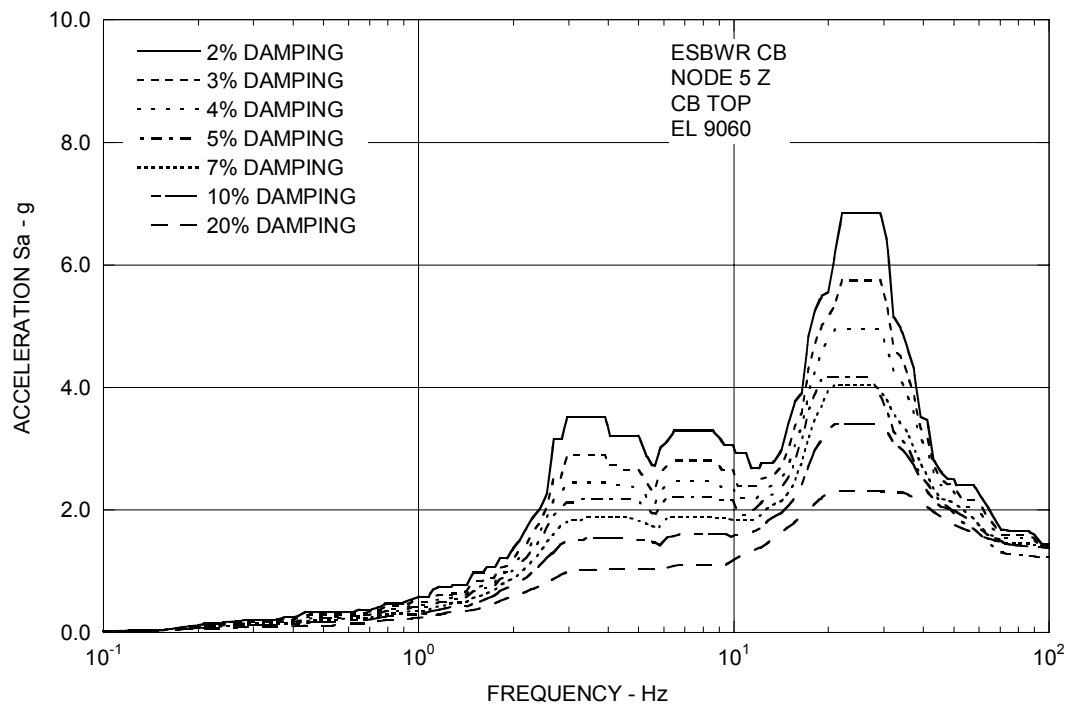


Figure 3A.9-3g. Enveloping Floor Response Spectra – CB Top Z

3B. CONTAINMENT HYDRODYNAMIC LOADS

3B.1 SCOPE

This appendix provides a description and load definition methodology for hydrodynamic loading conditions inside the primary containment in an ESBWR during a postulated Loss-of-Coolant Accident (LOCA) and/or a Safety Relief Valve (SRV) or Depressurization Valve (DPV) actuation. Overall, the load definition methodology used for the ESBWR containment design is similar to that used for prior BWR containment designs, such as the Advanced Boiling Water Reactor (ABWR, Reference 3B-1).

Any loads classified as minor, such as froth impingement or pool swell fall back, are not specified due to their insignificant impact on the structure.

3B.2 DESCRIPTION OF PHENOMENA

This section describes the assumed sequence of events for loads evaluation during a postulated LOCA event and/or an SRV/DPV actuation. This section also describes the potential containment loading conditions over the spectrum of LOCA break sizes and SRV/DPV actuation circumstances. The load combinations for the design evaluation are discussed in Subsection 3B.9.

3B.2.1 Loss-of-Coolant Accident

A Loss-of-Coolant Accident (LOCA) causes a pressure and temperature transient in the drywell and wetwell due to mass and energy released to the drywell. The severity of this transient loading condition depends upon the type and size of LOCA. Section 6.2 provides pressure and temperature transient data in the drywell and wetwell for a spectrum of postulated LOCA.

3B.2.1.1 Large Break Accident (*Design Basis Accident*)

Because the ESBWR has no recirculation lines, the main steam line break and the feedwater line break become the large break cases. In these breaks, the upper drywell pressure increases as a result of the mass and energy release from the break, and a steam-nitrogen¹ mixture is forced through the main vent system. The water initially contained in the vent system is accelerated out of the horizontal vents. During the horizontal vent clearing process, the water exiting the vents form submerged jets in the suppression pool, which can produce loads on structures near the vent exits and on the suppression pool floor.

Immediately following the water clearing, bubbles containing nitrogen and steam form at the horizontal vent exits. As the flow of nitrogen and steam from the drywell becomes established in the vent system, the initial bubbles at the horizontal vent exits expand. These bubbles possess a pressure nearly equal to the drywell pressure plus the hydrostatic pressure. The steam fraction of the flow into the pool is condensed, but the continuous injection of drywell nitrogen and the resultant expansion of the nitrogen bubbles produces a rapid rise of the suppression pool surface. This phenomenon is called Pool Swell (PS). The expanding bubble causes loads on both submerged structures and the suppression pool boundaries.

During the early stages of PS, a slug of water above the top vent is accelerated upward by the expanding nitrogen bubble. Structures and equipment close to the pool surface experience impact loads as the rising pool surface hits the bottom surface of the structures. Along with these impact loads, dissipative drag loads develop as water flows past structures and equipment at elevations above the vent exit and below the maximum PS height. This rising and expanding bubble eventually breaks through the water ligament and communicates with the wetwell airspace. Breakthrough occurs when the instabilities formed in the rising ligament cause the surface to become unstable and shatter. Froth continues upward until decelerated to zero velocity by gravity. A PS impact load on the diaphragm floor does not occur due to increasing wetwell gas space pressure.

Following the PS transient, a period of high steam flow rate through the horizontal vent system commences. As the reactor blowdown progresses, the flow rate through the horizontal vent

¹All references to “nitrogen” imply non-condensable gases.

system decreases. Overall, prior test data have indicated that the steam is condensed in the horizontal vent exit region.

The steam condensation process at the vent exit is influenced by the horizontal vent steam mass flow rate, the subcooling at the vent exit, and the vent flow nitrogen content fraction. At medium vent flow rates, the water-to-steam condensation interface oscillates causing pressure oscillations in the pool. This phenomenon, referred to as Condensation Oscillation (CO), produces oscillatory and steady loadings on the containment structure. As the vessel blowdown continues, the vent flow rate decreases and the vent flow nitrogen content becomes negligibly small. At lower vent flow rates (below a threshold level) the steam bubble at the vent exit alternatively grows, and, then nearly instantaneously collapses, in a condensation process referred to as Chugging (CH). The CH process produces transient dynamic loading on the vents and the suppression pool boundary, which must be considered in the design evaluation of the containment system.

As the LOCA event progresses, the water level in the vessel decreases. Upon the vessel water level reaching the Level 1 setpoint, the Automatic Depressurization System (ADS) is initiated. After a preset time delay following the Level 1 setpoint, the first set of SRVs automatically opens. This allows for an additional vessel depressurization path, which is routed directly to the suppression pool. Following another preset time delay, a second set of SRVs automatically opens. This provides for additional depressurization capacity to the suppression pool. After another preset time delay, a set of DPVs automatically opens. These DPVs allow for depressurization directly to the drywell. This sequence repeats itself until all the DPVs are open. At the point where the pressure of the drywell plus the gravitational head in the Gravity Driven Cooling System (GDCS) exceeds that of the RPV, low pressure coolant begins to flow into the vessel. No credit is taken for the Isolation Condenser System (ICS) in the scenario described above.

The Passive Containment Cooling System (PCCS) would serve to mitigate the PS loads calculated for the scenario described above. In the ESBWR, the PCCS receives a steam-gas mixture supply directly from the drywell. Since the PCCS does not have any valves, it starts into operation immediately following a LOCA. Non-condensable gases, together with steam, enter the PCCS condenser; steam is condensed inside the PCCS condenser tubes, and the non-condensable gases are purged to the wetwell.

3B.2.1.2 Intermediate Break Accident

The Intermediate Break Accident (IBA) is defined as a break size such that rapid depressurization of the RPV does not occur due to break flow. However, the reactor inventory loss is sufficiently rapid to cause a reduction in the reactor water level.

An IBA increases drywell pressure and temperature at a moderate rate, compared to that due to a large break accident. However, the hydrodynamic phenomenon is similar to DBA. Water initially contained in the vent system is accelerated from the vents. During the vent clearing process, the water exiting the vents forms water jets in the suppression pool, which cause loads on the submerged structures and equipment near the vent exits. The containment and submerged structure loads from an IBA are less severe than those from a design basis accident (DBA).

Immediately following vent water clearing, nitrogen and steam bubbles form at the vent exits. The drywell pressurization rate for an IBA is less than that due to a DBA. Consequently, the bubble pressure in the suppression pool is less severe and the moderate rate of drywell pressurization does not result in significant PS. The resulting IBA loads on pool boundaries, submerged structures, and equipment are bounded by the corresponding loads from a DBA.

A high drywell pressure signal scrams the reactor during the IBA. The sequence of events following the scram can lead to closure of the main steamline isolation valves (MSIVs) and subsequent increase in RPV pressure. The ICS would control the RPV pressure increase. However for loads evaluation, no credit is taken for the ICS. It is assumed that the pressure is relieved by opening the SRVs and the DPVs as in the DBA ADS function. SRV and DPV discharge may continue intermittently to regulate reactor pressure and remove decay heat. Consequently, the suppression pool boundary may be subjected to a pressure loading resulting from the SRV discharge during IBA.

For intermediate size breaks, the CO loads are equal to or less severe than those during a DBA. Therefore, the DBA CO load is used for IBA. Following nitrogen carryover, however, CH loads are experienced until the reactor vessel blowdown is reduced to a flow rate where CH becomes insignificant.

3B.2.1.3 Small Break Accident

The Small Break Accident (SBA) is defined as an event in which the fluid loss from the RPV is insufficient to either depressurize the reactor or result in a rapid decrease of reactor water level. Following the break, the drywell pressure slowly increases until the high drywell pressure scram setting is reached.

Consequently, the drywell pressure continues to increase at a rate dependent upon the size of the postulated break. The pressure increase depresses the water level in the vent system until the water is expelled and the nitrogen and steam mixture enters the suppression pool. The nitrogen flow rate is such that the nitrogen bubbles through the pool without causing any appreciable PS. The steam is condensed, and the drywell nitrogen passes through the pool into the wetwell gas-space. The wetwell gas-space gradually pressurizes at a rate dependent upon the nitrogen carryover rate, which in turn, depends upon the break size. Eventually, the steam and nitrogen flow through the vents transfers essentially all the drywell nitrogen to the wetwell gas space.

During SBA, the ADS operation occurs following a low level signal in the RPV. The DPV actuation provides a direct steam flow path from the RPV to the upper drywell. Thus, the operation of the DPVs increases the mass flux through the main vents and transforms the SBA into a subset of the DBA LOCA. Because the DBA LOCA vent mass flux bounds the SBA LOCA vent mass flux, the loads calculated for the DBA LOCA are used for design.

3B.2.2 Safety Relief Valve Discharge

Safety Relief Valves (SRVs) and Safety Valves (SVs) are utilized in ESBWR to provide pressure relief during certain reactor transients. Steam blowdown through the SRVs and SVs is routed through discharge lines into the pressure suppression pool, where it is condensed. At the end of each discharge line is a quencher. This enhanced heat transfer results in low pressure oscillations during high temperature steam condensation. The purpose of a quencher is to promote heat transfer during a sustained steam discharge from the valve.

Each SRV is routed to a separate quencher. The SVs are split into two groups with all valves in the group routed to a common header. Each of the two headers is routed to a separate quencher. Rupture disks on the headers allow discharge into the drywell when more than one SV is actuated.

SRV or SV actuation may occur for the following reasons:

- Pressure Actuation—For LOCA, five SRVs open at Level 1 setpoint and five SRVs open with a preset delay.
- Overpressure Protection – If the RPV pressure increases to the spring setpoint of the valves (SRV or SV), the valve opens.
- Manual Operation—A planned operator action resulting in the opening of anywhere from one to ten Automatic Depressurization System (ADS) SRVs.
- Inadvertent Opening—A failure or error affecting one SRV or SV resulting in the opening of a single valve.

The discharge piping of an SRV or SV contains ambient nitrogen and a column of water whose height is determined by the submergence of the SRV discharge line in the suppression pool and the pressure difference. Upon actuation, pressure builds up inside the piping as steam compresses the nitrogen and forces the water column through the quencher into the suppression pool. However, if more than one SV on a given discharge line actuates, the rupture disks on the common header are designed to open before the discharge line clears.

The expulsion of water from the discharge line into the suppression pool is called the water-clearing phase of the discharge. The loads associated with the water-clearing are:

- Transient pipe pressure and thermal loads.
- Pipe reaction forces from transient pressure waves and fluid motion in the pipe.
- Drag loads on structures located in the path of the submerged water jet.
- Pool boundary loads.

Following the expulsion of the water from the quencher, the nitrogen is expelled into the suppression pool in the form of high-pressure bubbles. Once the nitrogen bubbles are in the suppression pool, they expand because the ambient suppression pool pressure is lower than the nitrogen bubble pressure. The subsequent interaction of the nitrogen bubbles and the suppression pool manifests itself as an oscillatory pressure field which persists with decaying amplitude until the nitrogen bubble rises to the suppression pool surface. The frequency of the pressure oscillation is influenced by the initial mass of nitrogen in the line, the submergence of the discharge line in the pool, the suppression pool temperature, the pool geometry, and the wetwell gas space pressure. The loads associated with the nitrogen bubble dynamic phenomena are transient drag loads on submerged structures caused by the velocity field (standard drag) and the acceleration field (inertial drag), and oscillating pressure loads on the pool boundary.

Following the nitrogen-clearing phase, a steady discharge flow is established and continues until the valve is closed. The steam enters the pool from the quencher as a submerged jet emanating from multiple small holes in each quencher arm. The loads associated with the steady steam flow phase of the SRV discharge include:

- Pipe reaction forces caused by the steady steam flow through the pipe bends.
- Thrust forces on the quencher.
- Thermal loads on structures contacted by the steam.
- Pool boundary loads caused by the oscillation of the condensing steam jets at the quencher.

Following SRV or SV closure, the steam in the discharge line condenses, and the resulting vacuum draws water back into the line. To limit the water level rise within the pipe, vacuum breakers are provided to admit drywell nitrogen to the discharge line and allow the water level to return to near normal.

For multiple SRV or SV discharge conditions, the basic discharge line clearing phenomena are the same as those described for a single discharge. The loads in the suppression pool are the result of the combined effects of the discharges at a number of locations in the suppression pool.

3B.2.3 Depressurization Valve Actuation

Depressurization Valves (DPVs) are part of the ADS, in conjunction with the SRVs. When low water level is signaled, the reactor is automatically depressurized by SRVs in combination with the DPVs.

The operation of the DPVs increases the mass flux through the main vents; however, the DBA LOCA vent mass flux is the bounding mass flux. Therefore, for containment hydrodynamic loads (PS, CO, and CH), the loads calculated for DBA LOCA are used for design.

3B.3 POOL SWELL LOAD

The phenomena of Vent Clearing and Pool Swell (PS) that occur following a postulated DBA, are described in Subsection 3B.2.1.1. The PS related loads are evaluated using computational models that determine mass and energy flow into the suppression pool, and the swelling of the suppression pool water surface. No credit is taken for the operation of the Isolation Condenser System (ICS) and the Passive Containment Cooling System (PCCS) for calculating the PS related loads. The dominant loads that require consideration with this phenomenon are:

- The pool boundary loads and loads on submerged structures due to the nitrogen bubble formation.
- Wetwell nitrogen compression boundary loads due to the PS.
- Diaphragm floor pressure load due to wetwell gas-space pressurization.
- Impact and drag loads on the wetwell gas-space internal structures initially above the pool surface.

3B.3.1 Pool Swell (PS) Analytical Model

3B.3.1.1 Drywell Pressurization

The maximum drywell pressurization rate occurs during an instantaneous guillotine rupture of a main steam line or a feedwater line. The ESBWR short-term containment pressurization model (Reference 3B-2) is the same model utilized in earlier GE pressure suppression containment types, including the ABWR (Reference 3B-1). The model consists of three main modules: the vessel blowdown model, the drywell model and the wetwell model.

In modeling either the main steam line break (MSLB) or the feedwater line break (FWLB), the following major assumptions are made:

- (1) The reactor is operating at 102% of rated thermal power (4500 MWt) and the initial dome pressure is 1055 psia.
- (2) Reactor scram occurs at time zero.
- (3) Moody's HEM break flow model is assumed.
- (4) The GDCS, ICS, and PCCS systems are not modeled in the analysis.
- (5) Drywell and wetwell airspace are homogeneous mixtures of inert atmosphere, vapor and liquid water.
- (6) Wetwell and drywell structure heat transfer are not modeled.
- (7) The safety relief valves (SRV) and depressurization valves (DPV) are not modeled in the analysis.
- (8) Non-safety cooling systems are not modeled.
- (9) The drywell is modeled as a single node and all break flow into the drywell is homogeneously mixed with the drywell inventory.
- (10) The ANSI/ANS-5-1971 +20%/+10% decay heat is used.

- (11) The wetwell airspace and suppression pool are in thermal equilibrium.
- (12) The flow loss coefficient for the vent filter at the entrance to the main vertical vents is taken as 0.2. The vent filter will be designed as part of the COL phase ensuring a flow loss coefficient of 0.2 or less.
- (13) Because of the unique containment geometry of ESBWR, in the event of a pipe break in the upper DW, the inert atmosphere in the lower DW would not start transferring to the WW until the peak pressure in the upper DW is achieved. Because the lower DW is connected to the upper DW through openings in the vessel support, no gas can escape from the lower DW until the peak pressure occurs. The contents of the lower DW starts transferring to the WW as soon as the pressure starts decreasing. A conservative transfer of 50% of the lower DW contents into the WW is assumed, by modeling the upper DW and lower DW regions as a single volume node comprising of the upper DW volume plus 50% of the lower DW volume.

Other specific assumptions to the type of break are described below.

3B.3.1.1.1 Main Steam Line Break

Immediately following an instantaneous guillotine rupture of a main steam line, flow from both ends of the break accelerates to the maximum determined by critical flow considerations. Unsteady flow from the RPV side initially depletes the pipe inventory, and thereafter the flow corresponds to a steady critical flow in the flow restrictor in the steam nozzle. Blowdown flow through the other side of the break occurs because the steamlines are interconnected at a point upstream of the turbine by a header. This interconnection allows primary system fluid to flow from the unbroken steamline, through the header and back into the DW via the broken line, until the MSIVs are fully closed. Once the MSIVs are closed, the break flow is only from the RPV through the broken line.

In modeling the MSLB, the following major assumptions are made:

MSIVs begin to close at 0.5 seconds after event initiation and fully close in the maximum time (5 seconds). This assumption of a closure time of 5.0 seconds, which maximizes the calculated discharge of high-energy fluid to the DW, is used for conservatism.

The flow resistance of open MSIVs is considered. The effective flow area on the piping side reduces to 70% of a frictionless piping area.

During the inventory depletion period, the flow multiplier of 0.75 is applied (Reference 3B-2).

The break flow is steam for two seconds followed by a two-phase mixture.

3B.3.1.1.2 Feedwater Line Break

Immediately following a postulated double-ended rupture in one of the two main feedwater lines just outside the RPV, the blowdown flow into the drywell will come from both sides of the break - the RPV side and the feedwater system side.

In modeling the FWLB, the following major assumptions are made:

- MSIVs begin to close at 0.5 seconds after event initiation and fully close in the minimum time following closure initiation (3.5 seconds). This assumption of a closure time of 3.5 seconds, which minimizes the energy returned to the main condenser, is used for conservatism.
- The feedwater system side break flow is modeled by assuming the flow to be 164% of nuclear boiler rated, and the maximum flow is assumed to continue from time zero to 120 seconds.
- Choked flow is assumed from the beginning of the break. This is conservative as it bounds unsteady flow during inventory depletion of the FW line back to the nozzles. This is conservative because (a) all feedwater flow is assumed to go directly to the drywell, (b) flashing in the broken line is ignored, and (c) during the inventory depletion period, the flow rate will be less than 164% because of the highly subcooled blowdown.
- The break enthalpy from the vessel is equal to the initial enthalpy in the vessel downcomer until the break uncovers.

3B.3.1.2 Hydrodynamic Loads

The hydrodynamic loads during the pool swell phase of LOCA are determined using an analytical model described in Reference 3B-3. The analytical model is the same model reviewed and accepted for ABWR (Reference 3B-1), which has a similar containment suppression pool and vent system design. Both ESBWR and ABWR have a rectangular concentric suppression pool. The drywell and suppression pool are connected by a set of circular vertical vents each containing three circular horizontal vents. The horizontal and vertical vent diameters are the same for both designs. The horizontal vent elevations are the same for the two designs.

This analytical model is used to compute the pool boundary loads due to bubble formation, the pool swell velocity and acceleration, the pool surface elevation, and the wetwell airspace pressure. The assumptions inherent in the model maximize the nitrogen bubble pressure and, consequently, the pool swell velocity. The conservatism of the model in predicting PS velocity and wetwell gas-space pressure has been demonstrated for prior BWR plants.

In modeling and simulating the pool swell phenomenon, the following major assumptions are made:

- Non-condensable gases are assumed to follow ideal gas laws.
- Flow into the vent pipe following vent clearing is limited to non-condensable gases only.
- The flow rate of non-condensable gases in the vent pipe is calculated assuming one-dimensional flow under adiabatic conditions while taking the pipe friction into consideration.
- The non-condensable gases in the drywell are compressed isentropically.
- The temperature of the nitrogen bubble in the suppression pool is identical to the temperature of the non- gas located in the drywell.

- Following vent clearing, the slug of water located above the top horizontal vent is accelerated in an upward direction while maintaining a constant thickness.
- The non-condensable gases in the wetwell are compressed polytropically.
- To generate a bounding set of PS loads, different polytropic indices are used to generate the PS height and slug velocity results, as well as the wetwell airspace pressurization magnitude. In the calculation of the PS height and slug velocity, a polytropic index of 1.2 is used. Whereas, in the calculation of wetwell airspace pressurization, a polytropic index of 1.4 is used.
- The PS velocity is multiplied by a factor of 1.1 to be conservative.
- To account for a non-uniform rise in the suppression pool surface during the swell, the area of suppression pool which is assumed to be lifted is 0.8 times the actual suppression pool water surface.

3B.3.2 Pool Boundary Loads

The pool swell results for the ESBWR containment, using the methodology described above, are listed in Table 3B-1. The analytical values represent the calculated results while the design values provide margin and are used in subsequent loads evaluations. The suppression pool boundary pressure distribution corresponding to this bubble pressure is shown in Figure 3B-1. The pressure distribution shown in the figure is normalized to the maximum bubble pressure. The maximum wetwell gas-space pressure during pool swell, given in Table 3B-1, is to be used in conjunction with the bubble pressure loading for structural evaluation of the containment walls. The maximum pool swell velocity and pool swell height are also listed in Table 3B-1.

3B.3.3 Structural Impact and Drag Loads Above the Pool Surface

Any structure or component located above the initial pool surface and below the maximum PS height is subject to a water impact load and a water drag load.

The impact load is calculated from the following equation:

$$P(t) = P_{\max} [(1 - \cos(2\pi t/T))/2] \quad (3B-1)$$

where

$P(t)$	=	The pressure acting on the projected area of the structure.
P_{\max}	=	The temporal maximum of the pressure acting on the projected area of the structure.
	=	$1/g \cdot M_h V/A_v T$
g	=	The gravitational acceleration constant.
M_h	=	The hydrodynamic mass of the structure.
V	=	The PS velocity at the structure elevation
A_v	=	The projected area of the structure in the vertical direction.

T	=	The duration of the impact.
	=	0.0463D/V, for a cylindrical projected structure.
	=	0.011W/V, for a flat projected structure and $V > 2.1$ m/s.
	=	0.0052W, for a flat projected structure and $V < 2.1$ m/s.
D	=	The diameter of the cylindrical projected structure.
W	=	The width of the flat projected structure.
t	=	Time.

Following the initial impact load, a standard drag load acts on the structure. This drag load is calculated from the following equation:

$$P_D = C_{Dp} V^2 / 2g + \rho a V_A \quad (3B-2)$$

where

P_D	=	The drag pressure acting on the projected area of the structure.
C_D	=	The drag coefficient for the structure.
ρ	=	The density of the suppression pool water.
V	=	The PS velocity at the structure elevation.
g	=	The gravitational acceleration constant.
a	=	The PS acceleration at the structure height.
V_A	=	The acceleration drag volume.

The drag coefficient C_D is defined in Table 3B-2 and the acceleration drag volume V_A is defined in Table 3B-3. Values obtained by suitable alternate calculations may also be utilized.

3B.3.4 Vacuum Breaker Load Due to Wetwell Nitrogen Compression

The potential for rapid actuation of the wetwell-to-drywell vacuum breakers exists when the wetwell airspace compression exceeds the pressurization of the drywell. However, in the design of the ESBWR this potential load is not postulated due to the wetwell airspace pressure always remaining lower than the drywell pressure during the PS phase of the transient. Therefore, this load does not exist during the PS phase of the LOCA in the ESBWR.

3B.3.5 Loads on Diaphragm Floor

Rapid pressurization of the wetwell airspace during the pool swell transient has a potential for upward differential pressure loading on the diaphragm floor. Results from the pool swell analytical model, however, showed that wetwell airspace pressure did not exceed the drywell pressure during the pool swell transient. Hence, it is concluded that the diaphragm floor will not be subjected to an upward differential pressure loading. The diaphragm floor will be subjected to only downward pressure differential loading, during the pool swell phase.

3B.4 CONDENSATION OSCILLATION LOADS

The term Condensation Oscillation (CO) is used to represent a hydrodynamic/steam condensation phenomenon associated with a LOCA. During the initial phase of the DBA, pressurized drywell nitrogen is purged into the wetwell. Steam condensation then begins after the vents are cleared of water and the drywell nitrogen has been carried over into the wetwell. The CO phase is vibratory in nature and induces a bulk water motion. CO occurs typically at higher mass fluxes compared to Chugging (Section 3B.5). During this period of high steam flow rate, the liquid-steam interface is located inside the wetwell, just beyond the horizontal vent exit. Experiments for Mark III and ABWR indicate that the interface oscillates at frequencies ranging primarily from 2 to 10 Hz, thereby producing a cyclical loading on all submerged containment structures and boundaries due to acoustic propagation of the source pressure. The CO phase persists until the mass flux falls below the so-called chugging threshold level. At this point the relatively regular CO loads changes to the more stochastic, impulsive chugging phenomenon.

A CO load is defined for the ESBWR and used in evaluation of affected structures. Because of the similarity between the ESBWR and ABWR containment, the ESBWR CO load is defined based on the ABWR CO load definition. Section 3B.4 provides a description of the ABWR CO load definition, including the ABWR test program, the basis for application to the ESBWR, and any adjustments made to the ABWR CO load definition for application to the ESBWR.

3B.4.1 ABWR Horizontal Vent Test Program

LOCA loads with the horizontal vent system design have been well characterized during the Mark III Confirmatory Test Program. More than 200 tests have been performed to determine horizontal vent system performance and associated LOCA loads. However, all of these tests have utilized the relatively lower containment pressure characteristics of the Mark III containment system. Because of some thermodynamic and geometrical differences between the ABWR and Mark III designs, it was anticipated that condensation oscillation (CO) and chugging (CH) loads might differ from prior (Mark III) testing in horizontal-vent facilities. These included the following:

Increased ABWR wetwell airspace pressure, and hence subcooling,

The presence of a lower drywell,

The smaller number of vents (30 in ABWR vs. 120 in Mark III),

Extension of the vents in the pool,

Vent submergence, and

Suppression pool width.

Considering the existence of the above thermodynamic and geometrical differences, a test program was conducted to confirm the CO and CH loads which would occur in the event of a LOCA in an ABWR plant. The test program, test data, and interpretation of test data are documented in Reference 3B-4.

The test program consisted of 24 simulated blowdowns in a test facility representing the horizontal-vent ABWR design. The tests were divided into two parts utilizing sub-scale (SS) and partial full-scale (FS*) test configurations.

The SS facility had all linear dimensions reduced by a factor of 2.5 from prototypical dimensions. Thirteen SS tests were performed primarily for the purpose of obtaining CO data. A full-scale vertical and horizontal-vent configuration was installed for the FS* tests. The upper drywell was enlarged but not to prototypical dimensions. Eleven FS* tests were performed primarily for the purpose of obtaining CH data. The test matrix for the 24 blowdowns included variations in pool temperature, break size, wetwell backpressure, and type of break (steam or liquid). The test facility was equipped adequately with the data sensors to obtain necessary data for understanding the phenomena and establishing a database for defining CO and CH loads for the ABWR containment. In addition to the geometrical considerations, the facility was designed to minimize the potential for fluid-structure interaction (FSI). Measurements were taken at seven locations on the wetted suppression pool boundary to record dynamic pressure oscillations. Structural instrumentation (strain gauges and accelerometers on the basemat, pedestal, and containment walls) was used to confirm that FSI effects were minimal. Pressure transducers in the vertical and horizontal vents recorded dynamic loads on the vent system.

3B.4.1.1 Description of CO Database

A detailed description, evaluation, and discussion of CO data are given in Reference 3B-4.

The test program consisted of a total of 13 simulated blowdowns in sub-scaled test facility representing a one-cell (36°) sector of the horizontal vent design, which included a signal vertical/horizontal vent module. The subscaled (SS) test facility was geometrically (all linear dimensions scaled by a factor of 2.5) similar to the prototypical design, and the single vertical/horizontal vent module included all three horizontal vents. In these tests, full-scale thermodynamic conditions were employed. This approach is based on the belief that condensation phenomena at the vent exit are mainly governed by the thermodynamic properties of the liquid and vapor phases. In accordance with this scaling procedure, measured pressure amplitudes are equal to full-scale values at geometrically similar locations, whereas measured frequencies are 2.5 times higher than the corresponding full-scale frequencies. The technical basis for using this scaling approach was based on extensive review and evaluation of the available literature on CO scaling and scaled tests performed for Mark II and Mark III containments, as well as general consensus of technical experts in this field. The CO scaling studies, which have been performed independently by various technical experts, show that for tests in a geometrically scaled facility with full-scale thermodynamic conditions, the measured pressure amplitudes are the same as full-scale values at geometrically similar locations, and measured pressure frequencies are the scale factor times higher than the corresponding full-scale frequencies.

Therefore, CO frequencies for the full-scale prototypical design are obtained by scaling the frequencies measured in SS tests by a factor of 2.5. A similar technique is applicable to scaling adjustment in frequency for obtaining full-scale values. Thus, this scaling procedure made it possible to use the measured SS data (pressure time history) directly for load definition purpose after the time scale is compressed by a factor of 2.5.

Out of the 13 SS tests, the tests recommended for definition of the CO load are SST-1, 2, 3, 9, 11, and 12. These six tests were run at prototypical conditions. Of the remaining tests, SST-4, 5, 6, 7, 8, and 14 were run with a prepurged vent system, and SST- 10 was run with the lower drywell blocked off. These tests are valuable for understanding CO phenomena and the effects

of system variables, but they are not considered to be an appropriate basis for the CO load definition.

3B.4.1.2 Evaluation of CO Database

Each of the CO load definition tests showed significant frequency peaks at 5 and 9 Hz. The 9 Hz frequency is dominant early in the CO period and the 5 Hz frequency is dominant late in the CO period.

Further examination of the data shows that, in general, the largest amplitude loads occurred at a transducer located on the basemat, near the pedestal wall. It was observed that the highest amplitude CO loads occurred during the first 30 seconds of tests SST-1 and 2 (large liquid breaks at elevated pool temperature). Examination of the Power Spectral Density (PSD) data showed that the envelope PSD of the pressure from a 12-second segment in SST-1 and an 18-second segment in SST-2 matched the envelope PSD of the pressure from the six-test database.

3B.4.2 Source Load Approach

The CO load, termed as “Source Load Approach,” is used to develop a source load. The source load is a series of pulses which simulate the oscillation of the steam/water interface at the horizontal vent exits. In this approach the CO source load would be applied to a coupled fluid-structure model of the prototypical containment as an excitation of the steam/water interface at the exits of the horizontal vents. It is the oscillatory motion of the steam/water interface which produces the characteristic oscillatory pressure loading on the wall. With a source load, it is possible to account for the spatial distribution of the load and the variation of pool and vent fluid properties in a natural way. This approach avoids the problem of artificial resonant amplification at the system frequencies.

Figure 3B-2 describes the CO source load methodology. In order to develop a technically justified source loading function, the methodology includes the following elements:

- A comprehensive test database
- A coupled steam-water-structure interaction model of the test facility from which the data were obtained
- A procedure to develop a “test source” loading configuration
- A criteria to evaluate the test source loading configuration and test facility model
- A procedure to scale up the test source to a full-scale design source for the prototypical containment system
- A full-scale coupled steam-water-structure interaction model of the prototypical containment system
- A criteria to evaluate the design source loading condition for the prototypical containment system

- Calculation of CO design (wall pressure) from the prototypical analysis using the design source

Criteria for CO Source Load

An acceptance criterion is specified in order to provide a basis for judging the acceptability of the source loading function with respect to prediction of wall pressure loadings and their frequency contents. The criteria include the following elements:

Wall pressure histories for the SS test facility produced by the test source match with the pressures measured in the SS test facility.

- Frequency content of the predicted pressure histories, as defined by a power spectral density (PSD) and by an amplitude response spectrum, matches with the data obtained from the SS test facility.
- Spatial distribution of the root mean square (RMS) of the predicted loading matches with the data measured from the SS test facility.
- Wall pressures predicted by the design source for the prototypical ABWR match with the pressures measured in the SS test facility at geometrically similar locations. Note, this is required by the CO scaling laws (References 3B-5)

3B.4.3 Basis for ESBWR Load Definition

The ESBWR CO load definition utilizes the ABWR CO load definition. Adjustments, as necessary are made to the ABWR CO load definition for ESBWR application. The adjustments are determined from a review of predicted thermal-hydraulic conditions during CO in the ESBWR, a review of the ESBWR and ABWR geometry, and a review of test data from the ABWR Horizontal Vent Tests (HVT) Sub-Scale Tests (SST) and tests from the Mark III containment Pressure Suppression Test Facility (PSTF) tests.

3B.4.3.1 Review of ABWR and ESBWR Containment Geometry

The ESBWR and ABWR have a similar containment vent system design. In the ESBWR and ABWR designs, the drywell and suppression pool are connected by a set of circular vertical vents which are equally spaced around the containment. Each vertical vent contains a set of three horizontal vents, which connect the vertical vent to the suppression pool. The horizontal vent diameter and vertical vent diameters are the same for the ABWR and ESBWR designs. The distance from the suppression pool floor to the bottom horizontal vent and the distance between the bottom, middle and top horizontal vents are the same for the two designs. The distance the horizontal vents extend into the suppression pool is the same for the ESBWR and ABWR.

The containment design differences, which do exist, between the ABWR and ESBWR, will tend to produce lower CO pressure amplitudes for the ESBWR. These key differences include

- A lower pool depth and vent submergence for the ESBWR
- Two additional vertical vents for the ESBWR

- A longer distance between the horizontal vent exit and the outer containment wall

The ABWR contains 10 equally spaced vertical vents, at 36° intervals, whereas the ESBWR contains 12 vertical vents equally spaced at 30° intervals. However, the ESBWR containment size is larger than in the ABWR design. Consequently, the ESBWR has a pool surface area per vent which is approximately 30% greater than the value for the ABWR. This means that pressure disturbances in the suppression pool induced by CO are dispersed over a wider area before impacting pool-wall boundary surfaces resulting in lower wall pressures. The larger pool surface area per vent for the ESBWR will result in lower CO wall pressures. The smaller pool depth and associated lower vent submergence for the ESBWR increases the pressure attenuation to the pool surface. This produces lower CO wall pressure amplitudes at all submerged boundaries. The longer distance from the vent exit to the outer containment wall produces increases the pressure attenuation to the outer containment wall which further reduces the outer containment wall pressures.

3B.4.3.2 Review of Thermal-Hydraulic Conditions

Key parameters, which can affect the CO load, include, the vent steam mass flux and pool temperature. The ABWR HVT tests show that CO amplitudes increase significantly with increased vent steam mass flux and pool temperature. The HVT test data also indicated that higher containment pressures tended to reduce CO pressure amplitudes. This is attributed to the higher subcooling associated with the higher containment pressure.

The predicted steam mass flux vs. suppression pool temperature for the ESBWR MSLB and FWLB events are shown to be well below the measured test values for the load definition test. Consequently, CO pressure amplitudes associated with predicted ESBWR thermal-hydraulic conditions are bounded by the CO pressures determined from the ABWR HVT CO load definition tests.

3B.4.3.3 Frequency Content Evaluation

An additional consideration for the CO load is the CO frequency. The thermal hydraulic conditions at the vent exit (and vent diameter) mainly govern the condensation processes at the vent exit which establish the CO “driver frequency”. This is the basic premise of the scaling laws used to apply the subscale data to full scale. However, the vent system geometry can affect the vent acoustic modal frequencies, which may influence the CO frequency also.

Thermal-hydraulic Conditions

The key thermal-hydraulic parameters that affect the vent exit frequency include mass flow rate, nitrogen content and pool temperature. Additionally, the CO frequency is found to be directly proportional to the vent exit diameter. However, the vent diameters for the ABWR and ESBWR are the same and therefore do not present a source of frequency content change.

The range of conditions tested in the HVT tests cover the predicted range of thermal-hydraulic conditions for the ESBWR during the CO period. Because the maximum predicted ESBWR steam mass fluxes are expected to be lower, the CO frequencies are concentrated at the lower range and covered by the range of frequencies associated with the HVT SST CO data used to define the ABWR CO load.

Containment Vent Geometry

Differences in the ESBWR vent system geometry relative to the ABWR design, which can affect the vent acoustic modes, include the difference in the vertical vent length, and the difference in the lower drywell configuration. The ESBWR vertical vent length is smaller than the ABWR vent length. Additionally, in the ABWR containment design, there is a direct connection between the lower drywell and the vertical vent. For the ESBWR containment design this connection between the lower drywell and vertical vent is not present. Instead the lower drywell connects to the upper drywell through flow paths between the bottom of the upper drywell and top of the lower drywell.

To evaluate the effect of these differences, the HVT CO test data is reviewed. Additionally, data from the Mark III Containment PSTF tests are also reviewed. The purpose of the review is to establish the controlling influence on CO frequency.

Analytical studies of CO for Mark III containments are documented in Reference 3B-5 and in GESSAR II (Reference 3B-6). These studies have determined that high steam mass flux and low pool temperature conditions produce high CO vent exit driving frequencies while low steam mass flux and high suppression pool temperatures produce low frequencies. This trend is supported by the Mark III PSTF CO test data (Reference 3B-7).

As previously described, the load definition CO data show dominant peaks at 5 Hz and at 9 Hz. The 9 Hz peak is dominant early in the CO period of the tests whereas the 5 Hz peak is dominant late in the CO period. A high steam mass flux and low pool temperature characterize these tests early in the CO period and low steam mass flux and high pool temperature late in the CO period. CO data from a smaller sized liquid break and a steam break, both with relative low steam mass fluxes, show only one dominant peak near 5 and 6 Hz.

These HVT SST test results are consistent with CO frequencies which are controlled by the vent exit thermal-hydraulic conditions.

It had been postulated in Reference 3B-4 that the lower 5 Hz peak seen in the HVT tests, which occur with lower mass fluxes, may be tuned into the vent acoustic modal frequency associated with the lower drywell connection to the vertical vent. The results of a test, which did not model the connection between the lower drywell to the vertical vent, are reviewed to examine this possibility. The CO data for this test shows a dominant CO wall pressure frequency near 6 Hz and a small secondary wall pressure frequency peak near 13 Hz. The presence of a dominant PSD frequency peak near 6 Hz without lower drywell modeled, indicates that vent acoustic modes associated with the connection to the lower drywell did not have a significant influence on this CO frequency.

The Mark III PSTF CO data is also reviewed. The Mark III 1/3 area scale PSTF CO test data show that dominant frequencies in subscale when scaled up to full-scale are near 3 Hz, which is within the range of full-scale dominant frequencies of 2 – 4 Hz determined for the ABWR. The trends in the CO frequency with test conditions shown for the Mark III 1/3 scale PSTF tests are also similar to the ABWR HVT test results. As with the HVT CO tests, higher Mark III PSTF CO frequencies are observed at high mass flux and low pool temperature conditions and lower CO frequencies are observed at low mass flux and high pool temperature.

Considering that the Mark III PSTF and HVT test facilities have expectedly different vent acoustic modes, the fact that the Mark III (PSTF) and ABWR (HVT) produce similar dominant

CO frequencies supports the hypothesis that the ABWR (and ESBWR) CO frequency is mainly governed by the vent exit thermal-hydraulic conditions and not the vent acoustic modes.

From this review of ABWR HVT CO test data and Mark III PSTF CO tests data it is determined that, although there may be some contribution of vent acoustic modes, CO frequencies are controlled by vent exit thermal-hydraulic conditions. Therefore, differences in the vent geometry between the ESBWR and ABWR, and associated changes to the vent acoustic modes, would not impact the frequency content of the ABWR CO load definition when applied to the ESBWR.

3B.4.4 Application of the ABWR CO Load to the ESBWR

For the design evaluation of the containment structure, the pool boundary pressure load is obtained from an analysis of single-vent model of the ABWR prototypical design. The pool boundary pressure load obtained from the ABWR model analysis is applied over the full model of the ESBWR configuration. This CO loading specification implies that all vertical vents are in phase (i.e., no credit for phasing among vents), which is considered to be a conservative load definition approach.

For analysis of the structure, the pool boundary load is specified as a pressure time history. A total of four CO pool boundary pressure time histories are generated using the ABWR single vent model prototypical representing different observed periods of CO behavior. A fifth CO history is added for application to the ESBWR by compressing the time scale of the time history with highest frequency content. The time scale compression factor corresponds to the ratio of the ESBWR-to-ABWR vertical vent distance between the drywell entrance and top vent entrance. Although vent acoustic modes do not control CO frequency, this additional time history is added to account any possible influence of vent acoustic modes on the CO frequency.

An additional multiplication factor of 1.2 is also applied to the ABWR CO wall pressure history when applied to the ESBWR for added conservatism. Figure 3B-3 shows the spatial distribution of CO loads around the ESBWR submerged pool boundary normalized by the CO pressure time history.

3B.4.5 Local Condensation Oscillation Loads

In the horizontal vent confirmatory tests, a CO load with large positive pressure amplitude and short duration was observed on the bottom liner near the bottom vent exit. These pressure spikes were not observed outside a radius of two vent diameters from the bottom vent exit centerline.

Therefore, an additional CO load is considered in the design of the suppression pool floor/liner and submerged structures located within 2 vent diameters of each horizontal vent. The amplitude of this load represents the highest pressure measured during the HVT-SS tests. Structure responses from this local CO load are combined with responses from the pool boundary load specified in Section 3B.4.4 as absolute sum.

3B.5 CHUGGING LOADS

Chugging (CH), or unsteady condensation is a design consideration in pressure suppression containment systems using horizontal or vertical vents. It is generally used to represent a hydrodynamic phenomena associated with a LOCA. For the ESBWR design, CH is a manifestation of low horizontal vent steam mass flux. During chugging, rapid steam condensation causes the pool water to re-enter the vents. This is followed by a quiescent period until the steam-water interface is forced out into the pool. Thus, chugging, an intermittent event, is the result of unsteady condensation occurring in the last stages of the blowdown. Consequently, during a LOCA, chugging would typically occur following Condensation Oscillation as described earlier in the report. The exact transition between CO and CH is a function of mass flux and pool temperature.

The dominant pressure response in the suppression pool during CH is characterized by a prechug underpressure, an impulse (pressure spike), and a post chug oscillation. These are caused by the rapid condensation and subsequent collapse of a steam bubble located either inside or at the exit of one of the horizontal vents. As a result of this sudden collapse, water is allowed to re-enter the vent. After a short (one to five seconds) quiescent period, the pressure in the drywell again forces the steam water interface back out into the suppression pool. When the rate of pressurization can no longer keep up with the rate of condensation, the bubble collapses, and the cycle begins again. Overall, CH can be classified as an intermittent event resulting from the unsteady condensation of steam during the final phases of the drywell blowdown.

Specific tests were conducted to obtain chugging data for defining the chugging loads for the ABWR containment system.

As with CO, the ESBWR Chugging load is defined based on the ABWR Chugging load definition. A description of the ABWR Chugging load definition, the basis for application to the ESBWR, and any required adjustments made to the ABWR Chugging load definition for application to the ESBWR are described within Section 3B.5.

3B.5.1 Description of Chugging Data

There were 11 tests performed primarily for the purpose of establishing a database for definition of the CH load for a prototypical design evaluation. The HVT facility for the FS* test series was run with a full-scale vertical vent and horizontal vent system and an enlarged upper drywell. The tests were run at prototypical mass flux and pool temperature and with the vent system purged of nitrogen. It is known from previous blowdown testing and observations that presence of nitrogen in the vent reduces CH loads, so running chugging tests at prepurged conditions is conservative.

3B.5.2 Evaluation of Chugging Data

A detailed description and discussion of chugging data are contained in Reference 3B-4.

As previously described, Chugging is characterized by a small underpressure, followed by a positive pressure pulse, and a decaying ringout. These phenomena are associated with the initial contraction of the steam bubble, the rapid deceleration of pool water converging on the vent exit, and the excitation of an acoustic standing wave in the pool.

Chugging data from the Reference 3B-4 tests clearly show that the most severe chugging occurs for the steam breaks with an initial cold pool temperature. Both peak over pressure and Root-Mean-Square pressures decrease significantly as the pool temperature rises. In general, the data support the understanding (observed from prior tests) that chugging has some dependence on system parameters, such as mass flux and pool temperature, along with a substantial degree of randomness.

3B.5.3 Chugging Load Definition

Figure 3B-4 shows various elements of the source load methodology for defining the chugging load on the pool boundary. The database consisted of 11 tests conducted in the HVT facility with the full-scale vent system. From this database, key chugs were selected which serve as criteria for the development of the source load. The key-chug approach was used successfully for the definition of the chugging load for Mark II containment design (Reference 3B-8).

Key chug selection was determined by requiring that the PSD envelope of the selected key chugs matches the PSD envelope of the FS* chugging database. The criterion for a technically justifiable chug design source is that the design source load, when applied to an analytical model of the HVT facility, produces a wall pressure which matches the selected data and a PSD envelope which envelopes the PSD envelope of the selected data.

Eight different chugging design sources, represented by a single pulse acting at the exit of top vent in a full-scale model, were defined. The design sources were determined by imposing a requirement that the PSD envelope generated by these design sources bounds the PSD envelope from the selected chugging data.

3B.5.4 Basis for ESBWR Chugging Load Definition

The ESBWR chugging load definition is based on the ABWR definition. Adjustments to the ABWR definition for ESBWR application are determined from a review of expected conditions during chugging in the ESBWR, comparisons of the ESBWR and ABWR geometry, and a review of the ABWR HVT FS* testing.

3B.5.4.1 Review of ABWR and ESBWR Containment Geometry

As with CO, it was determined that the pool and horizontal vent geometry for the ESBWR and ABWR are sufficiently similar to allow a direct application of Chugging wall pressure amplitudes and wall pressure distributions. Also, as described in Section 3B.4 for CO, the differences in plant geometry, which do exist between the two designs, add to the conservatism of this approach.

3B.5.4.2 Review of Thermal-hydraulic Conditions

According to Reference 3B-4, the HVT Chugging data support that Chugging wall pressure amplitude has some dependence on mass flux and pool temperature, but with substantial randomness. Chugging will occur at the tail end of a LOCA event or for small break accident when low mass flux conditions occur. The ABWR Chugging loads were developed to bound the expected range of thermal hydraulic conditions during Chugging. Per Reference 3B-4 the highest Chugging amplitudes occur with steam breaks with an initially cold pool temperature. This indicates that the limiting conditions occur with colder pool temperatures. Consequently,

any potential increase in the pool temperature response introduced by differences between the ESBWR and ABWR does not impact Chugging. Additionally, the HVT FS* tests were performed with a pre-purged drywell (steam only condition in the drywell) which provides a bounding condition with respect to nitrogen content relative to the expected ESBWR response. Based on this review of the ABWR Chugging load definition basis it was been determined that the limiting thermal hydraulic conditions during Chugging, which affect the Chugging wall amplitude for the ESBWR are enveloped by the range of conditions tested in the development of the ABWR Chugging load.

3B.5.4.3 Frequency Content Evaluation

The HVT FS* test data shows that most of the Chugging energy is contained within frequencies associated with pool acoustic modes. This is attributed to the fact that the bubble collapse during chugging occurs predominately outside of the vent, in the suppression pool. Because the ESBWR pool depth is significantly less than the ABWR depth, the Chugging wall pressure “ring-out” frequencies, which are associated with the pool acoustic modes, do require adjustment. From a simple acoustic analysis of a pool with a rigid bottom and a free surface, the fundamental frequency is given in the terms of sound speed, c , and pool depth, L , by

$$f=c/4L$$

Therefore, to adjust the ABWR chugging frequency to the ESBWR, the ABWR chugging frequency is increased by the ratio of the ABWR pool depth-to-ESBWR pool depth. To accomplish the frequency adjustment, the time scales for the ABWR Chugging time histories are compressed by the ratio of the ESBWR pool depth-to-ABWR pool depth when applied to the ESBWR.

3B.5.5 Application of the ABWR Chugging Load To The ESBWR

The pool boundary Chugging pressure loads obtained from analysis of a single-vent sector model of the ABWR prototypical design are specified for application over the full model of the ESBWR configuration. To bound symmetric and asymmetric loading conditions, two load cases are defined.

All vents chugging in phase.

- (1) Vents in one half chugging 180° out of phase with the other half vents.

For structural analyses the pool boundary load is specified as a pressure-time history. A total of eight time pool boundary pressure histories, representing different chugging behavior, are specified.

Adjustments for ESBWR Application

Adjustments are made to the ABWR Chugging load pressure history amplitude and frequency to add conservatism and to account for the difference in suppression pool depth.

Pressure Amplitude

The chugging pressures determined from the ABWR model calculation are multiplied by a factor of 1.2 to obtain additional conservatism.

Frequency

The time scale is compressed to account for the frequency adjustment described in Section 3.B.5.4. The pressures are applied to the pool boundary using the normalized spatial distribution in Figure 3B-5.

3B.5.6 Horizontal Vent Loads

The HVT FS* facility was instrumented with two load cells on the top horizontal vent to measure the vertical force and bending moment experienced by the vent during chugging. Chugging has a potential to induce significant loading on the horizontal vent. With the prototypical vent system design, in which the horizontal vents project into the pool, it is anticipated that these anticipated loads may be of significance to containment structure design.

For structure evaluation of the ESBWR containment horizontal vent pipe and pedestal, an upward load, based on the ABWR HVT data, is conservatively defined.

For building structure response analysis and for the evaluation of RPV and its internals, a horizontal vent upward load is specified. To bound symmetrical and asymmetrical loading conditions, the following two load cases are considered and analyzed.

Upward load on the pedestal wall simultaneously at all top 12 horizontal vents.

Upward load on the pedestal wall simultaneously at top six vents in one-half side of pedestal.

3B.6 SAFETY RELIEF VALVE LOADS

3B.6.1 SRV Design

The ESBWR uses Mark III type X-quenchers in the suppression pool for condensing steam released through the safety relief valves (SRV) or safety valves (SV). During the actuation of a SRV or SV, the nitrogen initially contained inside the discharge line is compressed and subsequently expelled into the suppression pool by the RPV blowdown steam entering the discharge line. The nitrogen exits through holes drilled into an X-quencher device, which is attached to the discharge line. The X-quencher discharge device is utilized in ESBWR to promote effective heat transfer and stable condensation of discharged steam in the suppression pool, thereby minimizing suppression pool boundary loads.

The ESBWR design contains two types of relief valves, ten Automatic Depressurization System (ADS) safety relief valves and eight non-ADS safety valves.

Each ADS valve is piped to the suppression pool by a discharge line (SRVDL) to an X-quencher in the suppression pool. All ten valves have the same spring setpoint.

The eight non-ADS valves are split into two groups of four valves each. Each group is piped to a header with rupture disks on the ends. Each of the two headers is piped to a standard X-quencher in the suppression pool. All eight valves have the same spring setpoint.

3B.6.2 SRV Discharge Load

When a relief valve lifts, the effluent reactor steam causes a rapid pressure build up in the discharge pipe. This rapid compression of the column of nitrogen in the pipe causes a subsequent acceleration of the water slug in the submerged portion of the pipe. During this blowout process the pressure in the pipe builds to a peak as the last of the water is expelled. The compressed cushion of nitrogen between the water slug and the effluent vapor exits the quencher and forms four clouds of small bubbles that begin to expand to the lower pool pressure. This expansion leads to coalescence of the bubble cloud into four bubbles. The four bubbles continue to oscillate, displacing the water and propagating a pressure disturbance throughout the suppression pool. The dynamics of the submerged bubbles are manifested in pressure oscillations arising from the bubble expansion coupled with inertial effects of the moving water mass. The sequence of expansion and contraction is repeated with an identifiable frequency until the bubbles reach the pool surface.

The magnitude of the pressure disturbance in the suppression pool decreases with increasing distance from the point of discharge, resulting in a damped oscillatory load of varying magnitude on structures below the water surface.

After the nitrogen has been expelled, steam exits the quenchers and condenses in the pool. The condensing steam produces negligible (pressure) amplitude loads on the pool boundary, as observed from X-quencher discharge testing.

Calculational methodology for defining the quencher discharge loads for the ESBWR containment is the same as that used for prior ABWR, Mark III, and Mark II containments. Attachment A to Reference 3B-6 provides a detailed description of the calculational methodology. This methodology is based directly on empirical correlations based on and

obtained from mini-scale, small-scale, and large-scale (including in-plant tests) tests conducted to develop a load definition methodology for X-quencher discharge loads during the SRV actuation.

The X-quencher test data were statistically correlated to provide a relationship, which can be used to calculate the magnitude of quencher arm clearing pressure loads on the pool boundary as a function of several key parameters. The correlation was developed for use in both Mark II and Mark III containment systems using X-quencher discharge devices for the SRV lines. Detailed description of (1) the data base, (2) a quantitative assessment of the test data in terms of the physical phenomena, (3) the procedure for identification and justification of key parameters used in the statistical correlations, (4) the statistical analysis of the data, and (5) the resulting correlation equations, are provided in Section A12 of Reference 3B-9.

In summary, the calculational methodology consists of:

- A statistically derived correlation for predicting the magnitude of the peak positive bubble pressure and the relationship for calculating maximum negative pressure from the maximum positive pressure.
- An idealized oscillatory pressure history representing subsequent interaction of the quencher nitrogen bubble with the suppression pool.
- A relationship for determining the pressure field in the suppression pool as a function of distance from the quencher.
- A technique for determining the total nitrogen bubble pool boundary load for subsequent actuation from the first actuation loads, and when more than one quencher bubble exists in the pool (multiple valve actuation conditions).

3B.6.3 Pool Boundary Loads

The absolute pressure on the pool walls due to SRV discharge is calculated by the following equation:

$$P(a) = P_{w/w \text{ gas-space}} + P_h + P_r \quad (3B-4)$$

where

$P(a)$	=	Absolute pressure at point (a)
$P_{w/w \text{ gas-space}}$	=	Absolute pressure of wetwell gas-space
P_h	=	Hydrostatic pressure
P_r	=	Bubble pressure attenuated by distance, r to point (a).

The pressure decays with time.

The bubble pressure at point(a) P_r , is calculated from bubble pressure, P_b , using the following relationship.

$$\begin{aligned} P_r &= 2P_b r_0 / r : \text{for } r > 2r_0 \\ P_r &= P_b : \text{for } r \leq 2r_0 \end{aligned} \quad (3B-5)$$

where

r_o = the quencher radius,

and

r = the line of sight distance from the quencher centerpoint to the evaluation point.

Nitrogen bubble pressure loads from a particular quencher location are considered to act only on the boundaries, which can be viewed from the quencher with direct line of sight, as illustrated in Figure 3B-6. As an illustration, Figure 3B-7 shows the ideal pressure history, which is normalized for the maximum pressure value. This pressure time history profile is used in determining the pressure amplitude variation with time and the number of pressure cycles. It should be noted that the bubble pressure decays to $1/3 P_{max}$ within 5 cycles for any frequency between 5 and 12 Hz. The justification for this application is from examination of full-scale plant data where most traces were observed to decay to a small fraction of their peak value in two or three cycles. The design loads consider and include the following SRV actuation cases:

- Single valve discharge for first and subsequent actuations.
- Multiple valve discharge.

The spatial distribution of SRV boundary pressure is shown in Figure 3B-8.

3B.6.3.1 Single Valve Discharge

For the ESBWR, single SRV or SV discharge is not a normal operational event. However, the plant is designed for an inadvertent opening of a single valve. Therefore, pressure loadings resulting from both first and subsequent SRV or SV actuations are considered. The SRV and SV lines resulting in the most severe pressure loading are selected for design assessment.

The following major assumptions are made for single valve discharge load definition:

- Maximum SRV and SV discharge line volumes are used.
- Suppression pool is at high water level and peak normal operating temperature.
- SRV and SV setpoints are increased 3% to account for drift and tolerance.
- The minimum valve opening time is 20 msec.

Nitrogen bubble pressure loads from a particular quencher are considered to act only on boundaries, which can be viewed from the quencher bubble with direct line of sight as illustrated in Figure 3B-6.

3B.6.3.2 Multiple Valve Discharge

This case covers the events in which multiple SRVs or SVs actuate.

During a postulated LOCA as part of the normal ADS function, five SRVs open when the RPV water level drops below the Level 1 setpoint and another five SRVs open with a preset delay. However, because all of the SRVs have the same setpoint, assuming all SRVs actuate together is a bounding assessment.

While all of the SVs also have the same setpoint, if more than one SV on a given discharge line actuates, the rupture disks on the common header are designed to open before the discharge line

clears. In that case, there would be no discharge in the pool through the quencher. Therefore, the limiting multiple valve event for the SVs is to have two valves open, one on each discharge line.

In addition to the single valve discharge assumptions, the following assumptions are made for multiple valve discharge load definition:

- (1) Suppression pool is at an elevated high temperature.
- (2) All the drywell nitrogen (both upper and lower drywell) has been purged to the wetwell.

Variations in time of actuation, valve opening time, and individual discharge line lengths influence the time to complete line clearing, and introduce differences in phasing of the oscillating nitrogen bubbles in the suppression pool. However, these phase differences are neglected, in combining the loads from the individual SRV bubbles.

For multiple valve discharge, the pressure time history, normalized for the maximum pressure value, is shown in Figure 3B-7. The maximum positive pressure is given in Table 3B-4. The bubble frequency range for analysis is 5 to 12 Hz. Hence for frequencies other than 8 Hz, the cycle time in Figure 3B-7 has to be adjusted accordingly.

As a conservative approach, the multiple valve discharge case considers and includes the most severe symmetric and asymmetric load cases. The most severe symmetric load case assumes oscillating nitrogen bubbles (from all valves) in phase, and the most severe asymmetric case assumes one half of oscillating nitrogen bubbles out of phase with the other half of the oscillating nitrogen bubbles. These two load cases bound all multiple valve actuation cases. The combined pressure loading from multiple valves is obtained by SRSS (Square Root of the Sum of the Squares) of the loads of the single valves acting on the designated evaluation point.

Hence, for multiple SRV actuation the combined bubble pressure load ΔP_r , must be calculated using the following equations:

$$\Delta P_r = \left[\sum_{n=1}^n P_n^2 \right]^{1/2} \quad (3B-6)$$

where,

$$P_n = 2P_b \left(\frac{r_o}{r_n} \right) \quad \text{for } r_n > 2r_o$$

$$P_n = P_b \quad \text{for } r_n \leq 2r_o$$

If the calculated $\Delta P_r > P_b$, set $\Delta P_r = P_b$. Note that r_n = the distance from the center of the quencher to point a.

3B.6.3.3 SRV Bubble Pressure (P_b)

The SRV bubble pressure (P_b) is calculated by the methodology described in Subsection 3B.6.2. Pressures calculated by using this methodology have been shown to be conservative based on

previous plant test results (Reference 3B-9). These pressures are based on a 95-95% confidence level of the Caorso data (References 3B-10 and 3B-11).

Bubble pressures are reported below for three major cases:

- Single Valve First Actuation
- Single Valve Subsequent Actuation
- Multiple Valve Actuation

Two evaluations are performed; one for the ADS safety relief valves and one for the non-ADS safety valves. The bounding results from these two studies are used to define the SRV discharge line load definition. The maximum bubble pressures are reported in Table 3B-4. The analytical values represent the calculated results while the design values provide margin and are used in subsequent loads evaluations.

3B.6.3.4 Quencher Steam Condensation Loads

Previous test data (References 3B-10 and 3B-11) indicate negligible condensation loads for quencher devices. Additional data provided in Reference 3B-12, demonstrates that condensation loads over the full range of pool temperatures up to saturation, are low compared to loads due to SRV discharge, Condensation Oscillation, and Chugging, which is considered in containment design evaluation.

Hence, dynamic loads during quencher steam condensation process are not defined here nor considered for containment evaluation.

3B.7 ESBWR UNIQUE DESIGN FEATURES

3B.7.1 Passive Containment Cooling System

The PCCS receive a steam-gas mixture supply directly from the drywell; it does not have any valves, so it immediately starts into operation, following a LOCA event. Non-condensable gases, together with steam vapor, enter the PCCS condenser; steam is condensed inside PCCS condenser vertical tubes, and the condensate, which is collected in the lower headers, is discharged to the GDCS pool. The non-condensable gases are purged to the wetwell through the vent line, which is submerged in the suppression pool.

3B.7.1.1 PCCS Pool Swell Loads

Pool swell loads caused by PCCS vent discharge are not significant because of the following:

- The PCCS pipe area is significantly smaller than the main vent area.
- The PCCS vent submergence is less than the main vents.

Consequently, the main vent pool swell loads presented in Section 3B.3 are the bounding loads.

3B.7.1.2 PCCS Condensation Loads

Condensation Oscillation (CO) for the main vent system is described in Section 3B.4. CO may also be present at the PCCS vent exit during a LOCA when a nitrogen-steam mixture is discharged from the condenser, and the resultant steam is condensed in the suppression pool. However, since the diameter of the PCCS vent line is significantly smaller than the diameter of a main horizontal vent, the mass flow rate through the main vents during a DBA-LOCA would be significantly higher than the mass flow rate through the PCCS vents, and the CO loads derived for the main vent system would bound any CO loads resulting from the PCCS vent discharge. Consequently, CO loads presented in Section 3B.4 are the bounding loads.

Chugging at the vent discharge is prevented by the presence of the PCCS condenser. In order to have chugging at the PCCS vent exit, the amount of nitrogen in the mixture must be small or absent. Since the flow from the drywell to the suppression pool must first pass through the condenser tubes, most or all of the steam would be condensed, and the resultant mixture would have a high concentration of nitrogen. Therefore, chugging at the vent exit would not occur.

3B.7.2 Gravity-Driven Cooling System

The GDCS pools are equipped with spillover pipes (scuppers) that are piped to the main vent entrance. This is to ensure that any overflow (by PCC condensate for example) goes to the suppression pool rather than spilling on the upper DW floor and finding its way to the lower drywell. While these drainpipes will be designed as part of the COL phase, they are not expected to have any impact on the containment thermal-hydraulic loads.

At the start of any LOCA, both ends of the pipe are exposed to the drywell airspace and, hence, have the same pressure. Therefore, the drainpipe does not affect the pool swell blowdown flow through the main vent system.

Later during the transient, the PCCS condensate adds water to the GDCS tanks. However, the GDCS will actuate before the water level reaches the spillover pipe, and the tanks will drain into the RPV. Therefore, these spillover pipes have no impact on the main vent performance.

3B.7.3 Lower Drywell Spillover Pipes

Twelve spillover pipes are located in the inner suppression pool wall connecting the LDW airspace to the bottom of the suppression pool. While these drainpipes will be designed as part of the COL phase, they are not expected to have any impact on the containment thermal-hydraulic loads.

The spillover pipes are initially closed so that there is no blowdown flow through them. They will not be opened until the water level in the lower drywell reaches the elevation of the inlet, which will be after blowdown is completed. Therefore, the spillover pipes will be closed when pool swell, CO, or CH occur in the main vents.

3B.8 SUBMERGED STRUCTURE LOADS

Structures submerged in the suppression pool can be subjected to flow induced hydrodynamic loads due to a LOCA and/or SRV/DPV actuations.

During a LOCA, a steam/water mixture rapidly escapes from the break, and the drywell is rapidly pressurized. The water initially in the vent system is expelled out into the suppression pool. A highly localized induced flow field is created in the pool and a dynamic loading is induced on any submerged structures. After the water is expelled from the vent system, the nitrogen initially in the drywell is forced out through the horizontal vents into the suppression pool. The nitrogen exiting from the vents forms expanding bubbles, which create moderate dynamic loads on structures submerged in the pool. The nitrogen bubbles cause the pool water surface to rise until they break through the pool water surface. The pool surface water slug decelerates and falls back to the original pool level as the steam/water mixture from the break fills the drywell and is channeled to the pool via the vent system. Steam condensation starts and the oscillatory nature of the phenomena causes a vibratory load on submerged structures. The CO loading continues until the pressure in the drywell decreases. A less regular condensation loading called chugging (CH) follows this. During the CH period, a high frequency spike is propagated and causes an acoustic loading on submerged structures.

During SRV actuations, the dynamic process is quite similar to LOCA steam blowdown except that the X-quencher attached at the discharge end mitigates the induced load. Two types of loads are important. One is due to the water jet formed at the X-quencher arm discharge, and the second is due to the four gas bubbles formed between the arms of the X-quencher. These bubbles are smaller in size than the LOCA bubbles, reside longer in the pool and oscillate as they rise to the free surface of the suppression pool.

3B.8.1 Pool Swell Submerged Structure Loads

During the initial phase of the DBA, the drywell is pressurized and the water in the vents is expelled to the pool and induces a flow field throughout the suppression pool. This induced flow field creates a dynamic load on structures submerged in the pool. For submerged structures that are not in the direct path of these jets, the dynamic load on these structures is less than the load induced by the LOCA gas bubble that forms after the water is expelled out. Because the gas bubble induced dynamic load is bounding, this load is conservatively used in place of the water jet load. For submerged structures that are in the direct path of these jets, water jet loads are compared with bubble dynamic loads, and the higher load used.

After the vents are cleared of initially contained water, pressurized drywell nitrogen is purged into the suppression pool, and a single bubble is formed around each vent exit. It is during the bubble growth period that unsteady fluid motion is created within the suppression pool. During this period all submerged structures below the pool surface are exposed to transient hydrodynamic loads.

The load definition methodology for defining the LOCA bubble induced loads on submerged structures is consistent with the methodology used for prior plants, as described in Reference 3B-13.

3B.8.2 CO Submerged Structure Loads

During LOCA, after the vent has been cleared of water and the drywell nitrogen has been carried over into the wetwell, steam condensation begins. This condensation oscillation phase induces bulk water motion and, therefore, creates drag loads on the structures submerged in the pool.

The load definition methodology for defining the LOCA steam condensation oscillation loads on submerged structures is consistent with the methodology used for prior plants. The methodology is described in Reference 3B-14.

3B.8.3 CH Submerged Structure Loads

CH occurs after the drywell nitrogen has been purged and carried over into the wetwell, and the vent steam mass flux falls below a critical value. CH then induces acoustic pressure loads on structures submerged in the suppression pool. The load definition methodology for defining the LOCA CH loads on submerged structures is consistent with methodology used for prior plants. This methodology is described in Reference 3B-14.

3B.8.4 SRV Submerged Structure Load

Following the actuation of the SRVs, water contained initially in the line is rapidly purged through the X-quencher attached at the end of the SRV discharge line. A highly localized water jet is formed around the X-quencher arms. The hydrodynamic load due to the water jet outside a sphere circumscribed around the quencher arms, is conservatively bounded by the gas bubble induced dynamic load. There are no submerged structures located within the sphere mentioned above in the ESBWR arrangement.

After the water discharge, the nitrogen initially contained in the discharge line is forced into the suppression pool under high pressure. The gas bubbles that are formed interact with the surrounding water and produce oscillating pressure and velocity fields in the suppression pool. This pool disturbance gives rise to hydrodynamic loads on submerged structures in the pool.

The load definition methodology for defining the SRV bubble loads on submerged structures is consistent with that used for prior plants. This methodology is described in References 3B-13 and 3B-15.

3B.8.5 PCCS Vent Discharge Load

The load definition methodology for defining the PCCS non-condensable vent discharge loads on submerged structures, is similar to the methodology defined in Subsection 3B.8.4 for SRV loads.

3B.9 LOAD COMBINATIONS

Under certain plant conditions, the containment structures can be subjected simultaneously to hydrodynamic loads due to a LOCA event (DBA, IBA or SBA) and SRV actuations. Figure 3B-9 shows the combination history of these loads for the controlling DBA-LOCA events. Section 6.2 documents the containment pressure and temperature responses, which are used to derive the pressure/temperature loads. The chart shows the time intervals when specific loads could occur. At any given time on the chart, the containment structures may experience all the loading conditions in those boxes, which span that time. However, the loads may not be continuous over the entire range depicted in the chart, especially the SRV and CH loads.

Event-time relationships showing load combination histories for design assessment of the ESBWR containment system are, in general, consistent with the approach used for other BWR plants including ABWR (Reference 3B-1).

3B.10 REFERENCES

- 3B-1 General Electric Company, "Advanced Boiling Water Reactor, Standard Safety Analysis Report," 23A6100, Class III (Proprietary) and Class I (Non-proprietary), Revision 8, May 13, 1996 (Appendix 3B, Containment Hydrodynamic Loads).
- 3B-2 General Electric Company, "The General Electric Mark III Pressure Suppression Containment Analytical Model," NEDO-20533, Class I (Non-proprietary), Revision 0, June 1974.
- 3B-3 General Electric Company, "Mark II Pressure Suppression Containment Systems: An Analytical Model of the Pool Swell Phenomenon," NEDE-21544-P, Class III (Proprietary), Revision 0, December 1976, and NEDO-21544, Class I (Non-proprietary), Revision 0, December 1976.
- 3B-4 General Electric Company, "Containment Horizontal Vent Confirmatory Test, Part I," NEDC-31393, Class III (Proprietary), Revision 0, March 1987.
- 3B-5 General Electric Co., "Scaling Study of the General Electric Pressure Suppression Test Facility, Mark III Long-Range Program, Task 2.2.1," NEDE-25273, Class III (Proprietary), Revision 0, March 1980.
- 3B-6 General Electric Company, "GESSAR II, BWR/6 Nuclear Island Design," 22A7007, Class III (Proprietary) and Class I (Non-proprietary), Revision 19, May 28, 1985 (Appendix 3B, Containment Hydrodynamic Loads).
- 3B-7 General Electric Co., "Mark III Confirmatory Test Program - $1/\sqrt{3}$ Scale Condensation and Stratification Phenomena – Test Series 5807," NEDE-21596-P, Class III (Proprietary), Revision 0, March 1977, and NEDO-21596, Class I (Non-proprietary), Revision 0, March 1977.
- 3B-8 General Electric Co, "Mark II Containment Program, Generic Chugging Load Definition Report," NEDE-24302-P, Class III (Proprietary), Revision 0, April 1981, and NEDO-24302, Class I (Non-proprietary), Revision 0, July 1981.
- 3B-9 General Electric Company, "Containment Loads Report (CLR), Mark III Containment," 22A4365AB, Class III (Proprietary), Revision 4, January 25, 1980, and 22A4365, Class I (Non-proprietary), Revision 0, January 25, 1980.
- 3B-10 General Electric Company, "Mark II Containment Supporting Program, Caorso Safety Relief Valve Discharge Tests, Phase I Test Report," NEDE-25100-P, Class III (Proprietary), Revision 0, May 1979, NEDO-25100, Class I (Non-proprietary), Revision 0, August 1979, and NEDO-25100-EA, Class I (Non-proprietary), Revision 0, February 1981.
- 3B-11 General Electric Company, "Mark II Containment Supporting Program, Caorso Safety Relief Valve Discharge Tests, Phase II Apparent Test Results Report," NEDE-25118, Class III (Proprietary), Revision 0, August 1979.
- 3B-12 General Electric Company, "Elimination of Limit on BWR Suppression Pool Temperature for SRV Discharge With Quenchers," NEDO-30832-A, Class I (Non-proprietary), Revision 0, May 1995.

- 3B-13 General Electric Company, "Analytical Model for Estimating Drag Forces on Rigid Submerged Structures caused by LOCA and Safety Relief Valve Ramshead Air Discharges," NEDO-21471, Class I (Non-proprietary), Revision 0, September 1977.
- 3B-14 General Electric Company, "Analytical Model for Estimating Drag Forces on Rigid Submerged Structures Caused by Steam Condensation and Chugging, Mark III Containments" NEDO-25153, Class I (Non-proprietary), Revision 0, July 1979.
- 3B-15 General Electric Company, "Analytical Model for Estimating Drag Forces on Rigid Submerged Structures Caused by LOCA and Safety Relief Valve Ramshead Air Discharges, Supplement for X-Quencher Air Discharges," NEDO-21471-01, Class I (Non-proprietary), Revision 0, October 1979.

Table 3B-1
Pool Swell Results

Description	Calculated Value	Design Value	Units
Maximum Nitrogen Bubble Pressure ¹	152	250	kPa gauge
Maximum Pool Swell Velocity ^{2,3}	5	6	meters/second
Maximum Wetwell Gas Space Pressure ¹	138	250	kPa gauge
Maximum Pool Swell Height ²	4.2	5.5	meters

Notes:

- 1 Polytropic index = 1.4
- 2 Polytropic index = 1.2
- 3 Reflects conservative multiplier of 1.1

Table 3B-2
Standard Drag Coefficients for Various Objects








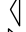
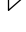
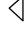






Body Shape		C_D	Reynolds Number	L/d
Circular cylinder	\leftrightarrow 	0.63	10^5	1
		0.74	10^5	5
		0.90	10^5	20
		1.20	10^5	∞
		0.35	$> 5 \times 10^5$	5
		0.33	$> 5 \times 10^5$	∞
Elliptical cylinder	\leftrightarrow  2:1	0.0	4×10^4	∞
		0.46	10^6	∞
	\leftrightarrow  4:1	0.32	2.5×10^4 to 10^5	∞
		0.29	2.5×10^4	∞
	\leftrightarrow  8:1	0.20	2×10^5	∞
Square cylinder	\leftrightarrow 	2.0	3.5×10^4	∞
	\leftrightarrow 	1.6	10^4 to 10^5	∞
Triangular cylinders	\leftrightarrow  120°	2.0	10^4	∞
	\leftrightarrow  120°	1.72	10^4	∞
	\leftrightarrow  90°	2.15	10^4	∞
	\leftrightarrow  90°	1.60	10^4	∞
	\leftrightarrow  60°	2.20	10^4	∞
	\leftrightarrow  60°	1.39	10^4	∞
	\leftrightarrow  30°	1.8	10^5	∞
	\leftrightarrow  30°	1.0	10^5	∞
Semitubular	\leftrightarrow 	2.3	4×10^4	∞
	\leftrightarrow 	1.12	4×10^4	∞
Circular disk, normal to flow	\leftrightarrow	1.12	$> 10^3$	0
		1.12	$> 10^3$	0
Circular cylinder parallel to flow	\leftrightarrow	0.91	$> 10^3$	1
		0.87	$> 10^3$	4
		0.99	$> 10^3$	7

Table 3B-2
Standard Drag Coefficients for Various Objects

Body Shape		C_D	Reynolds Number	L/d
Rectangular flat plate, normal to flow	1.10	1.10	$\geq 10^3$	1
	1.20	1.20	$> 10^3$	5
	1.50	1.50	$> 10^3$	20
	2.00	2.00	$> 10^3$	∞

Notes

L = Length

d = Maximum width of object measured normal to flow direction

Table 3B-3
Hydrodynamic Mass and Acceleration Drag Volumes for Two-Dimensional Structural Component


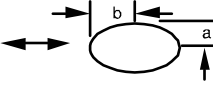
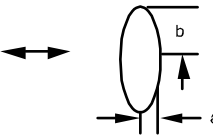
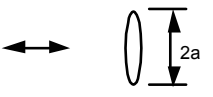
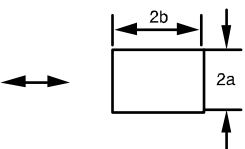
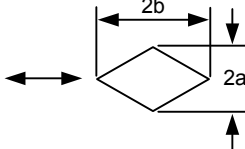
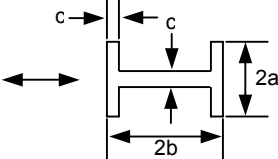
Body	Section Through Body and Uniform Flow Sirection	Hydrodynamic Mass (Patton, 1965)	Acceleration Drag Volume V_A
Circle		$\rho\pi R^2 L$	$2\pi R^2 L$
Ellipse		$\rho\pi a^2 L$	$\pi a(a+b)L$
Ellipse		$\rho\pi b^2 L$	$\pi b(a+b)L$
Plate		$\rho\pi a^2 L$	$\pi a^2 L$
Rectangular		a/b ∞ $\rho\pi a^2 L$ 10 $1.14\rho\pi a^2 L$ 5 $1.21\rho\pi a^2 L$ 2 $1.36\rho\pi a^2 L$ 1 $1.51\rho\pi a^2 L$ 1/2 $1.70\rho\pi a^2 L$ 1/5 $1.98\rho\pi a^2 L$ 1/10 $2.23\rho\pi a^2 L$	$aL(4b+\pi a)$ $aL(4b+1.14\pi a)$ $aL(4b+1.21\pi a)$ $aL(4b+1.36\pi a)$ $aL(4b+1.51\pi a)$ $aL(4b+1.70\pi a)$ $aL(4b+1.98\pi a)$ $aL(4b+2.23\pi a)$
Diamond		a/b 2 $0.85\rho\pi a^2 L$ 1 $0.76\rho\pi a^2 L$ 1/2 $0.67\rho\pi a^2 L$ 1/5 $0.61\rho\pi a^2 L$	$aL(2b+0.85\pi a)$ $aL(2b+0.76\pi a)$ $aL(2b+0.67\pi a)$ $aL(2b+0.61\pi a)$
I-Beam		$a/c=2.6, b/c=3.6$ $2.11\rho\pi a^2 L$	$[2.11\pi a^2 + 2c(2a+b-c)]L$

Table 3B-3
Hydrodynamic Mass and Acceleration Drag Volumes for Two-Dimensional Structural Component

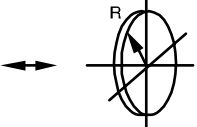
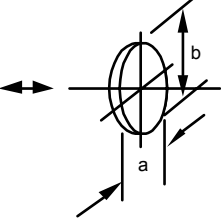
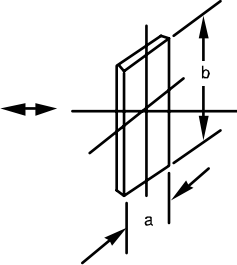
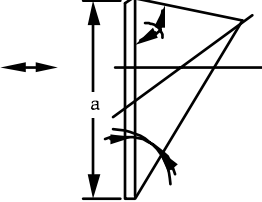
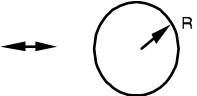
Body	Section Through Body and Uniform Flow Direction	Hydrodynamic Mass (Patton, 1965)	Acceleration Drag Volume V_A
Circular Disk		$\frac{8}{3}\rho R^3$	$\frac{8}{3}R^3$
Elliptical Disk		b/a $\infty \quad \rho\pi/6ba^2$ $3 \quad 0.9\rho\pi/6ba^2$ $2 \quad 0.826\rho\pi/6ba^2$ $1.5 \quad 0.748\rho\pi/6ba^2$ $1.0 \quad 0.637\rho\pi/6ba^2$	$\pi/6ba^2$ $0.9\pi/6ba^2$ $0.826\pi/6ba^2$ $0.748\pi/6ba^2$ $0.637\pi/6ba^2$
Rectangular Plate		b/a $1 \quad 0.478\rho\pi/4a^2b$ $1.5 \quad 0.680\rho\pi/4a^2b$ $2 \quad 0.840\rho\pi/4a^2b$ $2.5 \quad 0.953\rho\pi/4a^2b$ $3 \quad \rho\pi/4a^2b$ $\infty \quad \rho\pi/4a^2b$	$0.478\pi/4a^2b$ $0.680\pi/4a^2b$ $0.840\pi/4a^2b$ $0.953\pi/4a^2b$ $\pi/4a^2b$ $\pi/4a^2b$
Triangular Plate		$\rho a^3 \frac{(\tan \theta)^{3/2}}{3\pi}$	$a^3 \frac{(\tan \theta)^{3/2}}{3\pi}$
Sphere		$\rho^2/3\pi R^3$	$2\pi R^3$

Table 3B-4
SRV Bubble Pressure

	Calculated Value	Design Value
Peak Positive Pressure (kPa d)		
3B. Single Valve First Actuation	43	91
4B. Single Valve Subsequent Actuation	89	152
5B. Multiple Valves	45	76
Peak Negative Pressure (kPa d)		
6B. Single Valve First Actuation	32	54
7B. Single Valve Subsequent Actuation	46	63
8B. Multiple Valves	38	54

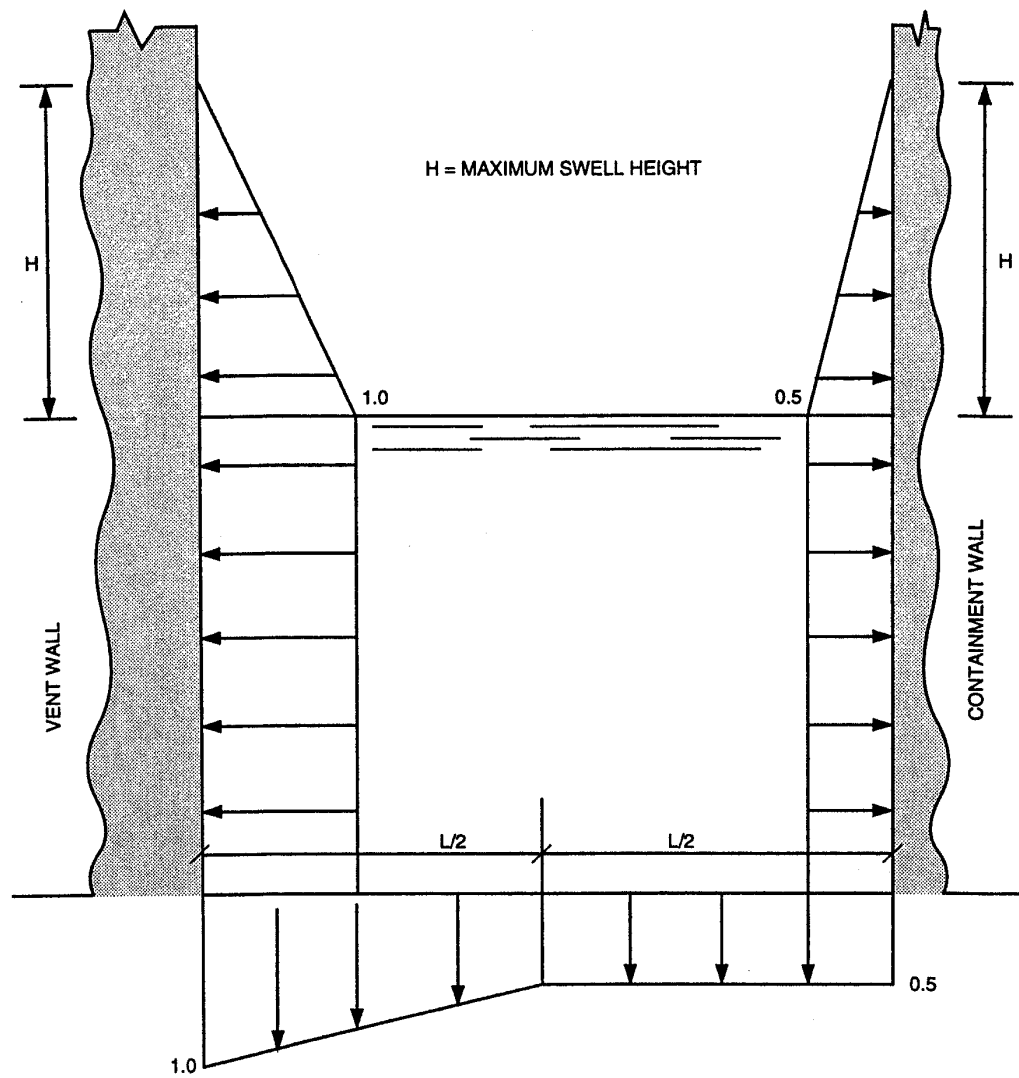


Figure 3B-1. Suppression Pool Swell Boundary Bubble Pressure Spatial Distribution, Normalized to Maximum Bubble Pressure

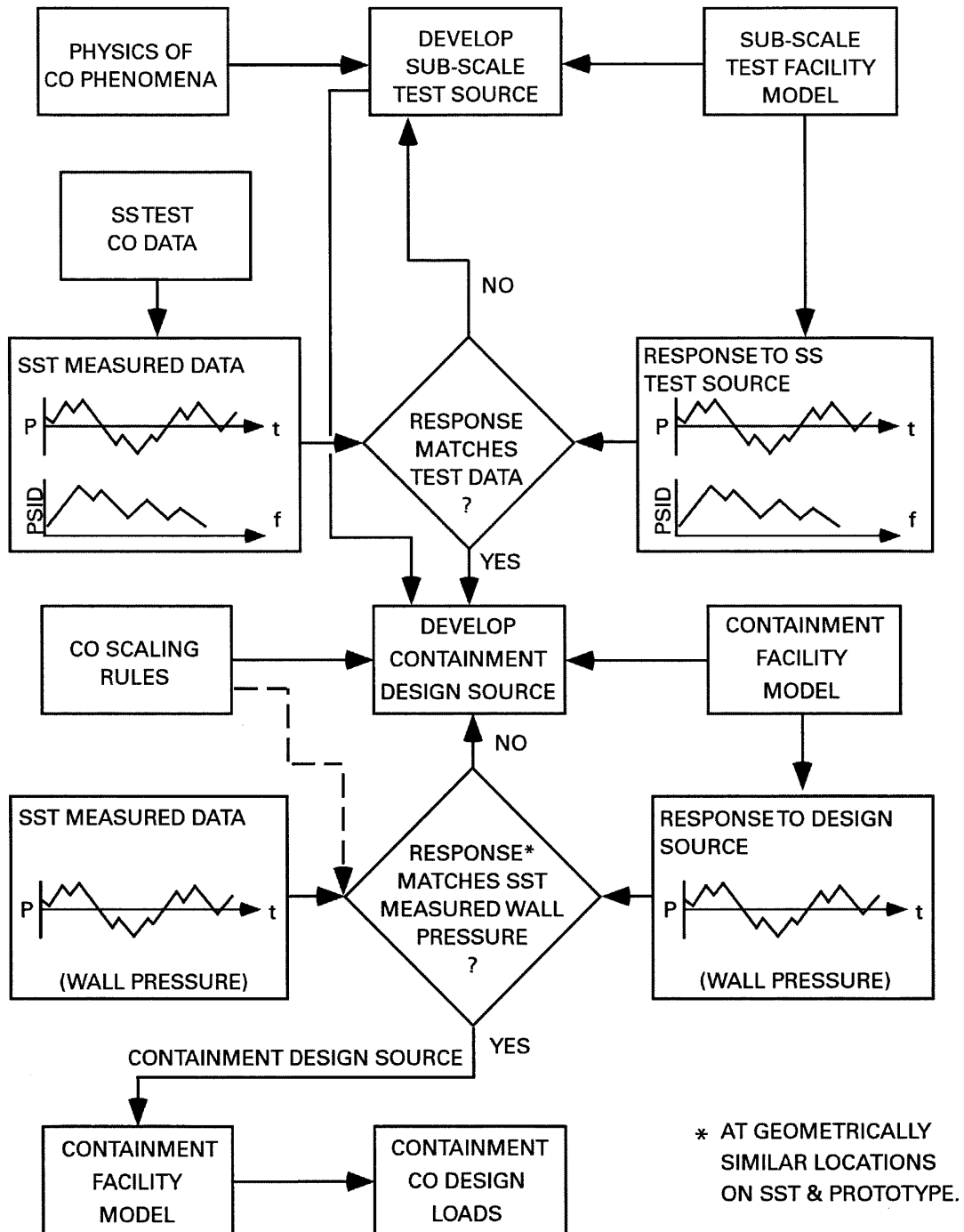


Figure 3B-2. Containment CO Source Load Methodology

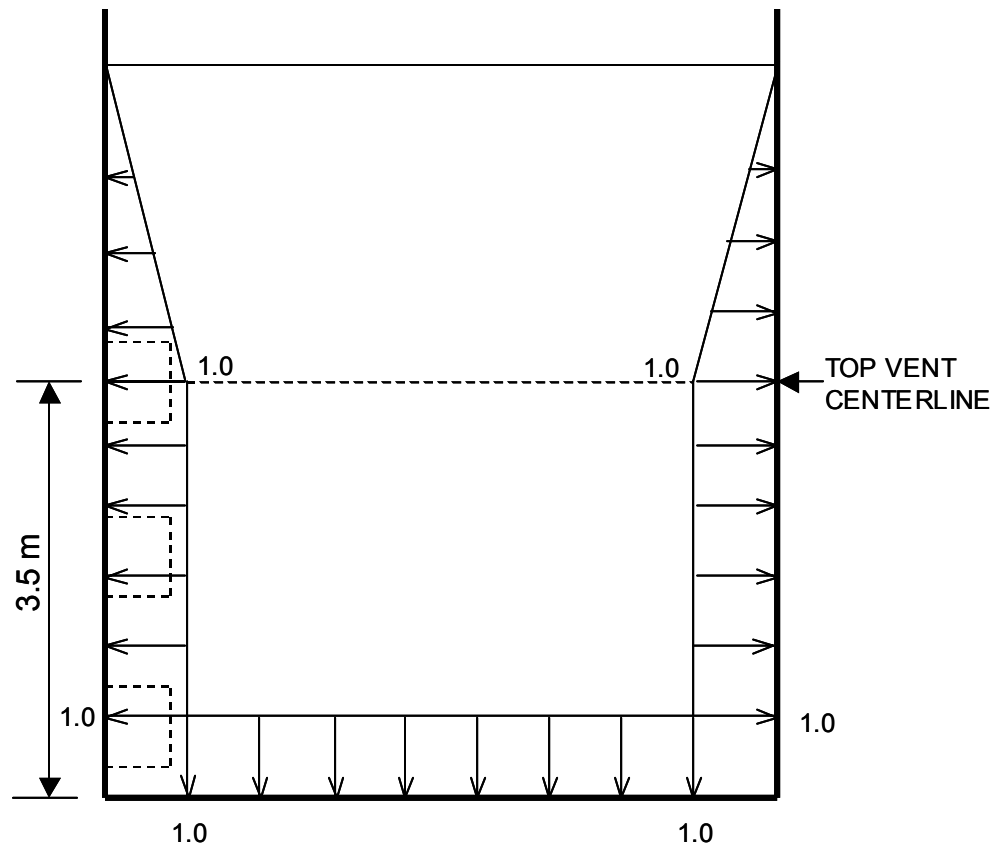


Figure 3B-3. Spatial Load Distribution for CO

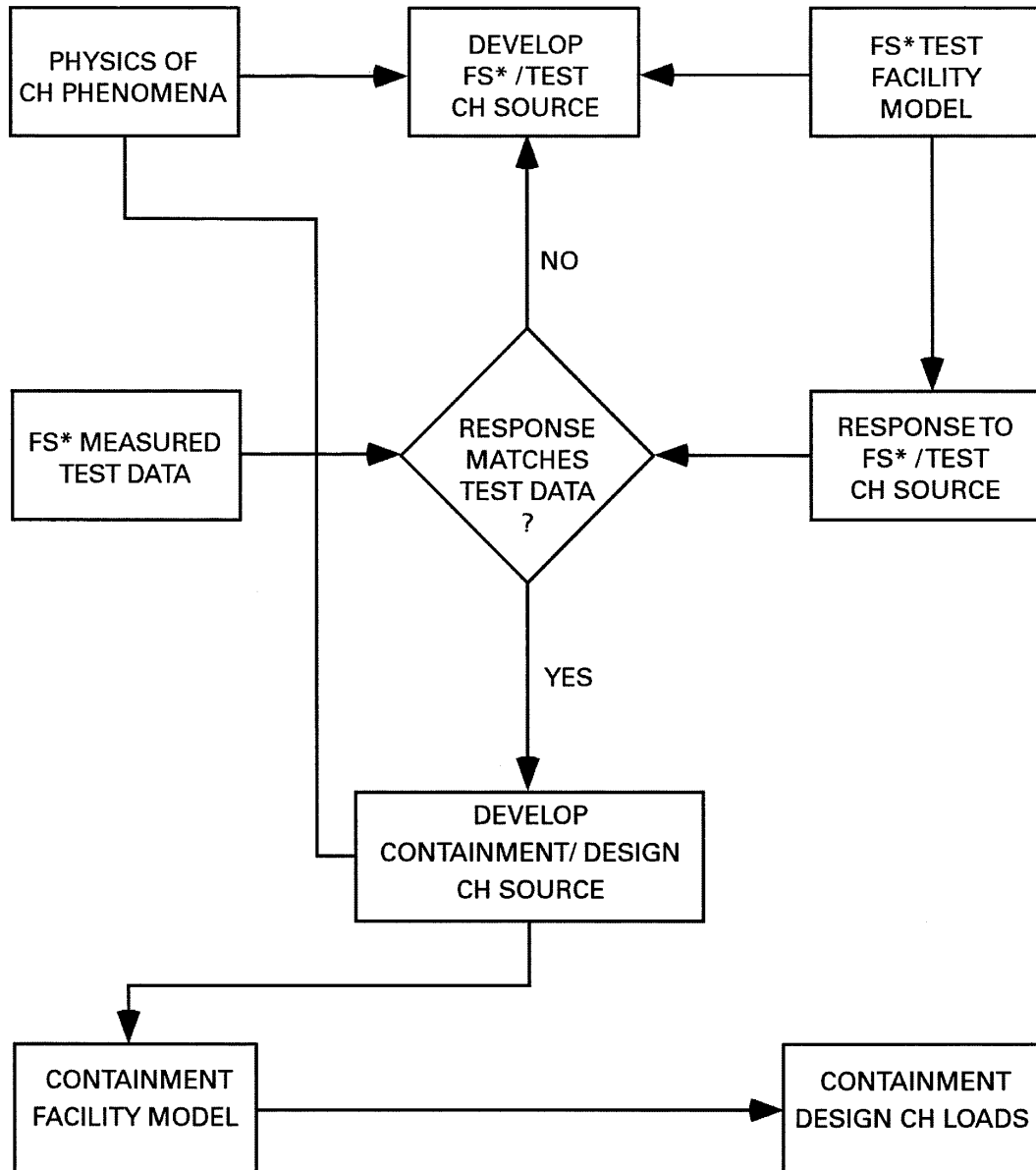


Figure 3B-4. Containment CH Source Load Methodology

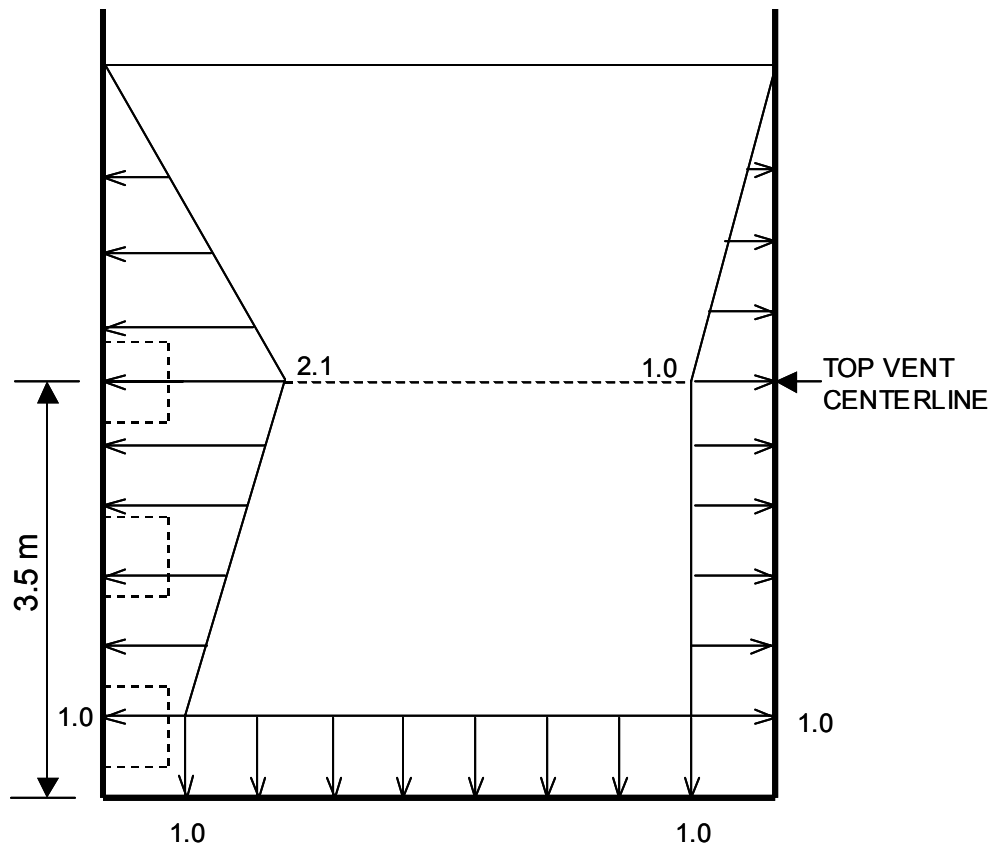


Figure 3B-5. Spatial Load Distribution for CH

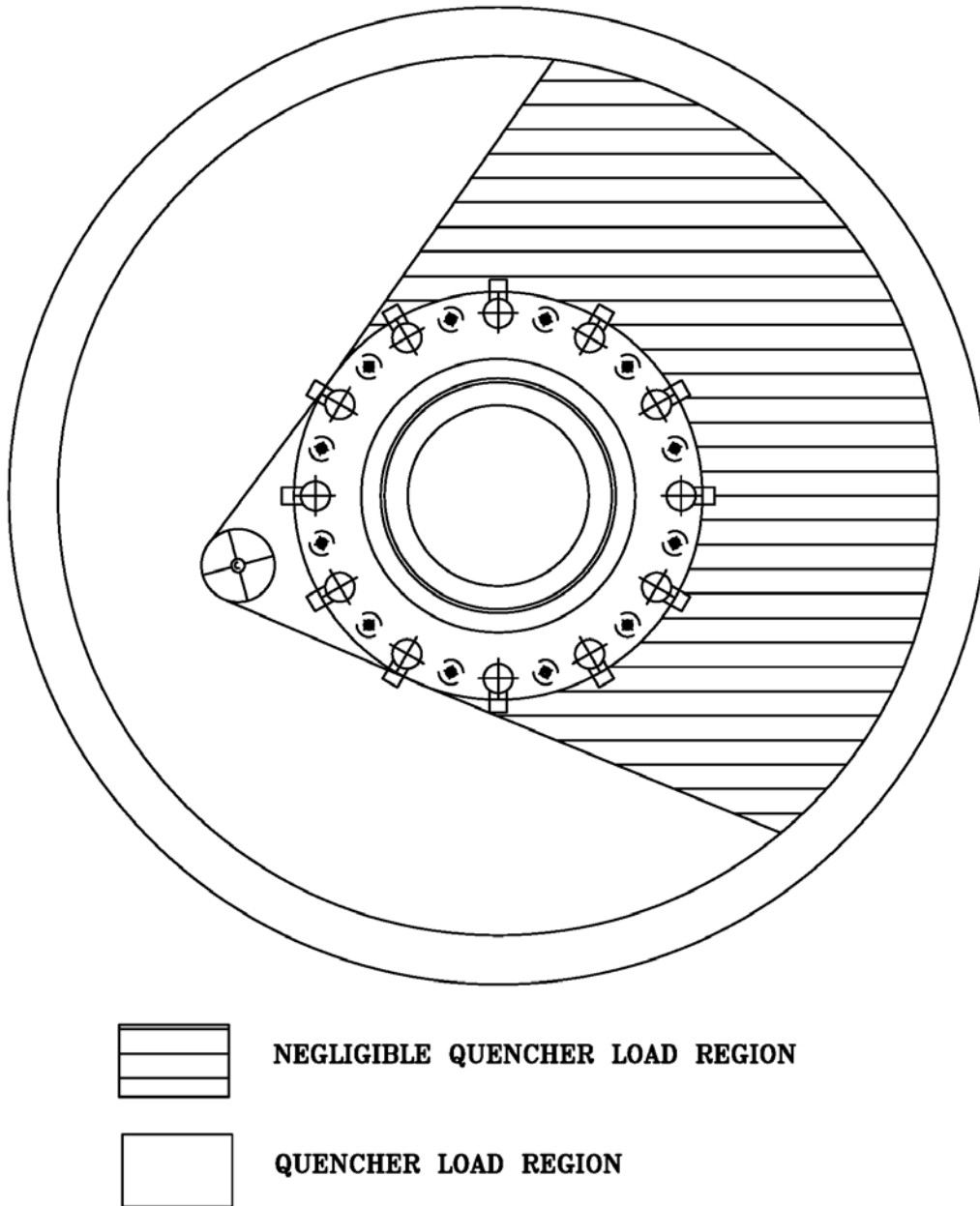


Figure 3B-6. Load Distribution Region of Influence

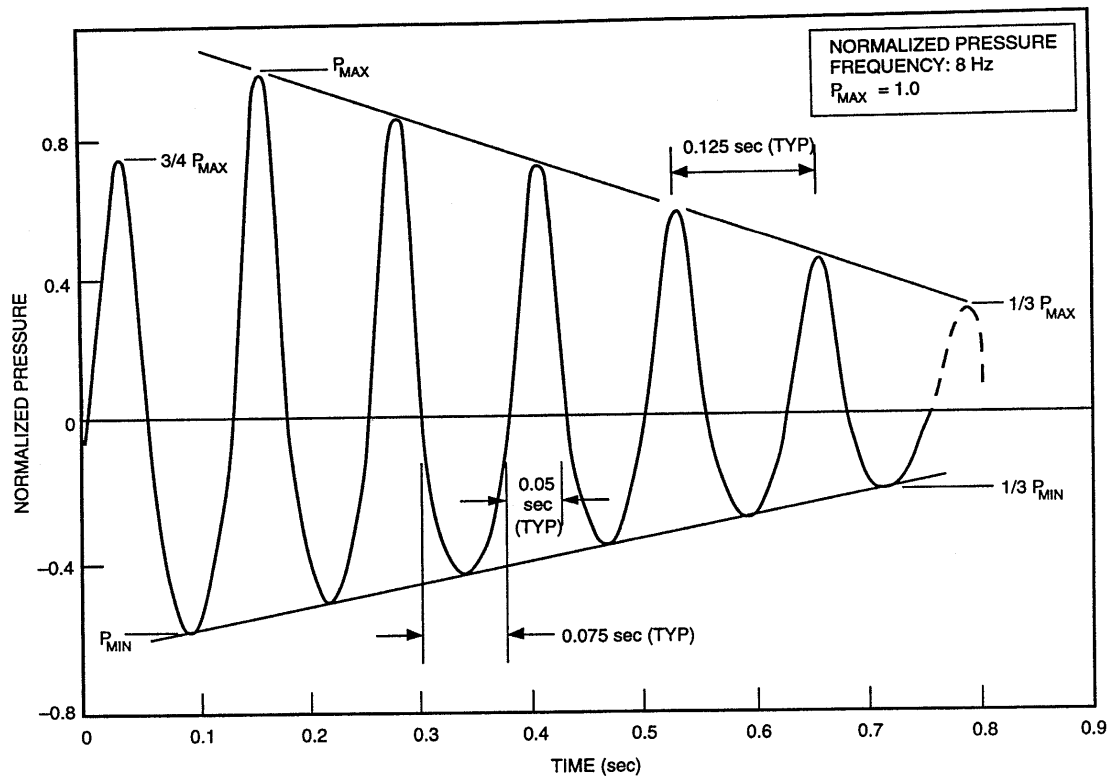


Figure 3B-7. Normalized Quencher Bubble Pressure Time History (Ideal)

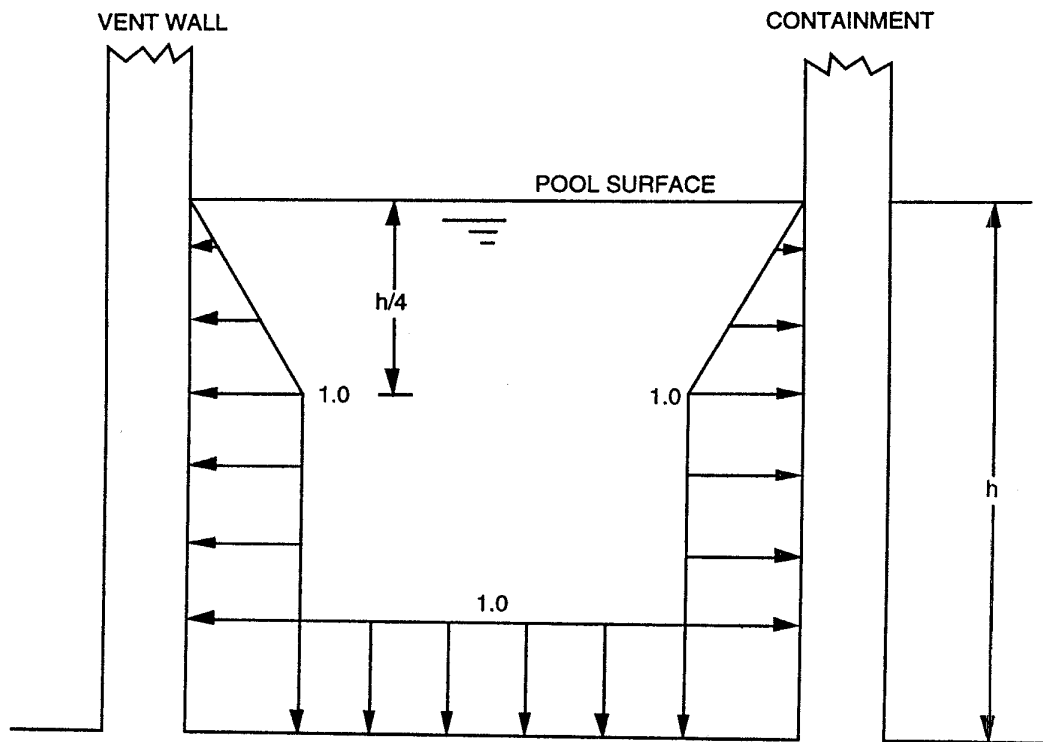
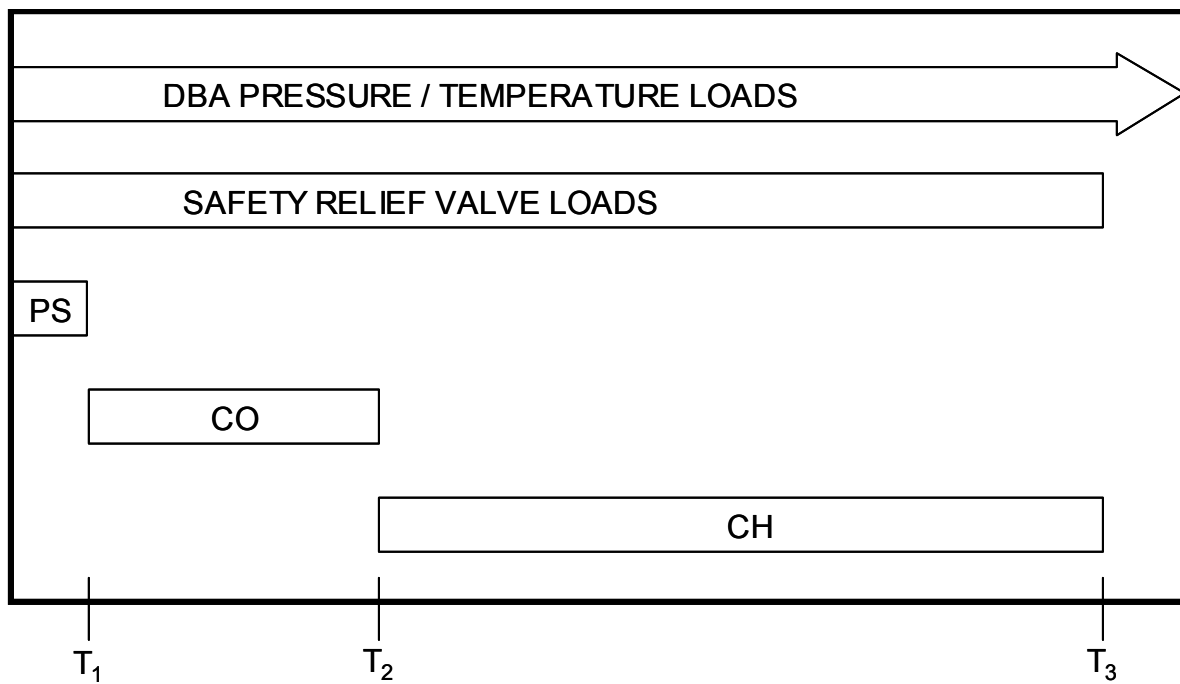


Figure 3B-8. SRV Boundary Pressure Spatial Distribution, Normalized to Maximum Pressure Amplitude



	T_1	T_2	T_3
MSLB	3 sec	500 sec	72 hr
FWLB	TBD	TBD	72 hr

Figure 3B-9. Time Relationship for a DBA-LOCA

3C. COMPUTER PROGRAMS USED IN THE DESIGN AND ANALYSIS OF SEISMIC CATEGORY I STRUCTURES

3C.1 INTRODUCTION

The following Seismic Category I structures and their foundations of the Nuclear Island are analyzed and/or designed using the computer programs described in this appendix:

- (1) Concrete Containment Structure
- (2) Reactor Building (RB)
- (3) Fuel Building (FB)
- (4) Control Building (CB)

3C.2 STATIC AND DYNAMIC STRUCTURAL ANALYSIS PROGRAM (NASTRAN)

3C.2.1 Description

NASTRAN is a general purpose computer program for finite element analysis; its capabilities include: static response to concentrated and distributed loads, to thermal expansion and to enforced displacements; dynamic response to transient loads, to steady-state sinusoidal loads, and to random excitation; and determination of eigenvalues for use in vibration analysis.

3C.2.2 Validation

The MSC.Software Corporation of Santa Ana, California developed NASTRAN. The program validation documentation is available at MSC.Software Corporation.

3C.2.3 Extent of Application

This program is used for the static and eigenvalue analysis of the concrete containment, RB, FB, and CB. This program is also used for the static and dynamic analysis of the Drywell Head and containment internal structures.

3C.3 ABAQUS AND ANACAP-U

3C.3.1 Description

ABAQUS/Standard is a widely used, commercially available finite-element program that has a broad range of analysis capabilities. Implicit formulations for steady state and transient thermal solutions and for static stress analyses were employed using 3-dimensional models of continuum concrete elements, truss-type reinforcement sub-elements, and plate and membrane elements for liners and other steel components. Classical Von Mises plasticity models, as well as strength degradation with elevated temperature, for the steel material is invoked for the nonlinear analyses. The ANACAP-U software is an advanced concrete constitutive model that is coupled to the ABAQUS software as a user subroutine. The ANACAP-U concrete material model provides formulations for concrete cracking under tensile and shear loads and post-cracking shear stiffness and shear capacity as a function of crack width and shear deformations, with

yielding and strain softening (crushing) under large compressive loads. Degradation in modulus and strength with increasing temperatures is also included for the concrete model.

3C.3.2 Validation

ABAQUS is written and maintained by ABAQUS, Inc. of Providence R.I., (formerly Hibbitt, Karlssen, and Sorensen, Inc). The program has an extensive library of example problems that are used for verification and validation testing. Additional descriptions and information on the quality controls can be found on the ABAQUS web site, (www.abaqus.com). The ANACAP-U concrete material model for use with the ABAQUS program is written and maintained by ANATECH Corp, San Diego, CA. This software has been extensively verified with test problems and also validated against large-scale test results for the performance of reinforced concrete structures

3C.3.3 Extent of Application

The ABAQUS/ANACAP-U software coupling is used for nonlinear analyses for the structural performance of the reinforced concrete containment under LOCA thermal conditions

3C.4 CONCRETE ELEMENT CRACKING ANALYSIS PROGRAM (SSDP-2D)

3C.4.1 Description

SSDP-2D computes stresses in a thick concrete element under thermal and/or non-thermal (such as dead load, service loads) loads, considering effects of concrete cracking. The element represents a section of a concrete shell or slab, and may include two layers of orthogonal reinforcing. It does not include the effect of the liner.

SSDP-2D calculates the stresses considering two-dimensional equilibrium conditions of section forces with the existence of thermal loads and concrete cracking. It is assumed in the code that concrete has an anisotropic property and that cracked concrete does not carry tensile forces. Concrete is assumed to have no tensile strength.

3C.4.2 Validation

SSDP-2D is written and maintained by Shimizu Corporation of Tokyo, Japan. Program validation documentation is available at Shimizu Corporation.

3C.4.3 Extent of Application

This program is used for the analysis of the concrete containment, RB, FB, and CB.

3C.1 HEAT TRANSFER ANALYSIS PROGRAM (TEMCOM2)

3C.4.4 Description

TEMCOM2 solves a temperature distribution in a two-dimensional model based on a finite differential method. It performs analyses under the following conditions.

- Element: triangle and quadrilateral elements
- Surface heat transfer: convection and radiation

- Temperature condition: steady-state and transient temperature conditions

3C.4.5 Validation

TEMCOM2 is written and maintained by Shimizu Corporation of Tokyo, Japan. Program validation documentation is available at Shimizu Corporation.

3C.4.6 Extent of Application

This program is used for the transient heat transfer analysis of the concrete containment and RB.

3C.5 STATIC AND DYNAMIC STRUCTURAL ANALYSIS SYSTEMS: ANSYS

3C.5.1 Description

ANSYS is a large, finite element program for a broad range of analyses types. The structural analysis capabilities include material and geometric non-linear analysis, static analysis and a variety of dynamic analyses.

The element for a concrete cracking analysis allows a full non-linear analysis of reinforced concrete with cracking and crushing of concrete.

3C.5.2 Validation

ANSYS is maintained by ANSYS INC., located at 275 Technology Drive, Canonsburg, PA, 15317

3C.5.3 Extent of Application

This program is used for the containment dynamic analysis of containment loads, for the containment ultimate capacity analyses and for containment seismic margin analysis.

3C.6 SOIL-STRUCTURE INTERACTION

3C.6.1 Dynamic Soil-Structure Interaction Analysis Program—DAC3N

3C.6.1.1 Description

DAC3N is a three-dimensional dynamic analysis program, which is used for the seismic response analysis of building considering soil-structure interaction. The response analysis is performed using the time history method solved by direct integration, Newmark's beta method. Eigenvalue analysis is performed using Subspace method.

In the DAC3N, soil-structure interaction system is modeled by the combination of soil spring and damping coefficient. Spring and damping coefficient are determined as frequency independent values, which fit the frequency dependent real and imaginary parts of soil spring obtained by the theoretical methods, such as vibration admittance theory based on three-dimensional wave propagation theory for uniform half space soil.

As mass elements, lumped mass and consistent mass are available. Structural elements, such as beam, truss, spring, damper, direct input matrix are available in this program.

This program also possesses nonlinear analysis functions.

3C.6.1.2 Validation

DAC3N is coded and maintained by Shimizu Corporation of Tokyo, Japan. Program validation documentation is available at Shimizu Corporation.

3C.6.1.3 Extent of Application

This program is used to perform the soil-structure interaction analysis required to obtain enveloped seismic design loads of the concrete containment, RB, FB and CB.

3D. COMPUTER PROGRAMS USED IN THE DESIGN OF COMPONENTS, EQUIPMENT AND Structures

3D.1 INTRODUCTION

As discussed in Subsection 3.9.1.2, this appendix describes the major computer programs used in the analysis of the safety-related components, equipment and structures. The quality of the programs and the computed results is controlled. The programs are verified for their application by appropriate methods, such as hand calculations, or comparison with results from similar programs, experimental tests, or published literature, including analytical results or numerical results to the benchmark problems.

3D.2 FINE MOTION CONTROL ROD DRIVE

3D.2.1 Fine Motion Control Rod Drive - FMCRD01

The FMCRD01A program is used to obtain scram performance data for various inputs to the fine motion control rod drive (FMCRD) stress analysis for both code and non-code parts. The use of this program is addressed in Subsection 3.9.1.3.2. Experimental data on pressure drops, friction factors, effects of fuel channel detection, etc., are used in the development and perfecting of this code. Internal drive pressures and temperatures used in the stress analysis are also determined during actual testing of the prototype FMCRD.

3D.2.2 Structural Analysis Programs

Structural analysis programs, such as NASTRO4V and ANSYS, that are mentioned in Subsections 3D.3 and 3D.4.9 are used in the analysis of the FMCRD.

3D.3 REACTOR PRESSURE VESSEL AND INTERNALS

Computer programs used in the analysis of the reactor pressure vessel, core support structures, and other safety class reactor internals: are described in Subsection 4.1.4.

3D.4 PIPING

3D.4.1 Piping Analysis Program - PISYS

PISYS is a computer code for analyzing piping systems subjected to both static and dynamic piping loads. Finite element models of a piping system formed by assembling stiffness matrices represent standard piping components. The piping elements are connected to each other via nodes called pipe joints. It is through these joints that the model interacts with the environment, and loading of the piping system becomes possible. PISYS is based on the linear elastic analysis in which the resultant deformations, forces, moments and accelerations at each joint are proportional to the loading and the superposition of loading is valid.

PISYS has a full range of static dynamic load analysis options. Static analysis includes dead weight, uniformly distributed weight, thermal expansion, externally applied forces, moments, imposed displacements and differential support movement (pseudo-static load case). Dynamic analysis includes mode shape extraction, response spectrum analysis, and time-history analysis by modal combination or direct integration. In the response spectrum analysis [i.e., uniform

support motion response spectrum analysis (USMA) or independent support motion response spectrum analysis (ISMA)], the user may request modal response combination in accordance with Regulatory Guide 1.92. In the ground motion (uniform motion) or independent support time history analysis, the normal mode solution procedure is selected. In analysis involving time varying nodal loads, the step-by-step direct integration method is used.

The PISYS program has been benchmarked against NRC piping models. The results are documented in Reference 3D-1 for mode shapes and USMA options. The ISMA option has been validated against NUREG/CR-1677 (Reference 3D-2).

3D.4.2 Component Analysis - ANSI7

ANSI7 is a computer code for calculating stresses and cumulative usage factors for Class 1, 2 and 3 piping components in accordance with articles NB, NC and ND-3650 of ASME Code Section III. ANSI7 is also used to combine loads and calculate combined service levels A, B, C and D loads on piping supports and pipe-mounted equipment.

3D.4.3 Area Reinforcement - NOZAR

The Nozzle Area Reinforcement (NOZAR) computer program performs an analysis of the required reinforcement area for openings. The calculations performed by NOZAR are in accordance with the rules of ASME Code Section III, 1974 edition.

3D.4.4 Dynamic Forcing Functions

3D.4.4.1 Relief Valve Discharge Pipe Forces Computer Program - RVFOR

The relief valve discharge pipe connects the pressure-relief valve to the suppression pool. When the valve is opened, the transient fluid flow causes time-dependent forces to develop on the pipe wall. This computer program computes the transient fluid mechanics and the resultant pipe forces using the method of characteristics.

3D.4.4.2 Turbine Stop Valve Closure - TSFOR

The TSFOR program computes the time-history forcing function in the main steam piping due to turbine stop valve closure. The program utilizes the method of characteristics to compute fluid momentum and pressure loads at each change in pipe section or direction.

3D.4.4.3 Hydraulic Transients-RELAP5/Mod 3.3

The RELAP5 computer code is a light water reactor transient analysis code developed for the U.S. Nuclear Regulatory Commission for use in rulemaking, licensing audit calculations, evaluation of operator guidelines, and as a basis for nuclear plant analyses. Specific applications of this capability have included simulations of transients such as loss of feed-water, loss of offsite power, station blackout, and turbine trip. RELAP5 is a highly generic code that, in addition to calculating the behavior of a reactor coolant system during a transient, can be used for simulating a wide variety of hydraulic and thermal transients in both nuclear and non-nuclear systems involving mixtures of steam, water, non-condensables, and solutes.

The RELAP5 hydrodynamic model is a one-dimensional, transient, two-fluid model for flow of a two-phase steam-water mixture that can contain non-condensable components in the steam phase and/or a soluble component in the water phase.

The two-fluid equations of motion (mass, momentum, and energy conservation for each phase) that are used as the basis for the RELAP5 hydrodynamic model are formulated in terms of volume and time-averaged parameters of the flow. Phenomena that depend upon transverse gradients, such as friction and heat transfer, are formulated in terms of bulk properties using empirical transfer coefficient formulations.

On the basis of geometry input data, and thermohydraulic initial conditions (pressure, temperature, fluid), the code integrates fluid equations in order to calculate time-histories of pressure, temperature, forces in the different nodes and sections of the piping network.

3D.4.4.4 Subcompartment Pressurization - Contain 2.0

The CONTAIN code is an analysis tool for predicting the physical, chemical, and radiological conditions inside the containment and connected buildings of a nuclear reactor in the event of an accident. CONTAIN was developed at Sandia National Laboratories under the sponsorship of the US Nuclear Regulatory Commission (USNRC) for analyzing containment phenomena under severe accident and design basis accident conditions. It is designed to and has capability to predict the thermal-hydraulic response inside the containment in the event of an accident.

CONTAIN is a highly flexible and modular code that can run both everything from quite simple to highly complex problems.

3D.4.5 Integral Attachment - LUGST

The computer program LUGST evaluates the stress in the pipe wall that is produced by loads applied to the integral attachments. The program is based on Welding Research Council Bulletin 198.

3D.4.6 Response Spectra Generation

3D.4.6.1 ERSIN Computer Program

ERSIN is a computer code used to generate response spectra for pipe-mounted and floor-mounted equipment. ERSIN provides direct generation of local or global acceleration response spectra.

3D.4.6.2 RINEX Computer Program

RINEX is a computer code used to interpolate and extrapolate amplified response spectra used in the response spectrum method of dynamic analysis. RINEX is also used to generate response spectra with nonconstant model damping. The non-constant model damping analysis option can calculate spectral acceleration at the discrete eigenvalues of a dynamic system using either the strain energy weighted modal damping or the ASME Code Class N-411-1 damping values.

3D.4.7 Piping Dynamic Analysis Program - PDA

PDA is a computer program used to determine the response of a pipe subjected to the thrust force occurring after a pipe break. It also is used to determine the pipe whip restraint design and capacity.

The program treats the situation in terms of generic pipe break configuration, which involves a straight, uniform pipe fixed (or pinned) at one end and subjected to a time-dependent thrust force at the other end. A typical restraint used to reduce the resulting deformation is also included at a location between the two ends. Nonlinear and time-independent stress-strain relations are used to model the pipe and the restraint. Using a plastic hinge concept, bending of the pipe is assumed to occur only at the fixed (or pinned) end and at the location supported by the restraint.

Effects of pipe shear deflection are considered negligible. The pipe-bending moment-deflection (or rotation) relation used for these locations is obtained from a static nonlinear cantilever beam analysis. Using moment angular rotation relations, nonlinear equations of motion are formulated using energy considerations, and the equations are numerically integrated in small time steps to yield the time-history of the pipe motion.

3D.4.8 Thermal Transient Program - LION

The LION program is used to compute radial and axial thermal gradients in piping. The program calculates a time-history of vT_1 , vT_2 , T_a , and T_b (defined in ASME Code Section III, Subsection NB) for uniform and tapered pipe wall thickness.

3D.4.9 Engineering Analysis System - ANSYS05

The ANSYS05 computer program is a finite element large-scale general-purpose program for the solution of several classes of engineering analysis problems. Analysis capabilities include static and dynamic, plastic, creep and swelling, small and large deflections, and other applications like thermal analysis, material non-linearities, contact analysis, etc.

This program is used to perform non-linear analysis of piping systems for time varying displacements and forces due to postulated pipe breaks. Also, this program is used to perform structural analysis of pressure retaining components and civil structures against the loads and events postulated in the design specifications.

3D.4.10 Piping Analysis Program - EZPYP

EZPYP links the ANSI-7 and PISYS program together. The EZPYP program can be used to run several PISYS cases by making user-specified changes to a basic PISYS pipe model. By controlling files and PISYS runs, the EZPYP program gives the analyst the capability to perform a complete piping analysis in one computer run.

3D.4.11 Differential Displacement Program - DISPL

The DISPL program provides differential movements at each piping attachment point based on building modal displacements.

3D.5 PUMPS AND MOTORS

Following are the computer programs used in the dynamic analysis to assure the structural and functional integrity of the ESBWR pump and motor assemblies.

3D.5.1 Structural Analysis Program - SAP4G07

SAP4G07 is used to analyze the structural and functional integrity of the pump/motor systems. This program is also identified in Subsections 4.1.4.1.2, 3D.3 and 3D.6. This is a general structural analysis program for static and dynamic analysis of linear elastic complex structures. The finite-element displacement method is used to solve the displacement and stresses of each element of the structure. The structure can be composed of unlimited number of three-dimensional truss, beam, plate, shell, solid, plane strain-plane stress and spring elements that are axisymmetric. The program can treat thermal and various forms of mechanical loading. The dynamic analysis includes mode superposition, time-history, and response spectrum analysis. Seismic loading and time-dependent pressure can be treated. The program is versatile and efficient in analyzing large and complex structural systems. The output contains displacement of each nodal point as well as stresses at the surface of each element.

3D.5.2 Effects of Flange Joint Connections - FTFLG01

The flange joints connecting the pump bowl casings are analyzed using the FTFLG01 program. This program uses the local forces and moments determined by SAP4G07 to perform flat flange calculations in accordance with the rules set forth in the ASME Code, Section III, Appendices XI and L.

3D.6 HEAT EXCHANGERS

The following computer programs are used in dynamic and static analyses to determine the structural and functional integrity of ESBWR heat exchangers.

3D.6.1 Structural Analysis Program - SAP4G07

The structural integrity of the heat exchanger is evaluated using SAP4G07. This program is described in Subsection 3D.5.1.

3D.6.2 Calculation of Shell Attachment Parameters and Coefficients - BILDR01

BILDR01 is used to calculate the shell attachment parameters and coefficients used in the stress analysis of the support to shell junction. The method per Welding Research Council Bulletin 107 is implemented in BILDR01 to calculate local membrane stress due to the support reaction loads on the heat exchanger shell.

3D.7 REFERENCES

- 3D-1 General Electric Co., "PISYS Analysis of NRC Benchmark Problems," NEDO-24210, August 1979.
- 3D-2 USNRC, "Piping Benchmark Problems Dynamic Analysis Independent Support Motion Response Spectrum Method," NUREG/CR-1677, August 1985.

3E. GUIDELINES FOR LEAK BEFORE BREAK APPLICATION

3E.1 INTRODUCTION

As discussed in Subsection 3.6.3, this appendix provides detailed guidelines for addressing Leak Before Break (LBB) for specific piping systems. Also included in this appendix are the fracture mechanics properties of ESBWR piping materials and analysis methods, including the leak rate calculation methods.

Piping qualified by LBB is excluded from the non-mechanistic postulation requirements of a Double Ended Guillotine Break (DEGB) specified in Subsection 3.6.3. The LBB qualification means that the throughwall flaw lengths that are detectable by leakage monitoring systems (Subsection 5.2.5) are significantly smaller than the flaw lengths that could lead to pipe rupture or instability.

The fracture mechanics properties aspects required for evaluation in accordance with Subsection 3.6.3 are addressed in Section 3E.2. The fracture mechanics techniques and methods for the determination of critical flaw lengths and evaluation of flaw stability are described in Section 3E.3. The determination of flaw lengths for detectable leakages with margin is explained in Section 3E.4. A brief discussion on the leak detection capabilities is presented in Section 3E.5.

Material selection and the deterministic LBB evaluation procedure are discussed in this section.

3E.1.1 Material Selection Guidelines

The LBB approach is applicable to piping systems for which the materials meet the following criteria:

- low probability of failure from the effects of corrosion (e.g., intergranular stress corrosion cracking); and
- adequate margin before susceptibility to cleavage type fracture over the full range of systems operating temperatures where pipe rupture could have significant consequences.

The ESBWR plant design specifies use of austenitic stainless steel piping made of material (e.g., nuclear grade or low carbon type) that is recognized as resistant to Inter-Granular Stress Corrosion Cracking (IGSCC). The carbon steel or ferritic steels specified for the reactor pressure boundary are described in Subsection 3E.2.2. These steels are assured to have adequate toughness to preclude a fracture at operating temperatures. A COL applicant is expected to supply a detailed justification in the LBB evaluation report considering system temperature, fluid velocity and environmental conditions.

3E.1.2 Deterministic Evaluation Procedure

The following deterministic analysis and evaluation is performed as an NRC-approved method to justify applicability of the LBB concept.

- Use the fracture mechanics and the leak rate computational methods that are accepted by the NRC staff, or are demonstrated accurate with respect to other acceptable computational procedures or with experimental data.

- Identify the types of materials and materials specifications used for base metal, weldments and safe ends, and provide the materials properties including toughness and tensile data, long-term effects such as thermal aging, and other limitations.
- Specify the type and magnitude of the loads applied (forces, bending and torsional moments), their source(s) and method of combination. For each pipe size in the functional system, identify the location(s), which have the least favorable combination of stress and material properties for base metal, weldments and safe ends.
- Postulate a throughwall flaw at the location(s) specified above. The size of the flaw should be large enough so that the leakage is assured detection with sufficient margin using the installed leak detection capability when pipes are subjected to normal operating loads. If auxiliary leak detection systems are relied on, they should be described. For the estimation of leakage, the normal operating loads (i.e., deadweight, thermal expansion, and pressure) are to be combined based on the algebraic sum of individual values.

Using fracture mechanics stability analysis or limit load analysis described below, and normal plus Safe Shutdown Earthquake (SSE) loads, determine the critical crack size for the postulated throughwall crack. Determine crack size margin by comparing the selected leakage detection size crack to the critical crack size. Demonstrate that there is a margin of 2 between the leakage detection and critical crack sizes. The same load combination method selected below is used to determine the critical crack size.

- Determine margin in terms of applied loads by a crack stability analysis. Demonstrate that the leakage detection size cracks does not experience unstable crack growth if 1.4 times the normal plus SSE loads are applied. Demonstrate that crack growth is stable and the final crack is limited such that a double-ended pipe break should not occur. The deadweight, thermal expansion, pressure, SSE (inertial), and Seismic Anchor Motion (SAM) loads are combined based on the same method used for the primary stress evaluation by the ASME Code. The SSE (inertial) and SAM loads are combined by Square Root of the Sum of the Squares (SRSS) method.
- The piping material toughness (J-Resistance curves) and tensile (stress-strain curves) properties are determined at temperatures near the upper range of normal plant operation.
- The specimen used to generate J-Resistance (J-R) curves is assured large enough to provide crack extensions up to an amount consistent with J/T condition determined by analysis for the application. Because practical specimen size limitations exist, the ability to obtain the desired amount of experimental crack extension may be restricted. In this case, extrapolation techniques are used as described in NUREG-1061, Volume 3, or in NUREG/CR-4575. Other techniques can be used if adequately justified.
- The stress-strain curves are obtained over the range from the preoperational limit to maximum load.
- Preferably, the materials tests should be conducted using archival materials for the pipe being evaluated. If archival material is not available, plant specific or industry wide generic material databases are assembled and used to define the required material tensile and toughness properties. Test material includes base and weld metals.

- To provide an acceptable level of reliability, generic databases are reasonable lower bounds for compatible sets of material tensile and toughness properties associated with materials at the plant. To assure that the plant specific generic data base is adequate, a determination is made to demonstrate that the generic data base represents the range of plant materials to be evaluated. This determination is based on a comparison of the plant material properties identified above with those of the materials used to develop the generic database. The number of material heats and weld procedures tested are adequate to cover the strength and toughness range of the actual plant materials. Reasonable lower bound tensile and toughness properties from the plant specific generic data base are to be used for the stability analysis of individual materials, unless otherwise justified.

Industry generic data bases are reviewed to provide a reasonable lower bound for the population of material tensile and toughness properties associated with any individual specification (e.g., A106, Grade B), material type (e.g., austenitic steel) or welding procedures.

The number of material heats and weld procedures tested should be adequate to cover the range of the strength and tensile properties expected for specific material specifications or types. Reasonable lower bound tensile and toughness properties from the industry generic data base are used for the stability analysis of individual materials.

If the data are being developed from an archival heat of material, three stress-strain curves and three J-Resistance curves from the one heat of material is sufficient. The tests should be conducted at temperatures near that upper range of normal plant operation. Tests should also be conducted at a lower temperature, which may represent a plant condition (e.g., hot standby) where pipe break would present safety concerns similar to normal operation. These tests are intended only to determine if there is any significant dependence of toughness on temperature over the temperature range of interest. The lower toughness should be used in the fracture mechanics evaluation. One J-R curve and one stress-strain curve for one base metal and weld metal are considered adequate to determine temperature dependence.

- There are certain limitations that currently preclude generic use of limit load analyses to evaluate leak-before-break conditions deterministically. However, a modified limit-load analysis can be used for austenitic stainless steel piping to demonstrate acceptable margins as described in Subsection 3E.3.3.

3E.2 MATERIAL FRACTURE TOUGHNESS CHARACTERIZATION

This Subsection describes the fracture toughness properties and flow stress evaluation for the ferritic and austenitic stainless steel materials used in ESBWR plant piping, as required for evaluation according to Subsection 3E.1.2.

3E.2.1 Fracture Toughness Characterization

When the Elastic-Plastic Fracture Mechanics (EPFM) methodology or the J-T methodology is used to evaluate the leak-before-break conditions with postulated throughwall flaws, the material toughness property is characterized in the form of J-integral Resistance curve (or J-R curve) (References 3E-1, 3E-2 and 3E-3). The J-R curve, schematically shown in Figure 3E-1, represents the material's resistance to crack extension. The onset of crack extension is assumed to occur at a critical value of J. Where the plane strain conditions are satisfied, initiation J is denoted by J_{IC} . Plane strain crack conditions, achieved in test specimen by side grooving, generally provide a lower bound behavior for material resistance to stable crack growth.

Once the crack begins to extend, the increase of J with crack growth is measured in terms of slope or the nondimensional tearing modulus, T, expressed as:

$$T = \frac{E}{(\sigma_f)^2} \cdot \frac{dJ}{da} \quad (3E-1)$$

The flow stress, σ_f , is a function of the yield and ultimate strength, and E is the elastic modulus. Generally, σ_f is assumed as the average of the yield and ultimate strength. The slope of the material J-R curve is a function of crack extension Δa . Generally, the slope decreases with crack extension thereby giving a convex upward appearance to the material J-R curve in Figure 3E-1.

To evaluate the stability of crack growth, it is convenient to represent the material J-R curve in the J-T space as shown in Figure 3E-1. The resulting curve is labeled as J-T material. Crack instability is predicted at the intersection point of the J/T material and J/T applied curves.

The crack growth variably involves some elastic unloading and distinctly nonproportional plastic deformation near the crack tip. J-integral is based on the deformation theory of plasticity (References 3E-4 and 3E-5), which inadequately models both of these aspects of plastic behavior. In order to use J-integral to characterize crack growth (i.e., to assure J-controlled crack growth), the following sufficiency condition, in terms of a nondimensional parameter proposed by Hutchinson and Paris (Reference 3E-6), is used:

$$\omega = \frac{b}{j} \cdot \frac{dJ}{da} \gg 1 \quad (3E-2)$$

where b is the remaining ligament. Reference 3E-7 suggests that $\omega > 10$ would satisfy the J-controlled growth requirements. However, if the requirements of this criteria are strictly followed, the amount of crack growth allowed would be very small in most test specimen geometries. Use of such a material J-R curve in J/T evaluation would result in grossly underpredicting the instability loads for large diameter pipes where considerable stable crack

growth is expected to occur before reaching the instability point. To overcome this difficulty, Ernst (Reference 3E-8) proposed a modified J-integral J_{mod} , which was shown to be effective even when limits on ω were grossly violated. The Ernst correction essentially factors in the effect of crack extension in the calculated value of J. This correction can be determined experimentally by measuring the usual parameters: load, displacement, and crack length.

The definition of J_{mod} is

$$J_{\text{mod}} = J - \int_{a_0}^a \left| \frac{\partial}{\partial a} (J - G) \right| \frac{da}{\delta_{\text{pl}}} \quad (3E-3)$$

where:

- J = is based on deformation theory of plasticity;
- G = is the linear elastic Griffith energy release rate of elastic J, J_{el} ;
- δ_{pl} = is the nonlinear part of the load-point displacement (or simply the total minus the elastic displacement); and
- a_0, a = are the initial and current crack length, respectively.

For the particular case of the compact tension specimen geometry, the preceding equation and the corresponding rate take the form:

$$J_{\text{mod}} = J + \int_{a_0}^a \gamma \cdot \frac{J_{\text{pl}}}{b} \cdot da \quad (3E-4)$$

where J_{pl} is the nonlinear part of the deformation theory J, b is the remaining ligament and γ is

$$\gamma = \left(1 + 0.76 \frac{b}{W} \right) \quad (3E-5)$$

Consequently, the modified material tearing modulus T_{mod} can be defined as:

$$T_{\text{mod}} = T_{\text{mat}} + \frac{E}{(\sigma_f)^2} \left(\frac{\gamma}{b} \cdot J_{\text{pl}} \right) \quad (3E-6)$$

Because in most of the test J-R curves the $\omega > 10$ limit was violated, all of the material J-T data were recalculated in the $J_{\text{mod}}, T_{\text{mod}}$ format. The $J_{\text{mod}}, T_{\text{mod}}$ calculations were performed up to crack extension of $a = 10\%$ of the original ligament in the test specimen. The J-T curves were then extrapolated to larger J values using the method recommended in NUREG 1061, Vol. 3 (Reference 3E-9). The $J_{\text{mod}} - T_{\text{mod}}$ approach is used in this appendix for illustrative purposes. It should be adopted if justified based on its acceptability by the technical literature. A J_D – approach is another more justifiable approach.

3E.2.2 Carbon Steels and Associated Welds

The carbon steels used in the ESBWR reactor coolant pressure boundary piping are SA 106 Gr. B, SA 333 Gr. 6, and SA 672 Gr. C70. The first specification covers seamless pipe and the second one pertains to both seamless and seam-welded pipe. The last one pertains to seam-welded pipe for which plate stock is specified as SA 516. Gr. 70. The corresponding material specifications used for carbon steel flanges, fittings and forgings are equivalent to the piping specifications.

While the chemical composition requirements for a pipe per SA 106 Gr. B and SA 333 Gr. 6 are identical, the latter is subjected to two additional requirements: (1) a normalizing heat treatment which refines the grain structure and (2) a Charpy test at -50°F with a specified minimum absorbed energy of 13 ft-lb. The electrodes and filler metal requirements for welding carbon steel to carbon or low alloy steel are as specified in Table 3E-1.

A comprehensive test program was undertaken at GE to characterize the carbon steel base and weld material toughness properties. The next section describes the scope and the results of this program.

3E.2.2.1 Fracture Toughness Test Program

The test program consisted of generating true stress-true strain curves, J-Resistance curves and the Charpy V-notch tests. Two materials were selected: (1) SA333 Gr. 6, 16-in. diameter Schedule 80 pipe and (2) SA516, Gr. 70, 1-1/4 in. thickness plate. Table 3E-2 shows the chemical composition and mechanical property test information provided by the material supplier. The materials were purchased to the same specifications as those to be used in the ESBWR applications.

To produce a circumferential butt weld, the pipe was cut in two pieces along a circumferential plane and welded back using the shielded metal arc process. The weld prep was a single V design with a backing ring. The preheat temperature was 200°F.

The plate material was cut along the longitudinal axis and welded back using the submerged arc weld (SAW) process. The weld prep was of a single V type with one side as vertical and the other side at 45 degrees. A backing plate was used during the welding with a clearance of 1/4 inch at the bottom of the V. The interpass temperature was maintained at less than 500°F.

Both the plate and the pipe welds were x-rayed according to Code (Reference 3E-10) requirements and were found to be satisfactory.

It is well-known that carbon steel base materials show considerable anisotropy in fracture toughness properties. The toughness depends on the orientation and direction of propagation of the crack in relation to the principal direction of mechanical working or grain flow. Thus, the selection of proper orientation of Charpy and J-R curve test specimen is important. Figure 3E-2 shows the orientation code for rolled plate and pipe specimen as given in ASTM Standard E399 (Reference 3E-11). Because a throughwall circumferential crack configuration is of most interest from the Double Ended Guillotine Break (DEGB) point of view, the L-T specimen in a plate and the L-C specimen in a pipe provide the appropriate toughness properties for that case. On the other hand, T-L and C-L specimens are appropriate for the axial flaw case.

Charpy test data are reviewed first because they provide a qualitative measure of the fracture toughness.

Charpy Tests

The absorbed energy or its complement, the lateral expansion measured during a Charpy V-notch test provides a qualitative measure of the material toughness. For example, in the case of austenitic stainless steel flux weldments, the observed lower Charpy energy relative to the base metal was consistent with the similar trend observed in the J-Resistance curves. The Charpy

tests in this program were used as preliminary indicators of relative toughness of welds, heat-affected zones (HAZs) and the base metal.

The carbon steel base materials exhibit considerable anisotropy in the Charpy energy as illustrated by Figure 3E-3 from Reference 3E-12. This anisotropy is associated with development of grain flow due to mechanical working. The Charpy orientation C in Figure 3E-3 (orientations LC and LT in Figure 3E-2) is the appropriate one for evaluating the fracture resistance to the extension of a throughwall circumferential flaw. The upper shelf Charpy energy associated with axial flaw extension (orientation A in Figure 3E-3) is considerably lower than that for the circumferential crack extension.

A similar trend in the base metal Charpy energies was also noted in this test program. Figure 3E-4 and Figure 3E-5 show the pipe and plate material Charpy energies for the two orientations as a function of temperature. The tests were conducted at six temperatures ranging from room temperature to 550°F. From the trend of the Charpy energies as a function of temperature in Figure 3E-4 and Figure 3E-5 it is clear that even at room temperature the upper shelf conditions have been reached for both the materials.

No such anisotropy is expected in the weld metal because it does not undergo any mechanical working after its deposition. This conclusion is also supported by the available data in the technical literature. The weld metal Charpy specimens in this test program were oriented the same way as the LC or LT orientations in Figure 3E-2. The Heat Affected Zone (HAZ) Charpy specimens were also oriented similarly.

Figure 3E-6 shows a comparison of the Charpy energies from the SA333 Gr. 6 base metal, the weld metal and the HAZ. In most cases two specimens were used. Considerable scatter in the weld and HAZ Charpy energy values is seen. Nevertheless, the average energies for the weld metal and the HAZ seem to fall at or above the average base metal values. This indicates that, unlike the stainless steel flux weldments, the fracture toughness of carbon steel weld and HAZ, as measured by the Charpy tests, is at least equal to the carbon steel base metal.

The preceding results and the results of the stress-strain tests discussed in the next section or other similar data are used as a basis to choose between the base and the weld metal properties for use in the J-T methodology evaluation.

Stress-Strain Tests

The stress-strain tests were performed at three temperatures: room temperature, 350°F, and 550°F. Base and weld metal from both the pipe and the plate were tested. The weld specimens were in the as-welded condition. The standard test data obtained from these tests are summarized in Table 3E-3.

An examination of Table 3E-3 shows that the measured yield strength of the weld metal, as expected, is considerably higher than that of the base metal. For example, the 550°F yield strength of the weld metal in Table 3E-3 ranges from 52 to 59 ksi, whereas the base metal yield strength is only 34 ksi. The impact of this observation in the selection of appropriate material (J/T) curve is discussed in later sections.

Figure 3E-7 through Figure 3E-10 show the plots of the 550°F and 350°F stress-strain curves for both the pipe and the plate used in the test. As expected, the weld metal stress-strain curve in every case is higher than the corresponding base metal curve. The Ramberg-Osgood format

characterization of these stress-strain curves is given in Subsection 3E.3.2 where appropriate values of α and n are also provided.

J-R Curve Tests

The test temperatures selected for the J-R curve tests were: room temperature, 350°F, and 550°F. Both the weld and the base metal were included. Due to the curvature, only the 1T plan compact tension (CT) specimens were obtained from the 16-in. diameter test pipe. Both 1T and 2T plan test specimens were prepared from the test plate. All of the CT specimens were side-grooved to produce plane strain conditions.

Table 3E-4 shows some details of the J-R curve tests performed in this test program. The J-R curve in the LC orientation of the pipe base metal and in the LT orientation of the plate base metal represent the material's resistance to crack extension in the circumferential direction. Thus, the test results of these orientations were used in the LBB evaluations. The orientation effects are not present in the weld metal. As an example of the J-R curve obtained in the test program, Figure 3E-11 shows the plot of J-R curve obtained from specimen OWLC-A.

3E.2.2.2 Material (J/T) Curve Selection

The normal operating temperatures for most of the carbon steel piping in the reactor coolant pressure boundary in the ESBWR generally fall into two categories: 528 to 550°F and 420°F. The latter temperature corresponds to the operating temperature of the feedwater piping system. The selections of the appropriate material (J/T) curves for these two categories are discussed next.

Material J/T Curve for 550°F

A review of the test matrix in Table 3E-4 shows that five tests were conducted at 550°F. Two tests were on the weld metal, two were on the base metal, and one was on the heat-affected zone. Figure 3E-12 shows the plot of material J_{mod} , T_{mod} values calculated from the $J-\Delta a$ values obtained from the 550°F tests. The value of flow stress, σ_f , used in the tearing modulus calculation (Equation 3E-1) was 52.0 ksi based on data shown in Table 3E-3. To convert the deformation J and dJ/da values obtained from the J-R curve into J_{mod} , T_{mod} , Equations 3E-4 and 3E-6 were used. Only the data from the pipe weld (Specimen ID OWLC-A) and the plate base metal (Specimen ID BMLI-12) are shown in Figure 3E-12. A few unreliable data points were obtained in the pipe base metal (Specimen ID OBLC-3) J-R curve test because of a malfunction in the instrumentation. Therefore, the data from this test were not included in the evaluation. The J-R curves from the other two 550°F tests were evaluated as described in the next paragraph. For comparison purposes, Figure 3E-12 also shows the SA106 carbon steel J-T data obtained from the J-R curve reported by Gudas (Reference 3E-13). The curve also includes extrapolation to higher J values based on the method recommended in NUREG 1061, Vol. 3 (Reference 3E-9).

The J_{mod} - T_{mod} data for the plate weld metal and the plate HAZ were evaluated. A comparison shows that these data fall slightly below those for the plate base metal shown in Figure 3E-12. On the other hand, as noted in Subsection 3E.2.2.1, the yield strength of the weld metal and the HAZ is considerably higher than that of the base metal. The material stress-strain and J-T curves are the two key inputs in determining the instability load and flaw values by the (J/T) methodology. Calculations performed for representative throughwall flaw sizes showed that the

higher yield strength of the weld metal more than compensates for the slightly lower J-R curve and, consequently, the instability load and flaw predictions based on base metal properties are smaller (i.e., conservative). Accordingly, it was concluded that the material (J-T) curve shown in Figure 3E-12 is the appropriate one to use in the LBB evaluations for carbon steel piping at 550°F.

Material J/T Curve for 420°F

Because the test temperature of 350°F can be considered reasonably close to the 420°F, the test J-R curves for 350°F were used in this case. A review of the test matrix in Table 3E-4 shows that three tests were conducted at 350°F. The J_{mod} , T_{mod} data for all three tests were reviewed. The flow stress value used in the tearing modulus calculation was 54 ksi based on Table 3E-3. Also reviewed were the data on SA106 carbon steel at 300°F reported by Gudas (Reference 3E-13).

Consistent with the trend of the 550°F data, the 350°F weld metal (J-T) data fell below the plate and pipe base metal data. This probably reflects the slightly lower toughness of the SAW weld in the plate. The (J/T) data for the pipe base metal fell between the plate base metal and the plate weld metal. Based on the considerations similar to those presented in the previous section, the pipe base metal J-T data, although they may lie above the weld J-T data, were used for selecting the appropriate (J-T) curve. Accordingly, the curve shown in Figure 3E-13 was developed for using the (J-T) methodology in evaluations at 420°F.

3E.2.3 Stainless Steels and Associated Welds

The stainless steels used in the ESBWR reactor coolant pressure boundary piping are either nuclear grade or low carbon Type 304 or 316. These materials and the associated welds are highly ductile and, therefore, undergo considerable plastic deformation before failure can occur. Toughness properties of Type 304 and 316 stainless steels have been extensively reported in the open technical literature and are, thus, not discussed in detail in this section. Due to high ductility and toughness, modified limit load methods can be used to determine critical crack lengths and instability loads (Subsection 3E.3.3).

3E.3 FRACTURE MECHANICS METHODS

This Subsection deals with the fracture mechanics techniques and methods for the determination of critical flaw lengths and instability loads for materials used in ESBWR. These techniques and methods comply with criteria described in Subsection 3E.1.2.

3E.3.1 Elastic-Plastic Fracture Mechanics or (J/T) Methodology

Failure in ductile materials such as highly tough ferritic materials is characterized by considerable plastic deformation and significant amount of stable crack growth. The EPFM approach outlined in this Subsection considers these aspects. Two key concepts in this approach are (1) J-integral (References 3E-14 and 3E-15) which characterizes the intensity of the plastic stress-strain field surrounding the crack tip and (2) the tearing instability theory (References 3E-16 and 3E-17) which examines the stability of ductile crack growth. A key advantage of this approach is that the material fracture toughness characteristic is explicitly factored into the evaluation.

3E.3.1.1 Basic (J/T) Methodology

Figure 3E-14 schematically illustrates the J/T methodology for stability evaluation. The material (J/T) curve in Figure 3E-14 represents the material's resistance to ductile crack extension. Any value of J falling on the material R-curve is denoted as J_{mat} and is a function solely of the increase in crack length Δa . Also defined in Figure 3E-14 is the "applied" J, which for given stress-strain properties and overall component geometry, is a function of the applied load P and the current crack length, a. Hutchinson and Paris (Reference 3E-17) also define the following two nondimensional parameters:

$$T_{applied} = \frac{E}{(\sigma_f)^2} \cdot \frac{\partial J_{applied}}{\partial a}$$

$$T_{mat} = \frac{E}{(\sigma_f)^2} \cdot \frac{dJ_{mat}}{da} \quad (3E-7)$$

where E is Young's modulus and σ_f is an appropriate flow stress.

Intersection point of the material and applied (J/T) curves denotes the instability point. This is mathematically stated as:

$$J_{applied}(a, P) = J_{mat}(a) \quad (3E-8)$$

$$T_{applied} < T_{mat}(\text{stable})$$

$$T_{applied} > T_{mat}(\text{unstable}) \quad (3E-9)$$

The load at instability is determined from the J versus load plot also shown schematically in Figure 3E-14. Thus, the three key curves in the tearing stability evaluation are: $J_{applied}$ versus $T_{applied}$, J_{mat} versus T_{mat} and $J_{applied}$ versus load. The determination of appropriate J_{mat} versus T_{mat} or the material (J/T) curve has been already discussed in Subsection 3E.2.1. The $J_{applied} - T_{applied}$ or the (J/T) applied curve can be easily generated through perturbation in the crack length once the $J_{applied}$ versus load information is available for different crack lengths. Therefore, only the methodology for the generation of $J_{applied}$ versus load information is discussed in detail.

3E.3.1.2 J Estimation Scheme Procedure

The J_{applied} or J as a function of load was calculated using the GE/EPRI estimation scheme procedure (References 3E-18 and 3E-19). The J in this scheme is obtained as sum of the elastic and fully plastic contributions:

$$J = J_e + J_p \quad (3E-10)$$

The material true stress-strain curve in the estimation scheme is assumed to be in the Ramberg-Osgood format:

$$\left(\frac{\varepsilon}{\varepsilon_0}\right) = \left(\frac{\sigma}{\sigma_0}\right) + \alpha \left(\frac{\sigma}{\sigma_0}\right)^n \quad (3E-11)$$

where, σ_0 is the material yield stress, $\varepsilon_0 = \sigma/E_0$, and α and n are obtained by fitting the preceding equation to the material true stress-strain curve.

The estimation scheme formulas to evaluate the J-integral for a pipe with a throughwall circumferential flaw subjected to pure tension or pure bending are as follows:

Tension

$$J = f_1\left(a_e, \frac{R}{t}\right) \frac{P^2}{E} + \alpha \sigma_0 \varepsilon_0 c\left(\frac{a}{b}\right) h_1\left(\frac{a}{b}, n, \frac{R}{t}\right) \left[\frac{P}{P_0}\right]^{n+1} \quad (3E-12)$$

where:

$$f_1\left(\frac{a}{b}, n, \frac{R}{t}\right) = \frac{a F^2\left(\frac{a}{b}, n, \frac{R}{t}\right)}{4\pi R^2 t^2}$$

$$P_0 = 2\sigma_0 R t \left[\pi - \gamma - 2 \sin\left(\frac{1}{2}\gamma\right) \right]$$

Bending

$$J = f_1\left(a_e, \frac{R}{t}\right) \frac{M^2}{E} + \alpha \sigma_0 \varepsilon_0 c\left(\frac{a}{b}\right) h_1\left(\frac{a}{b}, n, \frac{R}{t}\right) \left[\frac{M}{M_0}\right]^{n+1} \quad (3E-13)$$

where:

$$f_1\left(\frac{a}{b}, n, \frac{R}{t}\right) = \pi a \left(\frac{R}{I}\right)^2 F^2\left(\frac{a}{b}, n, \frac{R}{t}\right)$$

$$M_0 = M_0 \left[\cos\left(\frac{\gamma}{2}\right) - \frac{1}{2} \sin(\gamma) \right]$$

The non-dimensional functions f and h are given in Reference 3E-19.

While the calculation of J for given α , n , σ_0 and load type is reasonably straightforward, one issue that needs to be addressed is the tearing instability evaluation when the loading includes both the membrane and the bending stresses. The estimation scheme is capable of evaluating only one type of stress at a time.

This aspect is addressed next.

3E.3.1.3 Tearing Instability Evaluation Considering Both the Membrane and Bending Stresses

Based on the estimation scheme formulas and the tearing instability methodology just outlined, the instability bending and tension stresses can be calculated for various throughwall circumferential flaw lengths. Figure 3E-15 shows a schematic plot of the instability stresses as a function of flaw length. For the same stress level, the allowable flaw length for the bending is expected to be larger than the tension case.

When the applied stress is a combination of the tension and bending, a linear interaction rule is used to determine the instability stress or conversely the critical flaw length. The application of linear interaction rule is certainly conservative when the instability load is close to the limit load. The applicability of this proposed rule should be justified by providing a comparison of the predictions by the proposed approach (or an alternate approach) with those available for cases where the membrane and bending stresses are treated together.

The interaction formulas follow: (See Figure 3E-15)

Critical Flaw Length

$$a_c = \frac{(\sigma_t)}{\sigma_t + \sigma_b} a_{c,t} + \frac{(\sigma_b)}{\sigma_t + \sigma_b} a_{c,b} \quad (3E-14)$$

where:

- σ_t = applied membrane stress
- σ_b = applied bending stress
- $a_{c,t}$ = critical flaw length for a tension stress of $(\sigma_t + \sigma_b)$
- $a_{c,b}$ = critical flaw length for a bending stress of $(\sigma_t + \sigma_b)$

Instability Bending Stress

$$S_b = \left(1 - \frac{\sigma_t}{\sigma'_t} \right) \sigma'_b \quad (3E-15)$$

where:

- S_b = instability bending stress for flaw length, a , in the presence of membrane stress, σ_t
- σ_t = applied membrane stress
- σ'_t = instability tension stress for flaw length, a
- σ'_b = instability bending stress for flaw length, a

Once the instability bending stress, S_b , in the presence of membrane stress, σ_t , is determined, the instability load margin corresponding to the detectable leak-size crack (as required by LBB criterion in Subsection 3.6.3) can be calculated as follows:

$$\frac{\sigma_t + S_b}{\sigma_t + \sigma_b} \quad (3E-16)$$

It is assumed in the preceding equation that the uncertainty in the calculated applied stress is essentially associated with the stress because of applied bending loads and that the membrane stress, which is generally due to the pressure loading, is known with greater certainty. This

method of calculating the margin against loads is also consistent with the definition of load margin employed in Paragraph IWB-3640 of Section XI of Reference 3E-20.

3E.3.2 Application of (J/T) Methodology to Carbon Steel Piping

From Figure 3E-3, it is evident that carbon steels exhibit transition temperature behavior marked by three distinct stages: lower shelf, transition, and upper shelf. The carbon steels generally exhibit ductile failure mode at or above upper shelf temperatures. This would suggest that a net-section collapse approach may be feasible for the evaluation of postulated flaws in carbon steel piping. Such a suggestion was also made in a review report prepared by the Naval Research Lab (Reference 3E-21). Low temperature (i.e., less than 125°F) pipe tests conducted by GE (Reference 3E-22) and by Vassilaros (Reference 3E-23) which involved circumferentially cracked piping subjected to bending and/or pressure loading, also indicate that a limit load approach is feasible. However, test data at high temperatures, especially involving large diameter pipes, are currently not available. Therefore, a (J/T) based approach is used in the evaluation.

3E.3.2.1 Determination of Ramberg-Osgood Parameters for 550°F Evaluation

Figure 3E-7 shows the true stress-true strain curves for the carbon steels at 550°F. The same data is plotted here in Figure 3E-16 in the Ramberg-Osgood format. It is seen that, unlike the stainless steel case, each set for stress-strain data (i.e., data derived from one stress-strain curve) follows approximately a single slope line. Based on the visual observation, a line representing $\alpha = 2$, $n = 5$ in Figure 3E-16 was drawn as representing a reasonable upper bound to the data shown.

The third parameter in the Ramberg-Osgood format stress-strain curve is σ_0 , the yield stress. Based on the several internal GE data on carbon steels, such as SA 333 Gr. 6 and SA 106 Gr. B, a reasonable value of 550°F yield strength was judged as 34,600 psi. To summarize, the following values are used in this appendix for the (J/T) methodology evaluation of carbon steels at 550°F:

$$\begin{aligned}\alpha &= 2.0 \\ n &= 5.0 \\ \sigma_0 &= 34,600 \text{ psi} \\ E &= 26 \times 10^6 \text{ psi}\end{aligned}$$

3E.3.2.2 Determination of Ramberg-Osgood Parameters for 420°F Evaluation

Figure 3E-17 shows the Ramberg-Osgood (R-O) format plot of the 350°F true stress-strain data on the carbon steel base metal. Also shown in Figure 3E-17 are the CE data and SA 106 Gr. B at 400°F. Because the difference between the ASME Code Specified minimum yield strength at 350°F and 420°F is small, the 350°F stress-strain data were considered applicable in the determination of R-O parameters for evaluation at 420°F.

A review of Figure 3E-17 indicates that the majority of the data associated with any one test can be approximated by one straight line.

It is seen that some of the data points associated with the yield point behavior fall along the y-axis. However, these data points at low strain level were not considered significant and, therefore, were not included in the R-O fit.

The 350°F yield stress for the base material is given in Table 3E-3 as 37.9 ksi. Because the difference between the ASME Code specified minimum yield strengths of pipe and plate carbon steels at 420°F and 350°F is roughly 0.9 ksi, the σ_0 value for use at 420°F are chosen as (37– 0.9) or 37 ksi. In summary, the following values of R-O parameters are used for evaluation of 420°F:

$$\begin{aligned}\sigma_0 &= 37,000 \text{ psi} \\ \alpha &= 5.0 \\ n &= 4.0\end{aligned}$$

3E.3.3 Modified Limit Load Methodology for Austenitic Stainless Steel Piping

Reference 3E-24 describes a modified limit load methodology that may be used to calculate the critical flaw lengths and instability loads for austenitic stainless steel piping and associated welds. If appropriate, this or an equivalent methodology may be used in place of the (J/T) methodology described in Subsection 3E.3.1.

3E.3.4 Bimetallic Welds

For joining austenitic stainless steels to ferritic steels, the Ni-Cr-Fe Alloys 82 or 182 are generally used for weld metals. The procedures recommended in Section 3E.3.3 for the austenitic stainless steel welds are also applicable to these weld metals. This is justified based on the common procedures adopted for flaw acceptance in the ASME Code Section XI, Article IWB-3600 and Appendix C, for both types of the welds. If other types of bimetallic metals are used, proper procedures should be used with generally acceptable justifications.

3E.4 LEAK RATE CALCULATION METHODS

Leak rates of high pressure fluids through cracks in pipes are a complex function of crack geometry, crack surface roughness, applied stresses, and inlet fluid thermodynamic state. Analytical predictions of leak rates essentially consist of two separate tasks: calculation of the crack opening area, and the estimation of the fluid flow rate per unit area. The first task requires the fracture mechanics evaluations based on the piping system stress state. The second task involves the fluid mechanics considerations in addition to the crack geometry and its surface roughness information. Each of these tasks is now discussed separately considering the type of fluid state in ESBWR piping.

3E.4.1 Leak Rate Estimation for Pipes Carrying Water

EPRI-developed computer code PICEP (Reference 3E-25) may be used in the leak rate calculations. The basis for this code and comparison of its leak rate predictions with the experimental data is described in References 3E-26 and 3E-27. This code has been used in the successful application of LBB to primary piping system of a PWR. The basis for flow rate and crack opening area calculations in PICEP is briefly described first. A comparison with experimental data is shown next.

Other methods (e.g., Reference 3E-28) may be used for leak rate estimation at the discretion of the applicant.

3E.4.1.1 Description of Basis for Flow Rate Calculation

The thermodynamic model implemented in PICEP computer program assumes the leakage flow through pipe cracks to be isentropic and homogeneous, but it accounts for non-equilibrium “flashing” transfer process between the liquid and vapor phases.

Fluid friction caused surface roughness of the walls and curved flow paths has been incorporated in the model. Flows through both parallel and convergent cracks can be treated. The model uses some approximations and empirical factors, which were confirmed by comparison against test data because of the complicated geometry within the flow path.

For given stagnation conditions and crack geometries, the leak rate and exit pressure are calculated using an iterative search for the exit pressure starting from the saturation pressure corresponding to the upstream temperature and allowing for friction, gravitational, acceleration and area change pressure drops. The initial flow calculation is performed when the critical pressure is lowered to the backpressure without finding a solution for the critical mass flux.

A conservative methodology was developed to handle the phase transformation into a two-phase mixture or superheated steam through a crack. To make the model continuous, a correction factor was applied to adjust the mass flow rate of a saturated mixture to be equal to that of a slightly subcooled liquid. Similarly, a correction factor was developed to ensure continuity as the steam became superheated. The superheated model was developed by applying thermodynamic principles to an isentropic expansion of the single phase steam.

The code can calculate flow rates through fatigue or IGSCC cracks and has been verified against data from both types. The crack surface roughness and the number of bends account for the difference in geometry of the two types of cracks. The guideline for predicting leak rates

through IGSCCs when using this model was based on obtaining the number of turns that give the best agreement for Battelle Phase II test data of Collier et al. (Reference 3E-29). For fatigue cracks, it is assumed that the crack path has no bends.

3E.4.1.2 Basic for Crack Opening Area Calculation

The crack opening area in PICEP code is calculated using the estimation scheme formulas. The plastic contribution to the displacement is computed by summing the contributions of bending and tension alone, a procedure that underestimates the displacement from combined tension and bending. However, the plastic contribution is expected to be insignificant because the applied stresses at normal operation are generally such that they do not produce significant plasticity at the cracked location.

3E.4.1.3 Comparison Verification with Experimental Data

Figure 3E-18 from Reference 3E-27 shows a comparison PICEP prediction with measured leak rate data. It is seen that PICEP predictions are virtually always conservative (i.e., the leak flow rate is underpredicted).

3E.4.2 Flow Rate Estimation for Saturated Steam

3E.4.2.1 Evaluation Method

The calculations for this case were based on the maximum two-phase flow model developed by Moody (Reference 3E-30). However, in an LBB-report, a justification should be provided by comparing the predictions of this method with the available experimental data, or a generally acceptable method, if available, should be used. The Moody model predicts the flow rate of steam-water mixtures in vessel blowdown from pipes (see Figure 3E-19). A key parameter that characterized the flow passage in the Moody analysis is fL/D_h , where f is the coefficient of friction, L , the length of the flow passage and D_h , the hydraulic diameter. The hydraulic diameter for the case of flow through a crack is 2δ where δ is the crack opening displacement and the length of the flow passage is t , the thickness of the pipe. Thus, the parameter fL/D_h in the Moody analysis was interpreted as $ft/2\delta$ for the purpose of this evaluation.

Figure 3E-20 shows the predicted mass flow rates by Moody for fL/D_h of 0 and 1. Similar plots are given in Reference 3E-30 for additional fL/D_h values of 2 through 100. Because the steam in the ESBWR main steam lines would be essentially saturated, the mass flow rate corresponding to the upper saturation envelope line is the appropriate one to use. Table 3E-5 shows the mass flow rates for a range of fL/D_h values for a stagnation pressure of 960 psi which is roughly equal to the pressure in an ESBWR piping system carrying steam.

A major uncertainty in calculating the leakage rate is the value of f . This is discussed next.

3E.4.2.2 Selection of Appropriate Friction Factor

Typical relationships between Reynolds number and relative roughness ε/D_h , the ratio of effective surface protrusion height to hydraulic diameter, were relied upon in this case. Figure 3E-21, from Reference 3E-31, graphically shows such a relationship for pipes. The ε/D_h ratio for pipes generally ranges from 0 to 0.50. However, for a fatigue crack consisting of rough

fracture surfaces represented by a few mils, the roughness height ε at some location may be almost as much as δ . In such cases, ε/D_h would seem to approach one-half. There are no data or any analytical model for such cases, but a crude estimate based on the extrapolation of the results in Figure 3E-21 would indicate that f may be of the order of 0.1 to 0.2. For this evaluation an average value of 0.15 was used with the modification as discussed next.

For blowdown of saturated vapor, with no liquid present, Moody states that the friction factor should be modified according to

$$f_g = f_{GSP} \left(\frac{v_f}{v_g} \right)^{1/3} \quad (3E-17)$$

where:

f_g = modified friction factor

f_{GSP} = factor for single phase

$\frac{v_f}{v_g}$ = liquid/vapor specific volume ratio evaluated at an average static pressure in the flow path

This correction is necessary because the absence of a liquid film on the walls of the flow channel at high quality makes the two-phase flow model invalid as it stands. The average static pressure in the flow path is going to be something in excess of 480 psia if the initial pressure is 960 psia; this depends on the amount of flow choking and can be determined from Reference 3E-30. However, a fair estimate of $(v_f/v_g)^{1/3}$ is 0.3, so the friction factor for saturated steam blowdown may be taken as 0.3 of that for mixed flow.

Based on this discussion, a coefficient of friction of $0.15 \times 0.3 = 0.045$ was used in the flow rate estimation. Currently experimental data are unavailable to validate this assumed value of coefficient of friction.

3E.4.2.3 Crack Opening Area Formulation

The crack opening areas were calculated using LEFM procedures with the customary plastic zone correction. The loadings included in the crack opening area calculations were: pressure, weight, and thermal expansion.

The mathematical expressions given by Paris and Tada (Reference 3E-32) are used in this case. The crack opening areas for pressure (A_p) and bending stresses (A_b) were separately calculated and then added together to obtain the total area (A_c).

For simplicity, the calculated membrane stresses from weight and thermal expansion loads were combined with the axial membrane stress, σ_p , due to the pressure.

The formulas are summarized below:

$$A_p = \frac{\sigma_p}{E} (2\pi R t) G_p(\gamma) \quad (3E-18)$$

where:

σ_p = axial membrane stress caused by pressure, weight and thermal expansion loads

E = Young's modulus

R = pipe radius

t = pipe thickness
 $\lambda = \text{shell parameter} = \frac{a}{\sqrt{Rt}}$
a = half crack length

$$G_p(\lambda) = \lambda^2 + 0.16\lambda^4 (0 \leq \lambda \leq 1) \\ = 0.02 + 0.81\lambda^2 + 0.30\lambda^3 + 0.03\lambda^4 (1 \leq \lambda \leq 5) \quad (3E-19)$$

$$A_b = \frac{\sigma_b}{E} \cdot \pi \cdot R^2 \cdot \frac{(3 + \cos\theta)}{4} I_t(\theta) \quad (3E-20)$$

where:

σ_b = bending stress caused by weight and thermal expansion loads
 θ = half crack angle

$$I_t(\theta) = 2\theta^2 \left[1 + \left(\frac{\theta}{\pi} \right)^{3/2} \left\{ 8.6 - 13.3 \left(\frac{\theta}{\pi} \right) + 24 \left(\frac{\theta}{\pi} \right)^2 \right\} + \left(\frac{\theta}{\pi} \right)^3 \right. \\ \left. \left\{ 22.5 - 75 \left(\frac{\theta}{\pi} \right) + 205.7 \left(\frac{\theta}{\pi} \right)^2 - 247.5 \left(\frac{\theta}{\pi} \right)^3 + 242 \left(\frac{\theta}{\pi} \right)^4 \right\} \right] (0 < \theta < 100^\circ) \quad (3E-21)$$

The plastic zone correction was incorporated by replacing a and θ in these formulas by a_{eff} and θ_{eff} which are given by

$$\theta_{\text{eff}} = \theta + \frac{(K_{\text{total}})^2}{(2\pi R \sigma_Y)^2} \\ a_{\text{eff}} = \theta_{\text{eff}} \cdot R \quad (3E-22)$$

The yield stress, σ_y , was conservatively assumed as the average of the code specified yield and ultimate strength. The stress intensity factor, K_{total} , includes contribution caused by both the membrane and bending stress and is determined as follows:

$$K_{\text{total}} = K_m + K_b \quad (3E-23)$$

where:

$$K_m = \sigma_p \cdot \sqrt{a} \cdot F_p(\lambda) \\ F_p(\lambda) = \left(1 + 0.3225 \lambda^2 \right)^{1/2} (0 \leq \lambda \leq 1) \\ = 0.9 + 0.25 \lambda (1 \leq \lambda \leq 5) \\ K_b = \sigma_b \cdot \sqrt{\pi a} \cdot F_b(\theta) \\ F_b(\theta) = 1 + 6.8 \left(\frac{\theta}{\pi} \right)^{3/2} - 13.6 \left(\frac{\theta}{\pi} \right)^{5/2} + 20 \left(\frac{\theta}{\pi} \right)^{7/2} (0 \leq \theta \leq 100^\circ)$$

The steam mass flow rate, M, shown in Table 3E-5 is a function of parameter, $ft/2\delta$. Once the mass flow rate is determined corresponding to the calculated value of this parameter, the leak rate in gpm can then be calculated.

3E.5 LEAK DETECTION CAPABILITIES

A complete description of various leak detection systems is provided in Subsection 5.2.5. The leakage detection system gives separate considerations to: leakage within the drywell and leakage external to the drywell. The limits for reactor coolant leakage are described in Subsection 5.2.5.4.

The total leakage in the drywell consists of the identified leakage and the unidentified leakage. The identified leakage is that from pumps, valve stem packings, reactor vessel head seal and other seals, which all discharge to the equipment drain sump. The Technical Specifications (TS) limit on the identified leak rate is expected to be 25 gpm.

The unidentified leak rate in the drywell is the portion of the total leakage received in the drywell sumps that is not identified as previously described. The TS limit on unidentified leak rate is 1 gpm. To cover uncertainties in leak detection capability, although it meets Regulatory Guide 1.45 guidelines, a margin factor of 10 is required per Reference 3E-28 to determine a reference leak rate. A reduced margin factor may be used if accounts can be made of effects of sources of uncertainties such as plugging of the leakage crack with particulate material over time, leakage prediction, measurement techniques, personnel, and frequency of monitoring. For the piping in drywell, a reference leak rate of 10 gpm may be used, unless a smaller rate can be justified.

The sensitivity and reliability of leakage detection systems used outside the drywell must be demonstrated to be equivalent to Regulatory Guide 1.45 systems. Methods that have been shown to be acceptable include local leak detection, for example, visual observation or instrumentation. Outside the drywell, the leakage rate detection and the margin factor depend upon the design of the leakage detection systems.

3E.6 REFERENCES

- 3E-1 P. C. Paris, H. Tada, A. Zahoor, and H. Ernst, "The Theory of Instability of the Tearing Mode of Elastic-Plastic Crack Growth, Elastic-Plastic Fracture," ASTM STP 668, J. D. Landes, J. A. Begley, and G. A. Clarke, Eds., American Society for Testing Materials, 1979, pp. 5-36.
- 3E-2 USNRC, "Resolution of the Task A-11 Reactor Vessel Materials Toughness Safety Issue," NUREG-0744, Rev. 1 October 1982.
- 3E-3 P. C. Paris, and R. E. Johnson, "A Method of Application of Elastic-Plastic Fracture Mechanics to Nuclear Vessel Analysis, Elastic-Plastic Fracture, Second Symposium, Volume II-Fracture Resistance Curves and Engineering Application," ASTM STP 803, C. F. Shih and J. P. Gudas, Eds., American Society for Testing and Materials, 1983, pp. 11-5 through 11-40.
- 3E-4 J. R. Rice, "A Path Independent Integral and the Approximate Analysis of Strain Concentration by Notches and Cracks," J. Appl. Mech., 35, 379-386 (1968).
- 3E-5 J. A. Begley, and J. D. Landes, "The J Integral as a Fracture Criterion, Fracture Toughness, Proceedings of the 1971 National Symposium on Fracture Mechanics," Part II, ASTM STP 514, American Society for Testing Materials, pp. 1-20 (1972).
- 3E-6 J. W. Hutchinson, and P. C. Paris, "Stability Analysis of J-Controlled Crack Growth, Elastic-Plastic Fracture," ASTM STP 668, J. D. Landes, J. A. Begley, and G. A. Clarke, Eds., American Society for Testing and Materials, 1979, pp. 37-64.
- 3E-7 Electric Power Research Institute, V. Kumar, M. D. German, and C. F. Shih, "An Engineering Approach for Elastic-Plastic Fracture Analysis," EPRI Topical Report NP-1831, July 1981.
- 3E-8 H. A. Ernst, "Material Resistance and Instability Beyond J-Controlled Crack Growth, Elastic-Plastic Fracture: Second Symposium, Volume I—Inelastic Crack Analysis," ASTM STP 803, C. F. Shih and J. P. Gudas, Eds., American Society for Testing and Materials, 1983, pp. I-191 through I-213.
- 3E-9 USNRC, "Report of the U.S. Nuclear Regulatory Commission Piping Review Committee," NUREG-1061, Vol. 3, November 1984.
- 3E-10 ASME, ASME Boiler & Pressure Vessel Code, Section III, Division 1, "Nuclear Power Plant Components," 1980.
- 3E-11 ASTM Standard E399, "Plane-Strain Fracture Toughness of Metallic Materials."
- 3E-12 AEC, M.B. Reynolds, "Failure Behavior in ASTM A106B Pipes Containing Axial Through-Wall Flaws," GEAP-5620, AEC Research and Development Report, April 1968.
- 3E-13 USNRC, J. P. Gudas, and D. R. Anderson, "JI-R Curve Characteristics of Piping Material and Welds," NUREG/CP-0024, Vol. 3, March 1982.
- 3E-14 J. R. Rice, "A Path Independent Integral and the Approximate Analysis of Strain Concentration," Notches and Cracks, J. Appl. Mech., 35, 379, 386 (1968).

- 3E-15 J. A. Begley, and J. D. Landes, "The J Integral as a Fracture Criterion, Fracture Toughness, Proceedings of the 1971 National Symposium on Fracture Mechanics," Part II, ASTM STP 514, American Society for Testing Materials, pp. 1-20 (1972).
- 3E-16 P.C. Paris, H. Tada, A. Zahoor, and H. Ernst, "The Theory of Instability of the Tearing Mode of Elastic-Plastic Crack Growth, Elastic-Plastic Fracture," ASTM STP 668, J.D. Landes, J. A. Begley, and G. A. Clarke, Eds., American Society for Testing Materials, 1979, pp. 5-36.
- 3E-17 J.W. Hutchinson, and P.C. Paris, "Stability Analysis of J-Controlled Crack Growth, Elastic-Plastic Fracture," ATSM STP 668, J. D. Landes, J. A. Begley, and G. A. Clarke, Eds., American Society for Testing and Materials, 1979, pp. 37-64.
- 3E-18 Electric Power Research Institute, V. Kumar, M. D. German, and C. F. Shih, "An Engineering Approach for Elastic-Plastic Fracture Analysis," EPRI Topical Report NP-1831, July 1981.
- 3E-19 Electric Power Research Institute, "Advances in Elastic-Plastic Fracture Analysis," EPRI Report No. NP-3607, August 1984.
- 3E-20 ASME, ASME Boiler and Pressure Vessel Code, Section XI, "Rules for In-Service Inspection of Nuclear Power Plant Components," 1986 Edition.
- 3E-21 USNRC, C. I. Chang, et. al., "Piping Inelastic Fracture Mechanics Analysis," NUREG/CR-1119, June 1980.
- 3E-22 USAEC, "Reactor Primary Coolant System Rupture Study Quarterly Progress Report No. 14," July-September, 1968, GEAP-5716, AEC Research and Development Report, December 1968.
- 3E-23 USNRC, M. G. Vassilaros, et al, "J-Integral Tearing Instability Analyses for 8-Inch Diameter ASTM A10.6 Steel Pipe," NUREG/CR-3740, April 1984.
- 3E-24 USNRC, "Standard Review Plan," Public Comments Solicited, Federal Register, Volume 52, No. 167, Notices, Pages 32626 to 32633, August 28, 1987.
- 3E-25 Electric Power Research Institute, D. Norris, B. Chexal, and T. Griesbach, "PICEP: Pipe Crack Evaluation Program," NP-3596-SR, Special Report, Revision 1, 1987.
- 3E-26 B. Chexal, and J. Horowitz, "A Critical Flow Model for Flow Through Cracks in Pipes," to be presented at the 24th ASME/AICHE National Heat Transfer Conference, Pittsburgh, PA, August 9-12, 1987.
- 3E-27 B. Chexal and J. Horowitz, "A Crack Flow Rate Model for Leak-Before-Break Applications," SMIRT-9 Transachoir Vol. G, pp. 281-285 (1987).
- 3E-28 USNRC, "Evaluation and Refinement of Leak Rate Estimation Models," NUREG/CR-5128, April 1991.
- 3E-29 Electric Power Research Institute, R. P. Collier, et. al., "Two Phase Flow Through Intergranular Stress Corrosion Cracks and Resulting Acoustic Emission," EPRI Report No. NP-3540-LD, April 1984.

- 3E-30 F. J. Moody, "Maximum Two-Phase Vessel Blowdown from Pipes," J. Heat Transfer, Vol. 88, No. 3, 1966, pp. 285-295.
- 3E-31 R. L. Daugherty, and J. B. Franzini, "Fluid Mechanics with Engineering Applications," McGraw-Hill Book Company, New York 1965.
- 3E-32 USNRC, P. C. Paris and H. Tada, "The Application of Fracture Proof Design Postulating Circumferential Through-Wall Cracks," U.S. Nuclear Regulatory Commission Report NUREG/CR-3464, Washington, D.C., April 1983.

Table 3E-1**Electrodes and Filler Metal Requirements for Carbon Steel Welds**

Base Material	P-No.	Process	Electrode Specification or	Filler Metal Classification
Carbon Steel to Carbon Steel; or	P-1 to P-1, P-3	SMAW	SFA 5.1	E7018
Low Alloy Steel	P-4 or P-5	GTAW PAW	SFA 5.18	E70S-2, E70S-3
		GMAW	SFA 5.18 SFA 5.20	E70S-2, E70S-3, E70S-6 E70T-1
		SAW	SFA 5.17	F72EM12K, F72EL12

Table 3E-2**Supplier Provided Chemical Composition and Mechanical Properties Information**

		Chemical Composition				Mechanical Property			
Material	Product Form	C	Ma	P	S	Si	Sy (ksi)	Su (ksi)	Elongation (%)
SA 333 Gr. 6 Heat #52339	16 in. Sch. 80 Pipe	0.12	1.18	0.01	0.026	0.27	44.0	67.5	42.0
SA 516 Gr. 70 Heat #E18767	1.0 in. Plate	0.18	0.98	0.017	0.0022	0.25	46.5	70.5	31.0

Notes:

- (1) Pipe was normalized at 1650°F. Held for 2 hours and air-cooled.
- (2) Plate was normalized at 1700°F for one hour and air-cooled.

Table 3E-3
Standard Tension Test Data at Temperature

Specimen Number	Material	Test Temperature	0.2% YS (ksi)	UTS (%)	Elongation (%)	RA (%)
OW1	Pipe Weld	RT	66.1	81.6	32	77.2
OW2	Pipe Weld	550°F	59.0	93.9	24	56.7
ITWL2	Plate Weld	550°F	53.0	91.4	34	51.3
IBL1	Plate Base	RT	44.9	73.7	38	51.3
IBL2	Plate Base	350°F	37.9	64.2	34	68.9
IBL3	Plate Base	550°F	34.1	69.9	29	59.4
OB1	Pipe Base	RT	43.6	68.6	41	67.8
OB2	Pipe Base	350°F	42.2	74.9	21	55.4
OB3	Pipe Base	550°F	34.6	78.2	31	55.4

Table 3E-4
Summary of Carbon Steel J-R Curve Tests

Number	Specimen ID	Size	Description	Temperature
(1)	OWLC-A	1T	Pipe Weld	550°F
(2)	OBCL-1	1T	Pipe Base C-L Orientation	RT
(3)	OBLC2	1T	Pipe Base L-C Orientation	550°F
(4)	OBLC3-B	1T	Pipe Base L-C Orientation	350°F
(5)	BML-4	1T	Plate Base Metal, L-T Orientation	RT
(6)	BML4-14	2T	Plate Base Metal, L-T Orientation	RT
(7)	BML2-6	2T	Plate Base Metal, L-T Orientation	350°F
(8)	BML1-12	2T	Plate Base Metal, L-T Orientation	550°F
(9)	WM3-9	2T	Plate Weld Metal	RT
(10)	XWM1-11	2T	Plate Weld Metal	350°F
(11)	WM2-5	2T	Plate Weld Metal	550°F
(12)	HAZ	(Non-standard) Width = 2.793"	Heat-Affected Zone, Plate	RT
(13)	OWLC-7	1T	Pipe Weld	RT

Notes:

1. Pipe base metal, SA333 Gr. 6
2. Plate base metal, SA516 Gr. 70

Table 3E-5
Mass Flow Rate Versus f_l/D_h Values

f_l/D_h	Mass Flow Rate, lbm/sec-ft^2 M
0	3800
1	2200
2	1600
3	1150
4	920
5	800
10	580
20	400
50	260
100	185

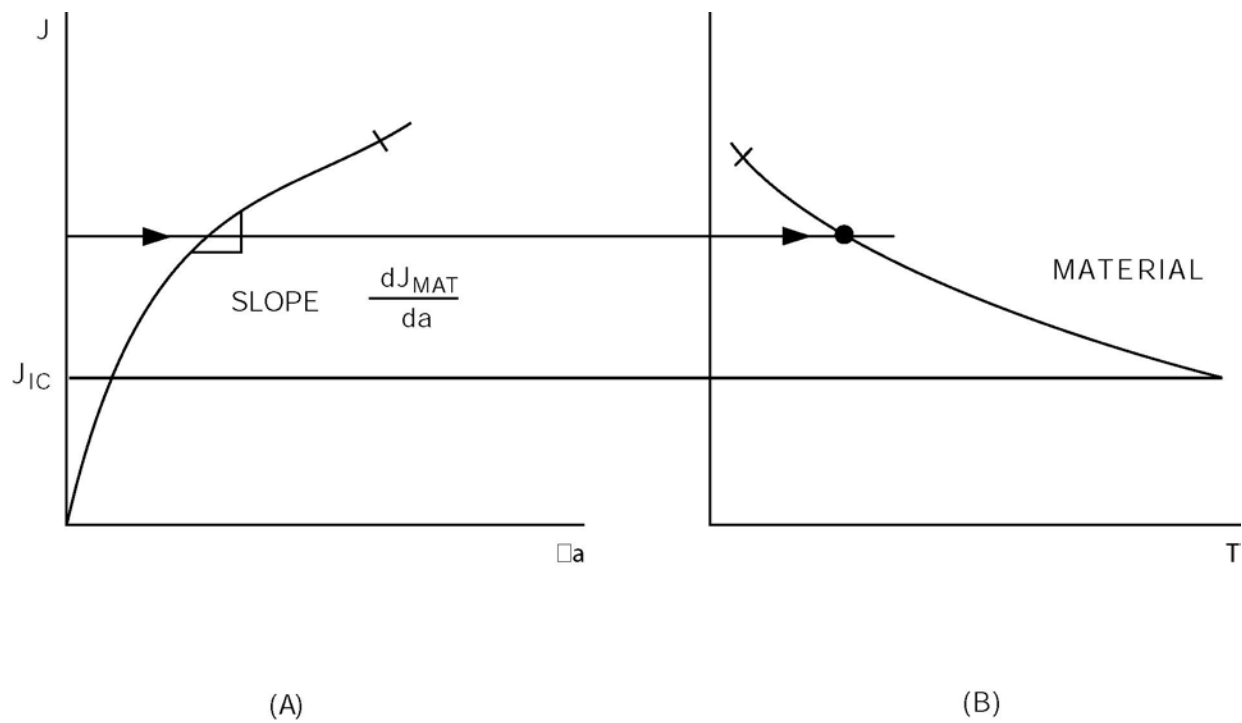
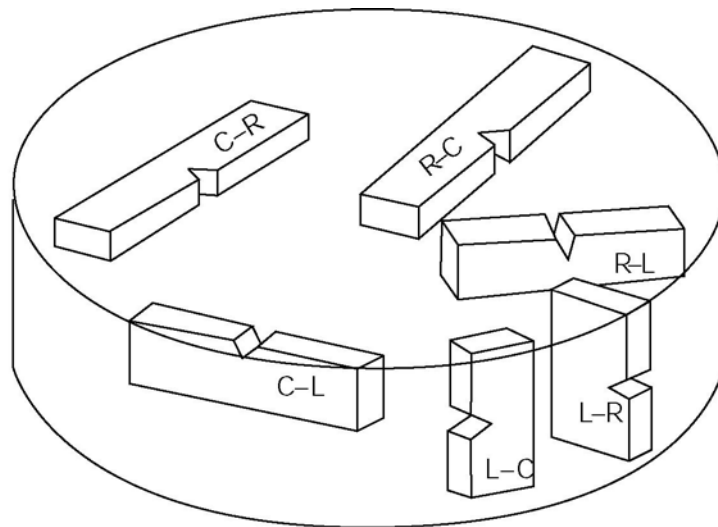
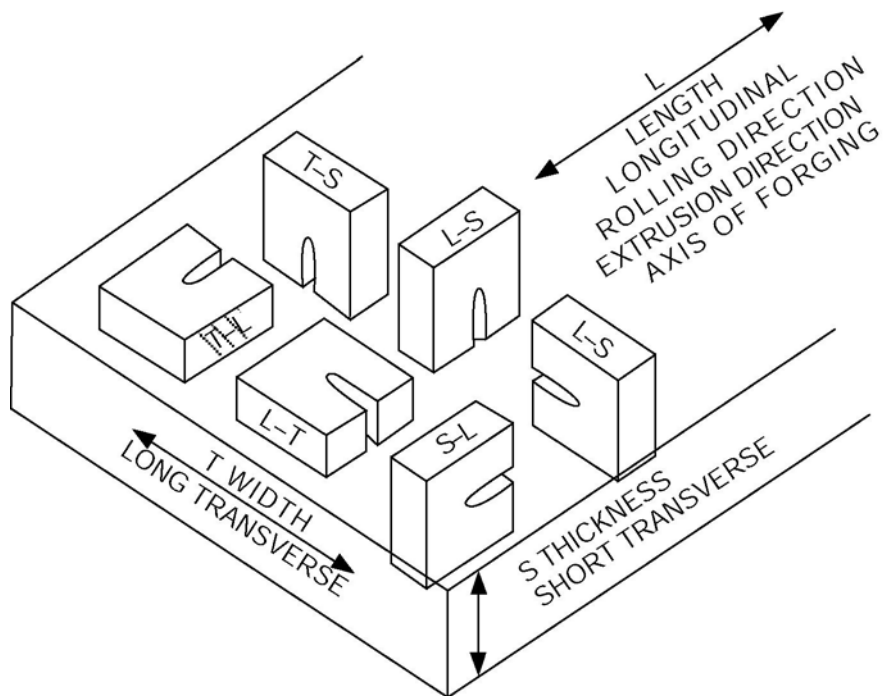


Figure 3E-1. Schematic Representation of Material J-Integral R and J-T Curves



CRACK PLANE ORIENTATION CODE FOR BAR AND HOLLOW CYLINDER



CRACK PLANE ORIENTATION CODE FOR RECTANGULAR SECTIONS

Figure 3E-2. Carbon Steel Test Specimen Orientation Code

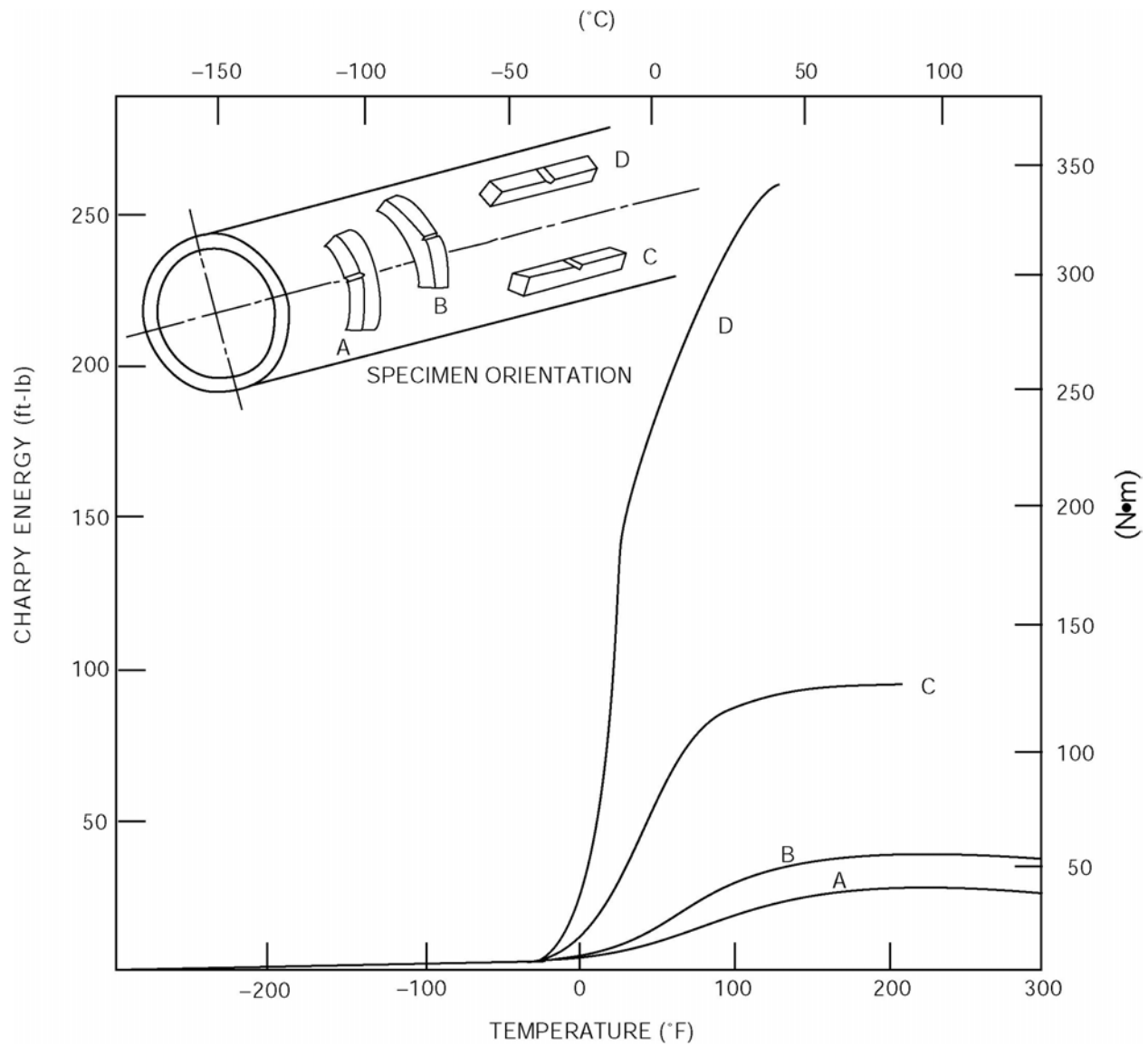
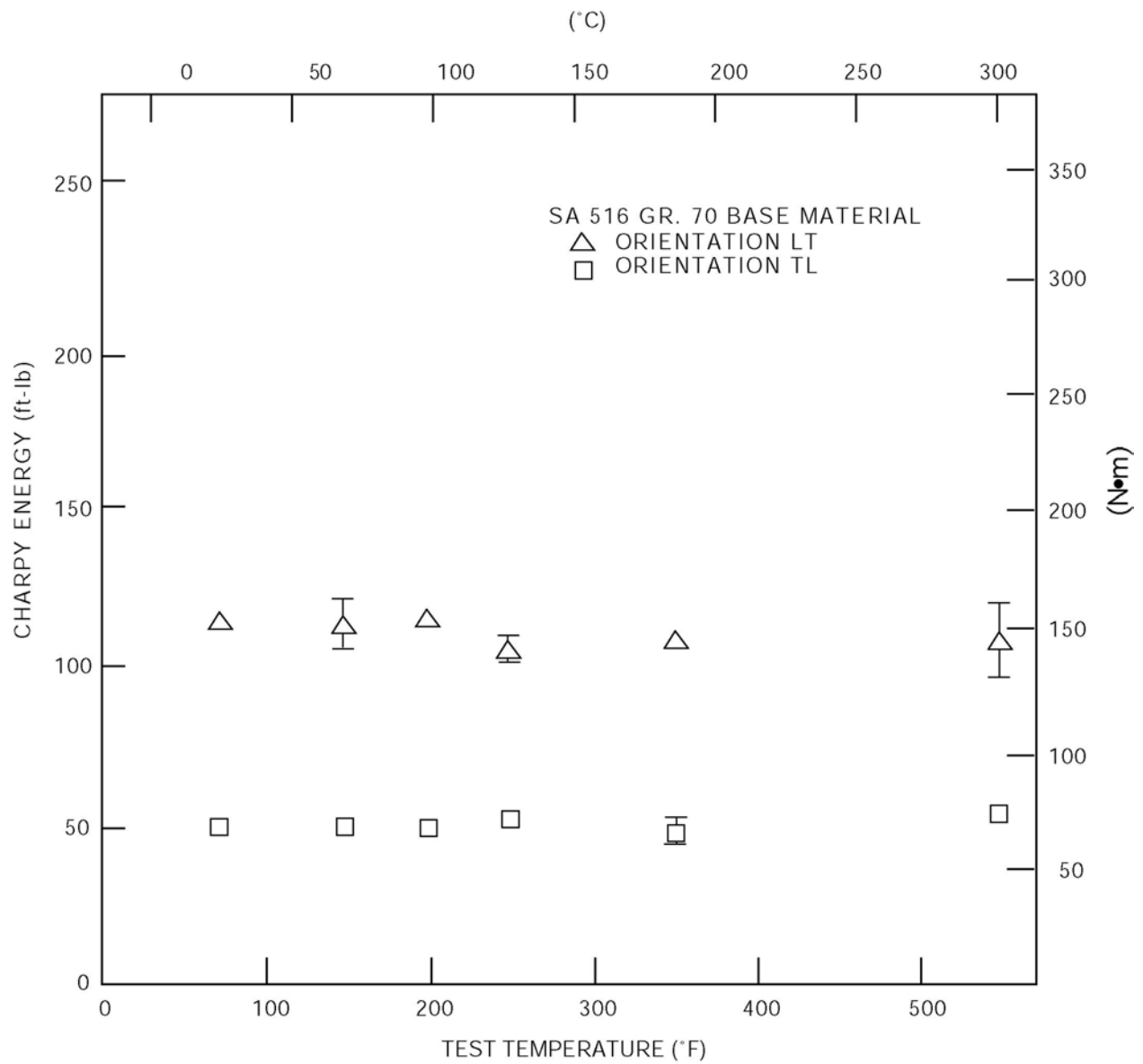
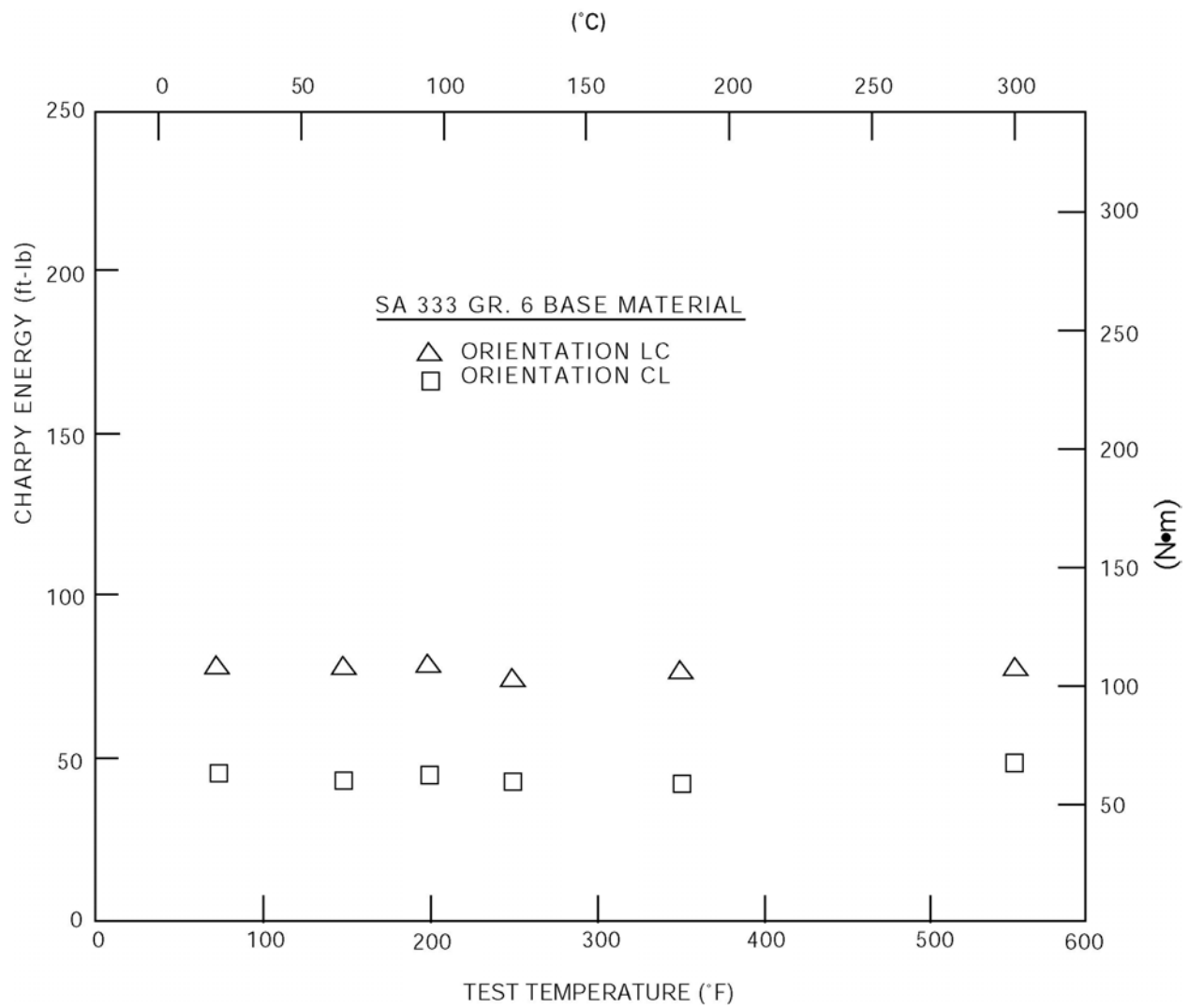


Figure 3E-3. Toughness Anisotropy of ASTM 106 Pipe (152 mm Sch. 80)



**Figure 3E-4. Charpy Energies for Pipe Test Material
as a Function of Orientation and Temperature**



**Figure 3E-5. Charpy Energies for Plate Test Material
as a Function of Orientation and Temperature**

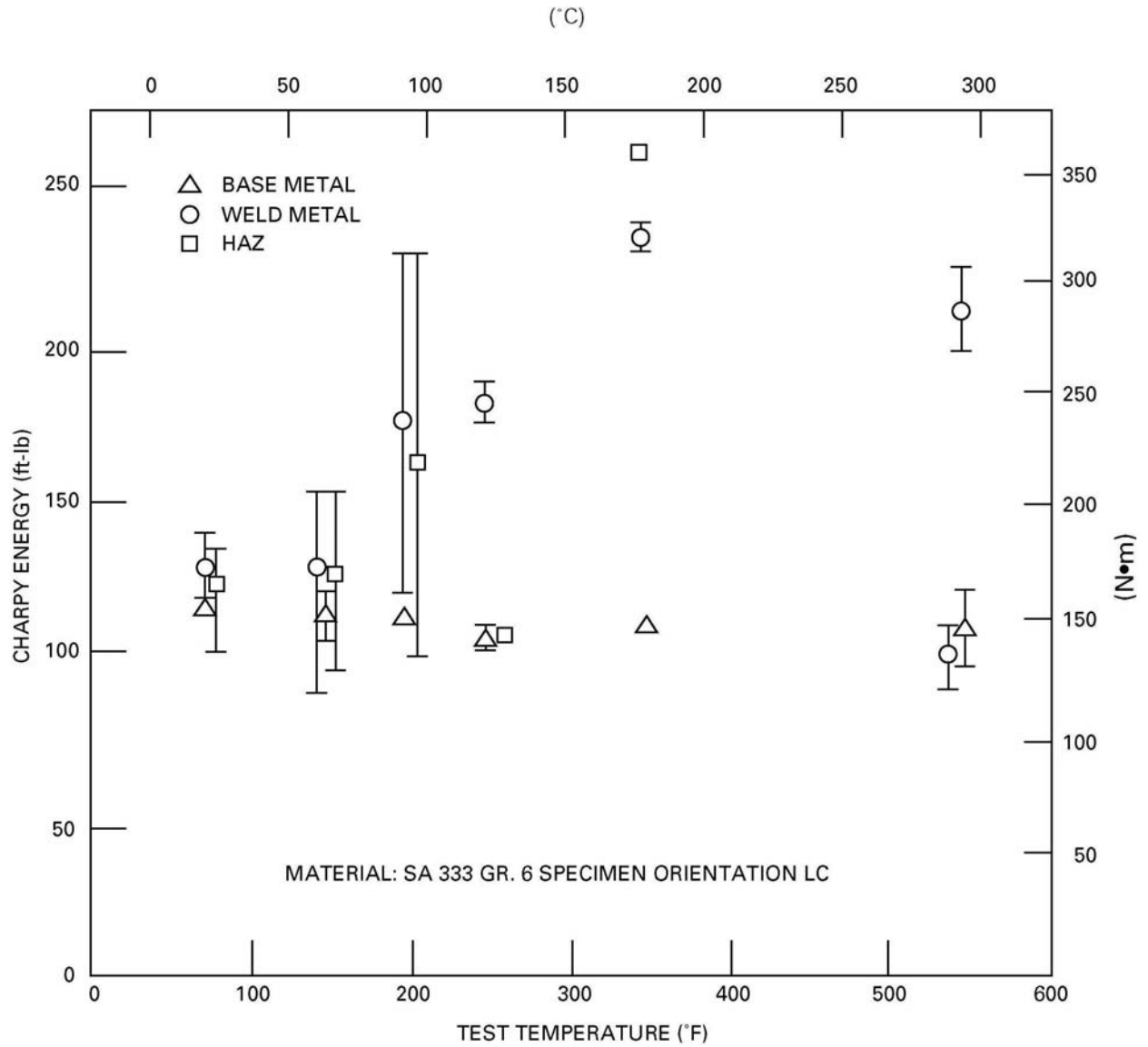


Figure 3E-6. Comparison of Base Metal, Weld and HAZ Charpy Energies for SA 333 Grade 6

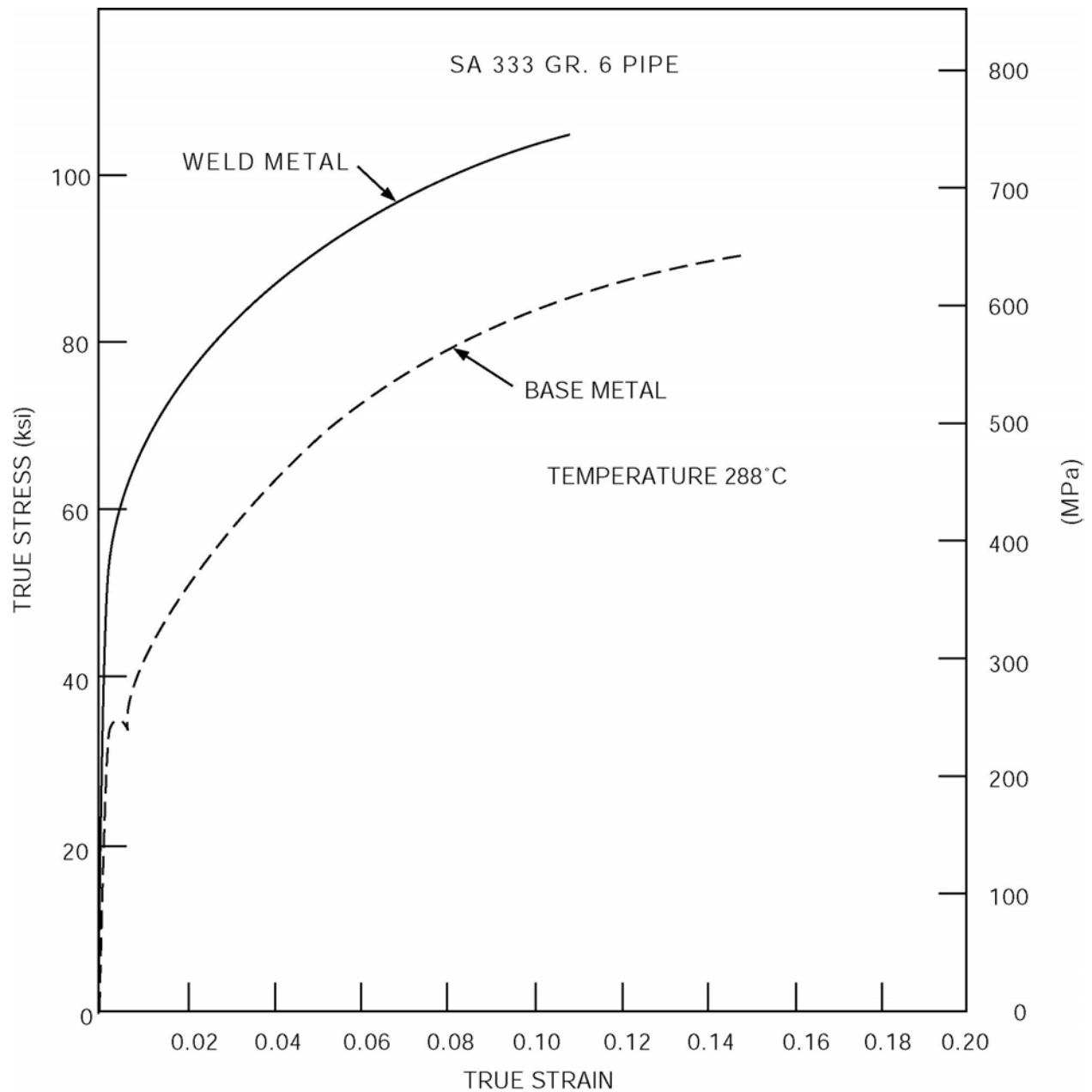


Figure 3E-7. Plot of 550°F True Stress-True Strain Curves for SA 333 Grade 6 Carbon Steel

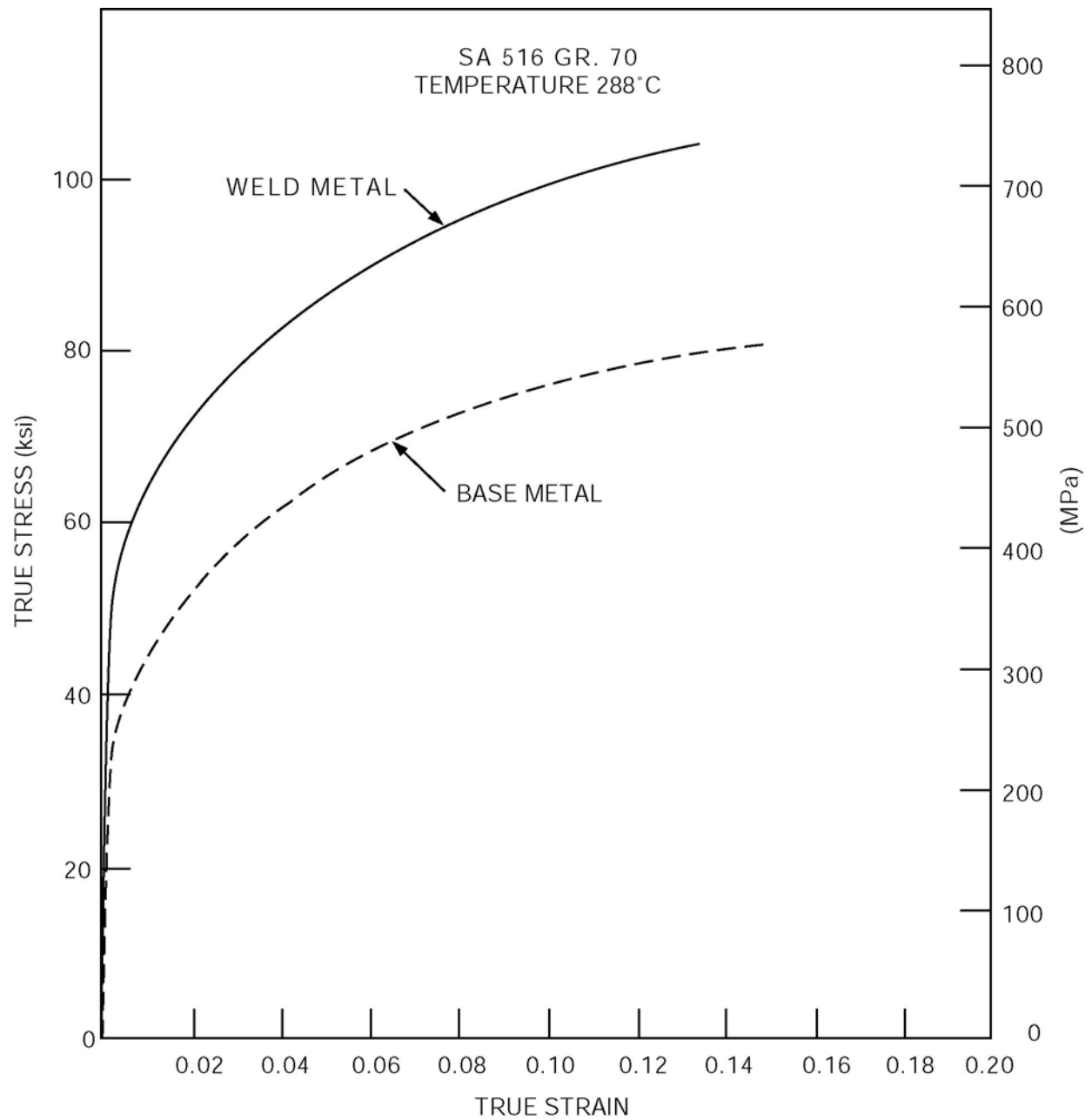


Figure 3E-8. Plot of 550°F True Stress-True Strain Curves for SA 516 Grade 70 Carbon Steel

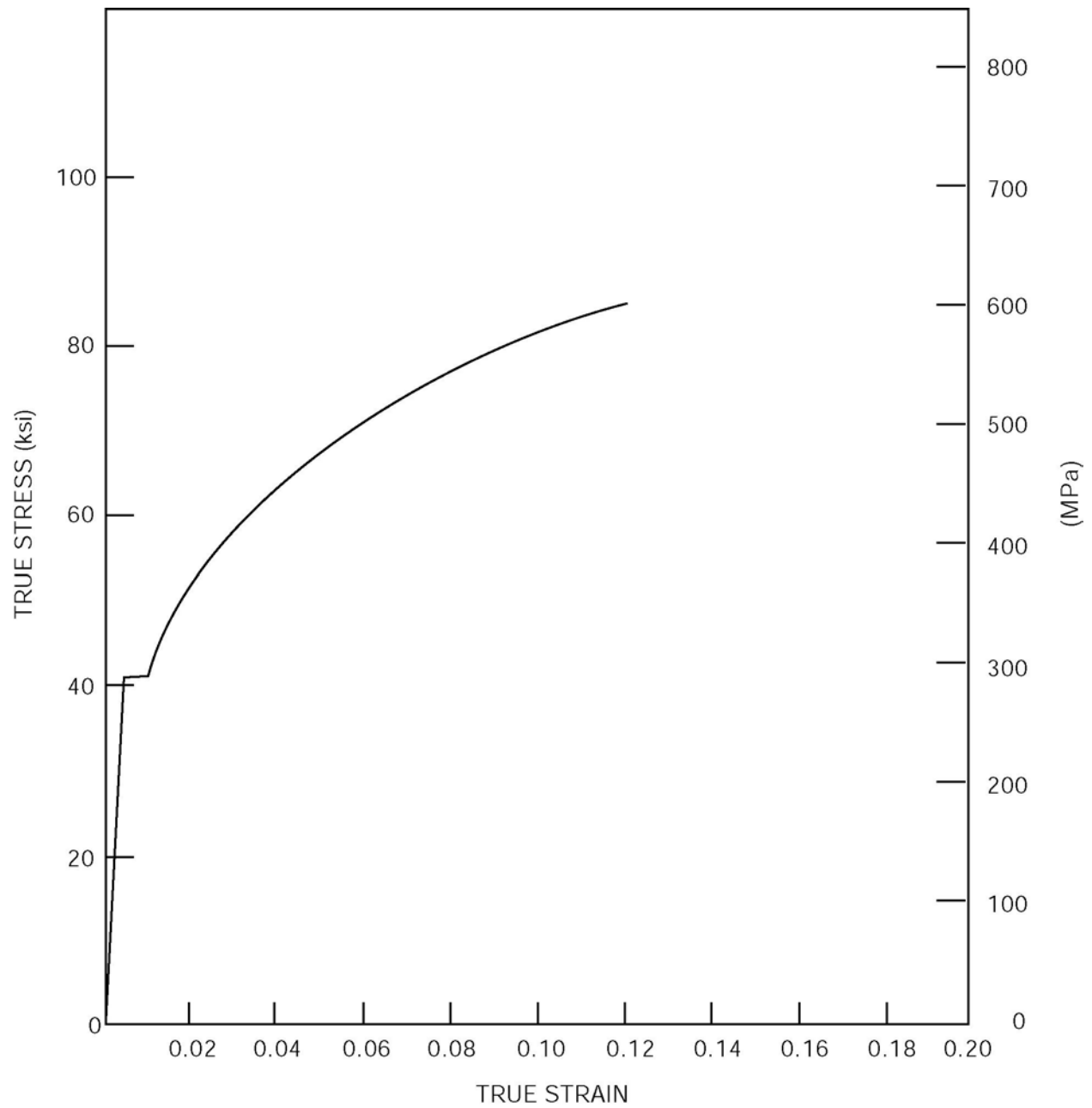


Figure 3E-9. Plot of 350°F True Stress-True Strain Curves for SA 333 Grade 6 Carbon Steel

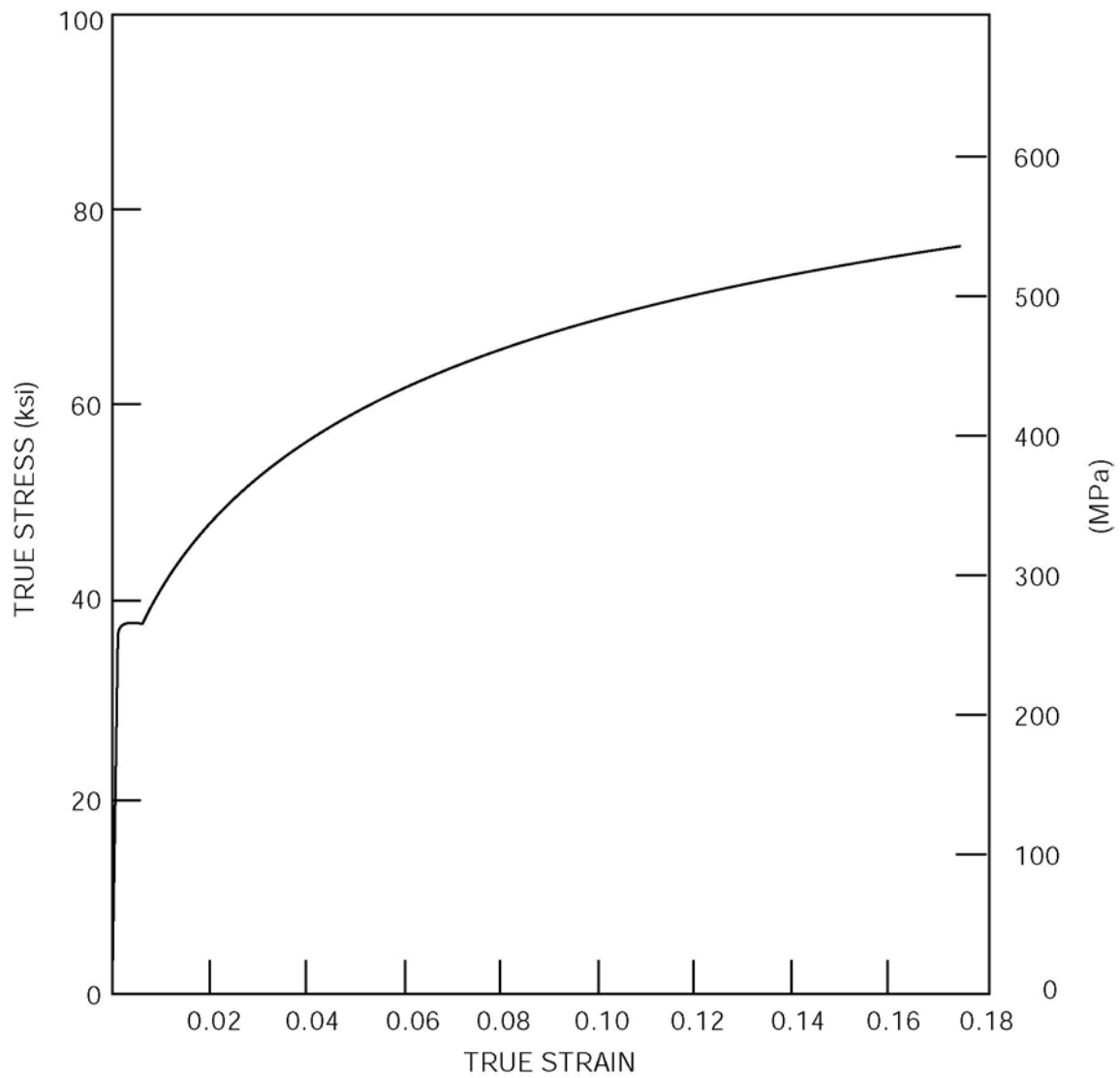


Figure 3E-10. Plot of 350°F True Stress-True Strain Curves for SA 516 Grade 70 Carbon Steel

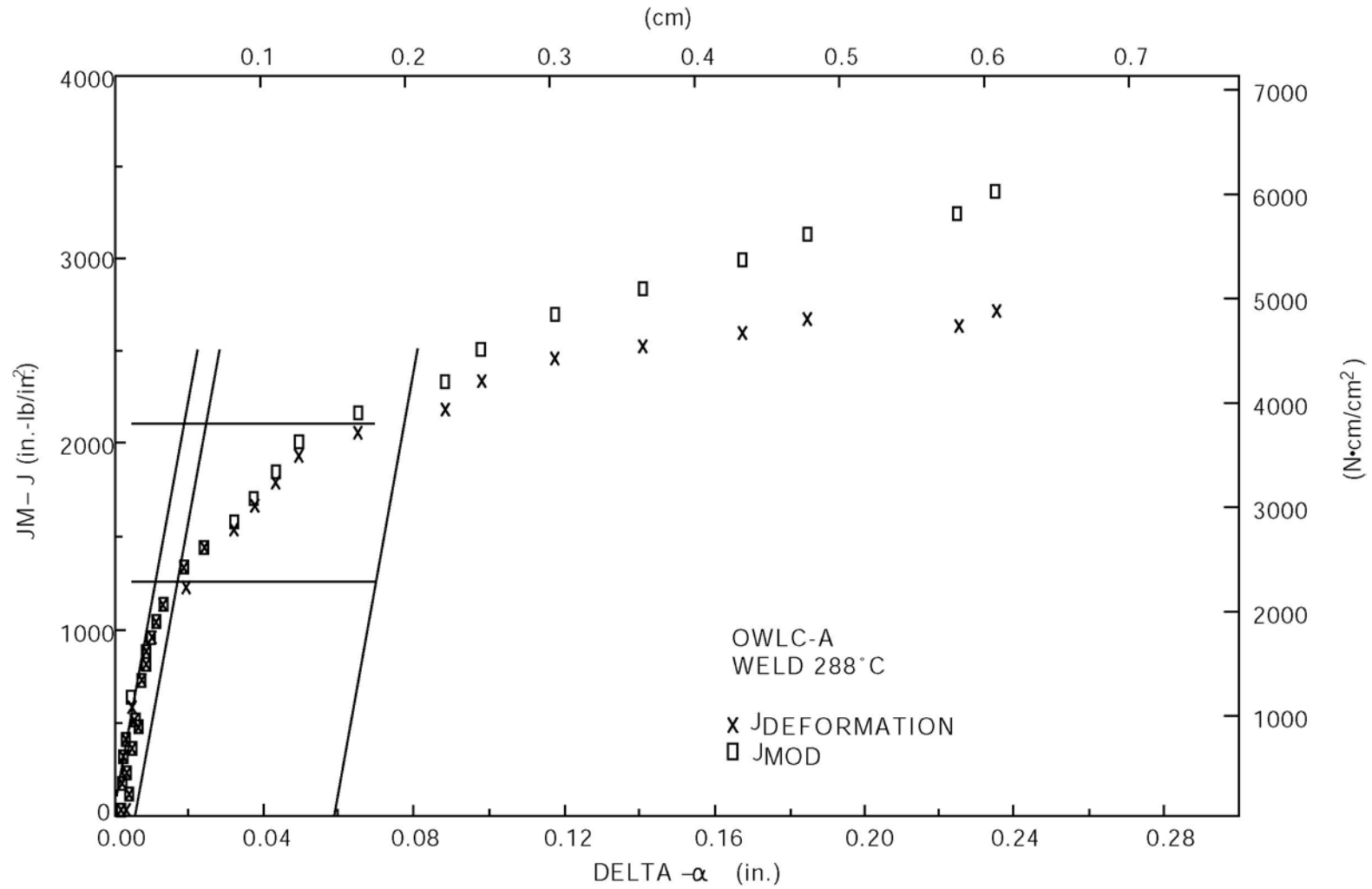


Figure 3E-11. Plot of 550°F Test J-R Curve for Pipe Weld

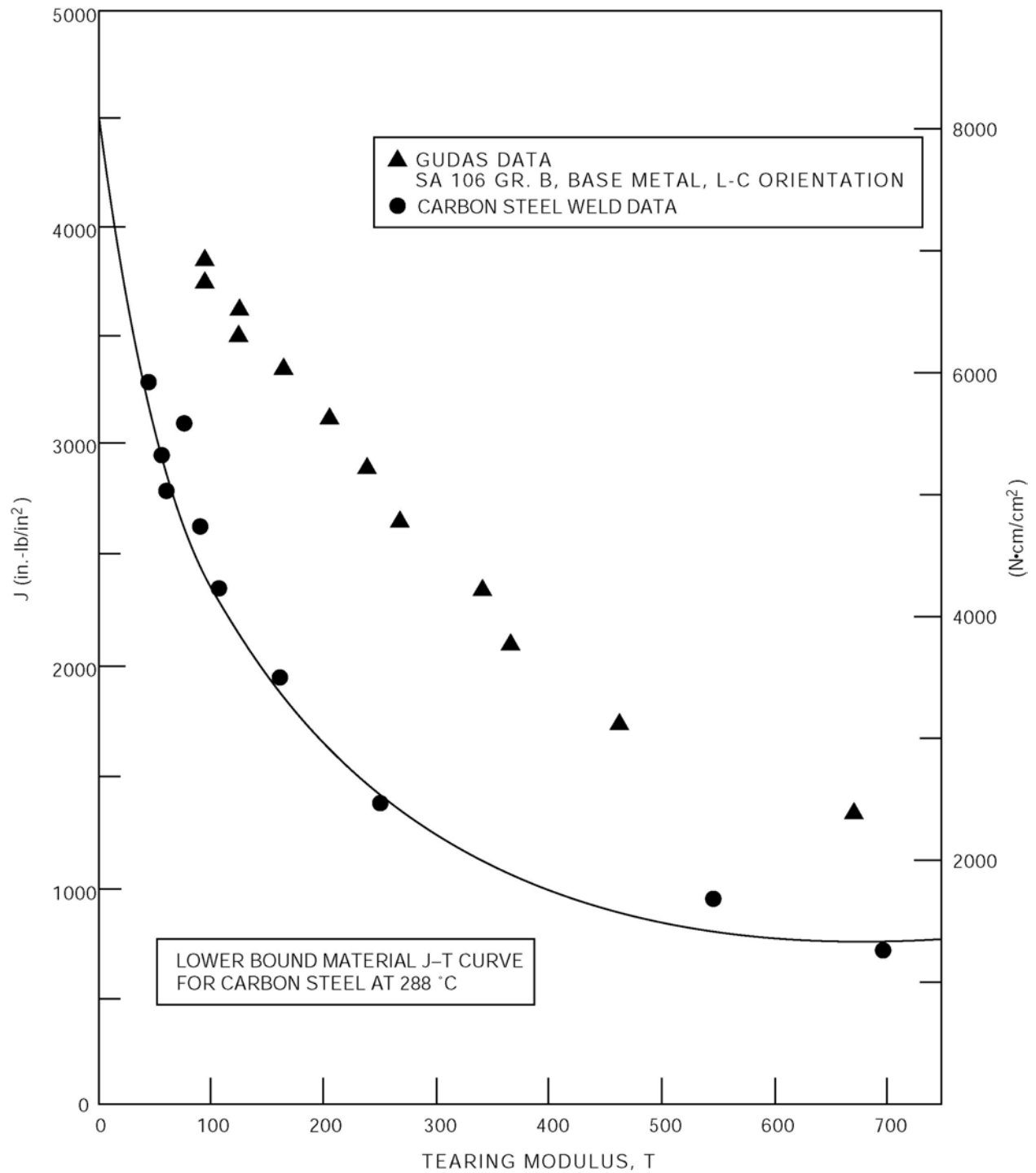


Figure 3E-12. Plot of 550°F Jmod, Tmod Data from Test J-R Curve

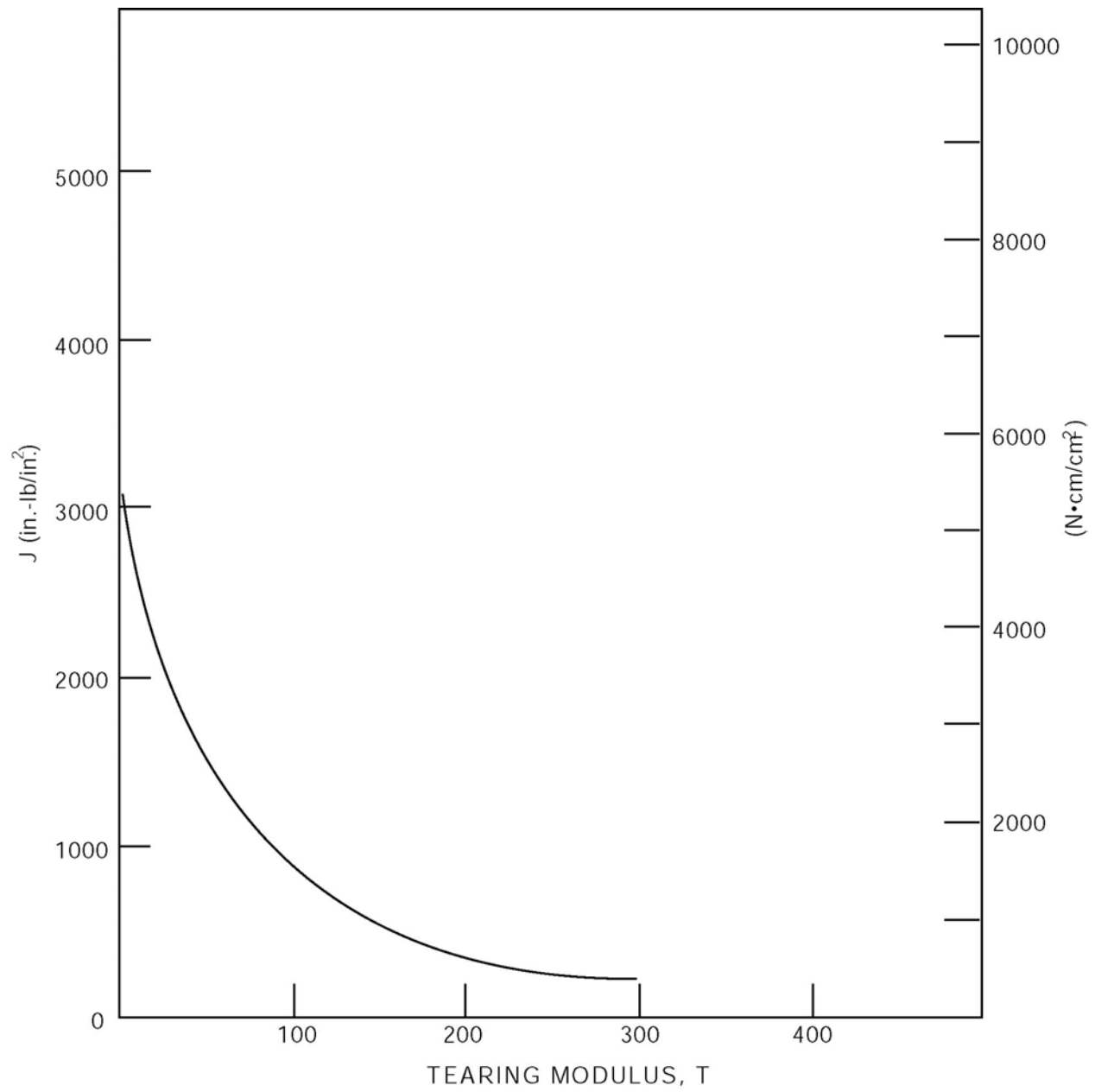


Figure 3E-13. Carbon Steel J-T Curve for 420°F

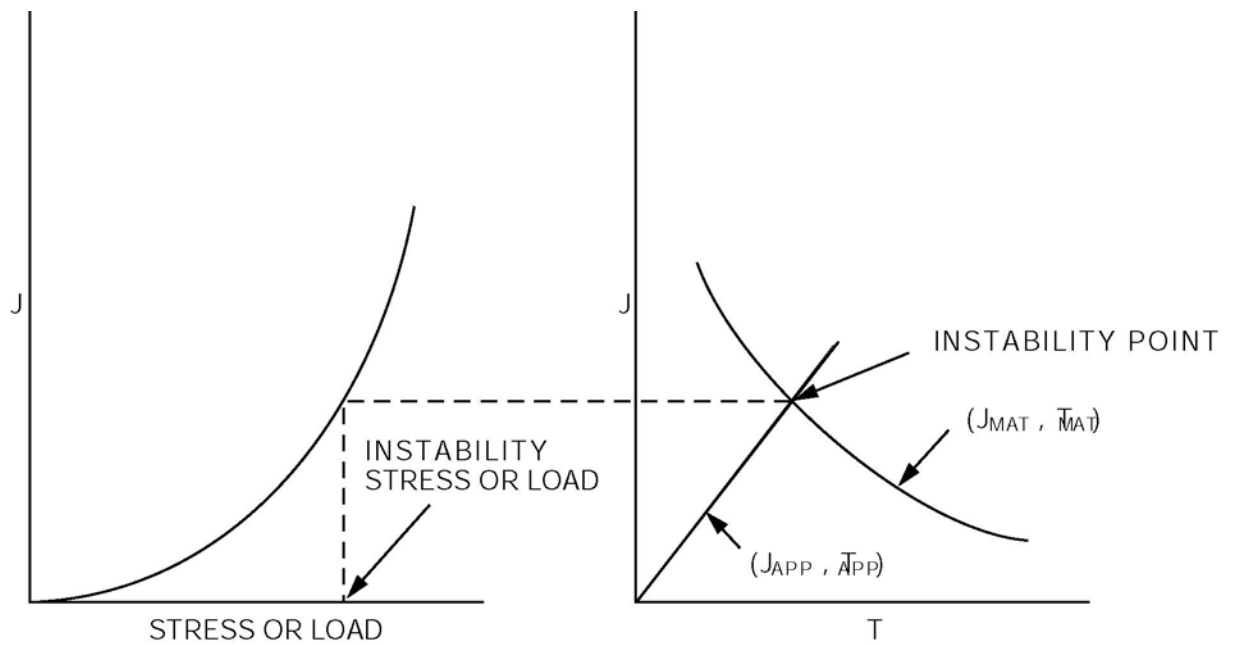


Figure 3E-14. Schematic Illustration of Tearing Stability Evaluation

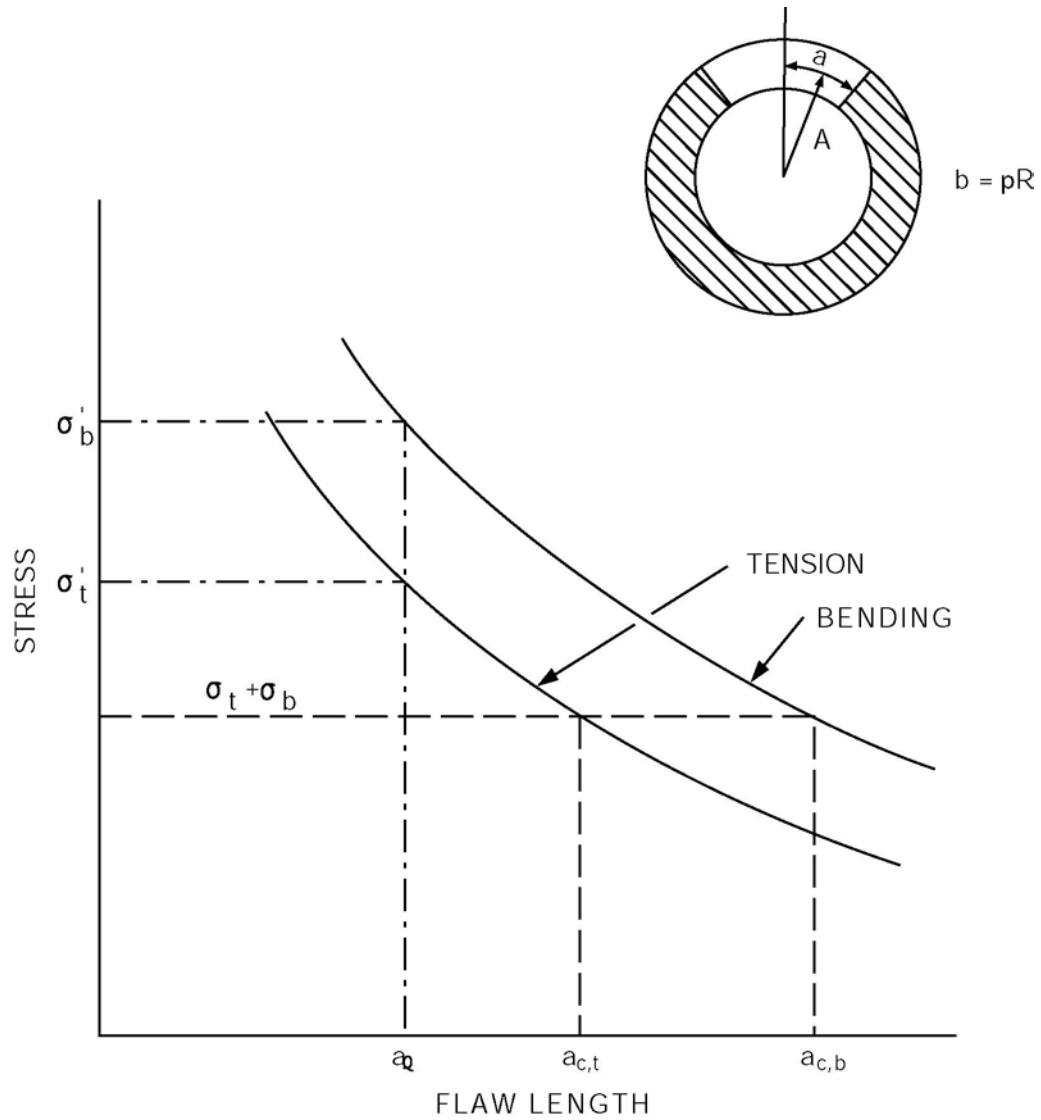


Figure 3E-15. Schematic Representation of Instability Tension and Bending Stresses as a Function of Flaw Strength

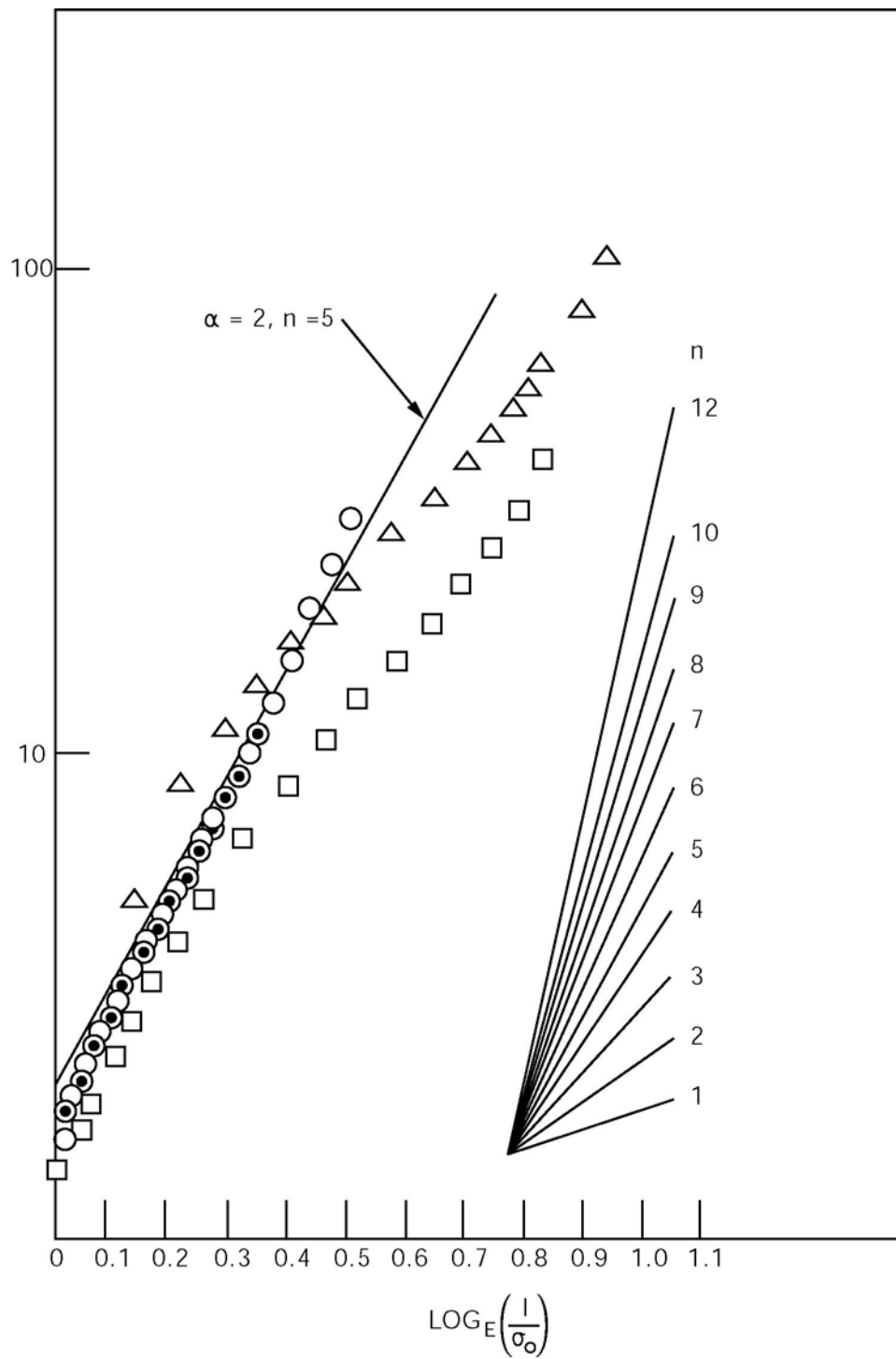


Figure 3E-16. SA 333 Grade 6 Stress-Strain Data at 550°F in the Ramberg-Osgood Format

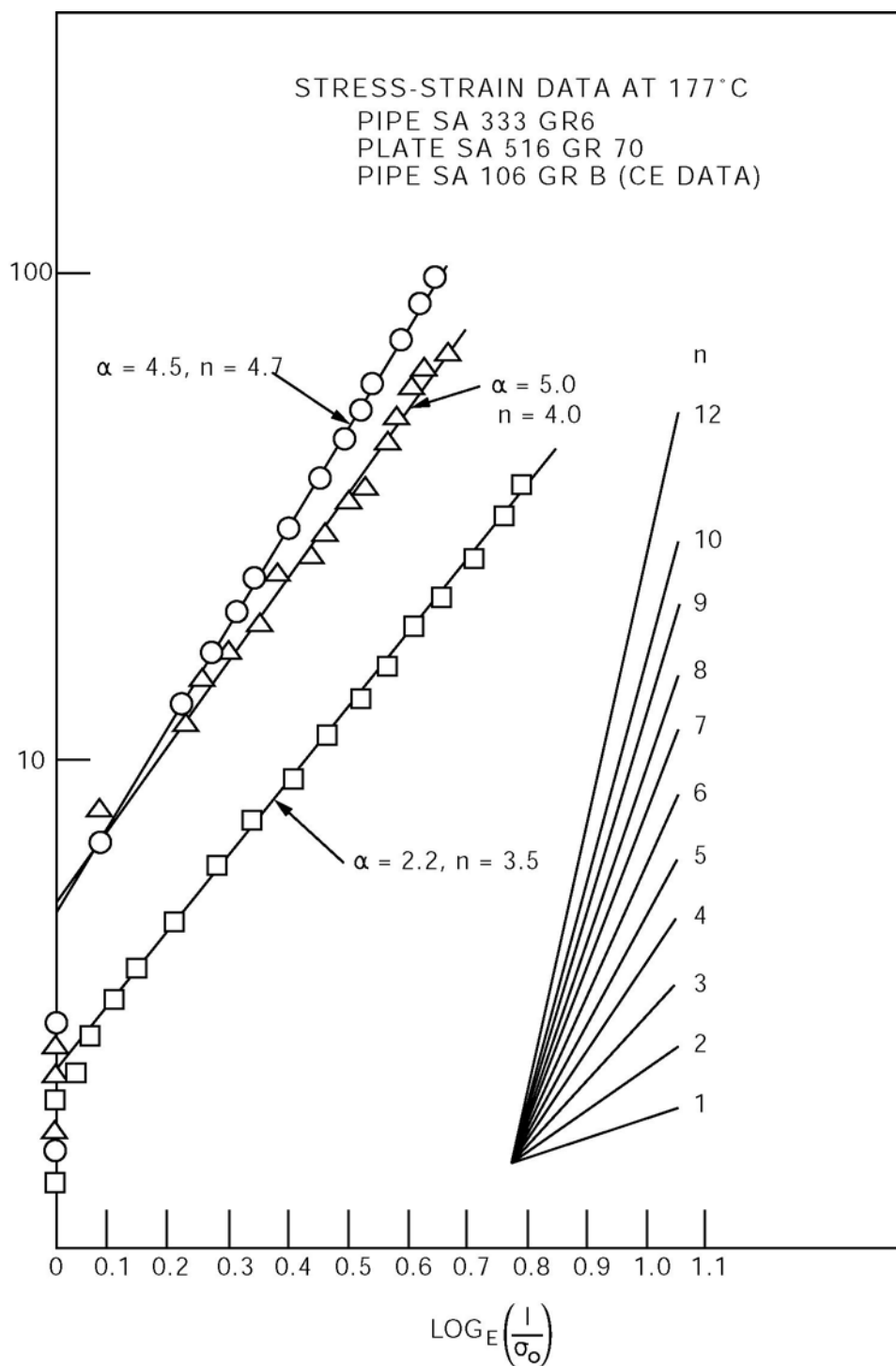
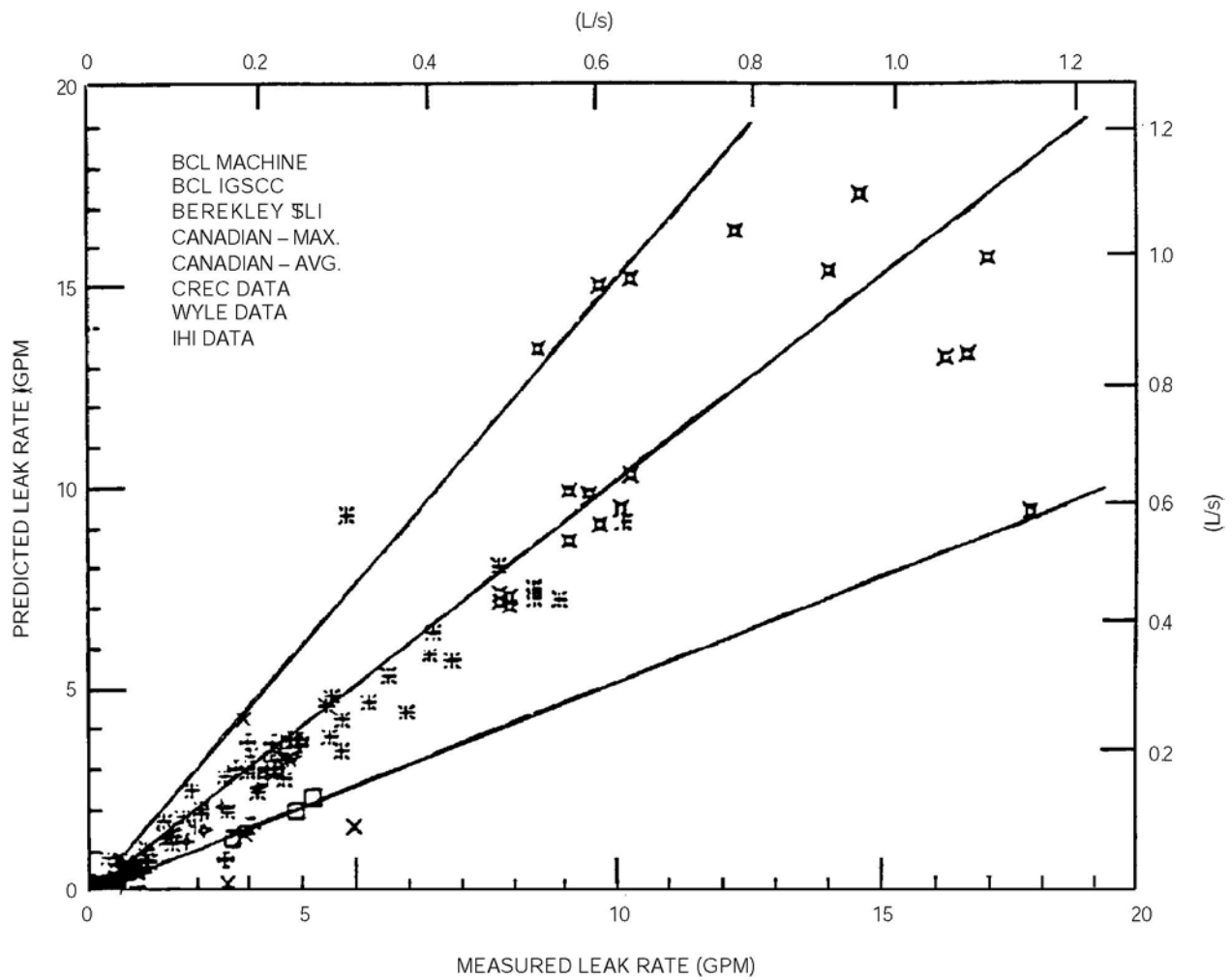
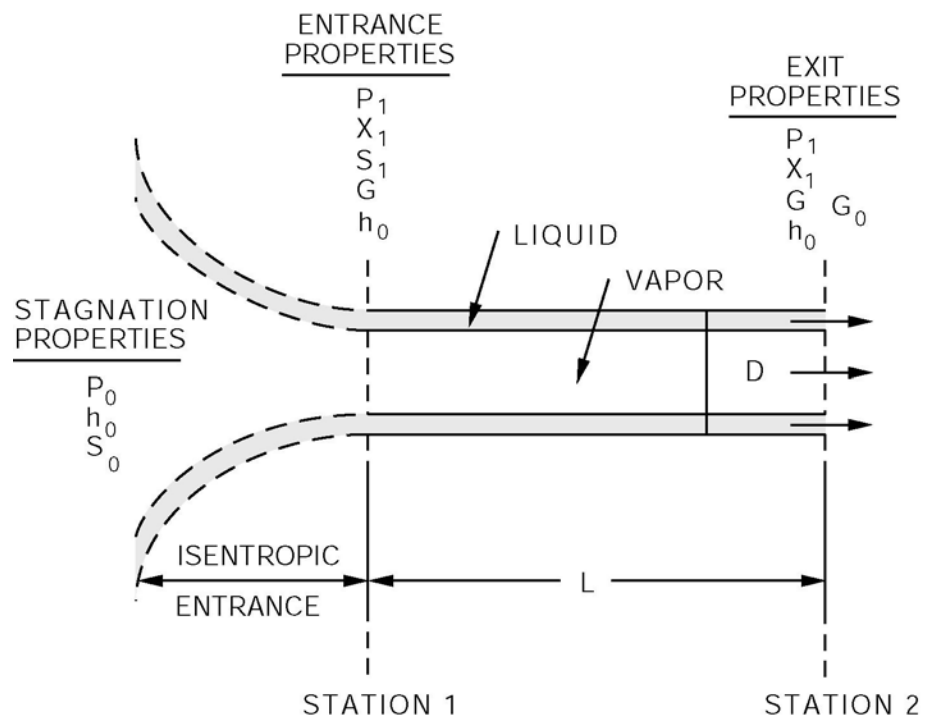


Figure 3E-17. Carbon Steel Stress-Strain Data at 350°F in the Ramberg-Osgood Format



**Figure 3E-19. Pipe Flow Model**

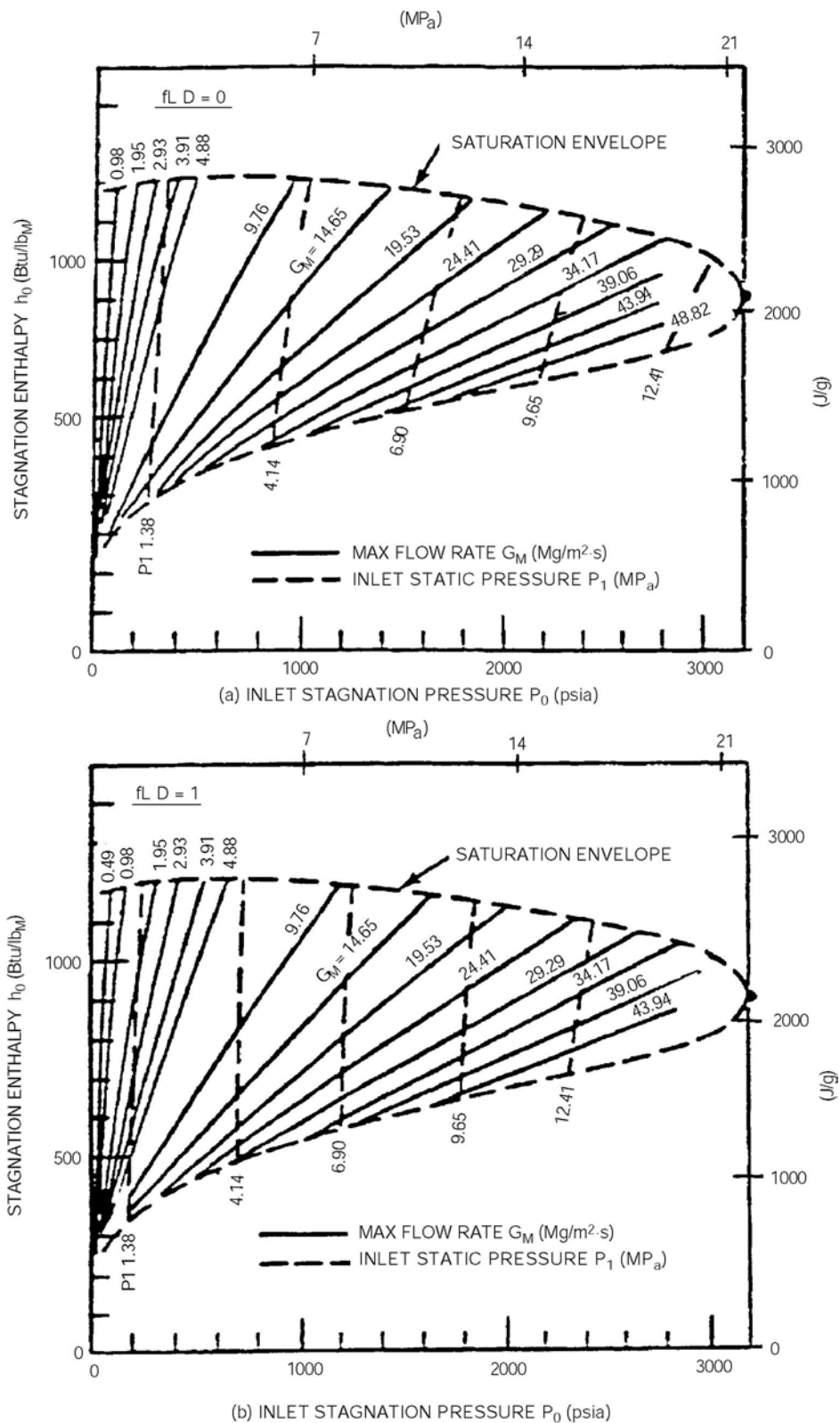


Figure 3E-20. Mass Flow Rates for Steam/Water Mixtures

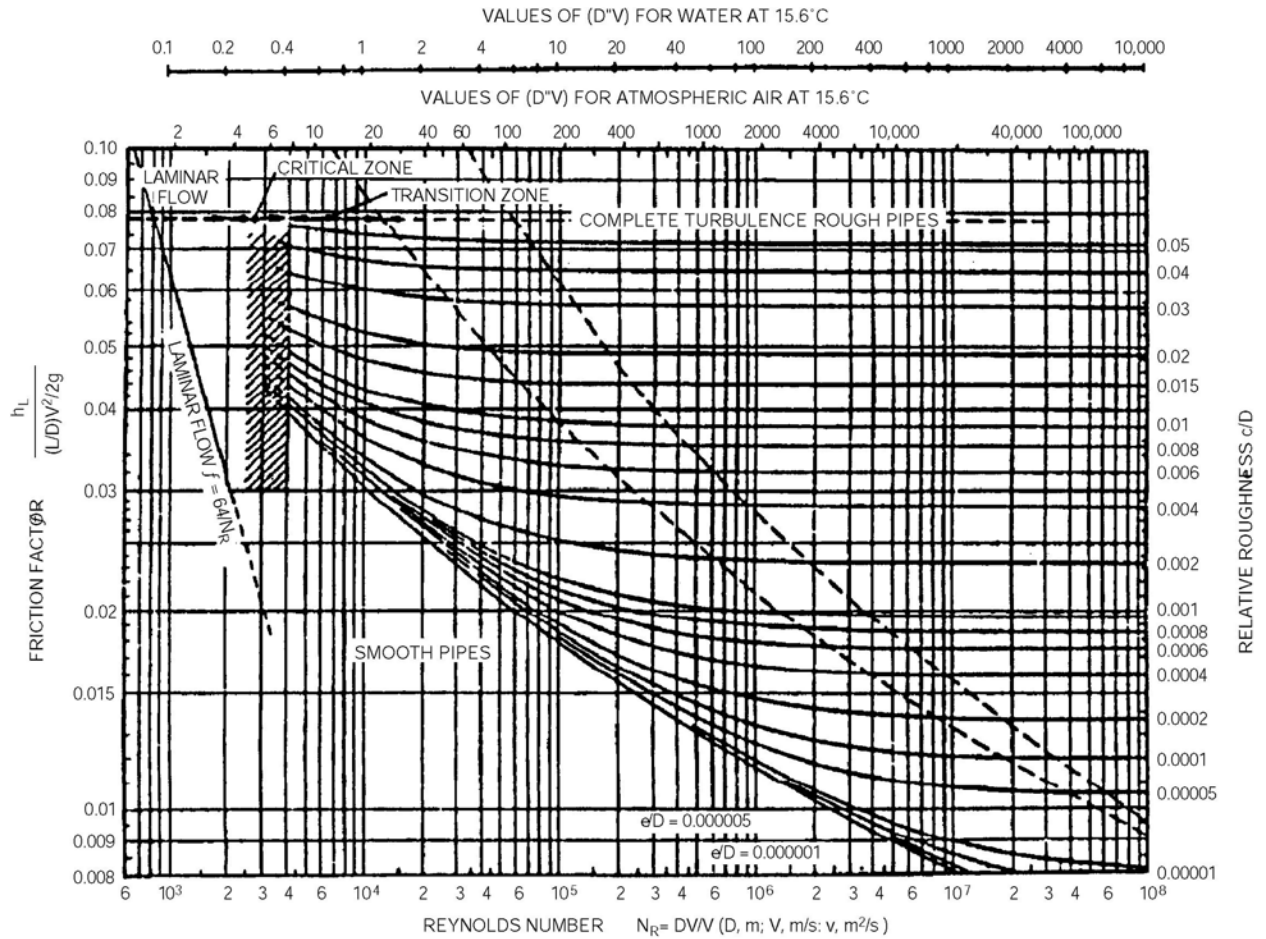


Figure 3E-21. Friction Factors for Pipes

3F. RESPONSE OF STRUCTURES TO CONTAINMENT LOADS

3F.1 SCOPE

This appendix specifies the design for safety-related structures, systems, and components as applicable due to dynamic excitations originating in the primary containment in the event of operational transients and LOCA. The input containment loads are described in Appendix 3B. The containment loads considered for structural dynamic response analysis are Condensation Oscillation (CO), Pool Chugging (CH), Horizontal Vent Chugging (HV) and Safety Relief Valve discharge (SRV) in the suppression pool, and Annulus Pressurization (AP) in the annulus between the Reactor Shield Wall (RSW) and Reactor Pressure Vessel (RPV).

3F.2 DYNAMIC RESPONSE

3F.2.1 Classification of Analytical Procedure

Analytical procedure of hydrodynamic loads is classified into following three groups:

- Pipe nozzle break loads for AP due to Main Steam (MS), Reactor Water Cleanup (RWCU) and Feedwater (FW) line breaks
- Symmetric loads in the suppression pool
- Asymmetric loads in the suppression pool

3F.2.2 Analysis Models

(1) Analysis Model

The structural models used in the analyses represent a synthesis of the Reactor Building (RB) model and the RPV model. The beam model used in the pipe break load analysis is illustrated in Figure 3F-1. The axisymmetric analysis model of the building structure is illustrated in Figure 3F-2 which is coupled with the RPV model shown in Figure 3F-3 for symmetric and asymmetric load cases.

(2) Structural Damping

Material damping values used for SRV and LOCA analyses are in accordance with Regulatory Guide 1.61.

3F.2.3 Load Application

(1) Pipe Break Nozzle Load

The AP pressures are converted to horizontal forces according to the following formula.

For RSW side:

$$F_j(t) = 2 \sum_{i=1}^8 P_{ij}(t) \int_{\theta=a_i}^{\theta=b_i} R \cos(\theta) d\theta \quad (3F-1)$$

For RPV side:

$$F_j(t) = -2 \sum_{i=1}^8 P_{ij}(t) \int_{\theta=a_i}^{\theta=b_i} r \cos(\theta) d\theta \quad (3F-2)$$

$F_j(t)$ = Force per unit height each level

$P_{ij}(t)$ = Pressure each level and angle

i = Cell No.

j = Level No.

R = RSW Inner Radius

r = RPV Outer Radius

l = Angle (180°)

a_i, b_i = Extreme angles of the arc on which the load is applied

Jet reaction, jet impingement, and pipe whip reaction forces are considered as constant force with a finite rise time of one millisecond. Pipe whip load is included as a transient load ending with a steady load.

(2) SRV Load

Symmetric SRV (all) response analysis is covered by $n=0$ harmonic. Asymmetric case of SRV (all) actuation is covered by $n=1$ harmonic that corresponds to overturning moment. The SRV air bubble frequencies are expected to be within a range of 5 to 12 Hz. Ways of selecting minimum number of bubble frequencies for dynamic analysis is selected as follows.

Frequency range of SRV Loads: $f_1 \leq f \leq f_2$ ($f_1 = 5$ Hz, $f_2 = 12$ Hz)

For vertical structural frequencies $(fs)_v$ ($n=0$):

- (a) If $(fs)_v > f_2$ then use f_2
- (b) If $f_1 < (fs)_v < f_2$ then use $(fs)_v$
- (c) If $f_1 > (fs)_v$ then use f_1

For horizontal structural frequencies $(fs)_h$ ($n=1$):

- (a) If $(fs)_h > f_2$ then use f_2
- (b) If $f_1 < (fs)_h < f_2$ then use $(fs)_h$
- (c) If $f_1 > (fs)_h$ then use f_1

In symmetric load case, three vertical frequencies of 5 Hz (SRV-V1), 6.06 Hz (SRV-V2) and 12 Hz (SRV-V3) are selected. In asymmetric load case, 3 horizontal frequencies of the

structure within the above range SRV-H1=5 Hz, SRV-H2=8.83 Hz and SRV-H3=12 Hz are adopted as bubble frequencies.

(3) HV Load

Both symmetric and non-symmetric upward loads are considered on the ventwall structure due to chugging in the top horizontal vents.

(4) Chugging, Condensation Oscillation Loads

According to the study of the natural frequencies of the structure and the frequencies of the input motion, 7 critical pressure time histories out of 16 for CH and 3 out of 4 for CO, are selected for dynamic analysis. Furthermore, one local spike load is added in CO response study.

3F.2.4 Analysis Method

(1) Pipe Nozzle Break Load Analysis

For these analyses, multi-input excitation time history analyses are performed using a full transient analysis. Material-dependent damping ratios are used in accordance with Subsection 3.7.2.13.

(2) Symmetric Load Analysis

For the dynamic response analyses of SRV and LOCA cases, the full harmonic analysis solution method is used. The input time history is first transformed into harmonic loads. Each harmonic loading is analyzed individually for Fourier $n=0$ spatial distribution in the frequency domain. Responses to each harmonic loading are transformed back to the time domain and then superimposed, on a time consistent basis, to obtain the total responses. Material-dependent damping ratios are used.

(3) Asymmetric Load Analysis

The same analysis approach as symmetric loads is used except that Fourier $n=1$ spatial distribution is considered.

3F.3 HYDRODYNAMIC LOAD ANALYSIS RESULTS

The acceleration response spectra at selected locations for each loading event are presented in Figures 3F-4 through 3F-22. The maximum displacements and accelerations at selected locations for each loading event are presented Tables 3F-1 through 3F-4.

The input excitation of suppression pool boundary horizontal loads (SRV, CH, and HV) is considered unidirectional which can be set at any direction in the horizontal plane, and the AP analysis is performed assuming that pipe break can be associated with any one of the vessel nozzles for each of the postulated line breaks.

The resulting response of structures considered in the analyses is thus unidirectional applicable to any azimuth angle for suppression pool loads and to the horizontal direction corresponding to the break direction for AP loads.

For subsystem analyses using floor response spectra and, if applicable, building displacement data, the input direction of the horizontal load is selected to result in the worst subsystem response.

As an alternate approach, the horizontal input to the subsystem may be taken to be the same in the two orthogonal horizontal directions.

Table 3F-1**Maximum Accelerations for AP Loadings (g)**

Location	Node	MS	RWCU	FW
Top of Vent wall	701	0.0007	0.01	0.0003
Top of pedestal	706	0.0006	0.0003	0.0002
Upper pool slab	208	0.0006	0.021	0.0003

Table 3F-2

Maximum Accelerations for Hydrodynamic Loads (g)

Location	Direction	Node	SRV	HV	CH	CO
Top of vent wall	Horizontal	1104	0.01	0.001	0.02	0.16
	Vertical	1104	0.07	0.023	0.121	
SP Floor	Horizontal	1254	0.02	0.001	0.038	0.14
	Vertical	1254	0.07	0.007	0.180	
RCCV Top slab side	Horizontal	1119	0.02	0.000	0.011	0.05
	Vertical	1119	0.04	0.000	0.045	
RCCV Top slab centre	Horizontal	1159	0.02	0.000	0.011	0.04
	Vertical	1159	0.03	0.000	0.016	

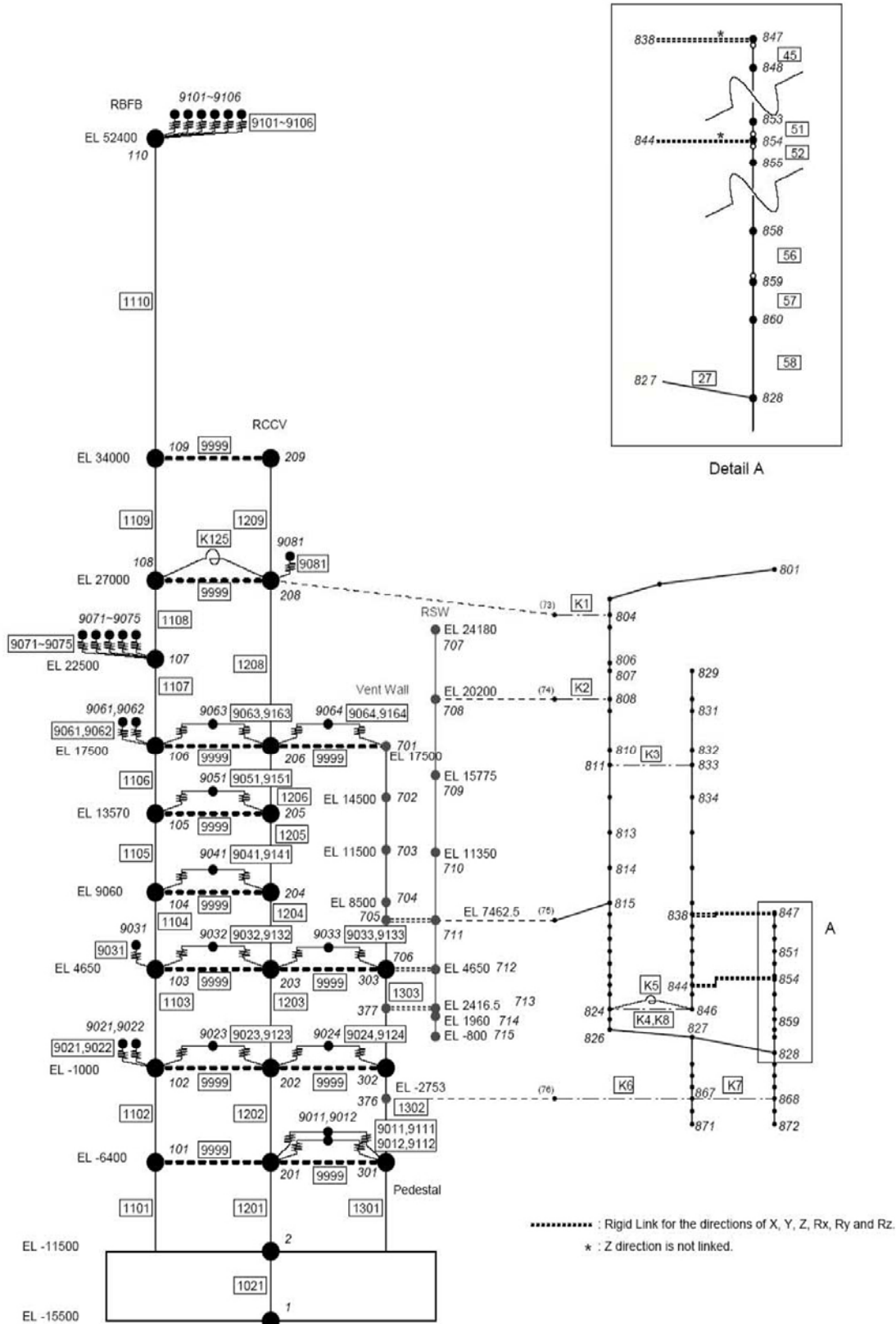
Table 3F-3**Maximum Displacements for AP Loadings (mm)**

Location	Node	MS	RWCU	FW
VW Top	701	0.004	0.0043	0.004
Top of Pedestal	706	0.003	0.002	0.003
Upper pool slab	208	0.0045	0.0075	0.005

Table 3F-4

Maximum Displacements for Hydrodynamic Loads (mm)

Location	Direction	Node	SRV	HV	CH	CO
VW Top	Horizontal	1104	0.14	0.0	0.005	1.66
	Vertical	1104	0.41	0.0	0.036	
SP Floor	Horizontal	1254	0.09	0.0	0.008	1.52
	Vertical	1254	0.38	0.0	0.040	
RCCV Top Slab Side	Horizontal	1119	0.17	0.0	0.006	1.17
	Vertical	1119	0.28	0.0	0.016	
RCCV Top Slab Centre	Horizontal	1159	0.17	0.0	0.006	1.23
	Vertical	1159	0.34	0.0	0.011	





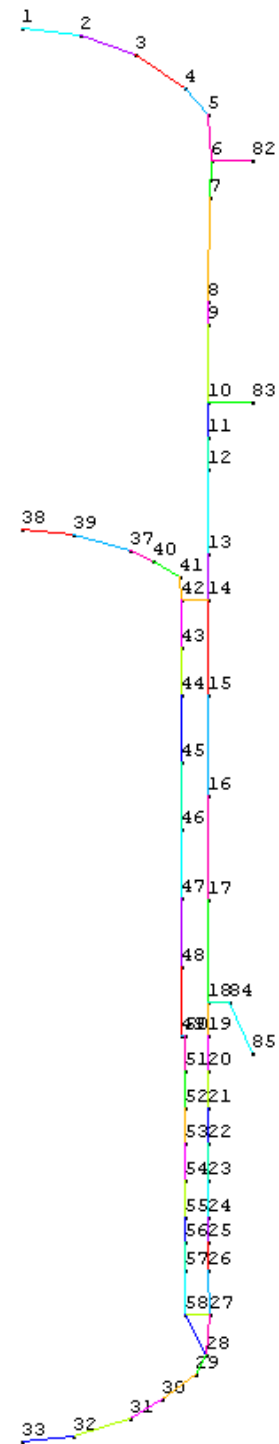


Figure 3F-3. RPV Shell Model

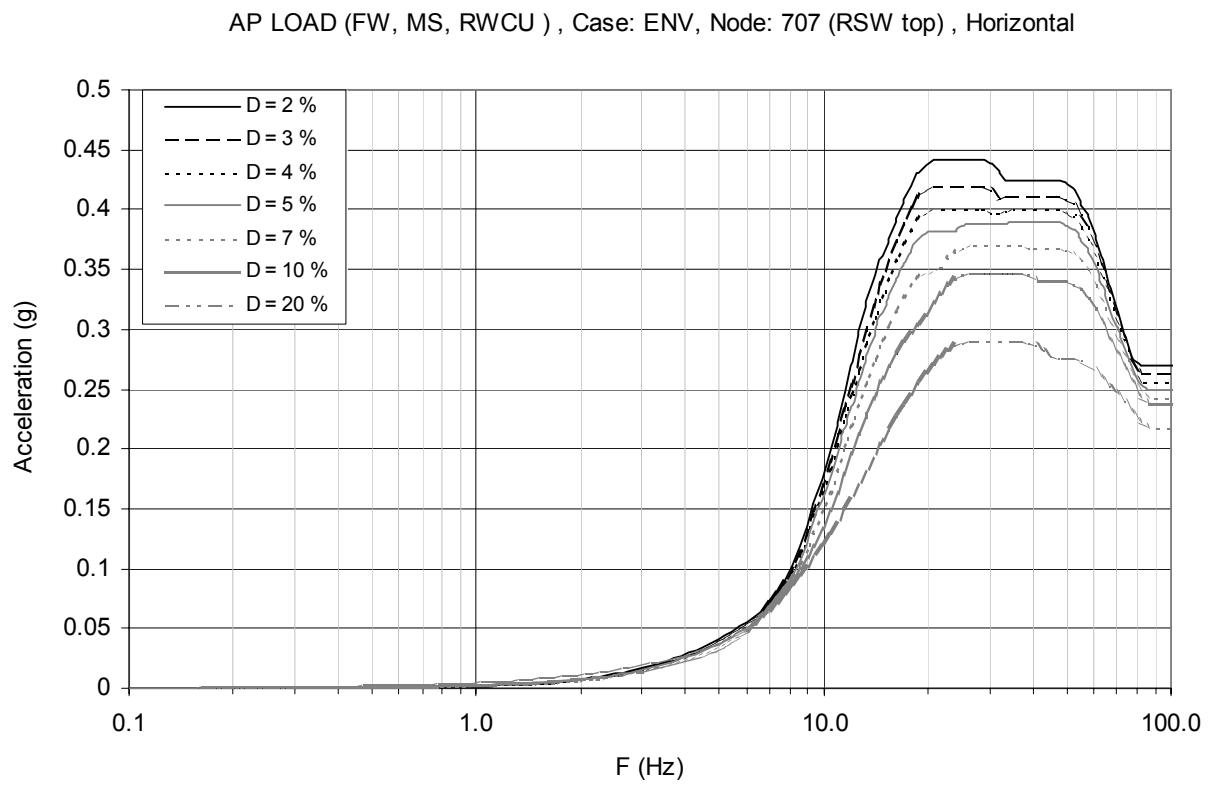


Figure 3F-4. Floor Response Spectrum—AP Envelope, Node: 701, Horizontal

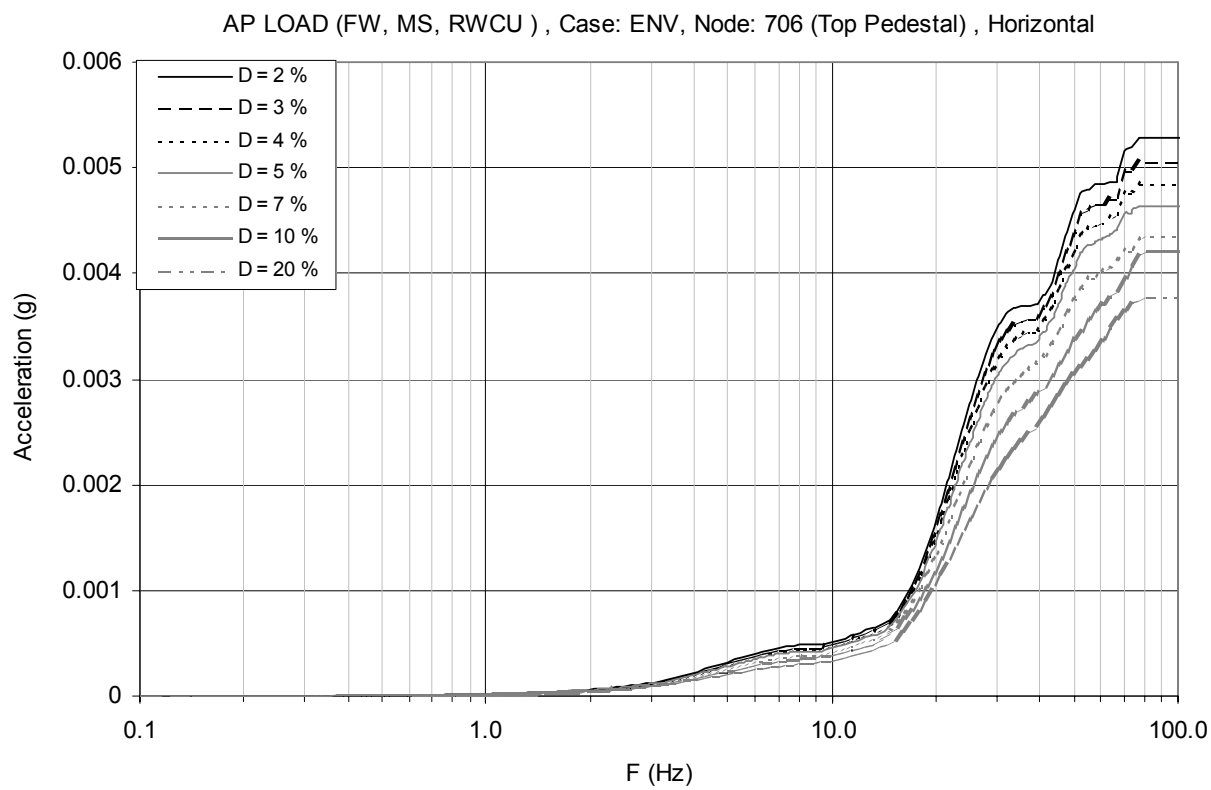


Figure 3F-5. Floor Response Spectrum—AP Envelope, Node: 706, Horizontal

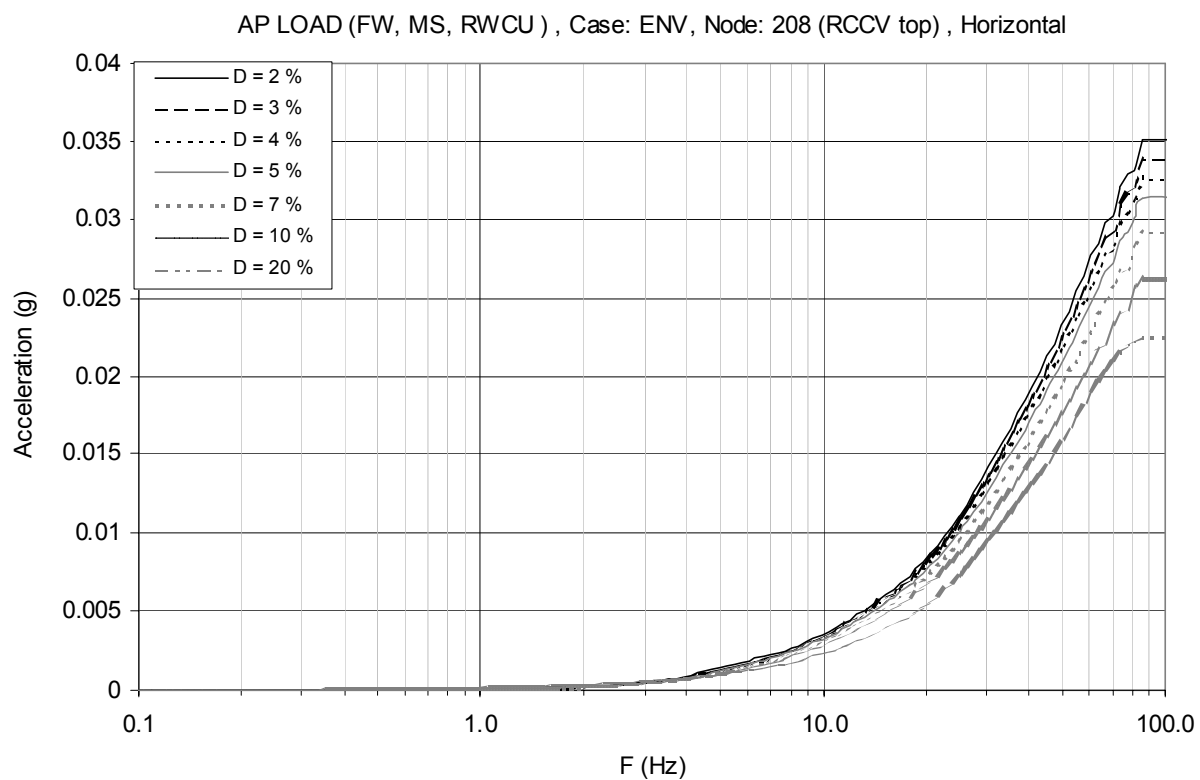


Figure 3F-6. Floor Response Spectrum—AP Envelope, Node: 208, Horizontal

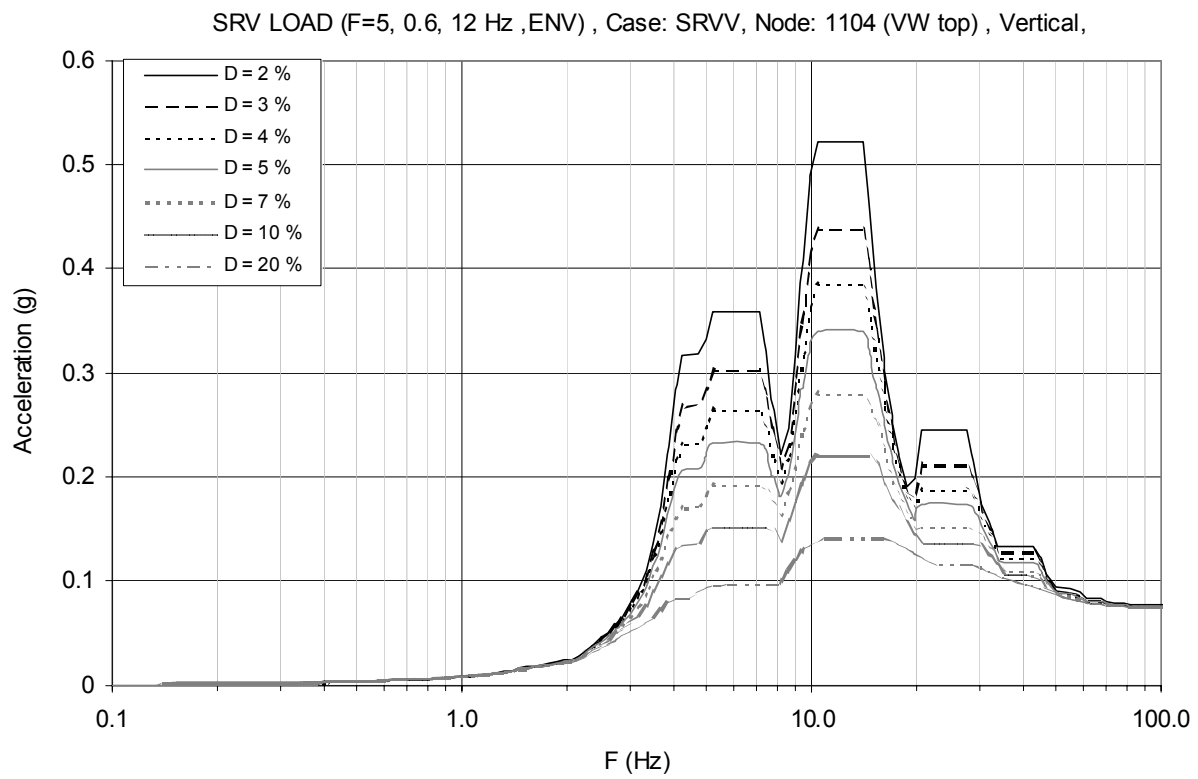


Figure 3F-7. Floor Response Spectrum—SRV Envelope , Node: 1104, Vertical

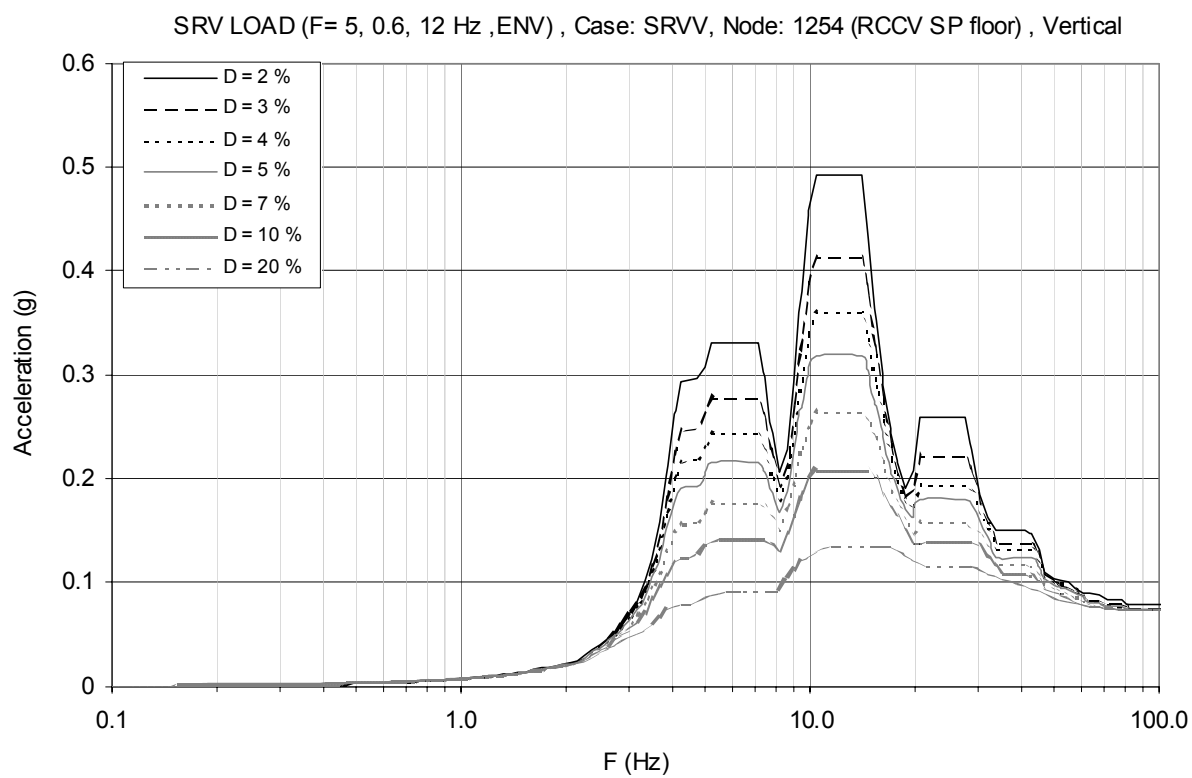


Figure 3F-8. Floor Response Spectrum—SRV Envelope , Node: 1254, Vertical

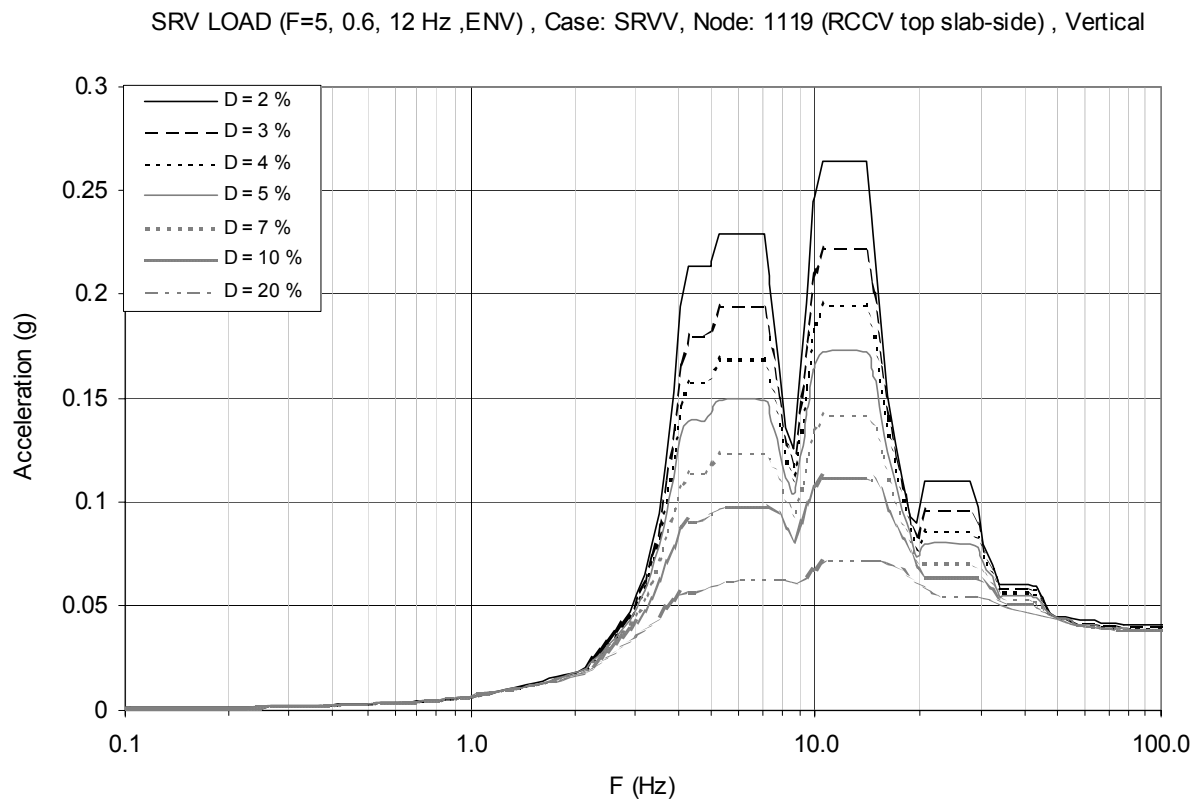


Figure 3F-9. Floor Response Spectrum—SRV Envelope , Node: 1119, Vertical

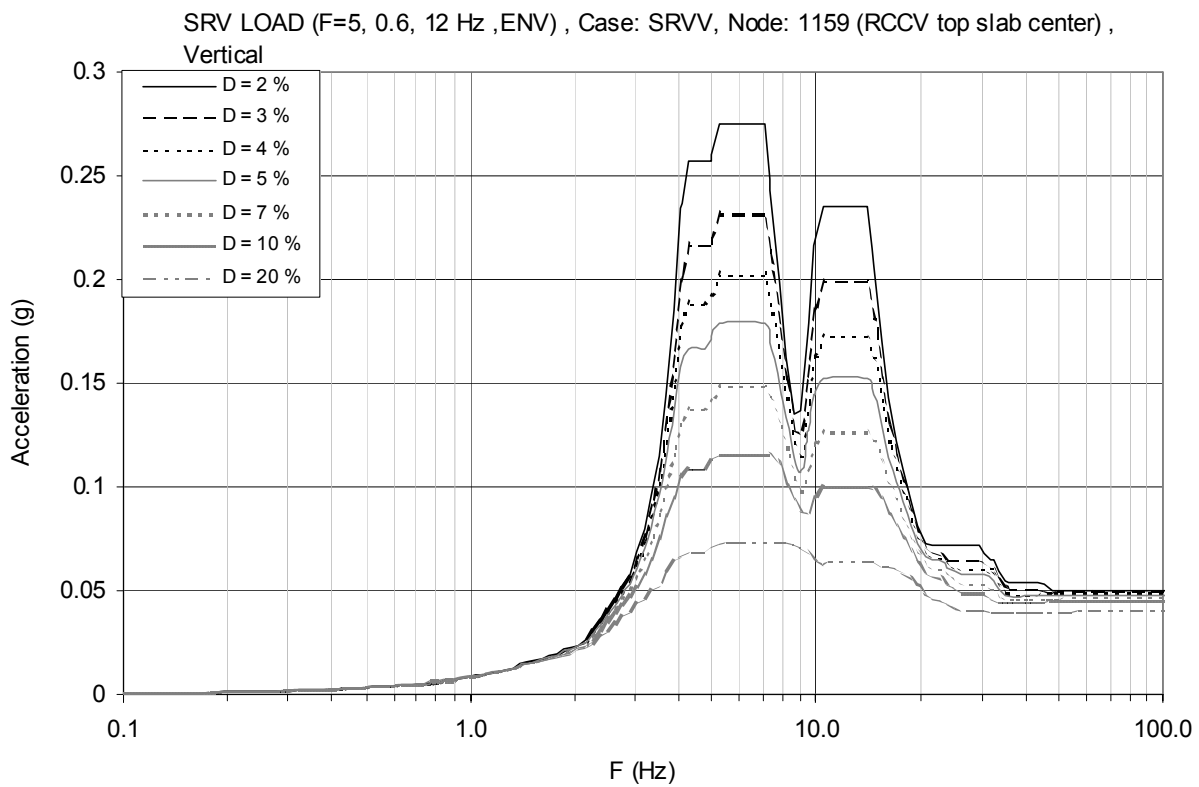


Figure 3F-10. Floor Response Spectrum—SRV Envelope , Node: 1159, Vertical

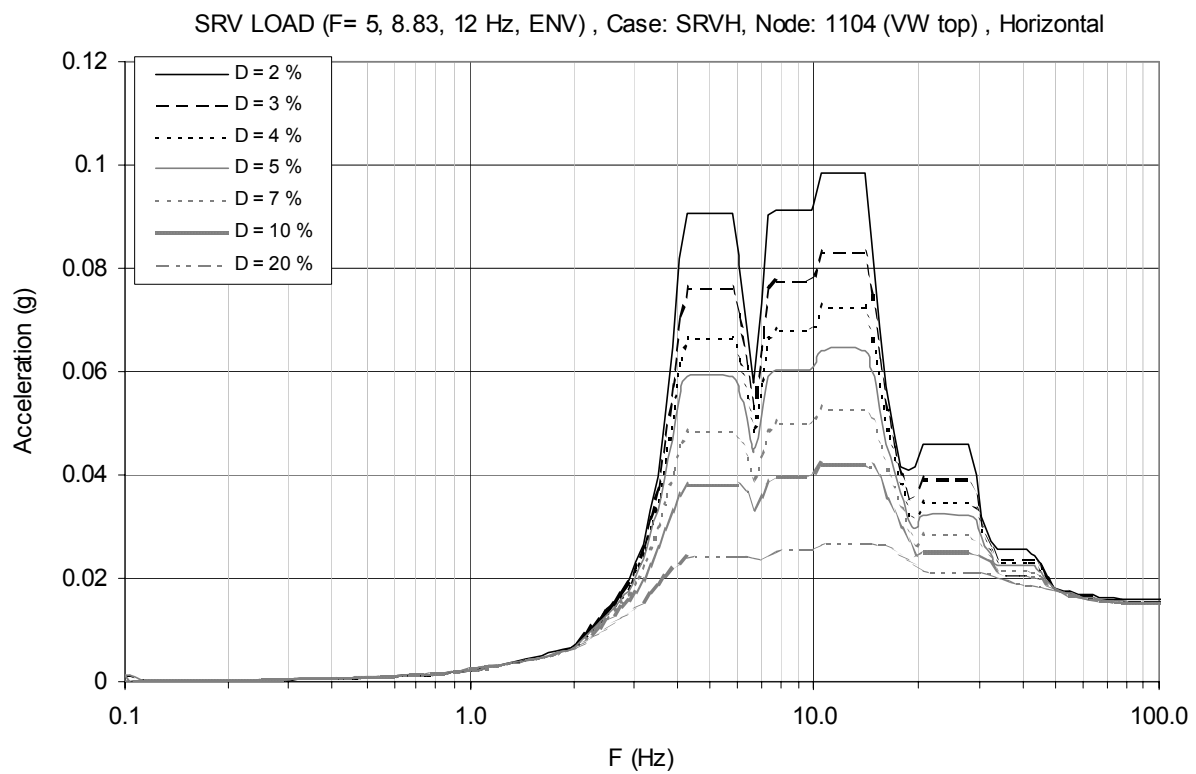


Figure 3F-11. Floor Response Spectrum—SRV Envelope , Node: 1104, Horizontal

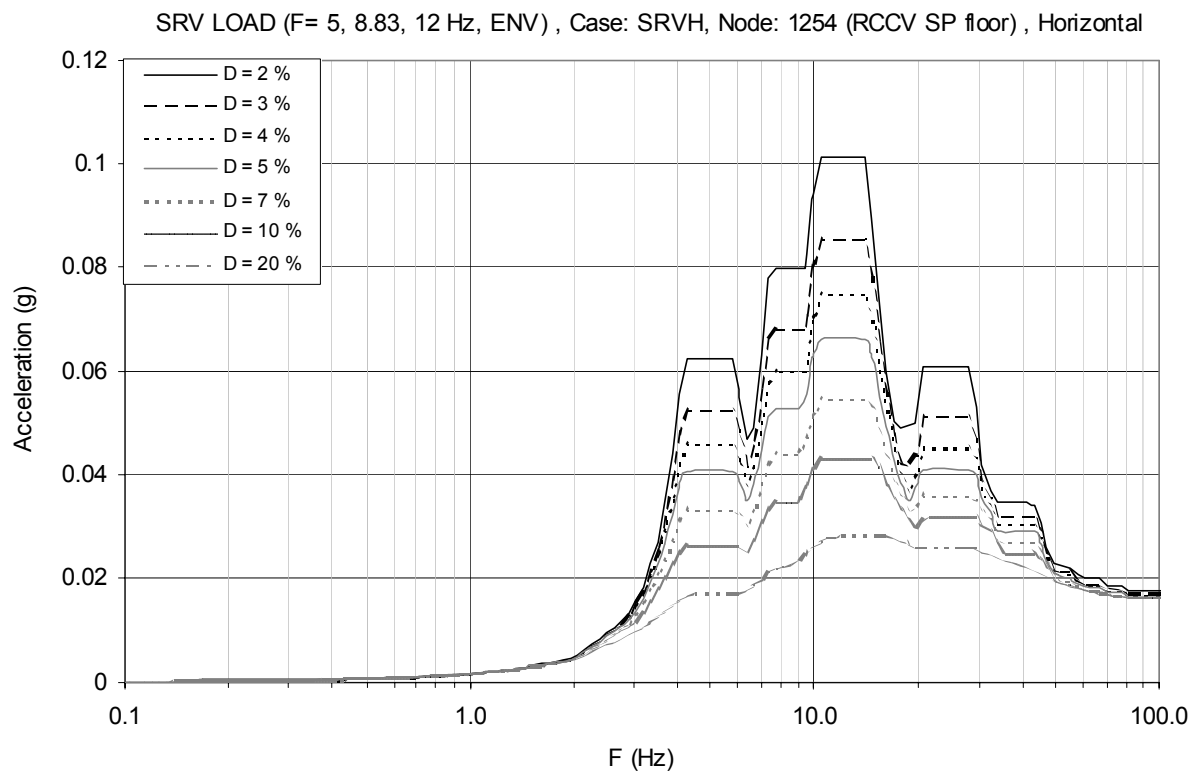


Figure 3F-12. Floor Response Spectrum—SRV Envelope , Node: 1254, Horizontal

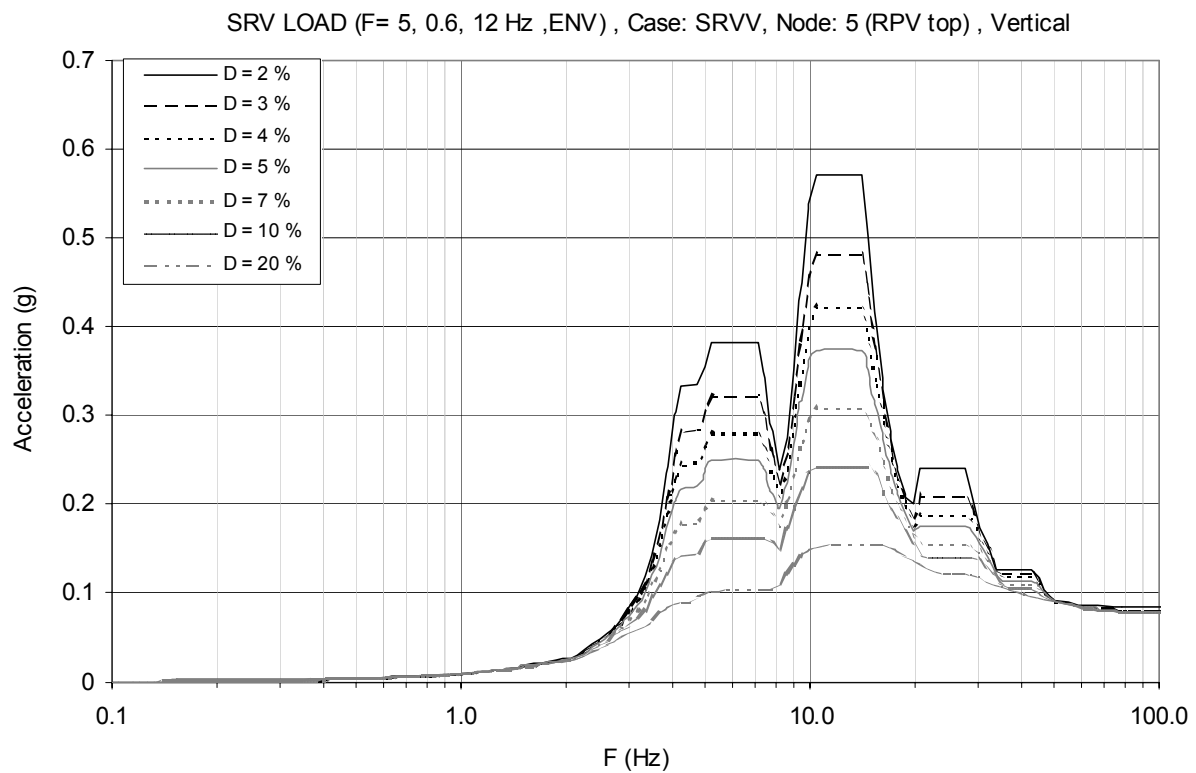


Figure 3F-13. Floor Response Spectrum—SRV Envelope, Node: 1119, Vertical

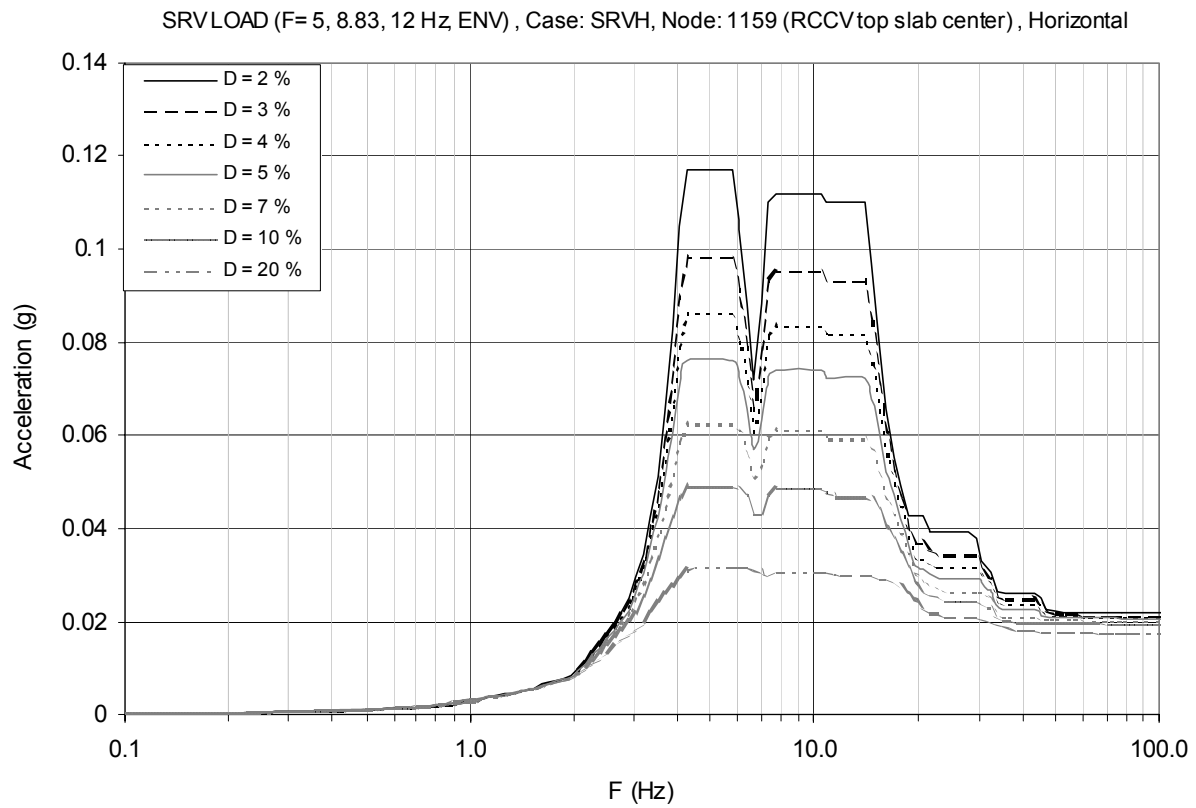


Figure 3F-14. Floor Response Spectrum—SRV Envelope, Node: 1159, Horizontal

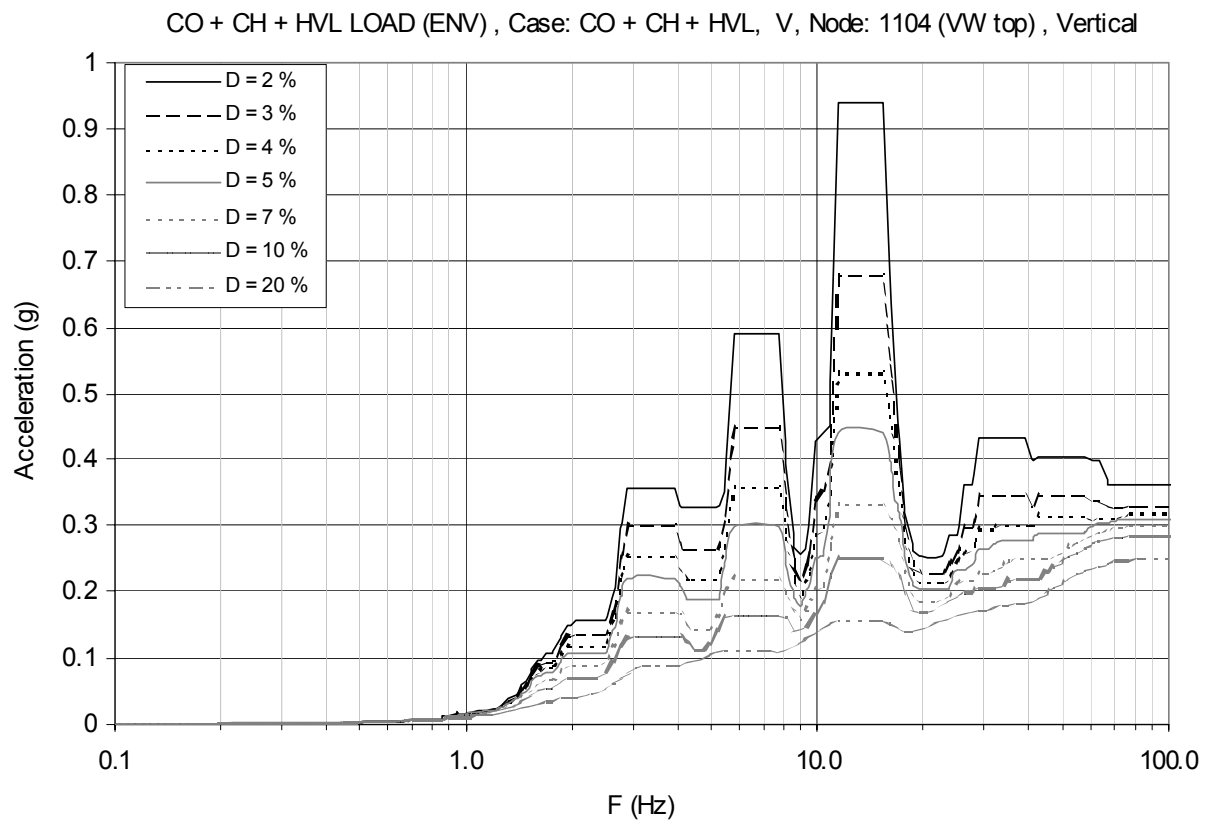


Figure 3F-15. Floor Response Spectrum—CH & CO Envelope, Node: 1104, Vertical

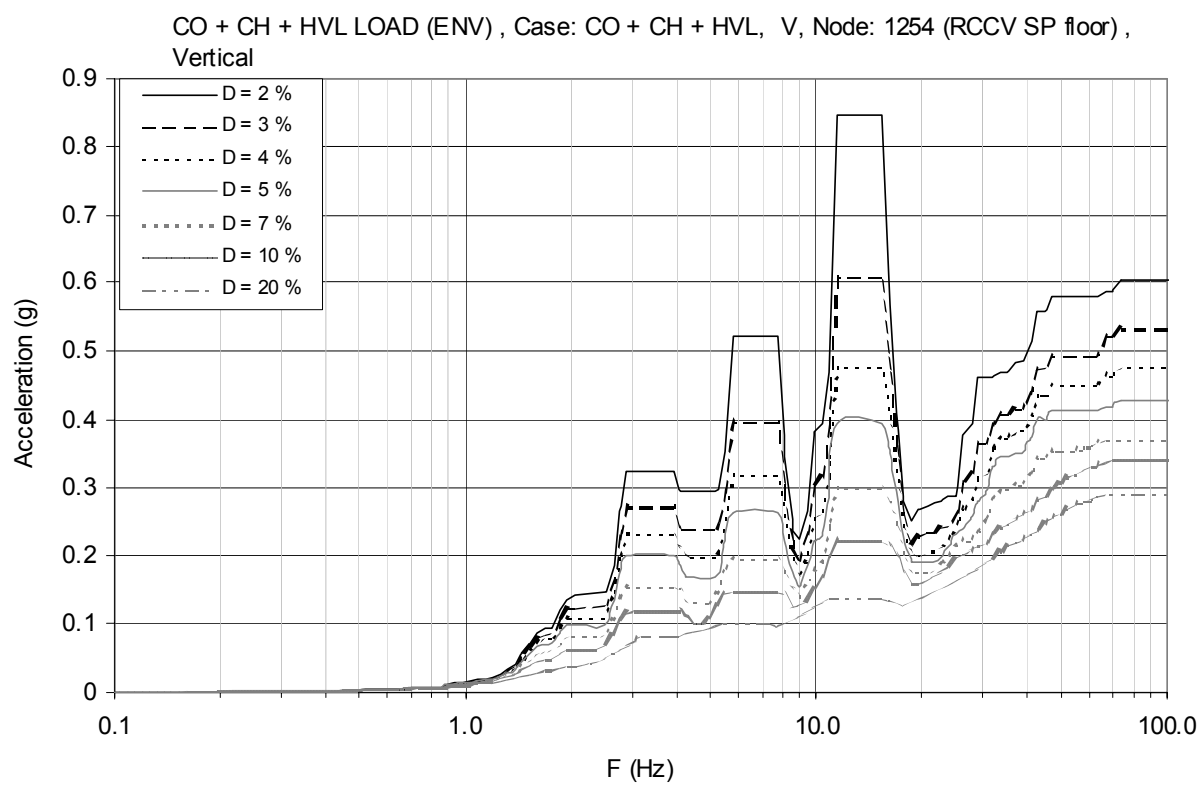


Figure 3F-16. Floor Response Spectrum—CH & CO Envelope, Node: 1254, Vertical

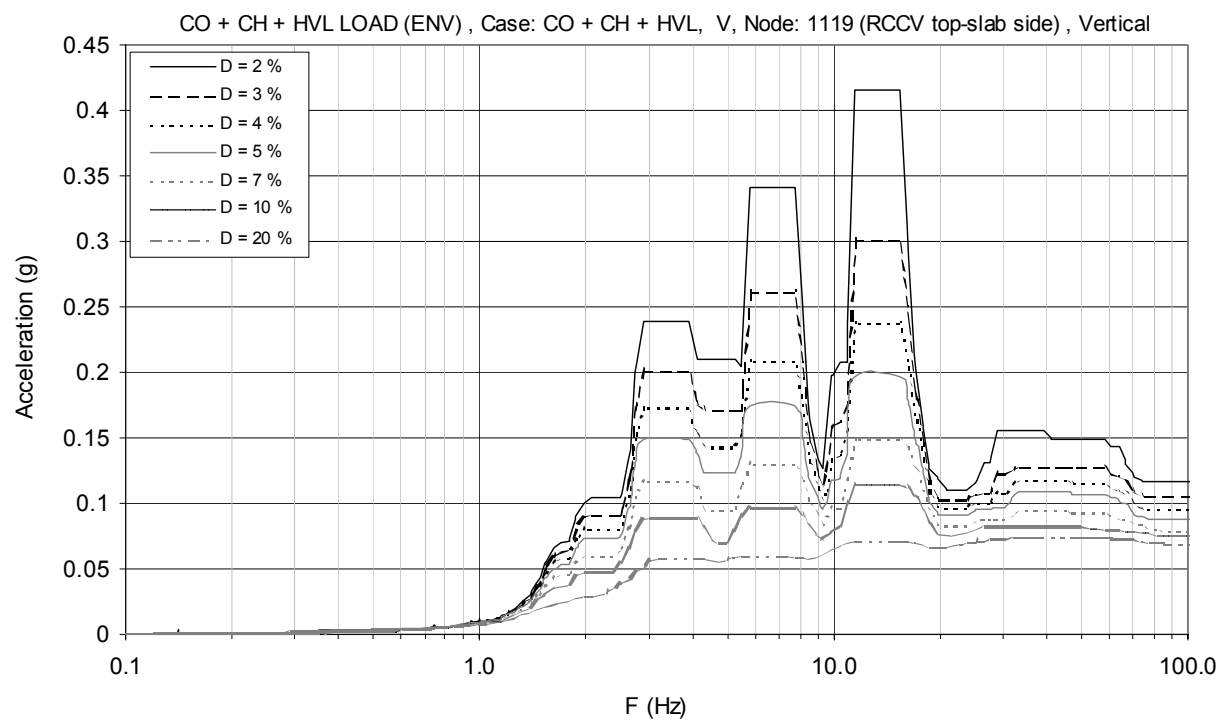


Figure 3F-17. Floor Response Spectrum—CH & CO Envelope, Node: 1119, Vertical

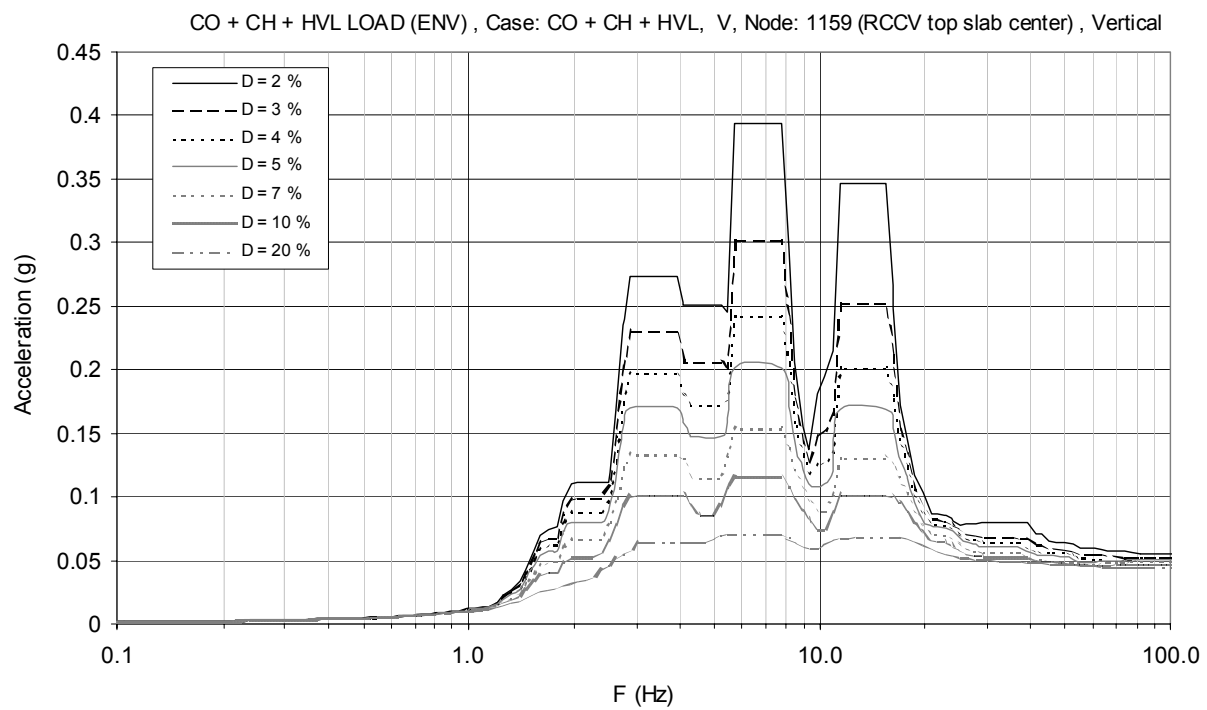


Figure 3F-18. Floor Response Spectrum—CH & CO Envelope, Node: 1159, Vertical

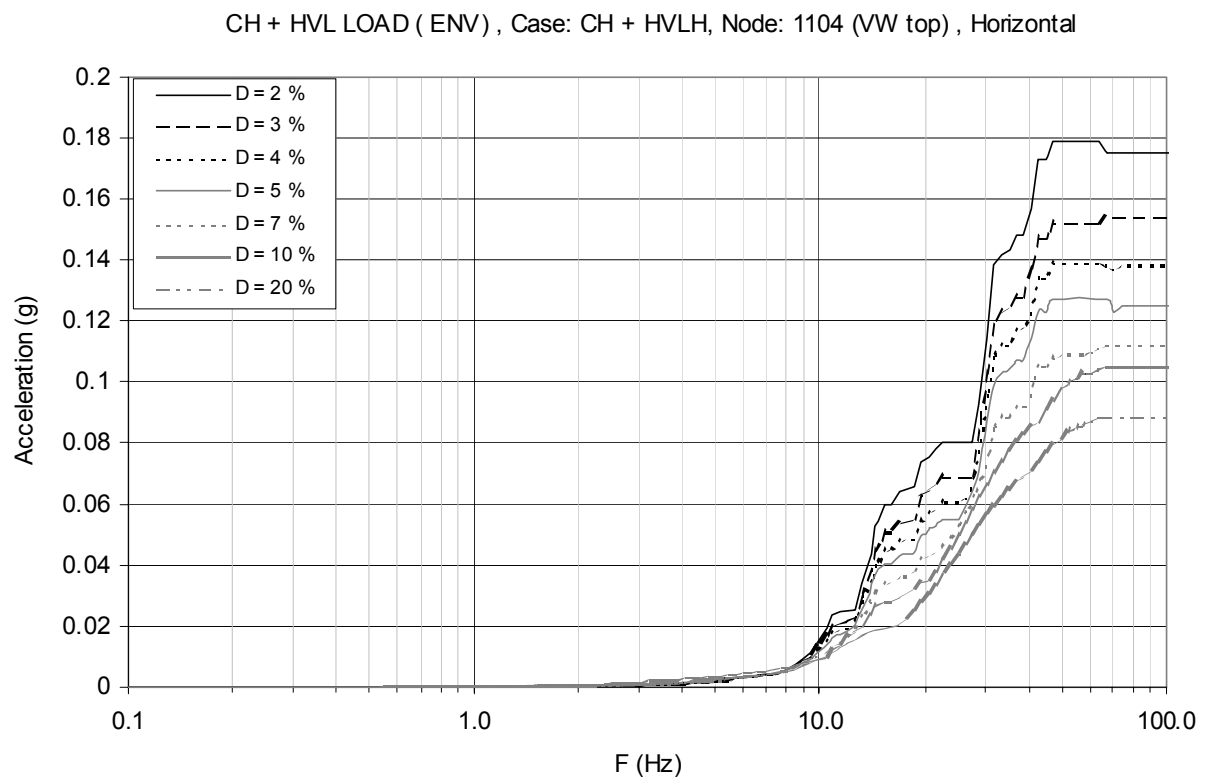


Figure 3F-19. Floor Response Spectrum—CH Envelope, Node: 1104, Horizontal

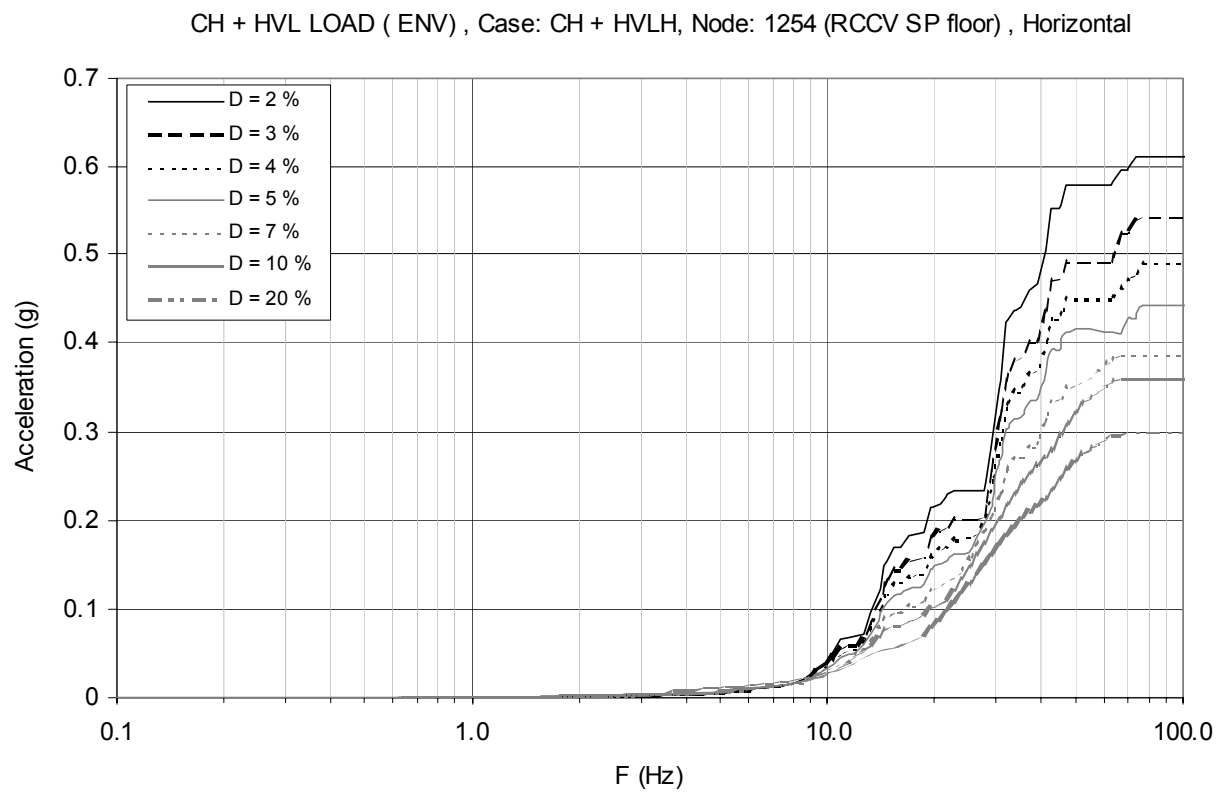


Figure 3F-20. Floor Response Spectrum—CH Envelope, Node: 1254, Horizontal

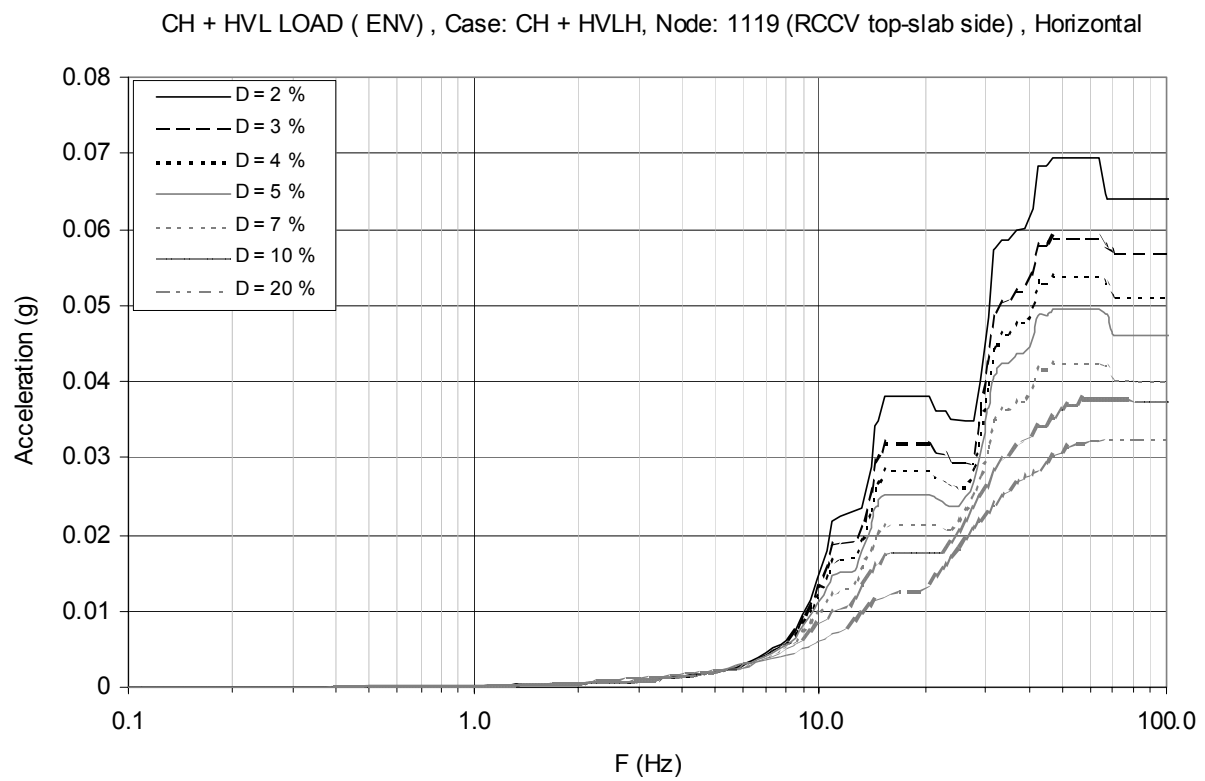


Figure 3F-21. Floor Response Spectrum—CH Envelope, Node: 1119, Horizontal

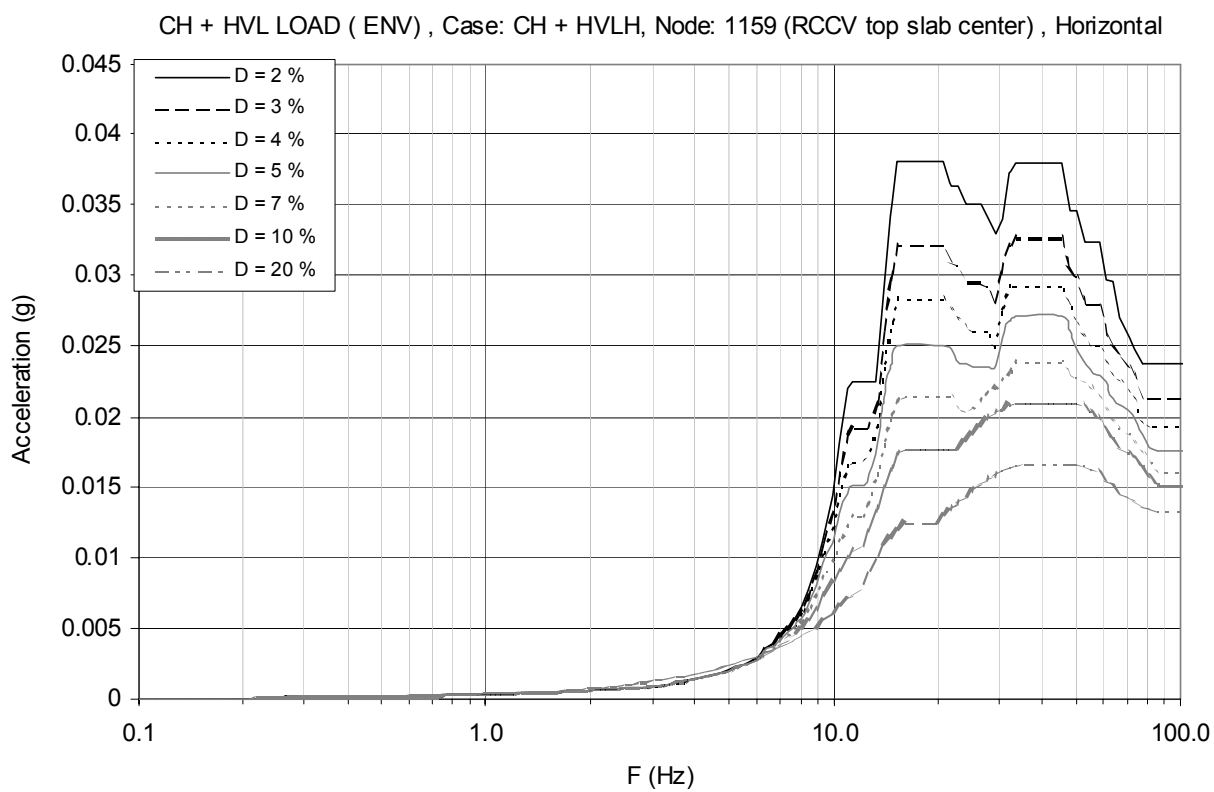


Figure 3F-22. Floor Response Spectrum—CH Envelope, Node: 1159, Horizontal